IMT School for Advanced Studies, Lucca
Lucca, Italy

Cohesive and Variational Methods for Fracture Mechanics in Statics and Fatigue

PhD Program in Systems Science

Track in Computer Science and Systems Engineering

XXXIV Cycle

By

Pavan Kumar Asur Vijaya Kumar

2022

The dissertation of Pavan Kumar Asur Vijaya Kumar is approved.

PhD Program Coordinator: Prof. Rocco De Nicola, IMT School for Advanced Studies Lucca

Advisor: Prof. Marco Paggi, IMT School for Advanced Studies Lucca

Co-Advisor: Prof. Jose Antonio Reinoso Cuevas, Universidad de Sevilla

The dissertation of Pavan Kumar Asur Vijaya Kumar has been reviewed by:

Prof. Julien Yvonnet, Université Paris-Est Marne-la-Vallée

Prof. Emilio Martínez Pañeda, Imperial College London

Prof. Daniela Addessi, La Sapienza University of Rome

IMT School for Advanced Studies Lucca
2022

That Thou Art. To the oneness of existence.

Contents

List of Figures

List of Tables

Acknowledgements

Samuel Taylor in 1828 stated *"The Dwarf sees further than the giant, when he has the giant's shoulders to mount on"*. Truly and surely, there were great scientists, philosophers, madman, who created science as their life, whom I owe my highest gratitude.

To start with, I consider myself lucky, feel humbled to be a PhD student under the guidance of Prof. Marco Paggi whose office doors were always open for discussions and talks. In spite of my silly questions, he never hesitated for a moment to guide me. He allowed me freedom to work on the topics which I preferred. The meetings and conversations were inspiring to me to analyse and understand research from multiple perspectives to form a comprehensive and objective critique. Thank you so much Prof. Marco Paggi.

I'm eternally grateful to my Co-Advisor Dr. José Reinoso Cuevas who pushed me to the edge and made me realize my true potential. A friend, mentor and moreover a great human being, under his guidance I spent six months during my visit to Seville. It would be impossible to count all the ways that you guided me in this three and half year of PhD. I admire you for your humility, unwavering purpose and great sense of values. I can't thank you enough.

I thank Dr. Aamir Dean for his enthusiasm for the project, support, encouragement and patience, with whom I share tons of memories. I am extremely grateful for our friendly chats at the end of our meetings and your personal support in my academic endeavours apart from the intellectually stimulating discussions. Your mentorship and friendship has been a valuable gift in last three years. One day, I hope to inspire someone else as you've inspired me.

Part of the present thesis is based on the articles published and listed in the publications section. The work presented in thesis are based on the article co-authored by Prof. Marco Paggi, Prof Jose Reinoso, Dr. Aamir Dean and Dr. Pietro Leonarda, Dr. Shadab Sahraee, Dr. Christian

Gerendt, Prof. Elsang Mahdi, Prof. Raimund Rolfes, and Zeng Liu. I express my sincere gratitude all my co-authors who inspired me and for the fruitful discussions.

I also would like to acknowledge funding's from the Italian Ministry of Education, University and Research to the Research Project of National Interest (PRIN "XFAST-SIMS: Extra fast and accurate simulation of complex structural systems" (Grant Agreement no. 20173C478N) and Consejería de Economía y Conocimiento of the Junta de Andalucía (Spain) for financial support under the contract US-1265577-Programa Operativo FEDER Andalucía 2014-2020. I also acknowledge the support of the Spanish Ministerio de Ciencia, Innovación y Universidades the under the grant PID2019-109723GB-I00 and Consejería de Economía y Conocimiento of the Junta de Andalucía (Spain) under the grant P2-00595.

Moreover, I would like to acknowledge the funding from the Erasmus+ program of the European Union for the traineeship which was utilized for six months of visiting period at the University of Seville (Spain) started in November 2019 and six months of visiting period at the Université Gustave Eiffel (France) starting from November 2021. The funding led to the investigation described in Chapter 3 and Chapter 5 respectively. I would like to sincerely thank Dr. Adrià Quintanas Corominas, Dr. Lorenzo and Dr. Isreal Garcia, for being available for open discussions and guiding in Seville and Prof Qi-Chang-HE and Prof Julien Yvonnet for their warmest welcome in Paris and guiding me to understand the fatigue effects and teaching me topology optimisation (Excluded in the thesis).

My Riches do not lie in the material possessions, but having great friends. Thank you, Francis John (Dada), for wise advice and the memories we share, Dila Suay for showing me new perspectives in life and making me open to experiences and life, Jiji (Virginio) for being an awesome roommate, Ángel Valverde González whose heart is as big as his height and , Maria Rosaria Marulli for sharing a lot of drinks (also projects) and memories in IMT and in Seville, Deison Preve (Coach) for guiding me in the gym and numerous discussions we had on all sort of things, Zainab Alwaisi for your inspiration and never giving up attitude, Wu Liang for all the kebab we shared, Yara El Rassi for showing me my own brain (also telling me about my tinnitus) and lots of interesting talks, Demetrio Grollero for being a beautiful friend, Victor Ortiz for all the excellent talks we had and the experience we shared.

Thank you very much, Niraj Rathod, for all the advice, Surya Soman for being an awesome senior, Sampath Mulagaleti for showing me how to remain calm and critical (but to scream inside), Evgenia Bednaya for introducing me to neuro-science and inner works of academic work, Laura Ferrarotti for many many discussions and Chaira Battaglini for advising me. Thanks you guys for all the parties together we had.

Not to forget, my fantastic friend Abhilash PK for being there with me for 7 long years, working together with me on a lot of projects and sharing a lot of adventures together, Arun Pandey for being roommate for 2 years and making me learn some manners, Bikas Adhikari for being a fantastic friend for 5 long years and helping me to become person, Mahalya for being there with me for 7 years and Vidya, who is my life long friend for 22 years with whom I share numerous memories. These not just bear me as a friend made me a better person without judging me for anything. I am grateful to have you all.

Finally, I thank my brother Shashank for sharing my spiritual journey. My Guru Sri Sadguru and Isha foundation, without ever meeting, changed my life completely. My inspiration was Late Vivekananda, whose books made me wiser than I could think.

Not to omit, I want to thank my parents and sisters for their love and belief in me for the last 27 years. Finally, I want to thank my partner Monisha for her love, care, affection, and presence in all situations of my life for the past 7 years. Thank you, my love.

Publications

1. **P.K Asur Vijaya Kumar**, A. Dean, J. Reinoso, P. Lenarda, M. Paggi, ”Phase field modeling of fracture in functionally graded materials: $\Gamma-$convergence and mechanical insight on the effect of grading”, Thin-Walled Structures 159 (2021) 107234. doi:https://doi.org/10.1016/j.tws.2020.107234.
2. A. Dean, **P.K Asur Vijaya Kumar**, J. Reinoso, C. Gerendt, M. Paggi, E. Mahdi, R. Rolfes, ”A multi phase-field fracture model for long fiber reinforced composites based on the puck theory of failure”, Composite Structures 251 (2020) 112446. doi:https://doi.org/10.1016/j.compstruct.2020.112446
3. **P.K Asur Vijaya Kumar**, A. Dean, J. Reinoso, M.paggi, ”A Multi Phase-Field-Cohesive Zone Model for Laminated Composites:Application to Delamination Migration”, Composite Structures, Volume 276, 15 November 2021, 114471. doi: https://doi.org/10.1016/j.compstruct.2021.114471
4. **P.K Asur Vijaya Kumar**, A. Dean, S. Sahraee, J. Reinoso, M.paggi, ”Non-linear thermoelastic and fracture analysis of thin-walled structures with cohesive–like interfaces relying on the solid shell concept”, Finite Elements in Analysis and Design, Volume 202, 1 May 2022, 103696. doi: https://doi.org/10.1016/j.finel.2021.103696
5. **P.K Asur Vijaya Kumar**, A. Dean, J. Reinoso, M.paggi, ”Nonlinear thermoelastic phase-field fracture of thin-walled structures relying on solid shell concepts: Theory and applications”, Computer Methods in Applied Mechanics and Engineering, Volume 396, 1 June 2022, 115096. https://doi.org/10.1016/j.cma.2022.115096
6. **P.K Asur Vijaya Kumar**, A. Dean, J. Reinoso, M.paggi, ” Thermo-Elastic Phase-Field Analysis of Thin Walled Functionally Graded Materials based on Solid Shell”, Thin-Walled Structures Volume 179, October 2022, 109535. https://doi.org/10.1016/j.tws.2022.109535

Conference/Talks

1. **P.K Asur Vijaya Kumar**, A. Dean, J. Reinoso, M. Paggi, ”A Multi Phase Field-Cohesive Zone Model(MPF-CZ) for fiber reinforced composites relying on Puck failure criteria”, ICCS23- 23^{rd} International Conference on Composite Structures, at Porto, Portugal.
2. A. Dean, **P.K. Asur Vijaya Kumar**, A.Babiker, M. Brod, S.E.M Ahmed, J. Reinoso, E. Mahdi, ”Phase-Field Modeling of Damage and Fracture in Laminated Unidirectional Fiber Reinforced Polymers” at CCE 2020: 3^{rd} Conference on Civil Engineering at Omdurman, Sudan.
3. **P.K Asur Vijaya Kumar**, A. Dean, J. Reinoso, M. Paggi, ”Nonlinear thermoelastic phase-field fracture of thin-walled structures relying on solid shell concepts: Theory and applications”, WorkShop-1, NewFrac, Seville, Spain.

Abstract

The widespread use of material over the past century has dramatically changed the world today. The reliability of any machine depends on the multiple complex interactions in the system leading to a failure. Hence, it is necessary to understand the failure mechanism of the structures with a multi-physics interaction. The present thesis explores the role of complex multi-physics in failure to understand the overall structural performance, including an interface between different materials.

Specifically, in Chapter-2, a phase field (PF) approximation of fracture for functionally graded materials (FGM) using a diffusive crack approach incorporating the characteristic length scale as a material parameter is herein proposed. A rule of mixture is employed to estimate the material properties, according to the volume fractions of the constituent materials, which have been varied according to given grading profiles. Based on the ideas stemming from the study of size-scale effects, Γ-convergence for the proposed model is proved when the internal length scale is either constant or a bounded function. Crack propagation events in conjunction with the differences with respect to their homogeneous surrogates are discussed through several representative applications, providing equivalence relationships for size-scale effects and demonstrating the applicability of the current model for structural analysis of FGMs.

Failure processes in Laminated Fiber-Reinforced Composites (LFRCs) entail the development and progression of different physical mechanisms and, in particular, the interaction between inter-laminar and intra-laminar cracking. Reliable modeling of such complex scenarios can be achieved by developing robust numerical predictive tools that allow for the interaction of both failure modes. In Chapter-3, a novel Multi Phase-Field (MPF) model relying on the Puck theory of failure for intra-laminar failure at ply level is coupled with a Cohesive Zone Model (CZM) for inter-laminar cracking. The computational tool is applied to qualitatively predict delamination migration in long laminated fiber-reinforced polymers composites comprising 44 cross-ply laminates. The reliability of the current approach is examined via the correlation with experimental results. Finally, the present study is complemented with additional representative examples with the aim of providing further insight into the potential role of different aspects of the system in the delamination migration, including (i) the variation of the ply angle in the migration zone, (ii) the load application point, and (iii) initial crack length.

The analysis of fracture phenomena of thin-walled structures has been a matter of intensive research in the last decades. These phenomena notably restrict the applicability of slender structures, especially under the influence of temperature. The research in Chapter-4 is concerned with the development of a thermodynamically consistent framework for the coupled thermo-mechanical phase-

field model for thin-walled structures using a fully-integrated finite elements. This enables the use of three-dimensional constitutive thermo-mechanical models for the materials. The proposed thermo-mechanical phase-field models are equipped with the EAS and ANS leading ti locking free element. Moreover, the same degradation function is used for both displacement field and thermal field. The coupled equations are numerically solved with ad hoc efficient solution schemes for nonlinear problems. Several numerical examples with and without phase-field (straight and curved shells) are provided to show the practicality and reliability of the proposed modeling framework. Moreover, the model is extended to incorporate FGM and the corresponding numerical examples are explored.

Using the framework developed in the Chapter-4, the locking free solid shell element is extended to include the fatigue effects in Chapter-5. As a natural consequence of the developed model, SN curve and crack extension curves are recovered for straight and curved shells.

Abstracto

El uso generalizado de los materiales durante el siglo pasado ha cambiado drásticamente el mundo actual. La fiabilidad de cualquier máquina depende de las múltiples interacciones complejas dentro de ella que pueden conducir a un fallo de la estructura. Por lo tanto, es necesario comprender el mecanismo de fallo de las estructuras con una interacción multi-física. La presente tesis explora el papel de la multi-física compleja en la fractura para comprender el rendimiento estructural general, teniendo en cuenta la consideración de una interfaz entre diferentes materiales.

Específicamente, en el Capítulo 2, se propone aquí una aproximación de la técnica de phase-field (PF) en fractura de functionally graded materials (FGM) usando un enfoque con fractura difusiva que incorpora la longitud de escala (length scale) como parámetro del material. Se emplea una regla de mezcla para estimar las propiedades del material, de acuerdo con las fracciones de volumen de los materiales constituyentes, que han variado de acuerdo con los perfiles de clasificación dados. Con base en las ideas derivadas del estudio de los efectos size-scale, se prueba la convergencia Γ para el modelo propuesto cuando la length scale es constante o una función acotada. Los fenómenos de propagación de grietas junto con las diferencias con respecto a sus sustitutos homogéneos se analizan a través de varias aplicaciones representativas, proporcionando relaciones de equivalencia para los efectos size-scale y demostrando la aplicabilidad del modelo actual para el análisis estructural de las FGM.

Los procesos de fractura en los Materiales Compuestos Laminados Reforzados con Fibra (MCLRF) implican el desarrollo y progresión de diferentes mecanismos físicos y, en particular, la interacción entre la fractura interlaminar e intralaminar. Se puede alcanzar un modelado confiable en escenarios tan complejos mediante el desarrollo de herramientas predictivas numéricas robustas que permitan la interacción de ambos modos de fractura. En el Capítulo 3, un nuevo modelo de multi phase-field (MPF) que se basa en el criterio de fallo de Puck para la fractura intralaminar a nivel de capa se combina con la técnica Cohesive Zone Model (CZM) para la fractura interlaminar. La herramienta computacional se aplica para predecir cualitativamente la migración de la delaminación en compuestos de polímeros reforzados laminados con fibras largas que comprenden 44 laminados de capas cruzadas. La fiabilidad del enfoque actual se examina a través de la correlación con los resultados experimentales. Finalmente, el presente estudio se complementa con ejemplos representativos adicionales con el objetivo de brindar una mayor comprensión en diferentes aspectos del sistema en la migración de la delaminación, incluida (i) la variación del ángulo de la capa en la zona de migración, (ii)) el punto de aplicación de la carga, y (iii) la longitud inicial de la grieta.

El análisis de los fenómenos de fractura en estructuras de paredes delgadas ha sido objeto de una intensa investigación en las últimas décadas. Estos fenómenos multi-physics restringen notablemente la aplicabilidad en estructuras esbeltas, especialmente cuando estbajo la influencia de la temperatura. La investigación en el Capítulo 4 se ocupa del desarrollo de un marco termodinámicamente consistente para un modelo de phase-field termomecánico acoplado para probetas con pequeños espesores utilizando elementos finitos completamente integrados. Esto permite el uso de modelos termomecánicos constitutivos tridimensionales para los materiales. Los modelos de phase-field termomecánicos propuestos están equipados con elementos finitos que incorporan las técnicas EAS y ANS. Además, se utiliza la misma función de degradación tanto para el campo de desplazamiento como para el campo térmico. Las ecuaciones acopladas se resuelven numéricamente con esquemas de solución eficiente ad hoc para problemas no lineales. Se proporcionan varios ejemplos numéricos con y sin phase-field (cáscaras rectas y curvas) para mostrar la aplicabilidad y fiabilidad del modelo propuesto. Además, el modelo se amplía para incorporar los FGM y se exploran los ejemplos numéricos correspondientes.

Usando el marco desarrollado en el Capítulo 4, el conocido elemento finito para placa/lámina, libre del fenómeno de locking, se amplía para incluir los efectos de fatiga en el Capítulo 5. Como consecuencia natural del modelo desarrollado, la curva S-N y las curvas de extensión de grietas se aplican para láminas rectas y curvas.

Chapter 1

Introduction

The material of choice of a given era is often a defining point. Historically, the Stone Age, Bronze Age, Iron Age, and Steel Age are bi-products of these material choices. The recent industrial relations led by the production and use of steel were a stepping stone to our world. Thousands of years ago, we learned how to extract metals from their ore and understood that to its core. For the first time on this planet, we understood how metals work. This led to increased protection by creating advanced tools. This increased our chances of survival and transformed us into modern humans. The origin moments as we can postulate. This knowledge had brought in at least two revolutions, and the third one in the making, changing from caveman to start a civilization (main factor) and industrial revolution.

On the other hand, computation utterly transformed our understanding of nature. The way modern technologies advanced flabbergasted how computation works. When metals were seen under the lens of computation, tall buildings, airplanes, rockets that could land on the moon, spaceships that one day will take us to another planet, machinery, and two world wars emerged. Today, we live in a world where our demands are served at our fingertips, new machines every day, and new revolutions every year. As these technologies continue to advance exponentially, where this means we are heading? An age of composites. All these technologies were done without a complete understanding of how an engine breaks and the effects of temperature on the design and materials. However, we have managed to create this magnificent world with those little things from the little we know. Prof Zdenek Basant, in his acceptance speech of Timoshenko medal, confessed, "The mechanics of damage and quasi-brittle fracture, with all its scaling and interdisciplinary couplings, is a problem of the same dimension as turbulence, which will not be closed even a century from now," after 120 years of fracture mechanics. And this thesis is one step towards that solution.

1.1 Rationale and motivation

Fracture mechanics is a subbranch of solid mechanics that deals with the cracks' initiation, propagation, and coalescence and provides a suitable qualitative relationship of the involved physics. Griffith's [1] theory- an energy approach postulated that the crack occurs as a microscopic manifestation of debonding at a microscopic crystalline level. This debonding process can be accurately represented as the competition between bulk energy (created due to applied load) and crack energy (due to the creation of new surfaces) at each point.

Even though Griffith's energy-based criterion provided great insight, Irwin's [2] well-known Stress Intensity Factor (SIF) approach proved to be more useful in engineering applications. Irwin provided the empirical formula, rather a way to link bulk energy release rate during crack advance (G) and stress intensity factor representing singularity at the crack tip (K_I, K_{II}, K_{III}) in the infinitesimal setting with the celebrated formula $G = \frac{K_I^2}{2\mu}$.

In parallel to fracture mechanics, post-Griffith's era is filled with an avalanche of various theories such as continuum damage mechanics (CDM) [3], viscous regularization [4], Cosserat micropolar theory [5], non-local continuum theory [6], gradient enhanced damage model [7, 8] , gradient damage model [9] to name a few.

Restricting ourselves to the numerical modeling of fracture, fracture in solids can be classified as (i) discontinuous approach and (ii) continuous approach. The fundamental differences between these approaches are that the displacement is allowed to have jumps in the discontinuous approach. In the continuous approach, the stresses are gradually reduced with a continuous displacement field everywhere. The Linear Elastic Fracture Mechanics (LEFM) is primarily based on Griffith [1] and Irwin [2], the Cohesive Zone Model (CZM) based on Dugdale [10] and Barenblat [11] are examples of discontinuous approaches. Fundamentally, the discontinuous approaches are not self-contained. Many theories are proposed in this context, such as maximum hoop stress criterion [12], Rankine criteria, and minimum strain energy criteria [13] as an additional ad hoc criteria to address the issue regarding crack initiation and propagation. Even though CZM-based models can naturally predict crack initiation, these methods remain unattractive due to their high computation. The advantages of such CZM based model include nucleating and propagating complex cracks without additional criteria. These drawbacks related to the discontinuous approach are restricted to a small group of problems and persuade other computational methods where crack paths are determined to solve some multi-physics phenomenon. And hence, the birth of the phase-field approach to fracture. This thesis addresses some of the issues and solutions of material modeling based on the phase-field approach and cohesive zone approach using mathematical modeling techniques for multi-physics problems.

In the forthcoming sections, a brief mathematical overview of Griffth's energy in the variational formulation is presented in Section 1.2.1. Later, a numerical approximation to the modified Griffith's theory is presented in Section 1.2.2. In Section 1.3, a brief survey of the phase-field methods to fracture is presented along with the mathematical formalism. Section 1.4 presents the survey of fatigue failure using the phase-field approach, and finally, Section 1.5 gives the objective and outline of the thesis.

1.2 Variational formulation

1.2.1 Griffith's variational formulation

Since Griffith's theory is postulated as the macroscopic manifestation of microscopic debonding, at the microscopic level, even the most simplistic model demonstrates that the energy spent in moving two atoms apart while the rest of the atoms stays additive leading to microscopic energy proportional to the separation area. In other words, the energy applied to a material is first used to displace the body, which creates tension at a microscopic level. After a certain threshold, the atom separates, creating new surfaces on a microscopic level. The new surface made also creates a discontinuity in the displacement field. Moreover, the energy required to break the atoms is proportional to energy required in creating new surfaces. If the body behaves as elastic, then the energy required to create a new surface is null, fetching the classical theory of elasticity. Francfort and Marigo [14] proposed the variational approach to brittle fracture, which seeks displacement and a set of cracks by minimizing the total energy of the generalized/ modified Griffith's theory.

Consider crack path $\tilde{\Gamma}$ assumed to be known priori in the continuum Ω with boundary $\partial\Omega$. The crack path is assumed to depend on the time t and length of the crack l. The kinematic unknown at any time t is given by $\mathbf{u}(t, l)$. The variational equivalence of the classical Griffith theory can be written as the following, see [15] for more details.

Assuming that the Griffith's like potential $\mathcal{D}(l, \dot{l})$ of the form

$$\mathcal{D}(l, \dot{l}) = \begin{cases} \mathcal{D}(\dot{l}) & \text{if } \nabla\tilde{l}(l), \dot{l} \geq 0 \\ +\infty & \text{Otherwise} \end{cases},$$

with $\mathcal{D} : \mathbb{R}^p \to \mathbb{R}^+$ positively 1-homogeneous, convex, and $\mathcal{D}(0) = 0$ for the value of p-uple $l = (l_1, l_2, \ldots, l_p)$ denoted as $\tilde{l}(l)$. Then, the Griffith's like energy $\mathcal{E}(t, \mathbf{u}, l)$ takes the form

$$\mathcal{E}(t, \mathbf{u}, l) = \int_{\Omega\setminus\Gamma(t)} \Psi(\nabla\mathbf{u})\mathrm{dV} - \mathcal{F}(t, \mathbf{u}) + \mathcal{D}(\tilde{l}(l); l - \tilde{l}). \tag{1.1}$$

Here, Ψ, and $\mathcal{F}$ are elastic energy and applied energy respectively, satisfies the following conditions. See [15] for a complete derivation.

1. **Unilateral Stationary Condition (USC):**
   For all l and $\mathbf{u} = g(t)$ on $\partial_d\Omega\setminus\Gamma(l)$, the points $(l(t), \mathbf{u}(t))$ is a stationary point of Eq. (1.1). Meaning that,
   $$\frac{d}{d\epsilon}\mathcal{E}(t; \mathbf{u}(t, \epsilon, l))\bigg|_{\epsilon=0} \geq 0.$$
2. **Irreversibility:** Cracks cannot heal. The set $\tilde{l}(l(t)) \cdot \dot{l} \geq 0$.
3. **Energy Balance:** The second law of thermodynamics has to be satisfied [16, 15], whose particular expression is discussed in the sequel.

It can be shown that (USC) accounts for the first-order optimality conditions for $(l(t), \mathbf{u}(t))$ to be local unilateral minimizer of $\mathcal{E}(t, \mathbf{u})$. Consequently, such stationarity conditions are mathematically unpleasant in the sense of providing the existence of the solution, let alone uniqueness. The point of departure from the classical Griffiths' to the more general Griffiths' is brought forth in the literature [15, 17, 14] as a relaxation to the unilateral stationary condition by means of local or global minimizers. i.e $(l(t), \mathbf{u}(t))$ is a local / global minimizer (in a suitable topology) for $\mathcal{E}(t, \mathbf{u}, l)$ among all $l \geq l(t)$, and all $\mathbf{u} = g(t)$ on $\partial_d\Omega\setminus\Gamma(l)$. In the sense of nonlinearity, local minimality conditions are usually preferred owing to the fact that Lyapunov stability is only restricted to local minimality. In contrast, global minimality lacks uniqueness. The path constraint on the $l(t)$ can be shown to be replaced by actual crack length $l(t)$ along the pre-determined path owing to the global/local minimizers. With $\Gamma(t)$ denoting the crack at time t, the unilateral local/global minimality takes the form

$(\Gamma(t), \mathbf{u}(t))$ is a local/global minimizers for

$$\mathcal{E}(t, \mathbf{u}, \Gamma) = \int_{\Omega \backslash \Gamma} \Psi(\nabla \mathbf{u}) \mathrm{dV} - \mathcal{F}(t, \mathbf{u}) + k\mathcal{H}^1(\Gamma), \tag{1.2}$$

for all $\Gamma(t) \subset \Gamma$ and $\mathbf{u} = g(t)$ on $\partial_d \Omega \backslash \Gamma$ in some topology.

Inspired by the Mumford-shah potential, the minimization problem in [18] is shown to be well-posed on a subspace SBV(Ω) (of BV(Ω)) of special functions of bounded variation of Ω. Ambrosio [19, 20, 15] established the compactness property in SBV(Ω) as follows:

For every subsequence $u_n \in$ SBV(Ω) with u_n bounded in $L^\infty(\Omega)$, $\left|\left|u_n\right|\right|_{L^\infty(\Omega)} \leq C$, the gradient of u_n is bounded in $L^q(\Omega; \mathbb{R}^2)$, $q \geq 1$, i.e $\left|\left|\nabla u_n\right|\right|_{L^q(\Omega;\mathbb{R}^2)} \leq \bar{C}$, and for the jump set $J(u_n)$ (the set of jump points of the u_n), the Hausdorff measure of jump set $J(u_n)$ is bounded i.e $\mathcal{H}(S(u_n)) \leq C^{'}$, then the following are true.

There exists a subsequence $u_{k_{(n)}}$ of u_n, and there exists a $u \in$ SBV(Ω) such that

- The subsequence $u_{k_{(n)}}$ converges to u strongly in $L^p(\Omega)$, for $p \leq \infty$. i.e $u_{k_{(n)}} \to u$ strongly in $L^p(\Omega)$, $p \leq \infty$.
- The gradient of the subsequence $\nabla u_{k_{(n)}}$ converges weakly to ∇u in $L^q(\Omega; \mathbb{R}^2)$. i.e $\nabla u_{k_{(n)}} \to \nabla u$ Weakly in $L^q(\Omega; \mathbb{R}^2)$.
- The limit of all infimum's (minimum if the functional is bounded) for the set $\mathcal{H}(J(u_{k_{(n)}}))$ containing the jump set of subsequence $u_{k_{(n)}}$ is greater than or equal to $\mathcal{H}(J_u)$. i.e

$$\liminf_n \mathcal{H}(J(u_{k_{(n)}})) \geq \mathcal{H}(J_u).$$

Then, using this compactness result, the existence of the solution to modified Griffith's like potential in Eq. (1.2) can be guaranteed, see [17, 21, 15] for detailed proof. With identifying the crack set $\Gamma(t)$ as a combination of jump set (this removes that Γ has to be known priori) as a combination of jump set J_u, i.e $\Gamma(t) = \Gamma_0 \cup_{s<t} J(u(\tau))$, the energy can be written as

$$\mathcal{E}(t, \mathbf{u}, \Gamma) = \int_{\Omega} \Psi(\nabla \mathbf{u}) \mathrm{dV} - \mathcal{F}(t, \mathbf{u}) + k\mathcal{H}^1(\Gamma),$$

with the following conditions

1. $\Gamma(0) = \Gamma_0$.
2. **Unilateral Local/Global Minima:** $(\Gamma(t), \mathbf{u}(t))$ is a local/ global minimizer for $\mathcal{E}(t, \mathbf{u}, \Gamma)$, for all $\bar{\Omega} \backslash \partial_s \Omega \supset \Gamma \supset \Gamma(t)$, $S(\mathbf{u}) \supset \Gamma$ and $\mathbf{u} = g(t)$ on $\partial_d \Omega$.
3. **Energy Balance:**

   The particular form of the energy balance takes the form

$$\frac{d\mathcal{E}}{dt}((t, \mathbf{u}, \Gamma))(t) = \int_{\Omega} \frac{\partial \Psi}{\partial F}(\nabla \mathbf{u}) \cdot \nabla \dot{g}(t) \mathrm{dV} - \dot{\mathcal{F}}(t, \mathbf{u}) - \mathcal{F}(t, g(t)).$$

4. **Irreversibility:** $\dot{\Gamma(t)} \geq 0$.

1.2.2 Numerical approximation

With the variational setting of Griffith's at hand, the roots of numerical approximation can be found in free-discontuinity problem [22, 21] based on an approximation of total energy in the sense of $\Gamma-$Convergence. Meaning that, find a sequence of functionals $\mathcal{F}_\varepsilon$ of some type that approximates the functional $\mathcal{F}$ such that as $\varepsilon \to 0$, the functional $\mathcal{F}_\varepsilon$ converges to $\mathcal{F}$ in the sense of $\Gamma-$Convergence. Writing this formally, consider a $\mathbb{R}-$vector valued functional $\mathcal{F}$, and its sequence $\mathcal{F}_\varepsilon$ defined over a metrizable topological space $\mathbf{X}$. Then $\mathcal{F}_\varepsilon$ converges to $\mathcal{F}$ as $\varepsilon \to 0$ if and only of the following two conditions satisfy

1. For any sequence $(\mathbf{u}_\varepsilon)_\varepsilon \to \mathbf{u}$, one has
$$\liminf_{\varepsilon \to 0} \mathcal{F}_\varepsilon(\mathbf{u}_\varepsilon) \geq \mathcal{F}(\mathbf{u}).$$
2. There exist a sequence $(\mathbf{u}_\varepsilon)_\varepsilon \to \mathbf{u}$ in $\mathbf{X}$ such that
$$\limsup_{\varepsilon \to 0} \mathcal{F}_\varepsilon(\mathbf{u}_\varepsilon) \leq \mathcal{F}(\mathbf{u}).$$

In other words, for any functional $\mathcal{F}$, let $\mathbf{u}$ be its minimizer. Then if a sequence of approximated functional $\mathcal{F}_\varepsilon$ has $\mathbf{u}_\varepsilon$ minimizers (hopefully). If the sequence of minimizers $\mathbf{u}_\varepsilon$ converge to the minimizer of original functional $\mathbf{u}$, then all the infimum (minimum in case of bounded) of the sequence $\mathcal{F}_\varepsilon(\mathbf{u}_\varepsilon)$ as $\varepsilon \to 0$ is less than $\mathcal{F}(\mathbf{u})$. If the supremum of one sequence $\mathcal{F}_\varepsilon(\mathbf{u}_\varepsilon)$ can go beyond or upto the functional $\mathcal{F}(\mathbf{u})$, then we say $\mathcal{F}_\varepsilon(\mathbf{u}_\varepsilon) \to \mathcal{F}(\mathbf{u})$. In other words, all the sequences are less than $\mathcal{F}(\mathbf{u})$, but one sequence has some subsequence which can go upto $\mathcal{F}(\mathbf{u})$. Meaning that, the particular subsequence should be the minimizer of $\mathcal{F}_\varepsilon(\mathbf{u}_\varepsilon)$.

With this at hand, phase-field methods to fracture evolved as a self-sufficient approximation whose short review is provided in the next Section. Following [23, 22], introduce a scalar variable $\mathfrak{d} \in W^{1,2}(\overline{\Omega}/\partial_s\Omega)$ and a small positive parameter l, and $\eta_l = O(l)$, for any kinematically admissible $\mathbf{u}$, with $\mathfrak{d} = 0$ representing sound material and we can define the Griffith's energy as

$$\mathcal{F}(\mathbf{u}, \mathfrak{d}) = \begin{cases} \int_\Omega \Psi(\nabla \mathbf{u}) \mathrm{dV} + K\mathcal{H}^1(S_u/\partial_s\Omega) & \text{if } \mathfrak{d} = 0 \\ +\infty & \text{otherwise} \end{cases} . \tag{1.3}$$

and the approximation sequence can be defined as

$$\mathcal{F}_\varepsilon(\mathbf{u}, \mathfrak{d}) = \int_\Omega \left(\left((1-\mathfrak{d})^2 + \eta_\varepsilon \right) \Psi(\nabla \mathbf{u}) \right) \mathrm{dV} + K \int_{\overline{\Omega}/\partial_s\Omega} \left(\frac{\mathfrak{d}^2}{4l} + l|\nabla \mathfrak{d}|^2 \right) \mathrm{dV} \tag{1.4}$$

whose proof of $\Gamma-$Convergence from $\mathcal{F}_\varepsilon \to \mathcal{F}$ is now standard. See [17, 15] for more details.

1.3 Phase-Field methods

This section concerns the fundamental of the phase-field approach. At first, a general variational formulation of the phase-field method along with the consistency conditions are presented (partially taken from [24]). Later, a brief discussion on the choice of degradation function, stored elastic energy, geometric crack functions in the literature are presented.

From this Section, we drop the mathematical intricacy and focus on the different approximations and methods proposed in the literature, some $\Gamma-$Converging and others (may or may not) based on the physics. To make the distinction, Griffith's potential is called as $\mathcal{E}$, whereas the phase-field approximation is refereed as Π.

1.3.1 Mathematical model

Summarizing and reformulating the phase-field approach to fracture, let $\mathcal{B} \subset \mathbb{R}^{n_{dim}}$ ($n_{dim} = 1, 2, 3$ denotes spatial dimension) be an arbitrary solid body in the n_{dim} Euclidean space $\mathbb{R}^{n_{dim}}$ with the crack set $\Gamma \subset \mathbb{R}^{n_{dim}-1}$. The body is characterized by the kinematic displacement field $\mathbf{u}(\mathbf{x})$ and the strain field is defined as a symmetric gradient of the displacement field $\boldsymbol{\varepsilon}(\mathbf{x}) := \nabla^s \mathbf{u}(\mathbf{x})$ for all $\mathbf{x} \in \mathcal{B}$, with $\left(\nabla^s(\cdot) = \dfrac{\nabla(\cdot) + \nabla^T(\cdot)}{2}\right)$. The external boundary $\partial\mathcal{B} \subset \mathbb{R}^{n_{dim}-1}$ is split into two disjoint sets, $\partial\mathcal{B}_\mathbf{u}$ and $\partial\mathcal{B}_t$, with $\partial\mathcal{B}_\mathbf{u} \cap \partial\mathcal{B}_t = \emptyset$ and $\overline{\partial\mathcal{B}_\mathbf{u} \cup \partial\mathcal{B}_t} = \partial\mathcal{B}$, such that displacement $\bar{\mathbf{u}}(\mathbf{x})$ for $\mathbf{x} \in \partial\mathcal{B}_\mathbf{u}$ and traction $\bar{\mathbf{t}}(\mathbf{x})$ for $\mathbf{x} \in \partial\mathcal{B}_t$ is applied as shown in the Figure 1. The external work $\mathcal{P}(\mathbf{u}(\mathbf{x}))$ due to the applied loading defined above is given by

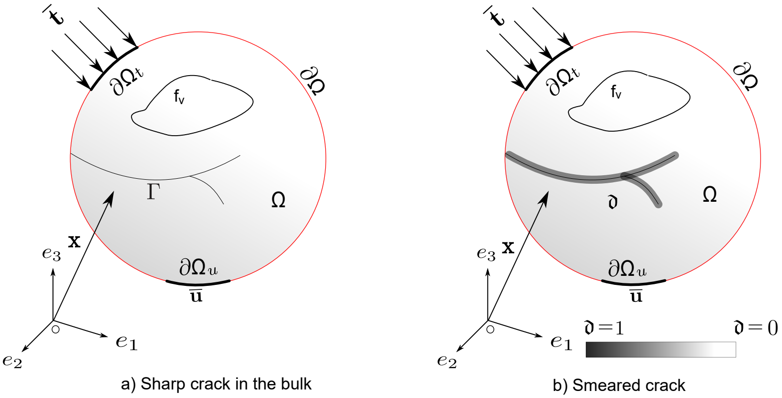

a) Sharp crack in the bulk

b) Smeared crack

Figure 1: Schematic representation of diffusive cracks.

$$\mathcal{P}(\mathbf{u}(\mathbf{x})) := \int_{\mathcal{B}} \boldsymbol{f_v} \cdot \mathbf{u}\, \mathrm{dV} + \int_{\partial\mathcal{B}_t} \bar{\mathbf{t}} \cdot \mathbf{u}\, \mathrm{dS}, \tag{1.5}$$

where $\boldsymbol{f_v} : \mathcal{B} \to \mathbb{R}^{n_{dim}}$ is the distributed body force.

The variational approach to fracture, according to Griffith's theory can be interpreted as the competition between the elastic energy $\Psi(\mathbf{u})$ created by the body due to external forces and the surface energy $\Psi_c(\Gamma)$ created by crack creation and propagation. In this context, the quasi-static displacement field $\mathbf{u}_t(\mathbf{x}) = \mathbf{u}(\mathbf{x}, t) = \mathbf{u}$, and the crack set Γ_t at any given discrete time step $t \in [0, T]$ are given as a minimization problem (see [16] for more details)

$$(\mathbf{u}_t, \Gamma_t) = \arg\min \mathcal{E}(\mathbf{u}, \Gamma)_{\mathbb{S}} := \int_{\mathcal{B}\backslash\Gamma} \Psi(\boldsymbol{\varepsilon})\,\mathrm{dV} + \mathcal{G}_C \mathcal{H}^{n_{dim}-1}(\Gamma \cap \overline{\mathcal{B}} \backslash \partial\mathcal{B}_t), \tag{1.6}$$

with $\mathbb{S} := [\mathbf{u} = \bar{\mathbf{u}} \,\text{on}\, \partial\mathcal{B}_{\mathbf{u}},\, \Gamma_t \supset \Gamma_{t-1}]$, $\mathcal{H}^{n_{dim}-1}(\Gamma)$ is the Hausdorff $(n_{dim} - 1)$ dimensional measure of the unknown crack set Γ, $\mathcal{G}_C$ [J/m^2] is the critical energy release rate, and $\Psi(\boldsymbol{\varepsilon})$ is the elastic energy density that depends on the strain field $\boldsymbol{\varepsilon}(\mathbf{u})$.

Since Γ in Eq. (1.6) is unknown a priori, the numerical approximation of the functional given in the former expression is crafted as a free-discontinuity problem based on the Tortorelli's elliptical regularization [19] of the Mumford-Shah potential used in image segmentation [25], and later adapted to brittle fracture in [14, 16]. In this framework, the crack set Γ is replaced by $(\mathcal{H}^{n_{dim}-1}, n_{dim} - 1)$ rectifiable borel jump set of $\mathbf{u}$, $J(\mathbf{u})$. Then, there exists a sequence $(\Gamma_i)_i^{\infty}$ of C^1 hyper-surfaces, covering almost all of $J(\mathbf{u})$. ie $\mathcal{H}^1(J_u / \bigcup\limits_{i=1}^{\infty} \Gamma_i) = 0$, in a suitable space such as $SBD(\Omega)/GSBD(\Omega)$, see [17, 26, 27] for more details. Hence, the surface energy associated with the crack is approximated using a scalar field $\mathfrak{d} \in [0, 1]$ (denominated as crack phase-field variable), and the internal length scale $l \in \mathbb{R}^+$ governing the width of the diffusive crack such that, $\mathfrak{d} = 0$ for an intact material and $\mathfrak{d} = 1$ for completely damaged material takes the form, see Fig. 1

$$\Psi_c(\Gamma) = \int_\Gamma \mathcal{G}_C \,\mathrm{dS} \approx \int_{\mathcal{B}} \frac{\mathcal{G}_C}{4c_w} \gamma(\mathfrak{d};\, \nabla\mathfrak{d})\mathrm{dV},$$

where, $\gamma(\mathfrak{d};\, \nabla\mathfrak{d})$ is the crack surface energy density function [28] defined as

$$\gamma(\mathfrak{d};\, \nabla\mathfrak{d}) := \frac{\alpha(\mathfrak{d})}{l} + l\,|\nabla\mathfrak{d}|^2 . \tag{1.7}$$

Here, $c_w := \int_0^s \sqrt{\alpha(s)}ds$ is the normalization parameter, $\alpha(\mathfrak{d})$ is a continuous monotonic function with $\alpha(0) = 0$ and $\alpha(1) = 1$, called as geometric crack function which determines the distribution of the phase field [29, 30, 31]. The term $\frac{\alpha(\mathfrak{d})}{l}$ is local part, and $l\,|\nabla\mathfrak{d}|^2$ is the non-local part, which incorporates the internal length scale l. Due to the regularization of the crack Γ by the phase field variable $\mathfrak{d}$, the elastic energy now not only depends on the displacement field $\mathbf{u}(\mathbf{x})$, but also on the phase-field variable $\mathfrak{d}$ as

$$\Psi(\mathbf{u}, \mathfrak{d}) = \int_{\mathcal{B}} g(\mathfrak{d})\Psi_0(\boldsymbol{\varepsilon}(\mathbf{u}))\,\mathrm{dV}, \tag{1.8}$$

where $g(\mathfrak{d}) : [0, 1] \to [1, 0]$ is the energetic degradation function characterized by the deterioration of the initial elastic energy function $\Psi_0(\boldsymbol{\varepsilon})$, with $g(0) = 1,\ g(1) = 0,\ \frac{dg}{d\mathfrak{d}} < 0$. Hence, the stored energy functional in Eq. (1.8) describes the transition from the intact state to the fully damaged state. Thus the regularized energy functional of the solid in Eq. (1.6) takes the form

$$\Pi(\mathbf{u}, \mathfrak{d}) = \int_\Omega [g(\mathfrak{d}) + \eta_l]\,\Psi_0(\boldsymbol{\varepsilon})\,\mathrm{dV} + \int_\Omega \frac{\mathcal{G}_C}{4c_w}\left[\frac{\alpha(\mathfrak{d})}{l} + l\,|\nabla\mathfrak{d}|^2\right]\mathrm{dV} - \mathcal{P}(\mathbf{u}(\mathbf{x})). \tag{1.9}$$

The details regarding each of the terms involved in the Eq. (1.9) such as $g(\mathfrak{d}),\ \Psi_0(\boldsymbol{\varepsilon})\,\alpha(\mathfrak{d})$ are explained in the sequel at length. The Eq. (1.9) approximates the Griffith's energy in Eq. (1.6) in the sense of $\Gamma-$Convergence under the conditions that the Eq. (1.9) satisfy

1. **Irreversibility:** The crack can always grow with time, but cannot close in time. i.e $\dot{\Gamma}(t) \geq 0$ or $\Gamma_t \subseteq \Gamma_{t+1}$.
2. **Unilateral Stationary/Minimality Condition [16]:** For the variations $(\delta\mathbf{u}, \delta\mathfrak{d})$ of $(\mathbf{u}, \mathfrak{d})$ in appropriate space, the variation of total energy functional (in the sense of Gateaux) implies
    - $\delta\Pi = 0$ for each $(\delta\mathbf{u}, \delta\mathfrak{d}) > 0$,
    - $\delta\Pi > 0$ for $(\delta\mathbf{u}, \delta\mathfrak{d}) = 0$.
3. **Energy Balance:** The energy Π has to satisfy the energy balance throughout the time evolution. i.e $\forall t \in [0, T]$,

$$\dot{\Pi} = \int_{\partial\mathcal{B}} (\boldsymbol{\sigma}\cdot\boldsymbol{n})\cdot\dot{\mathbf{u}}\mathrm{dA} - \int_{\mathcal{B}} \dot{\boldsymbol{f}}_v \cdot \mathbf{u}\mathrm{dV} - \int_{\partial\mathcal{B}_t} \dot{\bar{\mathbf{t}}}_{\mathbf{v}} \cdot \mathbf{u}\mathrm{dA}, \tag{1.10}$$

with stress $\boldsymbol{\sigma}$ defined as usual rate change of total energy with respect to strains $\boldsymbol{\varepsilon}$. i.e $\boldsymbol{\sigma} = \dfrac{\partial\Psi}{\partial\boldsymbol{\varepsilon}}$.

The solution $(\mathbf{u}, \mathfrak{d})$ of the total energy functional in Eq. (1.9) along with the conditions as mentioned above can be solved as

Determine $(\mathbf{u}, \mathfrak{d})$ such that

$$(\mathbf{u}, \mathfrak{d}) = \mathrm{Argmin}_{\mathbf{x}} \left\{\Pi(\mathbf{u}, \mathfrak{d})\right\}, \tag{1.11}$$

subjected the conditions mentioned above.

The governing equations under quasi-static loading conditions are determined by taking first variation of the functional in Eq. (1.9) for the variation $(\delta\mathbf{u}, \delta\mathfrak{d})$ of $(\mathbf{u}, \mathfrak{d})$ results in

$$g(\mathfrak{d})\nabla\cdot\frac{\partial\Psi_0(\boldsymbol{\varepsilon})}{\partial\boldsymbol{\varepsilon}} + \boldsymbol{f}_v = 0 \quad \text{on} \quad \mathcal{B}, \tag{1.12a}$$

$$\text{with} \quad \boldsymbol{\sigma}\cdot\boldsymbol{n} = \bar{\boldsymbol{t}} \quad \text{on} \quad \partial\mathcal{B}_t, \tag{1.12b}$$

$$\left[-g'(\mathfrak{d})\frac{\partial\Psi_0(\boldsymbol{\varepsilon})}{\partial g} - \mathcal{G}_C\left[\frac{\partial\gamma}{\partial\mathfrak{d}} - \nabla\cdot\left(\frac{\partial\gamma}{\partial\nabla\mathfrak{d}}\right)\right]\right] = 0 \quad \text{if} \quad \dot{\mathfrak{d}} > 0 \quad \text{in} \quad \mathcal{B}, \tag{1.12c}$$

$$\left[-g'(\mathfrak{d})\frac{\partial\Psi_0(\boldsymbol{\varepsilon})}{\partial g} - \mathcal{G}_C\left[\frac{\partial\gamma}{\partial\mathfrak{d}} - \nabla\cdot\left(\frac{\partial\gamma}{\partial\nabla\mathfrak{d}}\right)\right]\right] < 0 \quad \text{if} \quad \dot{\mathfrak{d}} = 0 \quad \text{in} \quad \mathcal{B}, \tag{1.12d}$$

$$\text{along with} \quad \frac{\partial\gamma}{\partial\nabla\mathfrak{d}}\cdot\boldsymbol{n}_B = 0 \quad \text{on} \quad \partial\mathcal{B}. \tag{1.12e}$$

Here, $\left[-g'(\mathfrak{d})\dfrac{\partial\Psi_0(\boldsymbol{\varepsilon})}{\partial g}\right]$ is called as energetic crack driving force associated with the energy functional $g(\mathfrak{d})\Psi_0(\boldsymbol{\varepsilon}) = \Psi(\boldsymbol{\varepsilon}, \mathfrak{d})$. The unilateral stationarity condition along with the irreversibility of the crack and boundedness of $\mathfrak{d}$ leads to the first order optimality condition, or often referred to as Karush-Kuhn-Tucker (KKT) condition

$$\dot{\mathfrak{d}} \geq 0, \tag{1.13a}$$

$$f(Y, \mathfrak{d}) \leq 0 \quad \text{and} \quad \dot{\mathfrak{d}}f(Y, \mathfrak{d}) \equiv 0, \tag{1.13b}$$

$\alpha(\mathfrak{d})$	c_w	Citing articles
$\mathfrak{d}$	$8/3$	[9] (AT-1)
$\mathfrak{d}^2$	2	[16] (AT-2)
$1-(1-\mathfrak{d})^{\frac{p}{2}}$	-	[9]
$1-(1-\mathfrak{d})^2$	π	[32]
$\zeta\mathfrak{d}+(1-\zeta)\mathfrak{d}$	-	[33]
$16\mathfrak{d}^2(1-\mathfrak{d}^2)$	$8/3$	[34]

Table 1: Common geometric crack functions in the literature.

with

$$f(Y,\mathfrak{d}) = \left[-g'(\mathfrak{d})\frac{\partial\Psi_0(\boldsymbol{\varepsilon})}{\partial g} - \mathcal{G}_C\left[\frac{\partial\gamma}{\partial\mathfrak{d}} - \nabla\cdot\left(\frac{\partial\gamma}{\partial\nabla\mathfrak{d}}\right)\right]\right]. \tag{1.14}$$

Notice that, in the above expression, irreversibility condition $\dot{\Gamma}(t) \geq 0$ is replaced by $\dot{\mathfrak{d}} \geq 0$. This can be attributed to the composition of the crack path and it is very easy to see that $\dot{\mathfrak{d}} \geq 0$ implies $\dot{\Gamma} \geq 0$.

1.3.2 Choice of functions

Geometric crack function

The geometric crack density function $\alpha(\mathfrak{d})$ considered in Eq. (1.9) only state that $\alpha(\mathfrak{d}) \in [0,1]$ with $\alpha(0) = 0$ and $\alpha(1) = 1$, then it is possible to find a class of functions that satisfy this condition. In the related literature different authors suggested different $\alpha(\mathfrak{d})$ and the resulting normalization values c_w, some of them are listed in Tab. 1.

When $\alpha(\mathfrak{d}) = \mathfrak{d}^2$, the phase-field problem renders linear (within a staggered scheme) and thus making the computation easier and cheaper. Moreover, $\mathfrak{d}$ is between $[0,1]$ is ensured easily, whereas in the other models of $\alpha(\mathfrak{d})$, the boundedness of $\mathfrak{d} \in [0,1]$ have to be formally enforced.

Stored energy function

The stored energy function describes the equilibrium state that defines the behavior of a solid. i.e., $\mathfrak{d} = 0$ everywhere, the stored energy function describes the physics of solid. A modification or rather choice of $\Psi_0(\boldsymbol{\varepsilon})$ in Eq. (1.9) presents different models such as brittle, ductile, plastic, thermo-elastic, thermo-plastic, viscous, etc., some commonly used functions are mentioned in the sequel.

(a) Isotropic Elastic Body: The stored energy function is defined as

$$\Psi_0(\boldsymbol{\varepsilon}) = \frac{1}{2}\boldsymbol{\varepsilon} : \mathbb{C} : \boldsymbol{\varepsilon} = \frac{1}{2}\lambda tr^2(\boldsymbol{\varepsilon}) + \mu\boldsymbol{\varepsilon} : \boldsymbol{\varepsilon}, \tag{1.15}$$

where $\mathbb{C}$ defines the linear elasticity tensor defined as $\mathbb{C} = 2\mu\mathbb{I} + \lambda 1 \otimes 1$ in terms of Lame constants λ and μ. Here $\mathbb{I}$ is the fourth order identity tensor and 1 is the second order identity tensor.

Miehe [35, 28] proposed a tension/compression split of the elastic energy to prevent cracking under compressed loads such that

$$\Psi(\boldsymbol{\varepsilon}) = g(\mathfrak{d})\Psi_0^+(\boldsymbol{\varepsilon}) + \Psi_0^-(\boldsymbol{\varepsilon}), \tag{1.16}$$

with degradation function $g(\mathfrak{d})$ applied only in the tension $\Psi_0^+(\boldsymbol{\varepsilon})$.

(b) Anisotropic Model:

The elastic energy due to Anisotropy can be defined as [36]

$$\Psi_0^+(\boldsymbol{\varepsilon}) = \mu\boldsymbol{\varepsilon}_D : \boldsymbol{\varepsilon}_D : \qquad \Psi_0^-(\boldsymbol{\varepsilon}) = \frac{1}{2}Ktr^2(\boldsymbol{\varepsilon}) \tag{1.17}$$

where K represents bulk modulus. Here, the total strain $\boldsymbol{\varepsilon}$ is decomposed into volumetric part $\boldsymbol{\varepsilon}_v$ and deviatoric parts $\boldsymbol{\varepsilon}_D$ [36] whose particular expression takes the form

$$\boldsymbol{\varepsilon} = \boldsymbol{\varepsilon}_V + \boldsymbol{\varepsilon}_D; \qquad \boldsymbol{\varepsilon}_V = \frac{1}{3}tr(\boldsymbol{\varepsilon})1, \qquad \boldsymbol{\varepsilon}_D = \boldsymbol{\varepsilon} - \frac{1}{3}tr(\boldsymbol{\varepsilon})1. \tag{1.18}$$

The resulting degraded stress due to the strain spilt takes the form

$$\boldsymbol{\sigma} = g(\mathfrak{d})2\mu\boldsymbol{\varepsilon}_D + Ktr(\boldsymbol{\varepsilon})1. \tag{1.19}$$

Another most famous anisitropic split is proposed by Amor in [37] where the elastic energy takes the form

$$\Psi_0^+(\boldsymbol{\varepsilon}) = \frac{1}{2}K\langle tr(\boldsymbol{\varepsilon})\rangle^2 + \mu\boldsymbol{\varepsilon}_D : \boldsymbol{\varepsilon}_D; \qquad \Psi_0^-(\boldsymbol{\varepsilon}) = \frac{1}{2}K\langle -tr(\boldsymbol{\varepsilon})\rangle^2, \tag{1.20}$$

and the stress becomes

$$\boldsymbol{\sigma} = g(\mathfrak{d})[K\langle tr(\boldsymbol{\varepsilon})1\rangle + 2\mu\boldsymbol{\varepsilon}_D] - K\langle -tr(\boldsymbol{\varepsilon})\rangle 1. \tag{1.21}$$

where $\langle\cdot\rangle$ is McAuley brackets defined as $\langle a\rangle := max\{a, 0\}$. The resulting model due to this particular spilt partially restricts the phase-field $\mathfrak{d}$ to initiate in compression.

(c) Spectral Split:

Due to polar decomposition theorem, strain tensor can be split written in terms of principle strains (eigenvalues) ε_n and the corresponding eigenvector $\mathbf{p}_n$ (for $n = 1, 2, 3$)

$$\boldsymbol{\varepsilon} = \sum_{n=1}^{3} \varepsilon_n \mathbf{p}_n \otimes \mathbf{p}_n = \boldsymbol{\varepsilon}^+ + \boldsymbol{\varepsilon}^-, \tag{1.22}$$

with positive and negative counterparts taking the form

$$\boldsymbol{\varepsilon}^+ = \sum_{n=1}^{3} \langle\varepsilon_n\rangle \mathbf{p}_n \otimes \mathbf{p}_n, \qquad \boldsymbol{\varepsilon}^- = \sum_{n=1}^{3} -\langle -\varepsilon_n\rangle \mathbf{p}_n \otimes \mathbf{p}_n. \tag{1.23}$$

With this split, the elastic energy takes the form

$$\Psi_0^\pm(\boldsymbol{\varepsilon}) := \frac{1}{2}\lambda\langle \pm tr(\boldsymbol{\varepsilon})\rangle^2 + \mu\boldsymbol{\varepsilon}^\pm : \boldsymbol{\varepsilon}^\pm. \tag{1.24}$$

The resulting stress due to spectral spilt takes the form

$$\boldsymbol{\sigma} = g(\mathfrak{d})\left[\lambda\langle tr(\boldsymbol{\varepsilon})\rangle 1 + 2\mu\boldsymbol{\varepsilon}^+\right] - \left[\lambda\langle -tr(\boldsymbol{\varepsilon})\rangle 1 + 2\mu\boldsymbol{\varepsilon}^-\right]. \tag{1.25}$$

$g(\mathfrak{d})$	Citing Article
$(1-\mathfrak{d})^2$	[16]
$3(1-\mathfrak{d})^2 - 2(1-\mathfrak{d})^3$	[34]
$(3-s)(1-\mathfrak{d})^2 - (2-s)(1-\mathfrak{d})^3$	[38]
$4(1-\mathfrak{d})^3 - 3(1-\mathfrak{d})^4$	[39]
$\dfrac{(1-\mathfrak{d})^2}{(1-\mathfrak{d})^2 + Q(\mathfrak{d})}, Q(\mathfrak{d}) = a_1\mathfrak{d} + a_1 p\mathfrak{d}^2$	[40]
$\dfrac{(1-\mathfrak{d})^p}{(1-\mathfrak{d})^p + Q(\mathfrak{d})}, Q(\mathfrak{d}) = a_1\mathfrak{d} + a_1 a_2\mathfrak{d}^2 + a_1 a_2 a_3\mathfrak{d}^3$	[33]

Table 2: Common degradation function.

The resulting model can completely suppress the initiation of the phase-field under compressive loads.

Energetic degradation function

Energetic degradation function $g(\mathfrak{d})$ plays a major role in phase-field methods since it links the elastic energy and crack phase-field $\mathfrak{d}$ by degrading the elastic energy. Since $\mathfrak{d}$ is bounded, the degradation function $g(\mathfrak{d}) = (1-\mathfrak{d})^2$ which maps $g(\mathfrak{d}) : [0,1] \to [1,0]$ is also bounded [24]. Naturally, the function $g(\mathfrak{d})$ satisfies the following conditions;

1. $g(0) = 1$ representing the intact state and $g(1) = 0$ represents completely broken state of initial elastic energy.
2. $g'(\mathfrak{d}) = \frac{dg}{d\mathfrak{d}} < 0$, meaning that the function $g(\mathfrak{d})$ is a monotonically decreasing.
3. $g'(\mathfrak{d}) = 0$, i.e when the material is fully broken, due to (1) and (2), $g(\mathfrak{d})$ is forced to stay complying $g'(1) = 0$. This condition also guarantees that the localization band doesn't grow orthogonally, which is usually observed in the other models such as gradient enhanced damage models [9].

The common choices regarding the function $g(\mathfrak{d})$ in the related literature are listed in Tab. 2

1.4 Fatigue

Fatigue introduced fracture is considered one of the most frequent damages accounting for up to 90% of all material failures. Its complex nature and inability to predict beforehand make it extremely dangerous failure modes. In classical material science, fatigue is attributed to material weakening due to small repeated loading. Micro-cracks develop energetically as a consequence of sub- or micro-structural changes in the material. These micro-cracks further depend on the material's microstructure, ruled by stochastic process eventually coalesce and leads to a macro-crack, where size is sufficient enough to overcome the microstructure's energy barrier to nucleate, eventually leading to failure.

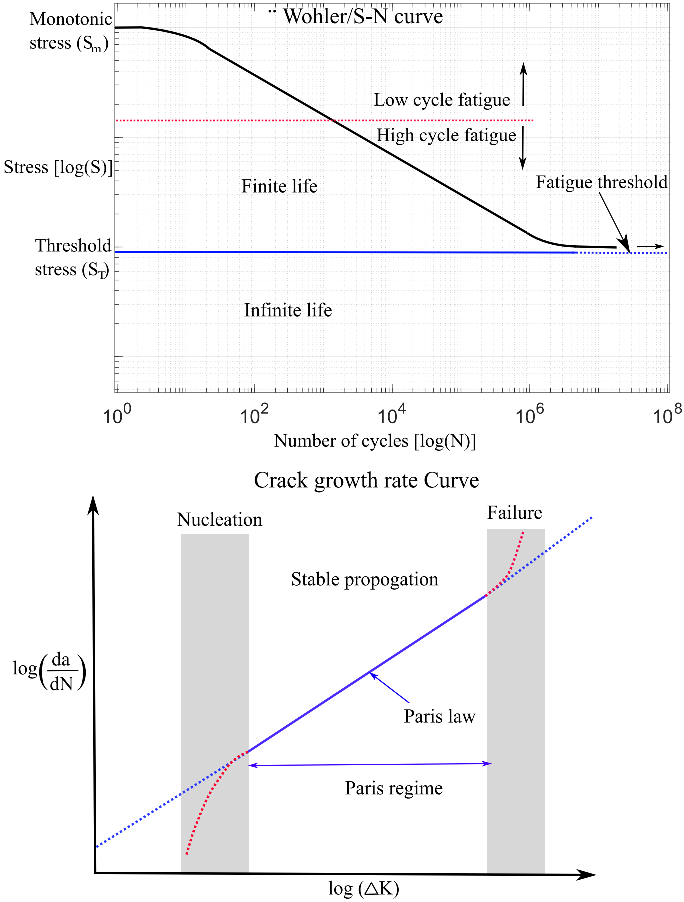

Figure 2: Schematic representation of a) SN curve, and b) Paris law.

The early studies regarding fatigue failure are dominated by empirical relations such as Wöhler curves [41], Paris law [42, 43], Coffin [44], and Manson [45] ideas, based on extensive experimental data fitting methods. Wöhler noticed the number of cycles (N) required to failure for an applied stress amplitude of $\boldsymbol{\sigma}_a$ is related as

$$\boldsymbol{\sigma}_a = AN^{\beta},$$

for some constants A and β that depend on the material. This curve, as in Fig. 2a), is named as the S-N curve or Wöhler Curve. This approach beholds some important observations, such as the presence of threshold amplitude below which the material is unlikely to fail. This also shows that the stress amplitude is directly proportional to the number of cycles N before fracture. Based in the number of cycles to failure N, fatigue can be broadly classified as (i) Ultra-low/oliocycle fatigue (ULC), (ii) Low cycle fatigue (LC), and (iii) High cycle fatigue (HC) as in Fig. 2b).

Following Wöhler, Palmgren [46] and Miner [47] introduce the idea of cumulative damage. For a k different stress amplitudes in loading history, the damage contribution independent of the order of applied load gives $\eta_i = \dfrac{1}{N\boldsymbol{\sigma}_a^i}$. Later, Paris [42] showed that in a single cycle with crack length $'a'$, the rate of change of crack length $\dfrac{da}{dN}$ is directly proportional to change in the stress intensity factor ΔK as

$$\frac{da}{dN} = C\Delta K^m,$$

for some constant C and m depend on the material property.

In the sense of a variational approach to fracture, as in the previous section, the phase-field approach has been extended to include behavior. In this approach, fatigue is seen as a degradation of the total crack energy by introducing scalar parameters that depend on the factors such as stress, bulk energy, $\mathcal{G}_C$, l_c, etc. Boldrini [48] presented thermo-mechanical phase-field fatigue by introducing an additional scalar parameter. Schreiber [49] proposed additional energy contribution to the total energy. A more intuitive approach regarding fatigue is proposed by [50, 51, 52, 53, 54], where stiffness and fracture energy are degraded as a function of cumulative stored potential. As a natural consequence, these models can accurately recover Paris-law and S-N curves, making them self-sufficient. Recently, Seles [52] proposed a cycle jumping technique to capture high cycle fatigue efficiently.

A summary of the proposed models is presented in this section. Recalling the regularized fracture energy functional of the solid in Eq. (1.9) takes the form

$$\Pi(\mathbf{u}, \mathfrak{d}) = \int_\Omega \left[g(\mathfrak{d}) + \eta_l\right] \Psi_0(\boldsymbol{\varepsilon})\, \mathrm{dV} + \int_\Omega \frac{\mathcal{G}_C}{4c_w}\left[\frac{\alpha(\mathfrak{d})}{l} + l\,|\nabla\mathfrak{d}|^2\right] \mathrm{dV} - \mathcal{P}(\mathbf{u}(\mathbf{x})). \tag{1.26}$$

To accommodate the fatigue behaviour, the crack energy in Eq. (1.26) is modified with a fatigue degradation function $f(\bar{\alpha}(\tau))$ for a properly defined cumulative history variable $\bar{\alpha}(\tau)$ that depends on the pseudo time τ as

$$\Pi(\mathbf{u}, \mathfrak{d}) = \int_\Omega \left[g(\mathfrak{d}) + \eta_l\right] \Psi_0(\boldsymbol{\varepsilon})\, \mathrm{dV} + \int_\Omega f(\bar{\alpha}(t))\frac{\mathcal{G}_C}{4c_w}\left[\frac{\alpha(\mathfrak{d})}{l} + l\,|\nabla\mathfrak{d}|^2\right] \mathrm{dV} - \mathcal{P}(\mathbf{u}(\mathbf{x})). \tag{1.27}$$

Notice that, in order for the second integral to be meaningful, it is necessary that $f(\bar{\alpha}(\tau)) \in L^1_{loc}(\mathcal{B})$. It is evident from Eq. (1.27) that fatigue degradation affects both local and non-local terms. This choice makes the support of phase-field not change from its optimal profile. Moreover, this further can be understood as reducing fracture toughness $\mathcal{G}_C$ of the material. Naturally, the fatigue degradation function has the following properties

$$f(\bar{\alpha} = 0) = 1; \qquad f(\bar{\alpha} \to \infty) = 0; \quad f \in [0, 1]; \quad f(\bar{\alpha} \leq \alpha_T) = 1; f'(\bar{\alpha}) \leq 0 \text{ for } 0 \leq f(\bar{\alpha}) \leq 1,$$

for some threshold α_T which triggers the fatigue effects.

1.4.1 Cumulative history variable

The term $\bar{\alpha}(t)$ describes the cumulative history effects due to fatigue. The related literature for some suitable quantity α, used is as follows.

(i) Mean independent load fatigue is defined as

$$\bar{\alpha}(\mathbf{x}, t) = \int_0^t H(\alpha\dot{\alpha})|\dot{\alpha}|d\tau,$$

where $H(\alpha\dot{\alpha})$ is heavy-side function defined as

$$H(\alpha\dot{\alpha}) = \begin{cases} 1 & \alpha\dot{\alpha} \geq 0 \quad \text{(loading)} \\ 0 & \text{otherwise (unloading)} \end{cases},$$

(ii) Mean load-dependent fatigue

$$\bar{\alpha}(\mathbf{x}, t) = \frac{1}{\alpha_N} \int_0^t H(\alpha\dot{\alpha})\alpha\dot{\alpha}d\tau,$$

where α_N is a normalization parameter used to achieve dimensional consistency. The standard choice of fatigue history variables (α) in literature are listed as follows:

(i) $\alpha = \boldsymbol{\varepsilon}$ (in 1D) [55], which in multi-dimension takes the form $\alpha = ||\boldsymbol{\varepsilon}||$. Due to strain singularity in crack tip, this choice is shown to be effective only in 1D, whereas in multi-dimensional setting leads to meh dependency issues.

(ii) $\alpha = \Psi(\boldsymbol{\varepsilon}, \mathfrak{d})$, [55, 56] the total degradation strain energy ensures that the model is not affected by crack tip singularity. However, this choice does not distinguish between compression and tension, where this can be solved by only considering the active part/ tensile part of the strain energy as $\alpha = \Psi^+(\boldsymbol{\varepsilon}, \mathfrak{d})$.

Notice that, in all the models mentioned above, due to the existence of the Heavy-side function, the energy accumulation increases only during loading.

1.4.2 Fatigue degradation function

The function $f(\bar{\alpha}(\tau))$ describes the degradation of the material property due to repeated loading. The functions can be mainly categorised into asymptotic degradation (i.e as $\bar{\alpha}(t) \to \infty$, $f(\bar{\alpha}) \to 0$) and symptomatic degradation (i.e for $\bar{\alpha}(t) > \alpha_\infty$, $f(\bar{\alpha}) = 0$).

The commonly used asymptotic degradation functions in the literature are

$$f(\bar{\alpha}) = \begin{cases} 1 & \text{if } \bar{\alpha}(t) \leq \alpha_T \\ \left(\dfrac{2\alpha_T}{\bar{\alpha}(t) + \alpha_T} \right)^2 & \text{if } \bar{\alpha}(t) \geq \alpha_T \end{cases}$$

$$f(\bar{\alpha}) = \begin{cases} 1 & \text{if } \bar{\alpha} = 0 \\ \left(1 - \dfrac{\bar{\alpha}(t)}{\bar{\alpha}(t) + \alpha_\infty} \right)^2 & \text{if } \bar{\alpha}(t) \in [0, \infty]. \end{cases}$$

The commonly defined symptomatic functions are

$$f(\bar{\alpha}) = \begin{cases} 1 & \text{if } \bar{\alpha}(t) \leq \alpha_T \\ \left[1 - k\, log \dfrac{\bar{\alpha}(t)}{\alpha_T}\right]^2 & \text{if } \alpha_T \leq \bar{\alpha}(t) \leq \alpha_T 10^{\frac{1}{k}} \\ 0 & \text{if } \bar{\alpha}(t) \geq \alpha_T 10^{\frac{1}{k}} \end{cases}$$

$$f(\bar{\alpha}) = \left(\zeta log \frac{\alpha_\infty}{\bar{\alpha}(t)}\right)^2 \text{ for } \bar{\alpha}(t) \in [\alpha_\infty, 10^{\frac{1}{\zeta}} \alpha_\infty],$$

for some material parameter α_∞. See [52] for more details.

1.5 Objective and outlines

In the view of state-of-the-art computational methods, this work presents a novel contribution to the variational approach to fracture for multi-physics applications in the spirit of phase-field methods. In particular, the objectives of this thesis are fourfold.

- Developing a robust phase-field model for functionally graded materials when the internal length scale is constant and proving that such model $\Gamma-$Convergence to original Griffith's criteria.
- Development of multi-phase field model based on Puck's failure criteria for anisotropic fracture of long fiber-reinforced composites. Combined with cohesive zone modeling methods, apply the model to capture delamination migration in the layered composites.
- Development of fully integrated non-linear thermo-elastic phase-field fracture method of thin-walled structures for large displacement. Within this framework is a comprehensive analysis of the thermo-elastic behavior and extension of such a model to functionally graded materials.
- Within this framework of thin-walled structures, extend the model to accommodate fatigue failure such that Paris law and Wöhler curves are the natural consequence of the developed model.

With these objectives in mind, this thesis is divided into six chapters:

1. Chapter 2 presents the phase-field approximation to fracture for Functionally Graded Materials (FGM) incorporating the characteristic length scale as a material parameter. A rule of the mixture is employed to estimate the material properties according to the volume fractions of the constituent materials. Based on the ideas stemming from size-scale effects, Γ-convergence for the proposed model is proved. A comprehensive sensitivity analysis discusses the effects of various model parameters. Moreover, We first prove that the fracture energy and the elastic energy of FGM are bounded by their homogeneous constituents, and tools to predict are provided. Finally, the model is validated against the benchmark example, and the applicability of the proposed model is studied using numerous examples.
2. Chapter 3 presents the Multi-Phase Cohesive Zone model for laminated composites. In this study, a novel Multi Phase-Field (MPF) model relying on the Puck theory of

failure for intra-laminar failure at ply level is coupled with a Cohesive Zone Model (CZM) for inter-laminar cracking. The model is applied to qualitatively predict delamination migration in long laminated fiber-reinforced polymers composites comprising 44 cross-ply laminates. The reliability of the current approach is examined via the correlation with experimental results. Furthermore, insight into the potential role of different aspects of the delamination migration, including (i) the variation of the ply angle in the migration zone, (ii) the load application point, and (iii) initial crack length, is provided.

3. Biggest among all the chapters, chapter 4 is dedicated to the study of thermo-mechanical analysis of thin-walled structures. A thermodynamically consistent framework for coupled thermo-mechanical phase field for thin-walled structure using a fully integrated finite element is developed. The model is equipped with Enhanced Assumed Strains (EAS) to alleviate Poison and volumetric locking pathologies. This technique is further combined with the Assumed Natural Strain (ANS) method leading to locking free elements. Moreover, the same degradation function is used for both displacement and thermal fields. The numeric of the model is further divided into three parts
    (a) Section 4.4 provides examples of the model for thermo-elastic structures. Moreover, the model is combined with a cohesive zone to capture interface effects. In addition to this, the model is validated against the benchmark examples, and the applicability of the proposed model is shown using several examples.
    (b) Section 4.5 provides the numerical implementation of the thermo-mechanical model with phase-field. The role of temperature in crack propagation is demonstrated using several benchmark examples. Examples regarding thin plates and curved beams are provided to show the model's capability.
    (c) Section 4.6 provides the extension of the proposed model to FGM. Several benchmark problems (straight and curved shells) are provided and are compared against their homogeneous surrogates. Moreover, crack deflection , and temperature distributions in the FGM are compared. Effects of several material properties on crack propagation are pinpointed. Finally, numerical modeling of the three-phase/double FGM, which is becoming popular in recent times, is studied.
4. Chapter 5 concerns about the extension solid shell to include fatigue effects. As a natural consequence of the proposed model, Paris Law and Wöhler curves are recovered. Several application examples are shown to demonstrate the predictive capabilities of the model.
5. Finally, chapter 6 summarizes the main results and draws the conclusion of the thesis. Furthermore, some lights are shed on the future development in the view of phase-field methods.

Chapter 2

Fracture in Functionally Graded Materials (FGMs): $\Gamma-$convergence and mechanical insight on the effect of grading

This chapter is organised as follows. In Section 2.2, the main aspects of the modeling framework to simulate crack propagation in FGMs are presented by considering the internal length scale constant. A rule of mixture is employed to estimate the material properties, according to the volume fractions of the constituent materials, which have been varied according to given grading profiles. Based on the ideas stemming from the study of size-scale effects, Γ-convergence for the proposed model is proved when the internal length scale is either constant or a bounded function. Section 2.3 provides the results of Γ-converges by constructing a sequence of minimisers such that the sequence of functionals converges to the Griffith's potential. In section 2.4, the finite element implementation of the proposed model is discussed using Broyden-Fetcher-Goldfard–shanno (BFGS) algorithm. Section 2.5 presents several representative examples starting with the validation experiment. In the sequel, mechanical insights for the effect of grading is explored. Firstly, it is proved that the bulk energy and surface energy of the FGM is bounded between those of its homogeneous constituents. Later, the issue of crack propagation, the effects of Young modulus, apparent strength, grading profile, initial crack length and position are addressed. An equivalence relationship based on size-scale effects is provided along with the examples so that the large models can be brought down to a smaller size to analyse them effectively and reduce computational efficiency. An application example for a single fiber-reinforced FGM matrix is explored to further assess the potential of the model for micro-mechanics. The content of this chapter is mainly taken from [24].

2.1 Introduction

Mismatch in the material properties of mechanical components generally leads to the occurrence of weak interfaces which induce abnormal stress concentrations, and eventually leading to failure. In order to prevent such phenomena, the concept of Functionally Graded Materials (FGM), i.e. materials with spatial composition, has been intensively exploited in the last decades precluding interfacial stress concentration, and hence ameliorate resistance to failure [57]. Such a technological solution has attracted attention in the engineering community and industry so far [58]. In the recent past, FGMs have gained a notable popularity and have been applied in (but not limited to) turbine blades [59], rocket engines [60], artificial bone implants [61], shell structures [62] and airplanes [57].

Various studies [63, 64] have shown that FGMs are fundamentally different from homogeneous materials, and hence their corresponding crack propagation behavior can be especially complex [65]. There are multitude of factors affecting the crack growth of FGMs including: the ratio of Young's moduli [66], intrinsic toughness, strength variations [67], geometry, residual stresses, grading laws, among many other aspects. These factors suggest that any predictive model for crack events in FGM should incorporate the intrinsic variation of material properties according to its grading profile.

Cracks oriented perpendicular to the grading profile experiences asymmetric loading at the crack tip and crack propagation may change its direction leading to mode-mixity, which in turn alters the stress intensity [68, 69], while grading parallel to cracks leads to straight propagation [67]. The effective composite properties of FGM generally vary in a continuous manner within the specimen domain as a combination of its homogeneous constituents [65, 70]. Introduction of the continuous grading alters the stress field, leading to modified stress intensity factors and mode mixity. Moreover, in this context, several studies revealed that spatial variation in the toughness and in the yield strain [71, 72, 65] meant that the failure stress/strain values at any point might depend on the grading. These factors inevitably restricts the study of cracks in FGM using conventional numerical methods and hence their general behavior with respect to crack propagation.

Derived from the previous complex response, computational methods such as the finite element methods (FEM) have been extensively used in the literature for exploring fracture in FGM and linear elastic fracture mechanics, see [73, 74, 75]. Early investigation of mixed-mode cracks within the context of FEM can be seen in [76]. Gu et al. [77] used domain integral technique to simplify the model for calculating crack tip field for FGM. Anlas et al. [78] estimated stress-intensity factors in FGM using FEM by assigning different homogeneous properties to each element. Bao et al. [79] studied multiple cracking in FGM coatings. Kim and paulino [80] developed and implemented general purpose FEM formulation considering mixed-mode cracks. Discrete numerical methods are widely used in the study of crack propagation phenomena such as XFEM [81, 82, 83], scaled boundary FE formulation [84], remeshing algorithms based on cohesive elements (relying on the cohesive zone model, CZM) [85, 86], isoparametric graded finite element formulation [87, 88, 89]. Recently, Hrishikesh et al. [90] explored the possibility to simulate fracture events in FGMs using the phase field (PF) approach for fracture due to its strong potential (especially for composite structures [91, 92, 93, 94] and heterogeneous media [95, 96, 97, 98, 99, 100, 101, 102]) and partially verified the results with the experimental evidence. In this direction, recent studies concerned dynamic crack propagation in FGM using the phase field method [103, 104], and meshfree methods

[105], showing a tremendous potential, and providing a plausible route for the thorough treatment of dynamic simulations.

In contrast to previous studies, in this investigation, we propose an extension of the phase field model for fracture in [90] by considering the internal characteristic length scale as a intrinsic material parameter. It has been proved in [106] that, when the internal length scale l of phase-field is constant, it is equivalent to gradient damage model. Whereas, there is a debate among the phase-field community that, when l is constant, the model cannot be considered as phase-field model since $\Gamma-$ Convergence of the model is lost. In this regard, first, we carefully analyze that for any given bounded characteristic length scale (not limited to FGM), proving that the total energy Γ-converges to the Griffith's theory under the size-scale effects using the mathematical setting as derived in [17]. Also, we gain a further insight into the general mechanical properties of FGM which can be used to analyze, create or modify future design of FGMs. Due to the underpinned internal length scale, the difference in the failure strain at any material point is addressed in line with [90, 65, 69]. With these arguments, we also prove in two dimensional settings, gradient damage model is equivalent to phase field. These ingredients yield to a novel PF crack method for FGMs which provides a further potential for the exploration of the different aspects of the characteristic material and length scale properties onto the overall cracking response of the specimen.

2.2 Variational formulation

2.2.1 Extension to FGM

Keeping in mind the mathematical model presented in Section 1.3, and total energy potential defined in Eq. (1.9), geometric crack function is chosen in line with AT-2 model [29, 30, 31] as $\alpha(\mathfrak{d}) := \mathfrak{d}^2$ with normalization parameter $c_w := \int_0^s \sqrt{\alpha(s)}ds$. The choice of $\alpha(\mathfrak{d})$ is motivated [28] by the fact that quadratic function for $\alpha(\mathfrak{d})$ ensures the admissible range $\mathfrak{d} \in [0, 1]$ with an infinite support. As a consequence, the phase field should be solved in the whole computational domain. However, the high computational time due to finer mesh size in order to resolve the gradients in the phase field is overcome by creating external localized band on the crack path.

The elastic energy function defined in Eq. (1.9) is defined as $\Psi_0(\boldsymbol{\varepsilon}) = \boldsymbol{\varepsilon}(\mathbf{u})^T : \mathbb{C} : \boldsymbol{\varepsilon}(\mathbf{u})$, where $\mathbb{C}$ is the constitutive tensor relating stresses and strains. The degradation of the initial elastic energy is performed using $g(\mathfrak{d}) = (1 - \mathfrak{d})^2 + \eta_l$.

In the context of FGMs, it is evident that the the material properties exhibit a spatial variation within the specimen domain, and therefore they are functions of the material point [107, 108], i.e. depending on the location. Consider a FGM with grading profile $V_f = V_f(\mathbf{x})$ as a function of spatial variable $\mathbf{x}$. Then all the material properties can be expressed as a function of $V_f(\mathbf{x})$ i.e $\mathcal{G}_C = \mathcal{G}_C(\mathbf{x}, V_f) = \mathcal{G}_C(\mathbf{x})$ and the compliance tensor $\mathbb{C} = \mathbb{C}(\mathbf{x}, V_f) = \mathbb{C}(\mathbf{x})$. The compliance tensor for the 2D plane strain takes the form:

$$\mathbb{C}(x) = \frac{E(\mathbf{x})}{(1+\nu(\mathbf{x}))(1-2\nu(\mathbf{x}))} \begin{bmatrix} 1-\nu(\mathbf{x}) & \nu(\mathbf{x}) & 0 \\ \nu(\mathbf{x}) & 1-\nu(\mathbf{x}) & 0 \\ 0 & 0 & \frac{1-2\nu(\mathbf{x})}{2} \end{bmatrix},$$

where $E(\mathbf{x})$ and $\nu(\mathbf{x})$ is the position-dependent Young's modulus and Poisson ratio respectively.

As an example, for $n_{dim} = 2$, and $\mathbf{x} =[x, y]$ within a rectangular plate of width $2w$ and height $2b$, and grading in the y-direction, the volume fraction V_f of the material A can be defined as $V_f(\mathbf{x}) = \left(\frac{1}{2} + \frac{y}{h}\right)^K$, where K represent a material gradient index.

Then, via the invocation of the rule of mixtures, the Young's modulus at a generic point $\mathbf{x} \in \mathcal{B}$ as $E(\mathbf{x}) = E_A + (E_B - E_A)V_f(\mathbf{x})$, where E_A, E_B are the Young's modulus of material A and material B, respectively. Similarly, the fracture toughness K_{IC} and the Poisson ratio ν are expressed as $K_{IC}(\mathbf{x}) = K_{ICA} + (K_{ICB} - K_{ICA})V_f(\mathbf{x})$ and $\nu(\mathbf{x}) = \nu_A + (\nu_B - \nu_A)V_f(\mathbf{x})$ and hence the fracture energy for plane strain condition takes the form $\mathcal{G}_{IC}(\mathbf{x}) = \frac{\left(1-\nu(\mathbf{x})^2\right)K_{IC}^2(\mathbf{x})}{E(\mathbf{x})}$.

The internal length scale l is largely considered as a material parameter [37]. This length scale l was experimentally determined in [109] for homogeneous materials, relating its value to the apparent material strength. Once the material parameter such as Young's modulus E , fracture toughness $\mathcal{G}_C$ are known, then the failure stress σ_c can be obtained using the closed-form relation $\sigma_c = \sqrt{\mathcal{G}_C E/L}$, where L is the characteristics size of the specimen. In particular, Tanné and co-authors [110] proposed that, once these material properties are known, i.e $\sigma_c,\ E, \mathcal{G}_C$, then the characteristic length l can be set as $l = \frac{27}{256}\left(\frac{\mathcal{G}_{Ic}E}{\sigma_c^2}\right)$.

The rationale behind the choice of constant length scale in [90] is due to the intricate relation between critical stress σ_c and fracture toughness $K_{IC} = \sigma_c Y\sqrt{\pi a}$, where Y is a geometric factor and ”a” is crack size. Under such conditions, the length scale given by $l = \frac{27}{256}\left(\frac{K_{IC}^2}{\sigma_c^2}\right) = \frac{27}{256}(Y^2\pi a)$ is a constant. However, within the context of FGM, this analysis can be assumed as simplification rendering the condition that the fracture toughness can be approximated as $K_{IC} = \sigma_\infty Y\sqrt{\pi a_c}$, where a_c is the smallest defect size, which in principle is an internal defect size depending upon the intrinsic material properties. Moreover, a general analysis might suggest that failure stress for FGM at different locations might also happen at different values, yielding that the critical stress σ_c required for cracking is also a function of grading. This later condition leads to approximate σ_c as a function of grading $V_f(\mathbf{x})$, and possibly the characteristics length scale l would be also a function of the spatial variation, i.e. function of the material point location $\mathbf{x}$. Thus, the variation of $E, \mathcal{G}_{Ic}, V_f$ on $\mathbf{x}$ suggests that each material point $\mathbf{x} \in \mathcal{B}$ has different characteristics, see [72] and the references therein. Accordingly, and without any loss of generality, we assume in the sequel that $\sigma_c = f(V_f)$ [110, 111]

$$l(\mathbf{x}) = \frac{27}{256}\left(\frac{\mathcal{G}_{Ic}(\mathbf{x})E(\mathbf{x})}{\sigma_c^2(\mathbf{x})}\right). \tag{2.1}$$

Analyzing the previous expression, it is worth noting that the variation of length scale $l(\mathbf{x})$ depends on the elastic mismatch. For certain elastic mismatch, the variation of $l(\mathbf{x})$ can span across one order of magnitudes, as is discussed in the forthcoming sections.

Consequently, the total energy functional of Eq.(1.9) in the context of FGM is given by

$$\begin{aligned}\Pi_{l(\mathbf{x})}(\mathbf{u}, \mathfrak{d}) = \int_{\mathcal{B}} \left[(1-\mathfrak{d})^2 + \eta_l\right] \Psi_0(\boldsymbol{\varepsilon})\ \mathrm{dV} + \int_{\mathcal{B}} \frac{\mathcal{G}_C(\mathbf{x})}{2}\left[\frac{\mathfrak{d}^2}{l(\mathbf{x})} + l(\mathbf{x})\left|\nabla\mathfrak{d}\right|^2\right]\ \mathrm{dV} \\ - \int_{\mathcal{B}} \boldsymbol{f_v} \cdot \mathbf{u}\ \mathrm{dV} - \int_{\partial\mathcal{B}} \bar{\mathbf{t}} \cdot \mathbf{u}\, \mathrm{dS},\end{aligned} \tag{2.2}$$

with $\Psi_0(\boldsymbol{\varepsilon}) = \boldsymbol{\varepsilon}(\mathbf{u})^T : \mathbb{C}(\mathbf{x}) : \boldsymbol{\varepsilon}(\mathbf{u})$

Note that in order for the second integral in Eq.(2.2) to be mathematically meaningful, i.e [112, 113]

$$\int_{\mathcal{B}} \frac{\mathcal{G}_C(\mathbf{x})}{2} \left[\frac{\mathfrak{d}^2}{l(\mathbf{x})} + l(\mathbf{x}) \left|\nabla \mathfrak{d}\right|^2\right] \, \mathrm{dV} \in L^1(\mathcal{B}),$$

$\mathcal{G}_C(\mathbf{x})$ and $l(\mathbf{x})$ has to be at least locally integrable functions, i.e $\mathcal{G}_C(\mathbf{x}), l(\mathbf{x}) \in L^1_{loc}(\mathcal{A})$ in a compact set $\mathcal{A} \subset \mathcal{B}$ with $l(\mathbf{x}) \neq 0$ for all $\mathbf{x} \in \mathcal{B}$. It is easy to see that, if $V_f(\mathbf{x}) \in L^1_{loc}(\mathcal{A})$, then by construction $\mathcal{G}_C(\mathbf{x}), l(\mathbf{x}) \in L^1_{loc}(\mathcal{A})$ for some compact set $\mathcal{A}$.

2.2.2 Governing equation

The solution to Eq. (2.2) can be obtained by solving it as a minimization problem, i.e determine $(\mathbf{u}, \mathfrak{d})$ from

$$(\mathbf{u}(\mathbf{x}),\, \mathfrak{d}(\mathbf{x})) = \arg\min_{\mathbf{x}} \{\Pi_{l(\mathbf{x})}(\mathbf{u}, \mathfrak{d})\}. \tag{2.3}$$

The governing (Euler-Lagrangian) equations under quasi-static conditions are determined by taking first variation of the functional $\Pi_{l(\mathbf{x})}(u, \mathfrak{d})$ in Eq. (2.2) in terms of Gateaux derivative for the variation $\delta\mathbf{u}$ and $\delta\mathfrak{d}$ of $\mathbf{u}$ and $\mathfrak{d}$ respectively, resulting in

$$\left[(1-\mathfrak{d})^2 + K_l\right] \nabla \cdot \boldsymbol{\sigma}(\mathbf{x}) + \boldsymbol{f_v} = 0 \quad \text{on } \mathcal{B}, \tag{2.4a}$$

$$\text{with } \ \boldsymbol{\sigma} \cdot \mathbf{n} = \bar{\mathbf{t}} \ \text{ on } \ \partial\mathcal{B}_t, \tag{2.4b}$$

$$\mathcal{G}_C(\mathbf{x}) \left[\frac{\mathfrak{d}}{l(\mathbf{x})} - l(\mathbf{x}) \boldsymbol{\Delta} \mathfrak{d}\right] - 2(1-\mathfrak{d})\Psi\left(\boldsymbol{\varepsilon}, \mathbf{x}\right) = 0 \, \text{on } \mathcal{B}, \tag{2.4c}$$

$$\text{with } \nabla\mathfrak{d} \cdot \mathbf{n} = 0 \text{ on } \partial\mathcal{B}, \tag{2.4d}$$

where $\mathbf{n}$ is the outward normal vector on $\partial\mathcal{B}$. Note that on boundary, $\nabla\mathfrak{d}\cdot\mathbf{n} = 0$ and residual stiffness $K_l = 0$ because of compactness property [17, 19].

The unilateral stationary condition [16] of the total energy functional implies that $\delta\Pi_{l(\mathbf{x})} = 0$ for each $\delta\mathfrak{d}, \delta\mathbf{u} > 0$ and $\delta\Pi_{l(\mathbf{x})} > 0$ for $\delta\mathfrak{d},\ \delta\mathbf{u} = 0$, along with the irriversibility [16, 114] and boundedness of $\mathfrak{d}$ leads to the following first order optimality (KKT) conditions for the quasi-static evolution.

$$\dot{\mathfrak{d}} \geq 0, \tag{2.5a}$$

$$\mathcal{G}_C(\mathbf{x}) \left[\frac{\mathfrak{d}}{l(\mathbf{x})} - l(\mathbf{x}) \boldsymbol{\Delta}\mathfrak{d}\right] - 2(1-\mathfrak{d})\Psi(\boldsymbol{\varepsilon}, \mathbf{x}) \leq 0, \tag{2.5b}$$

$$\dot{\mathfrak{d}} \left\{\mathcal{G}_C(\mathbf{x}) \left[\frac{\mathfrak{d}}{l(\mathbf{x})} - l(\mathbf{x}) \boldsymbol{\Delta}\mathfrak{d}\right] - 2(1-\mathfrak{d})\Psi(\boldsymbol{\varepsilon}, \mathbf{x})\right\} = 0, \tag{2.5c}$$

where $\dot{\mathfrak{d}} = \frac{d\mathfrak{d}}{dt}$. The expression $\mathcal{G}_C(\mathbf{x}) \left[\frac{\mathfrak{d}}{l(\mathbf{x})} - l(\mathbf{x})\boldsymbol{\Delta}\mathfrak{d}\right]$ indicates the energetic crack resistance and $2(\mathfrak{d}-1)\Psi(\boldsymbol{\varepsilon})$ is the crack driving force.

2.3 Γ-Convergence analysis

As mentioned above, due to the bounded nature of $l(\mathbf{x})$, which may also involve non-linearity due to heuristic differences in the material properties, the Γ-convergence in the sense of [19, 17, 22] can still be applied under the assumption that the domain $\mathcal{B}$ is size-scaled.

We use the existing results in [17] and prove that the model in Eq. (1.9), under scaling in two dimension, mimics that of the AT-2 model with a little variation. Note that, it is possible to apply the more recent advancements as in [115, 26, 116] with small modifications, but we choose to use [17] because of the mechanical insight that can be derived from the L^∞ bounds on $\mathbf{u}(\mathbf{x})$.

In order for this proof to be self-consistent, we provide few important definitions and results, while further details can be seen in [17] and references therein which are omitted here for the sake of brevity. The proof is organised as follows, first we redefine the problem in terms of a scaling function, convert the total energy in terms of scaling which is similar to that of the classical AT-2 model. Using density and compactness results of the space $SBD(\mathcal{B})$, we prove that the reduced energy functional satisfies lim-sup inequality by constructing a recovery sequence and later show that the results of [17] can be directly applied with small modification to get lim-inf inequality, if $l(\mathbf{x})$ is a bounded function (like in FGM) or even a constant (like in [117, 118]).

2.3.1 Mathematical setting

Given $\mathbf{u} \in \mathcal{B}$, where $\mathcal{B}$ is open subset of $\mathbb{R}^{n_{dim}}$, one says displacement $\mathbf{u} : \mathcal{B} \to \mathbb{R}^{n_{dim}}$ has bounded deformation (BD), whenever the symmetric part of the distributional derivative $\boldsymbol{\varepsilon}(\mathbf{u}) = \left(\dfrac{D\mathbf{u} + D^T\mathbf{u}}{2} \right)$ is a bounded radon measure [27]. Moreover $\boldsymbol{\varepsilon}(\mathbf{u})$ can be decomposed into three parts, one absolutely continuous part with respect to Lebesgue measure d$\mathbf{x}$, denoted by $\mathbf{e}(\mathbf{u})\mathrm{d}\mathbf{x}$, jump set carried by the rectifiable $(N-1)$ dimensional set J_u of points where the function $\mathbf{u}$ has approximate limits $\mathbf{u}^+(\mathbf{x})$ and $\mathbf{u}^-(\mathbf{x})$ together with some normal vector $\mathfrak{v}_u$ and Cantor part $\boldsymbol{\varepsilon}^c(\mathbf{u})$ which vanishes on Borel sets of finite $\mathcal{H}^{n_{dim}-1}$ measure. Meaning that, the crack set Γ (with respect to Lebesgue measure) is completely represented by the jump set J_u of $\mathbf{u}$. The space of $SBD(\mathcal{B})$ (special function of bounded deformation) is defined as

$$SBD(\mathcal{B}) := \{\mathbf{u} \in BD(\mathcal{B}); \boldsymbol{\varepsilon}^c(\mathbf{u}) = 0\}.$$

Restricting the analysis to 2D case, i.e. $\mathcal{B} \subset \mathbb{R}^2$. Let $\bar{\boldsymbol{u}}$ be a position vector $\bar{\mathbf{u}} = [\bar{u}, \bar{v}]$ defined on $\mathcal{B}$ such that for all $\bar{\mathbf{u}} \in \mathcal{B}$, the kinematic displacement field in $\mathcal{B}$ be defined as $\mathbf{u}(\bar{\boldsymbol{u}}) = [u(\bar{\boldsymbol{u}}),\, v(\bar{\boldsymbol{u}})]$. Define the scaling function $S_\epsilon := \left(\dfrac{1}{2} + \dfrac{1}{2\epsilon} \right)$ and the continuous map $S_u : \mathcal{B} \to \mathcal{B}'$ with $S_u \in \mathbb{R}^{2\times 2}$ as

$$S_u := S_\epsilon \begin{bmatrix} 1 & 0 \\ 0 & 1 \end{bmatrix}. \tag{2.6}$$

Define the inverse mapping $S_u^{-1} : \mathcal{B}' \to \mathcal{B}$ as

$$S_u^{-1} := \frac{1}{S_\epsilon} \begin{bmatrix} 1 & 0 \\ 0 & 1 \end{bmatrix},$$

where $\epsilon > 0$ is a positive constant that goes to zero, and $\mathcal{B}'$ is the scaled domain such that $\mathcal{B}' = S_u\mathcal{B} \subset \mathbb{R}^2$. Let $\boldsymbol{x}$ be a position vector $\boldsymbol{x} := [x, y]$ defined on $\mathcal{B}'$, then for all $\boldsymbol{x} \in \mathcal{B}'$, $\boldsymbol{x}$ is defined in terms of scaling as $\boldsymbol{x} = S_u\left(\bar{\mathbf{u}}\right)^T$. Meaning that

$$\boldsymbol{x} = [x, y] = S_\epsilon \begin{bmatrix} 1 & 0 \\ 0 & 1 \end{bmatrix} \begin{bmatrix} \bar{u} \\ \bar{v} \end{bmatrix} = S_\epsilon[\bar{u}, \bar{v}] = S_\epsilon\bar{\mathbf{u}}.$$

The corresponding displacement field on $\mathcal{B}'$ is defined as $\mathbf{u}(\boldsymbol{x})$. Assuming that each of the displacement field is bounded uniformly (by applied displacement) in $L^\infty(\mathcal{B}')$, for a fixed large enough applied displacement M', we have the following theorem.

Theorem 1. *Let $\mathcal{B}'$ be a Lipschitz-regular bounded open set. Let $M' > 0$, $\epsilon > 0$, for a positive bounded function $l(\boldsymbol{x}) \in L^1_{loc}(\mathcal{B}')$, define the functional for $(\mathbf{u},\, \mathfrak{d}) \in L^2(\mathcal{B}',\, \mathbb{R}^2) \times L^2(\mathcal{B}')$,*

$$\Pi_{l(\mathbf{x})}(\mathbf{u}, \mathfrak{d}) = \begin{cases} \int_{\mathcal{B}'} \left[(1-\mathfrak{d})^2 + K_\epsilon\right] \Psi(\mathbf{e}(\mathbf{u}))\, dV + \int_{\mathcal{B}'} \dfrac{\mathcal{G}_C(\mathbf{x})}{2} \left[\dfrac{\mathfrak{d}^2}{l(\mathbf{x})} + l(\mathbf{x})\left|\nabla\mathfrak{d}\right|^2\right] dV \\ \textit{if } (\mathbf{u},\, \mathfrak{d}) \in H^1(\mathcal{B}',\, \mathbb{R}^2) \times H^1(\mathcal{B}'), \textit{ and } \|u\|_{L^\infty} \le M' \\ +\infty \qquad \textit{otherwise}, \end{cases} \tag{2.7}$$

with $K_\epsilon = o(\epsilon) \to 0$ as $\epsilon \to 0$. Then, as $\epsilon \to 0$, $\Pi_{l(\mathbf{x})}(u, \mathfrak{d})$ $\Gamma-$converges (in $L^2(\mathcal{B}',\, \mathbb{R}^2) \times L^2(\mathcal{B}')$) to

$$\Pi(\mathbf{u}, \mathfrak{d}) = \begin{cases} \int_{\mathcal{B}} \Psi(\mathbf{e}(\mathbf{u}))\, dV + \mathcal{G}_C\mathcal{H}^1(J_u) & \textit{if } \mathbf{u} \in SBD(\mathcal{B}),\ \mathfrak{d} = 1 \textit{ and } \|u\|_{L^\infty} \le M' \\ +\infty & \textit{otherwise} \end{cases}. \tag{2.8}$$

First, consider for all $\bar{\boldsymbol{u}} \in \mathcal{B}$, for displacement $\mathbf{u}(\bar{\boldsymbol{u}})$, it is assumed that $\mathbf{u}(\bar{\boldsymbol{u}}) \in SBD(\mathcal{B})$, and is bounded by $\|\mathbf{u}\|_{L^\infty} \le M$. Then, it is easy to see that for all $\boldsymbol{x} \in \mathcal{B}'$, there exists a constant M' depending on the scaling factor S_ϵ and M such that the deformation $\|\mathbf{u}\|_{L^\infty(\mathcal{B}')} \le M'$. Hence, without loss of generality, we can assume that $\|\mathbf{u}\|_{L^\infty(\mathcal{B}')} \le M'$ where M' is applied displacement on $\mathcal{B}'$.

Physically, this means that, if body $\mathcal{B}$ with the applied displacement $M(\mathbf{u})$ produces a strain of $\boldsymbol{\varepsilon}(\mathbf{u})$, then, depending on the scaling factor S_ϵ, the same applied displacement $M(\mathbf{u})$ creates the strain proportional to $\dfrac{\boldsymbol{\varepsilon}(\mathbf{u})}{S_\epsilon}$ in $\mathcal{B}'$ (assuming uniform deformation). Hence, the applied displacement that is required to create the same strain $\boldsymbol{\varepsilon}(\mathbf{u})$ in $\mathcal{B}'$ depends on the scaling factor. To be precise $M' \propto S_\epsilon M$.

In [17], the compactness results for $\mathbf{u} \in SBD(\mathcal{B})$ are shown in [Theorem 5.1, [17]]: If a sequence $(\mathbf{u}_n)_{n\ge1}$ in $SBD(\mathcal{B})$ is such that $\sup_{n\ge1}\Pi_{l(\mathbf{x})}(\mathbf{u}, \Gamma) < \infty$, then up to a subsequence, there exists $\mathbf{u} \in SBD(\mathcal{B})$ such that $\mathbf{u}_n \to \mathbf{u}$ strongly in $L^2(\mathcal{B}, \mathbb{R}^2)$, $\mathbf{e}(\mathbf{u}_n) \to \mathbf{e}(\mathbf{u})$ weakly in $L^2(\mathcal{B}; \mathbb{S}^{2\times2})$ and $\mathcal{H}^{N-1}(J_u) \le \liminf_{n\to\infty}(J_{u_n})$. Also, [Theorem 2, [17]] provides the density results for $\mathbf{u} \in SBD(\mathcal{B}) \cap L^2(\mathcal{B}, \mathbb{R}^2)$. Assuming $\sup_{n\ge1}\Pi_{l(\mathbf{x})}(\mathbf{u}, \Gamma) < \infty$, then there exist a sequence $(\mathbf{u}_n)$ of displacement in $SBD(\mathcal{B}) \cap L^2(\mathcal{B}, \mathbb{R}^2)$, and $\|\mathbf{u}_n - \mathbf{u}\|_{L^2(\mathcal{B},\mathbb{R}^2)} \to 0$, such that J_{u_n} is closed in $\mathcal{B}$, contained in a finite union of closed connected pieces of C^1 curves, $\mathbf{u}_n \in H^1(\mathcal{B}/J_{u_n}; \mathbb{R}^2)$ and $\limsup_{n\to\infty}\Pi_{l(\mathbf{x})}(\mathbf{u}, \bar{J}_{u_n}) \le \Pi_(\mathbf{u}, J_u)$.

With compactness and density results at hand, the proof of the Theorem 1 is organized as follows. First we show that Eq. (2.7), by a simple change of variable can be reduced to the energy potential function similar to that of the potential used in [17], but with a little difference. Later, we show the existence of minimizing sequence $(\mathbf{u}_\epsilon, \mathfrak{d}_\epsilon)$ to the reduced model so as to prove the lim-sup inequality. Later, we show that for the lim-inf inequality, the reduced model follows the same proof of lim-inf as in [17]. Due to the existence of minimizing sequence, and lim-sup inequality assuming a suitable coercivity property of the functional, the proof of the Theorem 1 is immediate.

2.3.2 Model reduction

Consider the energy functional in Eq. (2.7)

$$\Pi_{l(\mathbf{x})}(\mathbf{u}, \mathfrak{d}) = \int\limits_{\mathcal{B}'} \left[(1-\mathfrak{d})^2 + K_\epsilon\right] \Psi(\mathbf{e}(\mathbf{u}))\, \mathrm{dV} + \int\limits_{\mathcal{B}'} \frac{\mathcal{G}_C(\mathbf{x})}{2} \left[\frac{\mathfrak{d}^2}{l(\mathbf{x})} + l(\mathbf{x})\, |\nabla \mathfrak{d}|^2\right] \mathrm{dV},$$

notice that $\mathcal{B}' = S_u \mathcal{B}$ is the sizing domain which contains S_ϵ, the size-scaling factor. The choice of S_ϵ is motivated by the fact that when $\epsilon = 1$, $S_\epsilon = 1$ which coincide with the domain $\mathcal{B}$. As $\epsilon \to 0$, $\mathcal{B}'$ expands and gives the same effect as if $l \to 0$ in $\mathcal{B}$, meaning that as $\epsilon \to 0$, the surface energy asymptotically goes to the $\mathcal{H}^1(J_u)$ approaching a sharp crack.

Since, dealing with the expanding boundaries is mathematically challenging, by using simple change of variable, it is possible to move S_ϵ inside the integral. For this reason, consider the scaling as defined before
$\boldsymbol{x} = S_\epsilon \bar{\mathbf{u}}$ implying $x = S_\epsilon \bar{u}$ and $y = S_\epsilon \bar{v}$.
From change of variable, we have

$$\int\limits_{\mathcal{B}'} f(x, y) \mathrm{d}\boldsymbol{x} = \int\limits_{\mathcal{B}} f(S_\epsilon \bar{u}, S_\epsilon \bar{v})\, |\mathbf{J}|\, \mathrm{d}\bar{\mathbf{u}},$$

for the Jacobian,

$$|\mathbf{J}| = \frac{\partial(x, y)}{\partial(\bar{u}, \bar{v})} = \begin{vmatrix} \dfrac{\partial x}{\partial \bar{u}} & \dfrac{\partial x}{\partial \bar{v}} \\ \dfrac{\partial y}{\partial \bar{u}} & \dfrac{\partial y}{\partial \bar{v}} \end{vmatrix} = \frac{\partial x}{\partial \bar{u}} \frac{\partial y}{\partial \bar{v}} = (S_\epsilon)^2 .$$

Now, the gradients can be defined as

$$\nabla \mathbf{u}(\boldsymbol{x}) = \left[\frac{\partial \mathbf{u}}{\partial x}, \frac{\partial \mathbf{u}}{\partial y}\right],$$

$$\frac{\partial \mathbf{u}}{\partial x} = \frac{\partial \mathbf{u}}{\partial \bar{u}} \frac{\partial \bar{u}}{\partial x} + \frac{\partial \mathbf{u}}{\partial \bar{v}} \frac{\partial \bar{v}}{\partial x} = \frac{\partial \mathbf{u}}{\partial \bar{u}} \frac{1}{S_\epsilon},$$

and

$$\frac{\partial \mathbf{u}}{\partial y} = \frac{\partial \mathbf{u}}{\partial \bar{u}} \frac{\partial \bar{u}}{\partial y} + \frac{\partial \mathbf{u}}{\partial \bar{v}} \frac{\partial \bar{v}}{\partial y} = \frac{\partial \mathbf{u}}{\partial \bar{v}} \frac{1}{S_\epsilon}.$$

Now, $\nabla \mathbf{u}(\boldsymbol{x}) = \dfrac{1}{S_\epsilon} \nabla \mathbf{u}(\bar{\mathbf{u}})$ where $\mathbf{u}(\bar{\mathbf{u}})$ is the displacement at scaled points. Notice that no assumption of the displacement is made here. Hence, we have $\boldsymbol{\varepsilon}(\mathbf{u}(\boldsymbol{x})) = \left(\dfrac{\nabla \mathbf{u} + \nabla^T \mathbf{u}}{2}\right) = \dfrac{1}{S_\epsilon} \boldsymbol{\varepsilon}(\mathbf{u}(\bar{\mathbf{u}}))$.

As in the case of the linear elasticity $\Psi(\boldsymbol{\varepsilon}(\mathbf{u})) = \boldsymbol{\varepsilon}(\mathbf{u}) : \mathbb{C}(\bar{\mathbf{u}}) : \boldsymbol{\varepsilon}(\mathbf{u})$, having a quadratic form and since $\mathbb{C}(\boldsymbol{x})$ is positive definite matrix, $\mathbb{C}(\bar{\mathbf{u}})$ is the continuous one to one mapping from $\mathcal{B}'$ to $\mathcal{B}$ without changing the matrix or its positive definiteness. From this, we can conclude that $\Psi(\boldsymbol{\varepsilon}(\mathbf{u}(\boldsymbol{x}))) = \dfrac{1}{S_\epsilon^2}\Psi(\boldsymbol{\varepsilon}(\mathbf{u}(\bar{\mathbf{u}})))$.

Now, the bulk energy becomes:

$$\begin{aligned}\int\limits_{\mathcal{B}'} \left[(1-\mathfrak{d})^2 + K_\epsilon\right] \Psi(\mathbf{e}(\mathbf{u}))\mathrm{d}\boldsymbol{x} &= \int\limits_{\mathcal{B}} \left[(1-\mathfrak{d})^2 + K_\epsilon\right] \frac{1}{S_\epsilon^2}\Psi(\boldsymbol{\varepsilon}(\mathbf{u}(\bar{\mathbf{u}})))\,|\mathbf{J}|\;\mathrm{d}\bar{\mathbf{u}} \\ &= \int\limits_{\mathcal{B}} \left[(1-\mathfrak{d})^2 + K_\epsilon\right] \Psi(\boldsymbol{\varepsilon}(\mathbf{u}(\bar{\mathbf{u}})))\,\mathrm{d}\bar{\mathbf{u}}.\end{aligned} \tag{2.9}$$

Physically, this means that for a fixed applied displacement M', the bulk energy released by body $\mathcal{B}$ and $\mathcal{B}'$ are equal which can also be readily seen numerically in forthcoming analysis. Now consider the surface energy in Eq. (2.7),

$$\int\limits_{\mathcal{B}'} \frac{\mathcal{G}_C(\mathbf{x})}{2}\left[\frac{\mathfrak{d}^2}{l(\mathbf{x})} + l(\mathbf{x})\,|\nabla\mathfrak{d}|^2\right]\mathrm{d}\boldsymbol{x}.$$

In order to inherit the result of [17], it is required that $\mathfrak{d}^* = 1$ for intact material and $\mathfrak{d}^* = 0$ for fully broken state. Hence, renaming $\mathfrak{d}$, set $\mathfrak{d}^* = (1-\mathfrak{d})$, we have surface energy as

$$\int\limits_{\mathcal{B}'} \frac{\mathcal{G}_C(\mathbf{x})}{2}\left[\frac{(1-\mathfrak{d}^*)^2}{l(\mathbf{x})} + l(\mathbf{x})\,|\nabla\mathfrak{d}^*|^2\right]\mathrm{d}\boldsymbol{x}.$$

Applying change of variable here would result in

$$\int\limits_{\mathcal{B}'} \frac{\mathcal{G}_C(\mathbf{x})}{2}\left[\frac{(1-\mathfrak{d}^*)^2}{l(\mathbf{x})} + l(\mathbf{x})\,|\nabla\mathfrak{d}^*|^2\right]\mathrm{d}\boldsymbol{x} = \int\limits_{\mathcal{B}} \frac{\mathcal{G}_C(\mathbf{x})}{2}\left[\frac{(1-\mathfrak{d}^*(S_\epsilon\bar{\mathbf{u}}))^2}{l(\mathbf{x})}S_\epsilon^2 + l(\mathbf{x})\,|\nabla\mathfrak{d}^*(S_\epsilon\bar{\mathbf{u}})|^2\right]\mathrm{d}\bar{\mathbf{u}}.$$

Without loss of generality, relabeling and renaming the variables leads to

$$\int\limits_{\mathcal{B}'} \frac{\mathcal{G}_C(\mathbf{x})}{2}\left[\frac{(1-\mathfrak{d}^*)^2}{l(\mathbf{x})} + l(\mathbf{x})\,|\nabla\mathfrak{d}^*|^2\right]\mathrm{d}\boldsymbol{x} = \int\limits_{\mathcal{B}} \frac{\mathcal{G}_C(\mathbf{x})}{2}\left[\frac{(1-\mathfrak{d}^*)^2}{l(\mathbf{x})}S_\epsilon^2 + l(\mathbf{x})\,|\nabla\mathfrak{d}^*|^2\right]\mathrm{d}\boldsymbol{x}. \tag{2.10}$$

Combining bulk energy and surface energy leads to

$$\Pi_{l(\mathbf{x}),\epsilon}(\mathbf{u},\mathfrak{d}^*) = \int\limits_{\mathcal{B}} \left[\mathfrak{d}^{*2} + K_\epsilon\right]\Psi(\boldsymbol{\varepsilon}(\mathbf{u}))\,\mathrm{d}\boldsymbol{x} + \int\limits_{\mathcal{B}} \frac{\mathcal{G}_C(\mathbf{x})}{2}\left[\frac{(1-\mathfrak{d}^*)^2}{l(\mathbf{x})}S_\epsilon^2 + l(\mathbf{x})\,|\nabla\mathfrak{d}^*|^2\right]\mathrm{d}\boldsymbol{x}, \tag{2.11}$$

with $\|\mathbf{u}\|_{L^\infty} \leq M'$, $\mathfrak{d}^* = 0$ for fully broken state and $\mathfrak{d}^* = 1$ for intact state and $\mathfrak{d}^* : \mathcal{B} \to [0,1]$.

Now, it becomes clear identify that functional in Eq. (2.7) and Eq. (2.11) are equivalent to each other. Also, this equivalence has an important consequence as an engineering application which is explained in Section 2.5.3. With the results on $SBD(\mathcal{B})$ and L^∞ bounds on $\mathbf{u}$, Theorem 1 is equivalent to showing the $\Gamma-$convergence to the following Theorem.

Theorem 2. *Let $\mathcal{B}$ be a lipschitz-regular bounded open set. Let $M' > 0$, $\epsilon > 0$, for a positive bounded function $l(\boldsymbol{x}) \in L^1_{loc}(\mathcal{B})$, define the functional for $(\mathbf{u}, \mathfrak{d}^*) \in L^2(\mathcal{B}, \mathbb{R}^2) \times L^2(\mathcal{B})$,*

$$\Pi_{l(\mathbf{x}),\epsilon}(\mathbf{u}, \mathfrak{d}^*) = \begin{cases} \int_{\mathcal{B}} \left[\mathfrak{d}^{*2} + K_\epsilon\right] \Psi(\boldsymbol{\varepsilon}(\mathbf{u}))\, d\boldsymbol{x} + \int_{\mathcal{B}} \dfrac{\mathcal{G}_C(\mathbf{x})}{2} \left[\dfrac{(1-\mathfrak{d}^*)^2}{l(\mathbf{x})} S_\epsilon^2 + l(\mathbf{x}) \left|\nabla \mathfrak{d}^*\right|^2\right] d\boldsymbol{x} \\ \textit{if } (\mathbf{u}, \mathfrak{d}^*) \in H^1(\mathcal{B}, \mathbb{R}^2) \times H^1(\mathcal{B}) \textit{ and } \|\mathbf{u}\|_{L^\infty} \le M' \\ +\infty \qquad \textit{otherwise}, \end{cases} \tag{2.12}$$

with $K_\epsilon = o(\epsilon) \to 0$ as $\epsilon \to 0$. Then, as $\epsilon \to 0$, $\Pi_{l(\mathbf{x}),\epsilon}(\mathbf{u}, \mathfrak{d}^*)$ $\Gamma-$converges (in $L^2(\mathcal{B}, \mathbb{R}^2) \times L^2(\mathcal{B})$) to

$$\Pi(\mathbf{u}, \mathfrak{d}^*) = \begin{cases} \int_{\mathcal{B}} \Psi(\mathbf{e}(\mathbf{u}))d\boldsymbol{x} + \mathcal{G}_C \mathcal{H}^1(J_u) & \textit{if } \mathbf{u} \in SBD(\mathcal{B}),\ \mathfrak{d}^* = 1 \textit{ and } \|\mathbf{u}\|_{L^\infty} \le M' \\ +\infty & \textit{otherwise} \end{cases}. \tag{2.13}$$

Proof. First notice that mechanical energy is the same in both Eq. (2.7) and (2.12) , also recall that J_u is $\left(\mathcal{H}^1, 1\right)$ rectifiable. Because of Theorem 3 of [17], we just need to prove lim-inf inequality for $(\mathbf{u}, \mathfrak{d}^*)$ with $\mathfrak{d}^* = 0$ and $\mathbf{u} \in SBD(\mathcal{B})$ with $\mathcal{H}^1(\bar{J}_u) < \infty$, replacing $\mathcal{H}^1(J_u)$ by $\mathcal{H}^1(\bar{J}_u)$ in the energy (also assuming the closure of J_u, i.e $\bar{J}_u$ is rectifiable). Define distance function

$$d(\boldsymbol{x}) := \operatorname{dist}(\boldsymbol{x}, \bar{J}_u).$$

The volume of the area bounded by s-level set of d is

$$\boldsymbol{l}(s) = \left|\left\{\boldsymbol{x} \in \mathbb{R}^2;\ d(\boldsymbol{x}) \le s\right\}\right| \text{ for all } s > 0.$$

The distance function is 1-lipshitz, i.e $|\nabla d(\boldsymbol{x})| = 1$ a.e. Now the co-area formula for lipshitz functions is given by

$$\boldsymbol{l}(s) = \int_0^s \mathcal{H}^1(\{\boldsymbol{x};\ d(\boldsymbol{x}) = t\})\mathrm{d}t,$$

so that, in particular we have that

$$\boldsymbol{l}'(s) = \mathcal{H}^1(\{\boldsymbol{x};\ d(\boldsymbol{x}) = s\}).$$

Now, we can easily see that

$$\lim_{s\to 0} \frac{\boldsymbol{l}(s)}{s} = \lim_{s\to 0} \int_0^s \mathcal{H}^1(\{\boldsymbol{x};\ d(\boldsymbol{x}) = t\})\mathrm{d}t = \mathcal{H}^1(\bar{J}_u),$$

as $s \to 0$, $d(\boldsymbol{x}) \to 0$ much faster than s itself and hence $\dfrac{\boldsymbol{l}(s)}{s}$ shrinks to $\mathcal{H}-$measure. i.e

$$\lim_{s \to 0} \frac{\boldsymbol{l}(s)}{s} = \mathcal{H}^1(\bar{J}_u).$$

The proof of the lim-inf inequality result is mostly now standard [119, 21, 120] and Chambolle el at. [17] proved the result for linear elasticity. Hence, we show that the functional in Eq. (2.12) reduces to the already proven results and sketch the proof afterwards.

Consider a sequence $(\mathbf{u}_\epsilon, \mathfrak{d}^*_\epsilon)$ that converges to $(\mathbf{u}, \mathfrak{d}^*)$ such that $\sup_{\epsilon \geq 1} \Pi_{l(\mathbf{x}),\epsilon}(\mathbf{u}_\epsilon, \mathfrak{d}^*_\epsilon) < \infty$, then it is easy to show by taking for each ϵ a level set with $s_\epsilon \simeq 1/2$ such that

$\sup_{\epsilon > 0} \mathcal{H}^1\left(\partial_* \left\{\mathfrak{d}^*_j > s\right\}\right) < \infty$, then there exists a sub-sequence $(\mathbf{u}_{\epsilon_j}, \mathfrak{d}^*_{\epsilon_j})$ converges to some $(\mathbf{u}, \mathfrak{d}^*)$ in $L^2(\mathcal{B})$ as $\epsilon_j \to 0$(or $j \to \infty$) such that $\sup_{j \geq 1} \Pi_{l(\mathbf{x}),\epsilon}(\mathbf{u}_{\epsilon_j}, \mathfrak{d}^*_{\epsilon_j}) < \infty$. First note that, we must have $\mathfrak{d}^* = 1$, and consider the surface energy functional, and apply young's inequality in $L^2(\mathcal{B})$ with $a^2 = \dfrac{(1-\mathfrak{d}^*)^2}{l(\mathbf{x})} S^2_\epsilon$, $b^2 = l(\mathbf{x}) \left|\nabla \mathfrak{d}^*\right|^2$ and $2ab \leq a^2 + b^2$, we have

$$\begin{aligned}
\int_{\mathcal{B}} \left[\frac{\left(1-\mathfrak{d}^*_j\right)^2}{l(\mathbf{x})} S^2_{\epsilon_j} + l(\mathbf{x}) \left|\nabla \mathfrak{d}^*_j\right|^2\right] \mathrm{d}\boldsymbol{x} &\geq \int_{\mathcal{B}} \left[\left|(1-\mathfrak{d}^*_j)\right| \left(1 + \frac{1}{\epsilon_j}\right) \left|\nabla \mathfrak{d}^*_j\right|\right] \mathrm{d}\boldsymbol{x}, \\
&\geq \int_{\mathcal{B}} \left[\left|(1-\mathfrak{d}^*_j)\right| \left|\nabla \mathfrak{d}^*_j\right|\right] \, d\boldsymbol{x} \\
&+ \int_{\mathcal{B}} \left[\left|(1-\mathfrak{d}^*_j)\right| \left(\frac{1}{\epsilon_j}\right) \left|\nabla \mathfrak{d}^*_j\right|\right] \mathrm{d}\boldsymbol{x}, \\
&\geq \int_{\mathcal{B}} \left[\left|(1-\mathfrak{d}^*_j)\right| \left|\nabla \mathfrak{d}^*_j\right|\right] \, \mathrm{d}\boldsymbol{x},
\end{aligned}$$

so that, using the co-area formula, we obtain

$$\Pi_{l(\mathbf{x}),\epsilon_j}(\mathbf{u}_j, \mathfrak{d}^*_j) \geq \int_0^1 \mathrm{d}s \left(\int_{\left\{\mathfrak{d}^*_j > s\right\}} 2s\Psi(\boldsymbol{\varepsilon}(\mathbf{u}_j)) \, d\boldsymbol{x} + (1-s)\mathcal{H}^1\left(\partial_* \left\{\mathfrak{d}^*_j > s\right\}\right)\right).$$

Here, $\left(\partial_* \left\{\mathfrak{d}^*_j > s\right\}\right)$ is the reduced boundary of the finite perimeter set $\left\{\boldsymbol{x};\, \mathfrak{d}^*_j\,(\boldsymbol{x}) > s\right\}$ as in [121, 27, 17]. We can adopt here the results of SBD case with uniform L^∞ bound on the $\mathbf{u}$ as in proof of [lemma 5.1 [17]], we have for almost each $s \in (0,1)$, we have that

$$\begin{aligned}
&\int_{\mathcal{B}} 2s\Psi(\boldsymbol{\varepsilon}(\mathbf{u})) \, \mathrm{d}\boldsymbol{x} + 2(1-s)\mathcal{H}^1\left(J_u\right) \\
&\leq \liminf_{\epsilon \to 0} \int_0^1 \mathrm{d}s \left(\int_{\left\{\mathfrak{d}^*_j > s\right\}} 2s\Psi(\boldsymbol{\varepsilon}(\mathbf{u}_j)) \, d\boldsymbol{x} + (1-s)\mathcal{H}^1\left(\partial_* \left\{\mathfrak{d}^*_j > s\right\}\right)\right).
\end{aligned}$$

Integrating over s and using Fatou's lemma and pass to the limits, we have the lim-inf inequality. i.e

$$\Pi_{l(\mathbf{x})}(\mathbf{u}, \mathfrak{d}^*) \leq \liminf_{\epsilon \to 0} \Pi_{l(\mathbf{x}), \epsilon_j}(\mathbf{u}_j, \mathfrak{d}^*_j).$$

Now for the lim-sup inequality, we construct a sequence $(\mathbf{u}_\epsilon, \mathfrak{d}^*_\epsilon)$ which converge in L^2 to $(\mathbf{u}, \mathfrak{d}^*)$, meaning that there exists a sequence that can go upto the Griffith's energy potential. If the constructed sequence of minimizers converges to a minimum, and sequence of functional also converge to the minimum value of the functional, then the limit of the sequence functions of minimizing sequence also converges upto a subsequence.

Consider the following sequence of minimizers

$$\mathbf{u}_\epsilon(\boldsymbol{x}) = \begin{cases} \dfrac{d(\boldsymbol{x})}{\alpha_\epsilon} \mathbf{u}(\boldsymbol{x}) & \text{if } 0 \leq d(\boldsymbol{x}) \leq \alpha_\epsilon \\ \mathbf{u}(\boldsymbol{x}) & \text{Otherwise,} \end{cases} \tag{2.14}$$

$$\mathfrak{d}^*_\epsilon(\boldsymbol{x}) = \begin{cases} 0 & \text{if } 0 \leq d(\boldsymbol{x}) \leq \alpha_\epsilon \\ 1 - \dfrac{\epsilon}{\sqrt{2l(\boldsymbol{x})}} exp\left(-\dfrac{d(\boldsymbol{x}) - \alpha_\epsilon}{\epsilon^2}\right) & \text{if } d(\boldsymbol{x}) \geq \alpha_\epsilon. \end{cases} \tag{2.15}$$

Clearly $\mathbf{u}_\epsilon(\boldsymbol{x}) \to \mathbf{u}$ in $L^2(\Omega)$ as $\epsilon \to 0$ i.e

$$\int\limits_{\Omega} (\mathbf{u}_\epsilon - \mathbf{u})^2 \, \mathrm{d}\boldsymbol{x} = \int\limits_{0 \leq d(\boldsymbol{x}) \leq \alpha_\epsilon} \left(\frac{d(\boldsymbol{x})}{\alpha_\epsilon} \mathbf{u}(\boldsymbol{x}) - \mathbf{u}(\boldsymbol{x})\right)^2 \mathrm{d}\boldsymbol{x} + \int\limits_{d(\boldsymbol{x}) \geq \alpha_\epsilon} (\mathbf{u}(\boldsymbol{x}) - \mathbf{u}(\boldsymbol{x}))^2 \, \mathrm{d}\boldsymbol{x} = 0,$$

meaning that $\|\mathbf{u}_\epsilon - \mathbf{u}\|_{L^2(\mathcal{B})} = 0$.
Similarly, $\mathfrak{d}^*_\epsilon(\boldsymbol{x}) \to 1$ as $\epsilon \to 0$ almost everywhere since

$\mathfrak{d}^*_\epsilon \leq 1$ and $\dfrac{\epsilon}{\sqrt{2l(\boldsymbol{x})}} \exp\left(-\dfrac{d(\boldsymbol{x}) - \alpha_\epsilon}{\epsilon^2}\right) \to 0$ as $\epsilon \to 0$.

Hence, we have that $\|\mathfrak{d}^*_\epsilon - \mathfrak{d}^*\|_{L^2(\mathcal{B})} = 0$.
Now consider the bulk energy

$$\begin{aligned} \int\limits_{\mathcal{B}} \left[\mathfrak{d}^{*^2} + K_\epsilon\right] \Psi(\boldsymbol{\varepsilon}(\mathbf{u})) \, \mathrm{d}\boldsymbol{x} \leq & \int\limits_{0 \leq (\boldsymbol{x}) \leq \alpha_\epsilon} \left[\mathfrak{d}^{*2}_\epsilon + K_\epsilon\right] \Psi(\boldsymbol{\varepsilon}(\mathbf{u}_\epsilon)) \, \mathrm{d}\boldsymbol{x} \\ & + \int\limits_{d(\boldsymbol{x}) \geq \alpha_\epsilon} \left[\mathfrak{d}^{*2}_\epsilon + K_\epsilon\right] \Psi(\boldsymbol{\varepsilon}(\mathbf{u}_\epsilon)) \, \mathrm{d}\boldsymbol{x}, \\ \int\limits_{\mathcal{B}} \left[\mathfrak{d}^{*^2} + K_\epsilon\right] \Psi(\boldsymbol{\varepsilon}(\mathbf{u})) \, \mathrm{d}\boldsymbol{x} \leq \int\limits_{0 \leq (\boldsymbol{x}) \leq \alpha_\epsilon} & \leq \int\limits_{0 \leq d(\boldsymbol{x}) \leq \alpha_\epsilon} K_\epsilon \Psi(\boldsymbol{\varepsilon}(\mathbf{u}_\epsilon)) \, \mathrm{d}\boldsymbol{x} \\ & + \int\limits_{d(\boldsymbol{x}) \geq \alpha_\epsilon} \left[1 + K_\epsilon\right] \Psi(\boldsymbol{\varepsilon}(\mathbf{u}_\epsilon)) \, \mathrm{d}\boldsymbol{x}. \end{aligned}$$

Note that for $d(\boldsymbol{x}) \leq \alpha_\epsilon$,

$$\nabla \mathbf{u}_\epsilon(\boldsymbol{x}) = \frac{d(\boldsymbol{x})}{\alpha_\epsilon}\nabla\mathbf{u}(\boldsymbol{x}) + \frac{\nabla d(\boldsymbol{x})}{\alpha_\epsilon}\mathbf{u}(\boldsymbol{x}) \leq \frac{d(\boldsymbol{x})}{\alpha_\epsilon}\nabla\mathbf{u}(\boldsymbol{x}) + \frac{M'}{\alpha_\epsilon}.$$

Here, we used 1-Lipshitz characteristic of $d(\boldsymbol{x})$ and L^∞ bounds on the $\mathbf{u}$. With this it is immediate that as $\epsilon \to 0$, the volume of the integral between $0 \leq d(\boldsymbol{x}) \leq \alpha_\epsilon$ shrinks to zero and for $d(\boldsymbol{x}) \geq \alpha_\epsilon$,

$$\Psi(\boldsymbol{\varepsilon}(\mathbf{u}_\epsilon)) \leq \left(\frac{d(\boldsymbol{x})}{\alpha_\epsilon}\nabla\mathbf{u}(\boldsymbol{x})\right)^2 + \left(\frac{M'}{\alpha_\epsilon}\right)^2 + \frac{d(\boldsymbol{x})}{\alpha_\epsilon}\left|\nabla\mathbf{u}(\boldsymbol{x})\right|\frac{M'}{\alpha_\epsilon},$$

$$\begin{aligned}\int_{\mathcal{B}} \left[\mathfrak{d}^{*2} + K_\epsilon\right]\Psi(\boldsymbol{\varepsilon}(\mathbf{u}))\,\mathrm{d}\boldsymbol{x} \leq & \int_{0\leq d(\boldsymbol{x})\leq\alpha_\epsilon} K_\epsilon\left(\frac{d(\boldsymbol{x})}{\alpha_\epsilon}\right)^2\Psi(\boldsymbol{\varepsilon}(\mathbf{u}_\epsilon))\,\mathrm{d}\boldsymbol{x} \\ & + \int_{0\leq d(\boldsymbol{x})\leq\alpha_\epsilon} K_\epsilon\left(\frac{M'}{\alpha_\epsilon}\right)^2\mathrm{d}\boldsymbol{x} \\ & + \int_{0\leq d(\boldsymbol{x})\leq\alpha_\epsilon} K_\epsilon\left(\frac{d(\boldsymbol{x})}{\alpha_\epsilon}\right)^2 M'\sqrt{\Psi(\boldsymbol{\varepsilon}(\mathbf{u}_\epsilon))}\,\mathrm{d}\boldsymbol{x} \\ & + \int_{d(\boldsymbol{x})\geq\alpha_\epsilon} \left[1 + K_\epsilon\right]\Psi(\boldsymbol{\varepsilon}(\mathbf{u}_\epsilon))\,\mathrm{d}\boldsymbol{x}.\end{aligned}$$

Now as $\epsilon \to 0$, $\alpha_\epsilon = o(\epsilon) \to 0$ faster than ϵ. Setting $K_\epsilon = o(\alpha_\epsilon) \to 0$ faster than α_ϵ . So, $\dfrac{K_\epsilon}{\alpha_\epsilon} \to 0$, $\dfrac{d(\boldsymbol{x})}{\alpha_\epsilon} \to 0$ and

$$\int_{0\leq d(\boldsymbol{x})\leq\alpha_\epsilon} K_\epsilon\left(\frac{M'}{\alpha_\epsilon}\right)^2\mathrm{d}\boldsymbol{x} = K_\epsilon\left(\frac{M'}{\alpha_\epsilon}\right)^2\boldsymbol{l}(\alpha_\epsilon) \to 0.$$

With this, we can conclude that

$$\limsup_{\epsilon\to 0}\int_{\mathcal{B}} \left[\mathfrak{d}^{*2} + K_\epsilon\right]\Psi(\boldsymbol{\varepsilon}(\mathbf{u}))\,\mathrm{d}\boldsymbol{x} \leq \int_{\mathcal{B}} \Psi(\boldsymbol{\varepsilon}(\mathbf{u}))\,\mathrm{d}\boldsymbol{x}. \tag{2.16}$$

Similarly, consider the surface energy term without $\mathcal{G}_C(\boldsymbol{x})$.

$$\begin{aligned}\int_{\mathcal{B}} \left[\frac{(1-\mathfrak{d}^*)^2}{2l(\mathbf{x})}S_\epsilon^2 + \frac{l(\mathbf{x})}{2}\left|\nabla\mathfrak{d}^*\right|^2\right]\mathrm{d}\boldsymbol{x} \leq & \int_{0\leq d(\boldsymbol{x})\leq\alpha_\epsilon}\left[\frac{(1-\mathfrak{d}_\epsilon^*)^2}{2l(\mathbf{x})}S_\epsilon^2 + \frac{l(\mathbf{x})}{2}\left|\nabla\mathfrak{d}_\epsilon^*\right|^2\right]\mathrm{d}\boldsymbol{x} \\ & + \int_{d(\boldsymbol{x})\geq\alpha_\epsilon}\left[\frac{(1-\mathfrak{d}_\epsilon^*)^2}{2l(\mathbf{x})}S_\epsilon^2 + \frac{l(\mathbf{x})}{2}\left|\nabla\mathfrak{d}_\epsilon^*\right|^2\right]\mathrm{d}\boldsymbol{x}\end{aligned}$$

For $d(\boldsymbol{x}) \geq \alpha_\epsilon$

$$\mathfrak{d}_\epsilon^* = 1 - \frac{\epsilon}{\sqrt{2l(\boldsymbol{x})}}exp\left(-\frac{d(\boldsymbol{x})-\alpha_\epsilon}{\epsilon^2}\right),$$

$$\left(\frac{1+\epsilon}{2\epsilon}\right)^2 |1-\mathfrak{d}^*_\epsilon|^2 = \frac{(1+\epsilon)^2}{2l(\boldsymbol{x})} exp\left(-\frac{d(\boldsymbol{x})-\alpha_\epsilon}{\epsilon^2}\right).$$

Calculating $|\nabla\mathfrak{d}^*_\epsilon|^2$, with a simple algebraic manipulation results in

$$l(\boldsymbol{x})\,|\nabla\mathfrak{d}^*_\epsilon|^2 \le \frac{1}{2\epsilon^2} exp\left(-\frac{d(\boldsymbol{x})-\alpha_\epsilon}{\epsilon^2}\right).$$

Putting this in the surface energy, we have

$$\begin{aligned}\int\limits_{\mathcal{B}} \left[\frac{(1-\mathfrak{d}^*)^2}{2l(\mathbf{x})} S_\epsilon^2 + \frac{l(\mathbf{x})}{2}\left|\nabla\mathfrak{d}^*\right|^2\right] \mathrm{d}\boldsymbol{x} \le & \int\limits_{0\le d(\boldsymbol{x})\le\alpha_\epsilon} \frac{1}{2l(\mathbf{x})} S_\epsilon^2 \,\mathrm{d}\boldsymbol{x} \\ & + \int\limits_{d(\boldsymbol{x})\ge\alpha_\epsilon} \frac{(1+\epsilon)^2}{2l(\boldsymbol{x})} exp\left(-\frac{d(\boldsymbol{x})-\alpha_\epsilon}{\epsilon^2}\right) \mathrm{d}\boldsymbol{x} \\ & + \int\limits_{d(\boldsymbol{x})\ge\alpha_\epsilon} \frac{1}{2\epsilon^2} exp\left(-\frac{d(\boldsymbol{x})-\alpha_\epsilon}{\epsilon^2}\right) \mathrm{d}\boldsymbol{x}.\end{aligned}$$

In this inequality, first term and second term goes to zero as $\epsilon \to 0$ is immediate. Consider the third term

$$\begin{aligned}\int\limits_{d(\boldsymbol{x})\ge\alpha_\epsilon} \frac{1}{2\epsilon^2} exp\left(-\frac{d(\boldsymbol{x})-\alpha_\epsilon}{\epsilon^2}\right) \mathrm{d}\boldsymbol{x} &= \frac{1}{2\epsilon^2} \int\limits_{d(\boldsymbol{x})\ge\alpha_\epsilon} exp\left(\frac{-s}{\epsilon^2}\right) exp\left(\frac{\alpha_\epsilon}{\epsilon^2}\right) \mathcal{H}^1(\{\,\mathrm{d}(\boldsymbol{x})=s\})\mathrm{d}\boldsymbol{x}, \\ &= \frac{1}{2\epsilon^2} \int\limits_{d(\boldsymbol{x})\ge\alpha_\epsilon} exp\left(\frac{-s}{\epsilon^2}\right) exp\left(\frac{\alpha_\epsilon}{\epsilon^2}\right) \boldsymbol{l}'(s)\mathrm{d}\boldsymbol{x}.\end{aligned}$$

by setting $\frac{s}{\epsilon^2} := t$, changing the variable and integrating it by parts would result in

$$\int\limits_{d(\boldsymbol{x})\ge\alpha_\epsilon} \frac{1}{2\epsilon^2} exp\left(-\frac{d(\boldsymbol{x})-\alpha_\epsilon}{\epsilon^2}\right) \mathrm{d}\boldsymbol{x} = \frac{\boldsymbol{l}'(\alpha_\epsilon)}{2} + \frac{e^{\left(\frac{\alpha_\epsilon}{\epsilon^2}\right)}}{2\epsilon^2} \int\limits_{d(\boldsymbol{x})\ge\alpha_\epsilon} \left(\frac{\alpha_\epsilon}{\epsilon^2}+t\right) \frac{\boldsymbol{l}(\alpha_\epsilon+\epsilon^2 t)}{2\left(\alpha_\epsilon+\epsilon^2 t\right)} e^{-t}\mathrm{d}t.$$

Taking limit of the function as $\epsilon \to 0$ leads to

$$\limsup_{\epsilon\to 0} \int\limits_{\mathcal{B}} \left[\frac{(1-\mathfrak{d}^*)^2}{2l(\mathbf{x})} S_\epsilon^2 + \frac{l(\mathbf{x})}{2}\left|\nabla\mathfrak{d}^*\right|^2\right] \mathrm{d}\boldsymbol{x} \le \mathcal{H}^1(\bar{J}_u).$$

Combining both surface energy and bulk energy we have the lim-sup inequality.

i.e

$$\limsup_{\epsilon\to 0} \Pi_{l(\mathbf{x}),\epsilon}(\mathbf{u}_\epsilon, \mathfrak{d}^*_\epsilon) \le \Pi(\mathbf{u}, \mathfrak{d}^*).$$

and hence the proof of Theorem 2. By equivalence relation as stated, we also have the proof of Theorem 1.

□

2.4 Finite element formulation

In this section, the FE implementation of the multi-field displacement-phase field model proposed in Eqs. (2.4a) and (2.4c) is presented. In order to construct the numerical solution of the corresponding initial boundary value problem (IBVP), we consider the weak form of the former set of equations for the test functions $\delta\mathbf{u}$ and $\delta\mathfrak{d}$ of the primary fields $\mathbf{u}$, $\mathfrak{d}$ respectively:

$$\int_{\mathcal{B}} \left[(1-\mathfrak{d})^2 + K_l\right] \boldsymbol{\sigma} : \boldsymbol{\varepsilon}(\delta\mathbf{u})\mathrm{dV} - \int_{\mathcal{B}} \boldsymbol{f_v}\delta\mathbf{u}\ \mathrm{dV} - \int_{\partial\mathcal{B}} \bar{\mathbf{t}}\delta\mathbf{u}\,\mathrm{dS} = 0,$$

$$\int_{\mathcal{B}} \mathcal{G}_C(\mathbf{x}) \left[\frac{\mathfrak{d}}{l(\mathbf{x})}\delta\mathfrak{d} + l(x)\nabla\mathfrak{d}\cdot\nabla\delta\mathfrak{d}\right] \mathrm{dV} - \int_{\mathcal{B}} 2(1-\mathfrak{d})\Psi\left(\boldsymbol{\varepsilon},\mathbf{x}\right)\delta\mathfrak{d}\ \mathrm{dV} = 0.$$

Note that, it is often recommended to use unequal interpolation orders for the coupled multi-field problems in order to avoid stress oscillations and potential numerical interlocking. Notwithstanding, it can be argued from previous investigations [122, 8, 123] that this strategy is not required in the present study since the stress oscillations and numerical locking might only arise in a very narrow band of crack propagation and have negligible effects on the convergence rates and numerical results of the overall problem.

Accordingly, we define dicretization $\mathcal{B} \to \mathcal{B}_e$, $\mathbf{u} \to \mathbf{u}_e$, $\delta\mathbf{u} \to \delta\mathbf{u}_e$, $\mathfrak{d} \to \mathfrak{d}_e$, $\delta\mathfrak{d} \to \delta\mathfrak{d}_e$ such that $\mathbf{u}_e \in \mathcal{U}_h$, $v_e \in \mathcal{V}_h$, $\mathfrak{d}_e \in \mathcal{U}_{\mathfrak{d}}$, $\delta\mathfrak{d}_e \in \mathcal{U}_{\delta\mathfrak{d}}$, and partition of unity holds for the functional space for approximate functions

$$\mathcal{U}_h(\mathbf{u}) = \left\{ \mathbf{u} \in H^1(\mathcal{B}) \middle| \nabla\mathbf{u} \in L^2(\mathcal{B});\ \mathbf{u} = \mathbf{u}_d \text{ on } \partial\mathcal{B}_d \right\}, \tag{2.17a}$$

$$\mathcal{V}_h(\delta\mathbf{u}) = \left\{ \delta\mathbf{u} \in H^1(\mathcal{B}) \middle| \nabla\delta\mathbf{u} \in L^2(\mathcal{B});\ \delta\mathbf{u} = 0 \,\text{on}\, \partial\mathcal{B}_d \right\}, \tag{2.17b}$$

$$\mathcal{U}_{\mathfrak{d}}(\mathfrak{d}) = \left\{ \mathfrak{d} \in H^1(\mathcal{B}) \middle| \mathfrak{d}(x) \in [0,1],\ \dot{\mathfrak{d}} \geq 0\ \forall\mathbf{x} \in \mathcal{B} \right\}, \tag{2.17c}$$

$$\mathcal{U}_{\delta\mathfrak{d}}(\delta\mathfrak{d}) = \left\{ \delta\mathfrak{d} \in H^1(\mathcal{B}) \middle| \delta\mathfrak{d} \geq 0\,\forall\mathbf{x} \in \mathcal{B} \right\}. \tag{2.17d}$$

Upon the above setting, the displacement field $\mathbf{u}_e$ and the strain field $\boldsymbol{\varepsilon}(\mathbf{u}_e)$ are interpolated in terms of the nodal displacements $\mathbf{d}_{\mathbf{u}}$ as follows

$$\mathbf{u}_e(\mathbf{x}) \approx \mathbf{N}(\mathbf{x})\mathbf{d}_{\mathbf{u}} \quad \nabla\mathbf{u}_e(\mathbf{x}) \approx \mathbf{B}(\mathbf{x})\mathbf{d}_{\mathbf{u}}, \tag{2.18}$$

where $\mathbf{N}(\mathbf{x})$ is the matrix that arranges the shape functions associated with at the element in computational domain $\mathcal{B}_e$, and $\mathbf{B}(\mathbf{x})$ identifies its corresponding spatial derivative (also denominated as compatibility operator).

In a similar manner, complying with an isoparametric formulation, the FE discretization of phase field $\mathfrak{d}$ variable and the gradient $\nabla\mathfrak{d}$ in terms of nodal phase field $\mathbf{d}_{\mathfrak{d}}$ renders

$$\mathfrak{d}_e(x) \approx \mathbf{N}(\mathbf{x})\mathbf{d}_{\mathfrak{d}} \quad \nabla\mathfrak{d}_e(x) \approx \mathbf{B}^{\mathfrak{d}}(\mathbf{x})\mathbf{d}_{\mathfrak{d}}, \tag{2.19}$$

where the same order of interpolation is chosen for the displacement and the phase field variables.

Through the insertion of the previous interpolation scheme for the displacement and the crack-like phase field variable, the discrete versions of the element residual vectors for both fields are given by

$$\mathbf{r_u} = \int_{\mathcal{B}_e} \left((1-\mathfrak{d})^2 + K_l\right) \mathbf{B}^{\mathrm{T}}(\mathbf{x})\boldsymbol{\sigma} \,\mathrm{dV} - \int_{\mathcal{B}_e} \mathbf{N}^{\mathrm{T}}(\mathbf{x})\boldsymbol{f_v} \;\mathrm{dV} - \int_{\partial\mathcal{B}_e} \mathbf{B}^{\mathrm{T}}(\mathbf{x})\bar{\mathbf{t}}\,\mathrm{dS},$$

$$\mathbf{r}_{\mathfrak{d}} := \int\limits_{\mathcal{B}_e} -2(1-\mathfrak{d})\mathbf{N}^{\mathrm{T}}(\mathbf{x})\Psi\left(\boldsymbol{\varepsilon},\mathbf{x}\right)\;\mathrm{dV} + \int_{\mathcal{B}_e} \frac{\mathcal{G}_C(\mathbf{x})}{l(\mathbf{x})}\left[\mathbf{N}^{\mathrm{T}}\mathfrak{d} + l(\mathbf{x})^2(\mathbf{B}^{\mathfrak{d}})^T\nabla\mathfrak{d}\right]\;\mathrm{dV}.$$

The solution is computed using quasi-newton solver. In line with [124, 125], the stiffness matrix is updated after each iteration according to Broyden-Fletcher-Goldfarb-Sahnno(BFGS) algorithm . In such case the initial guess for BFGS to estimate $(t+\Delta t)^{th}$ time step takes the form

$$\begin{bmatrix} \mathbf{d}_u \\ \mathbf{d}_{\mathfrak{d}} \end{bmatrix}_{t+\Delta t} = \begin{bmatrix} \mathbf{d}_u \\ \mathbf{d}_{\mathfrak{d}} \end{bmatrix}_t - \begin{bmatrix} \mathbf{K_{uu}} & 0 \\ 0 & \mathbf{K}_{\mathfrak{d}\mathfrak{d}} \end{bmatrix}_t^{-1} \begin{bmatrix} \mathbf{r_u} \\ \mathbf{r}_{\mathfrak{d}} \end{bmatrix}_t. \tag{2.20}$$

Equivalently, we can express

$$(\mathbf{z})_{t+\Delta t} = (\mathbf{z})_t - \mathbf{K}_t^{-1}(\mathbf{r})_t, \tag{2.21}$$

where

$$\frac{\partial\mathbf{R_u}}{\partial\mathbf{d}_u} = \mathbf{K_{uu}} = \int_{\mathcal{B}_e} \left((1-\mathfrak{d})^2 + K_l\right)\mathbf{B}^T\mathbb{C}(\mathbf{x})\mathbf{B}\;\mathrm{dV}, \tag{2.22}$$

$$\frac{\partial\mathbf{R}_{\mathfrak{d}}}{\partial\mathbf{d}_{\mathfrak{d}}} = \mathbf{K}_{\mathfrak{d}\mathfrak{d}} = \int\limits_{\mathcal{B}_e} 2\mathbf{N}^T\mathbf{N}\hat{\mathcal{H}}\,\mathrm{dV} + \int\limits_{\mathcal{B}_e} \frac{\mathcal{G}_C(\mathbf{x})}{l(\mathbf{x})}\left[\mathbf{N}^T\mathbf{N} + l(\mathbf{x})^2(\mathbf{B}^{\mathfrak{d}})(\mathbf{B}^{\mathfrak{d}})^T\right]\;\mathrm{dV}. \tag{2.23}$$

are the elemental tangent stiffness matrix.

The above system of equations incorporates the history variable as in [35], denoted as $\hat{\mathcal{H}}$, in order to ensure irreversibility of the crack defined as

$$\hat{\mathcal{H}} = \max_{\tau\in[0,t]}(\Psi(t)). \tag{2.24}$$

The approximated stiffness matrix $\tilde{\mathbf{K}}$ is updated after a set number of iterations in case of not having an converged solution using

$$\tilde{\mathbf{K}} = \tilde{\mathbf{K}}_t - \frac{(\tilde{\mathbf{K}}_t\Delta\mathbf{z})(\tilde{\mathbf{K}}_t\Delta\mathbf{z})^T}{\Delta\mathbf{z}\tilde{\mathbf{K}}_t\Delta\mathbf{z}} + \frac{\Delta\mathbf{r}\Delta\mathbf{r}^T}{\Delta\mathbf{z}^T\Delta\mathbf{r}}, \tag{2.25}$$

where $\Delta \mathbf{z} = \mathbf{z}_{t+\Delta t} - \mathbf{z}_t$, and $\Delta \mathbf{r} = \mathbf{r}_{t+\Delta t} - \mathbf{r}_t$. Therefore, that the approximated stiffness matrix $\tilde{K}$ satisfies

$$\tilde{\mathbf{K}} \Delta \mathbf{z} = \Delta \mathbf{r}. \tag{2.26}$$

The system of equations has been implemented in finite element software `ABAQUS` in order to take advantage of the in-built BFGS solver. For this purpose, a user defined `UEL` is written for the coupled equilibrium equations. Moreover, with regard to the FGM formulation, the corresponding variation of material properties has been implemented at each material integration point in a continuous manner by fetching the data `COORDS(nnode, mcrd)` in abaqus `UEL` subroutine.

2.5 Virtual testing

In this section, for validation purposes, a comprehensive numerical example of asymmetric three-point bending of PMMA beam is discussed. A qualitative assessment of crack path is performed, which is validated against available experimental results in order to show the predictive capabilities of the proposed model. Subsequently, using the classical benchmark problem of single-edge notched plate under tensile loading conditions, mechanical insights based on variation of Young's modulus ratio, initial crack length and position of the model are pinpointed, in conjunction with a final discussion on size-scale effects emphasizing the equivalence relationship. Finally, the current PF method for FGM is applied to study the failure initiation and propagation at the micro-scale in a single-fiber reinforced FGM matrix problem.

2.5.1 Properties and grading function

Let A and B are two material compositions of the functionally graded material with the volume fraction of material A in the y-direction given as

$$V_f(\mathbf{x}) = \left(\frac{1}{2} + \frac{y}{h} \right)^K, \tag{2.27}$$

where K is a grading constant. The volume fraction of material B can be estimated as $V_B(\mathbf{x}) = 1 - V_f(\mathbf{x})$. Based on the rule of mixtures, the corresponding Young's modulus, fracture toughness, Poisson ratio and apparent strength in terms of volume fractions takes the form

$$E(\mathbf{x}) = E_1 + (E_2 - E_1) V_f(\mathbf{x}), \tag{2.28a}$$

$$K_{IC}(\mathbf{x}) = K_{1c,1} + (K_{1c,2} - K_{1c,1}) V_f(\mathbf{x}), \tag{2.28b}$$

$$\nu(\mathbf{x}) = \nu_1 + (\nu_2 - \nu_1) V_f(\mathbf{x}), \tag{2.28c}$$

$$\sigma_c(\mathbf{x}) = \sigma_{c1} + (\sigma_{c2} - \sigma_{c1}) V_f(\mathbf{x}). \tag{2.28d}$$

Assuming plain strain condition for all the numerical experiments, we have

y(mm)	E_A(MPa)	ν	$K_{IC,A}$ (MPa$\sqrt{\text{m}}$)
0	1780	0.41	0.99
60	4000	0.39	1.19

Table 3: Material Properties of PMMA beam

$$\mathcal{G}_C(\mathbf{x}) = \frac{(1-\nu(\mathbf{x})^2)K_{IC}(\mathbf{x})^2}{E(\mathbf{x})}, \quad l(\mathbf{x}) = \frac{27}{256}\left(\frac{\mathcal{G}_C(\mathbf{x})E(\mathbf{x})}{\sigma_c^2(\mathbf{x})}\right). \tag{2.29}$$

All the material properties in the subsequent sections take the form as mentioned, unless specified.

2.5.2 Model validation

In this section, we investigate crack propagation in a graded PMMA beam subjected to three-point bending with unsymmetrical loading conditions. In this example, we consider the grading along the y-direction with the boundary condition shown in Fig. 3. All the material properties are taken as the linear combination of the homogeneous properties in the grading direction according to the rule of mixtures as in Section 5.1. The material properties of the PMMA beam are listed in Table 3 in line with [126].

The domain is discretized with 97371 4-node quadrilateral plane stress elements. The length of each side of element near the process zone is kept less than 0.2 mm in order to ensure that gradient of the phase-field is resolved properly.

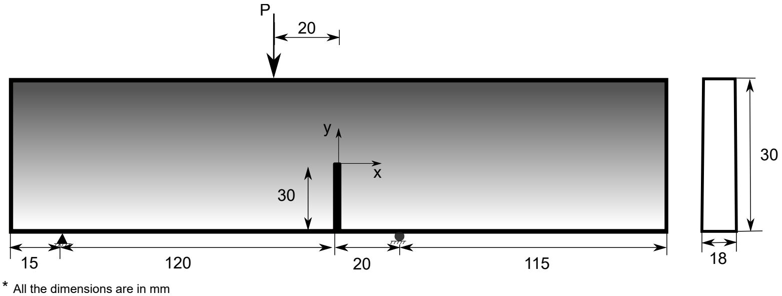

Figure 3: A crack in a beam subjected to three-point unsymmetrical loading.

Fig. 4a shows the crack propagation path due to asymmetrical loading. Fig. 4b shows the comparison of the crack trajectories for the graded PMMA beam obtained by the present model and the experimental (averaged) results as in [126]. The crack propagation path due to the present model shows an excellent agreement with the experimental results. Moreover, Fig. 5 shows the comparison of the reaction force v/s displacement curve for the constant characteristic length scales of $l = 1.49$, $l = 2.51$ and the variable length scale $l(\mathbf{x})$. The results indicates that the small variation in the length scale affects the system behaviour which are

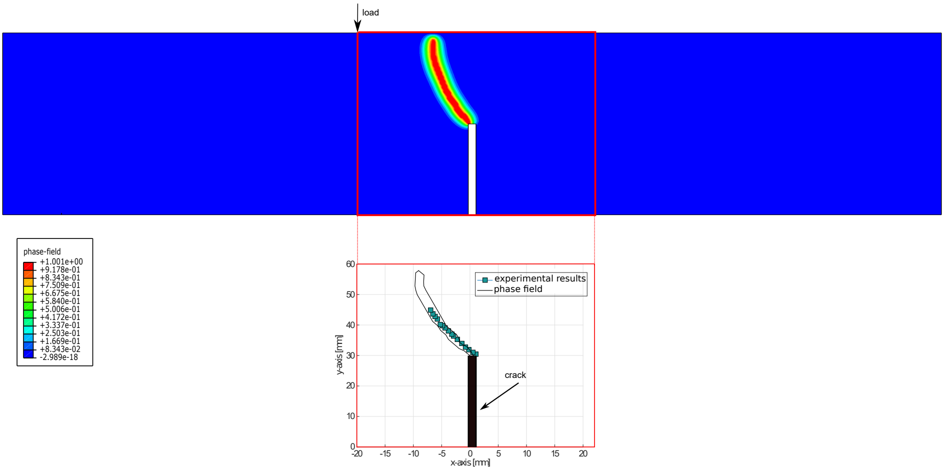

Figure 4: Crack propagation of PMMA beam under unsymmetrical loading condition. a)Crack propagation, and b)comparison with experimental results.

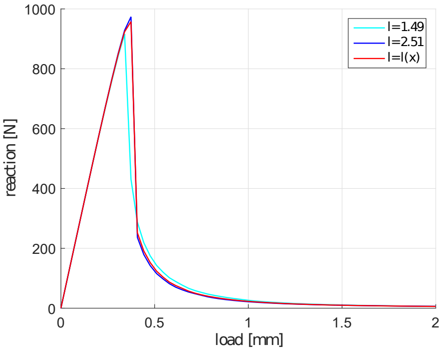

Figure 5: Comparison between constant l and $l(\mathbf{x})$ for the reaction forces of asymmetrical three-point loading.

reflected in the reaction force vs displacement curve (note that the grading profile chosen in this application is relatively smooth).

2.5.3 Insight on grading

In this section, we present several numerical examples which include a classical benchmark problem, corresponding a single-edge notched plate under monotonic tensile loading conditions up to failure. For each of the examples herein investigated, the effects of Young's modulus ratio, size effects, crack length and position effects, grading profiles on the crack propagation are pinpointed. Also, we provide a general behavior discussion on the response of FGM specimens using simple mathematical manipulations in order to support the numerical examples.

With the aim of understanding the effects of change of l at every material point, we invoke the following theorem.

Theorem 3. *With the usual notations mentioned before, for every* $\mathbf{x} \in \mathbb{R}^{n_{dim}}$, *under the same domain* $\mathcal{B}$ *and loading conditions, for any given grading function* $V_f \in L^1_{loc}(\mathcal{B})$,

1. Elastic energy $\Psi(\mathbf{u}, \mathfrak{d})$ *of FGM is comprised (bounded from above and below) between its homogeneous material composition. i.e*

$$\Psi(\mathbf{u}, \mathfrak{d})\Bigg|_{E_{min}} \leq \Psi(\mathbf{u}, \mathfrak{d}) \leq \Psi(\mathbf{u}, \mathfrak{d})\Bigg|_{E_{max}}.$$

2. Surface energy $\Psi_c(\mathfrak{d})$ *created due to fracture is bounded between its homogeneous material composition if the function* $f(x) = \frac{\boldsymbol{\sigma}^2(\mathbf{x})}{E(\mathbf{x})}$ *is monotonic*

$$\Psi_c(\mathfrak{d})\Bigg|_{f(x)_{min}} \leq \Psi_c(\mathfrak{d}) \leq \Psi_c(\mathfrak{d})\Bigg|_{f(x)_{max}}.$$

Proof. **Part-1:** Let FGM has its constituents as material A and B. Assume $E_A > E_B$, then for all $\mathbf{x} \in \mathcal{B}$, $V_f(\mathbf{x}) \in L^1_{loc}(\mathcal{B})$ is a function such that, by construction

$$E_B = E_{min} \leq E(\mathbf{x}) \leq E_{max} = E_A \text{ meaning that } E(\mathbf{x}) \in [E_B, E_A].$$

Extending this inequality for the compliance tensor $\mathbb{C}(x)$ along with the fact that $\mathbb{C}(x)$ is positive definite[1] leads to

$$\mathbb{C}\Bigg|_{E_B} \leq \mathbb{C}(x) \leq \mathbb{C}\Bigg|_{E_A}. \tag{2.30}$$

Consider the elastic energy of the FGM

$$\Psi(\mathbf{u}, \mathfrak{d}) = \int\limits_{\mathcal{B}} \left[(1-\mathfrak{d})^2 + K_l\right] \Big(\boldsymbol{\varepsilon}(\mathbf{u})^T : \mathbb{C} : \boldsymbol{\varepsilon}(\mathbf{u})\Big) \, \mathrm{dV}, \tag{2.31}$$

then for all $\mathbf{x} \in \mathcal{B}$, $\mathfrak{d} \in [0,1]$ implies that $\left[(1-\mathfrak{d})^2 + K_l\right] \geq 0$. Hence, the Eq. (2.31) can be bounded using Eq. (2.30) as

$$\Psi(\mathbf{u}, \mathfrak{d})\Bigg|_{E_B} \leq \Psi(\mathbf{u}, \mathfrak{d}) \leq \Psi(\mathbf{u}, \mathfrak{d})\Bigg|_{E_A}.$$

---

[1] [Note that Youngs modulus E is many orders of magnitude larger than Poisson ratio ν, and hence the effect of ν is almost zero].

Now, if $E_B > E_A$, then the above arguments holds true with $E_A \leq E(\mathbf{x}) \leq E_B$ and hence the inequality now takes the form

$$\Psi(\mathbf{u}, \mathfrak{d})\bigg|_{E_A} \leq \Psi(\mathbf{u}, \mathfrak{d}) \leq \Psi(\mathbf{u}, \mathfrak{d})\bigg|_{E_B}.$$

In both case, the elastic energy is bounded by its homogeneous constituent materials.

Part-2:- We will only prove for the case $E_A > E_B$, since the case $E_B > E_A$ is a trivial extension. Consider the surface energy of the FGM

$$\Psi_c(\mathfrak{d}) = \int_{\mathcal{B}} \frac{\mathcal{G}_C(\mathbf{x})}{2l(\mathbf{x})}\mathfrak{d}^2 + \mathcal{G}_C(\mathbf{x})l(\mathbf{x})\left|\nabla\mathfrak{d}\right|^2 \text{ dV},$$

from Eq. (2.1), we have

$$\mathcal{G}_C(\mathbf{x}) = \frac{\left(1 - \nu(\mathbf{x})^2\right) K_{IC}^2(\mathbf{x})}{E(\mathbf{x})}, \qquad l(\mathbf{x}) = \frac{27}{256}\left(\frac{\mathcal{G}_C(\mathbf{x})E(\mathbf{x})}{\sigma_c^2(\mathbf{x})}\right).$$

Surface energy can be bounded by the following chain of inequalities

$$\begin{aligned}
&\int_{\mathcal{B}} \frac{256\sigma_{min}^2}{27E_A}\mathfrak{d}^2 + \frac{27\left(1 - \nu(\mathbf{x})^2\right)^2 K_{IC}^4(\mathbf{x})}{256\sigma_{min}^2 E_A}\left|\nabla\mathfrak{d}\right|^2 \text{ dV} \\
\leq &\int_{\mathcal{B}} \frac{256\sigma_c^2(\mathbf{x})}{27E(\mathbf{x})}\mathfrak{d}^2 + \frac{27\left(1 - \nu(\mathbf{x})^2\right)^2 K_{IC}^4(\mathbf{x})}{256\sigma_c^2(\mathbf{x})E(\mathbf{x})}\left|\nabla\mathfrak{d}\right|^2 \text{ dV} \\
\leq &\int_{\mathcal{B}} \frac{256\sigma_{max}^2}{27E_B}\mathfrak{d}^2 + \frac{27\left(1 - \nu(\mathbf{x})^2\right)^2 K_{IC}^4(\mathbf{x})}{256\sigma_{max}^2 E_B}\left|\nabla\mathfrak{d}\right|^2 \text{ dV}.
\end{aligned} \tag{2.32}$$

Case-1: When $\sigma_{min} = \sigma_A$ **and** $\sigma_{max} = \sigma_B$

If $\sigma_{min} = \sigma_A$ and $\sigma_{max} = \sigma_B$ meaning that $\sigma_B \geq \sigma_A$, then $\sigma(\mathbf{x}) \in [\sigma_A, \sigma_B]$, then the surface energy of FGM is trivially bounded between its homogeneous constituents. i.e

$$\Psi_c(\mathfrak{d})\bigg|_A \leq \Psi_c(\mathfrak{d}) \leq \Psi_c(\mathfrak{d})\bigg|_B.$$

Case-2: When $\sigma_{min} = \sigma_B$ **and** $\sigma_{max} = \sigma_A$

If $\sigma_{min} = \sigma_B, \sigma_{max} = \sigma_A$ then the bound for surface energy in terms of its homogeneous constituents exist if

$$\frac{\sigma_{min}^2}{E_A} \leq \frac{\sigma^2(\mathbf{x})}{E(\mathbf{x})} \leq \frac{\sigma_{max}^2}{E_B},$$

is true.

In many materials, $E(\mathbf{x})$ is some orders of magnitude greater than $\boldsymbol{\sigma}^2(\mathbf{x})$, (assuming that both are in MPa) otherwise, clearly $\boldsymbol{\sigma}^2(\mathbf{x})$ is dominant. But in some materials, $E(\mathbf{x})$ can be of same order or less than $\boldsymbol{\sigma}^2(\mathbf{x})$. Under these circumstances, we incorporate an extra condition such as the function $f(x) = \frac{\boldsymbol{\sigma}^2(\mathbf{x})}{E(\mathbf{x})}$ is monotone. Thus, if $f(x)$ is monotonic, then clearly the extremes of the function lies on the boundaries since $f(x)$ is bounded function. Hence, we have

$$\left.\frac{\boldsymbol{\sigma}^2}{E}\right|_A \le \frac{\boldsymbol{\sigma}^2(\mathbf{x})}{E(\mathbf{x})} \le \left.\frac{\boldsymbol{\sigma}^2}{E}\right|_B \quad or \quad \left.\frac{\boldsymbol{\sigma}^2}{E}\right|_B \le \frac{\boldsymbol{\sigma}^2(\mathbf{x})}{E(\mathbf{x})} \le \left.\frac{\boldsymbol{\sigma}^2}{E}\right|_A,$$

depending on weather the function is monotonically increasing or decreasing. Hence substituting this in the surface energy inequality Eq. (2.32), we have that surface energy of FGM is bounded by its homogeneous constituents if the function $f(\mathbf{x})$ is monotone[2 3]. Physically, this also means that the function $f(\mathbf{x})$ is also constituent for the crack driving force and not just $E(\mathbf{x})$. ☐

Effect of grading on the Young's modulus

Consider a pre-cracked plate with displacement on one side of the boundary and fix the other side as shown in the Fig. 6. In this specimen configuration, a denotes the length of the initial crack, b and w are the height and the width centered at $(0, 0)$. In this section, we consider values of $K_{1cA} = 3.5\text{MPa}\sqrt{\text{m}}$, $K_{1cB} = 8\text{MPa}\sqrt{\text{m}}$, $\nu_A = 0.21$ and $\nu_B = 0.31$ as the effects of small perturbation to their values shows to be non-sensitive and have no significant difference in the overall system behaviour. The model is discretized with 118400 4-node quadrilateral plane stress elements.

In the context of crack propagation, the initial characterization for FGM can be done in terms of elastic mismatch and further can be made based on the apparent strength. Theoretically, it is possible to create a functionally graded materials with any combination of materials and hence it is better to consider an abstract value than that of the exact material properties so that the extreme effects can be simulated for further research development. To support this claim, consider Alumina-Zirconia which has Young's modulus ratio of approximately 1.65, similarly Aluminum-Alumina, Alumina-Silica, Alumina-Epoxy have ratios of 4.78, 10, 100 respectively, see [65] for more details. Hence, in this section, we consider four ratios of $\frac{E_A}{E_B}$ with 2,5,10 and 20 by setting $E_A = 300$ GPa, to demonstrate the effects of elastic mismatch.

As in Theorem 3, the influence of Young's modulus cannot be considered in a separate manner, since the effect of fracture stress plays a major role in the crack propagation and surface energy release rates of the FGM. For this reason, we consider cases when material A has strength greater than material B (case-1 in Theorem 3) and when material B has greater strength than material-A (case-2 in Theorem 3). The reaction curves for the $\frac{E_A}{E_B} = 2$ can be seen in Fig. 7 with material properties as reported in Table 4 along with their constitutive

---

[2] **Note:** The case that $f(\mathbf{x})$ is not monotone would arise if $\frac{\sigma_{min}^2}{E_A} \simeq \frac{\sigma_{max}^2}{E_B}$, in other words if the ratio $\left(\frac{\sigma_{min}}{\sigma_{max}}\right)^2 \left(\frac{E_{min}}{E_{max}}\right) \simeq 1$,then the bounds are very tight and hence the function $f(\mathbf{x})$ losses its monotonicty since $f(\mathbf{x})$ is quadratic function. Example of such case is given in Fig. 10. Also notice that if the ratio $\left(\frac{\sigma_{min}}{\sigma_{max}}\right)^2 \left(\frac{E_{min}}{E_{max}}\right) < 1$, then the system behaves like in case-1 and hence bounds are guaranteed. We give numerical example showing all the cases in the example-1.

[3] **Note:** Notice that the constants in the non-local part of the surface energy is very small due to the product $\sigma^2(\mathbf{x})E(\mathbf{x})$, also the variation of the surface energy would lead to negative constants and hence have no effect on the bounds.

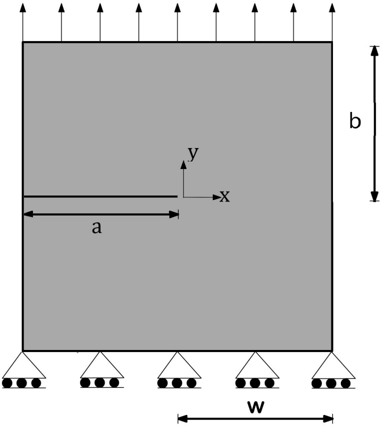

Figure 6: Plate with an edge crack under uni-axial tension.

	E_A(GPa)	E_B(GPa)	σ_A(MPa)	σ_B(MPa)	$K_{IC,A}$ (MPa$\sqrt{\text{m}}$)	$K_{IC,B}$(MPa$\sqrt{\text{m}}$)	ν_A	ν_B
Case-1	300	150	600	300	3.5	8	0.21	0.31
Case-2			300	600				

Table 4: Material Properties for $\frac{E_A}{E_B} = 2$

behaviour as in Eq. (4.5) and (2.29) for different values of the grading constant K. Similarly, for the reaction curves for the ratios $\frac{E_A}{E_B} = 5$ and $\frac{E_A}{E_B} = 10$ are given in Fig. 8.

Analyzing the present results, it is possible to observe that when $\frac{E_A}{E_B} = 20$ is considered, as in Fig. 9, the results are not different from that outlined in Theorem 3. For any material property with $\frac{E_A}{E_B} = 20$ (which is usually the case), the difference in length scale parameter is at least one order magnitude greater than the smallest length scale. In such cases, relying on the present computational results, we can argue that the variation of the length scale within the specimen domain cannot be neglected. We have also shown previously that the failure stress plays a major role in the crack propagation which is inversely proportional to the length scales, which is also consistent with the previous investigations on the matter, see [90, 127, 107, 111].

Continuing with the analysis of the present results, we notice that with the material properties used to obtain the results plotted in Fig. 7, 8 and 9, the crack propagation direction is towards minimum Young's modulus. The steepness in the reaction forces representing the crack nucleation is due to the mismatch in Young's modulus. As expected, configurations with the highest mismatch exhibit the steepest gradients. The FGM variation in this case is linear as the difference in mechanical energy release rate due to the change of grading of volume fraction is linear, see Eq. (2.30). This implies, depending on the volume fraction, the crack nucleation in the FGM is a linear combination of its homogeneous constituents.

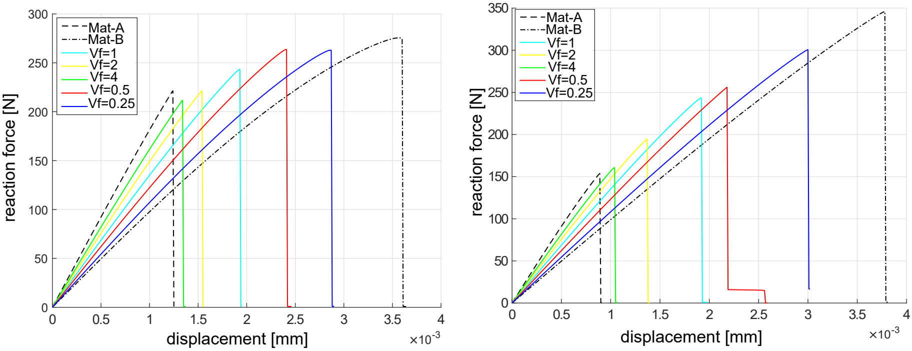

Figure 7: Material properties for $\frac{E_A}{E_B} = 2$ (Left) reaction forces for the case-1, (Right) reaction forces for case-2.

q

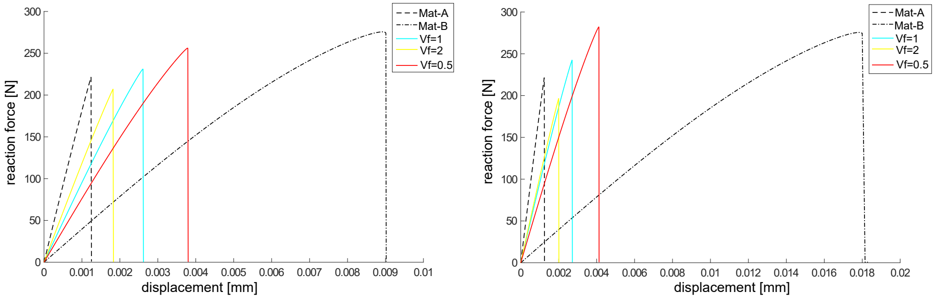

Figure 8: Reaction curves with $\sigma_A = 600$MPa and $\sigma_B = 300$ MPa for (Left) $\frac{E_A}{E_B} = 5$, (Right) $\frac{E_A}{E_B} = 10$

Similarly, $\boldsymbol{\sigma}$ determines the maximum value (cut-off) of the reaction curves, with a trend consistent with what is expected for homogeneous materials. FGM formed due to variation of $\boldsymbol{\sigma}$ in turn on l is quadratic in nature from Eq. (2.1). Meaning that, depending on volume fraction and $\frac{\boldsymbol{\sigma}^2}{E}$ ratio, the apparent strength is a quadratic combination of its homogeneous constituents. In order to understand what happens when the monotonicity of $\frac{\boldsymbol{\sigma}^2}{E}$ is lost, consider the following example with the Young's modulus ratio $\frac{E_A}{E_B} = 1.5$, and $\sigma_A = 300$ MPa and $\sigma_B = 245$ MPa and keeping the rest as in Table-4 can be seen in Fig. 10. Even though all intrinsic material properties are monotone, the ratio of $\frac{\boldsymbol{\sigma}^2}{E}$ is not monotonic so far, and hence the surface energies neither fall under case-1 nor case-2, hence crack propagation and the reaction forces of these FGMs cannot be predicted using its homogeneous constituents only in an accurate manner. This aspect suggests that the crack path cannot be easily predicted, requiring either the conduction of a careful experimental campaign (producing such complex samples) or the use of suitable numerical models that enabling capturing such intricate response.

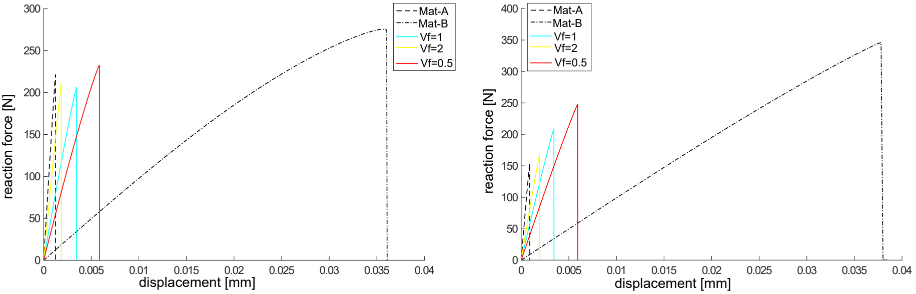

Figure 9: (Left) Reaction forces for the case-1, (Right) reaction forces for case-2 with $\frac{E_A}{E_B} = 20$.

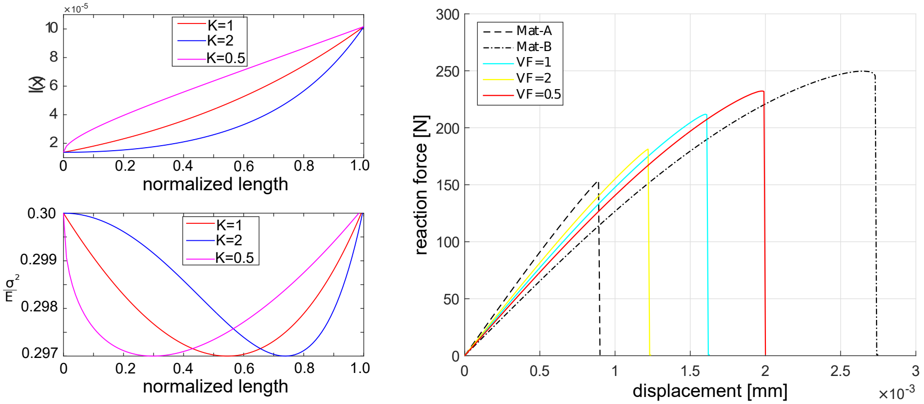

Figure 10: Material properties along with $\frac{E_A}{E_B} = 1.5$ (Left) material properties, (Right) corresponding reaction forces.

Effect of initial crack position and crack length

In this subsection, we explore the effect of the initial crack position and crack length in the FGM with linear grading, by considering $\frac{E_A}{E_B} = 2$, with $E_A = 300$ GPa and $\sigma_A = 600$MPa and $\sigma_B = 300$MPa, $K_{1cA} = 3.5$ MPa$\sqrt{\text{m}}$ and $K_{1cA} = 8$ MPa$\sqrt{\text{m}}$. The overall behavior with respect to any other cases (as well as grading profiles) are similar. In this concern, if a represents the length of crack as in Fig. 6, keeping the $w = b = 1$ the variation of the crack length keeping everything else the same results in the reaction curves as shown in Fig. 11 (a). Stemming from these results, it becomes evident that, as the initial crack length decreases the elastic energy required for the crack to propagate is higher. Hence, we can see that the steepness in reaction curves due to the elastic energy release rate increases as crack length decreases. Similarly, the surface energy required for the material to fracture is also higher with decrease in crack length.

In line with the previous discussion, if a square plate with $a = w = b = 1$ in Fig. 6 is taken, but the crack is placed at a distance c in the y-direction from center of the specimen, then we obtain the results depicted in Fig. 11 (b). Analyzing this graph, we can observe that the overall mechanical energy is nearly coincident for all the experiments, since the initial crack length is the same for each of the cases, but the surface energy is slightly different from each other due to asymmetric loading on the crack tip. As a major conclusion, by changing position of the initial crack tip in the direction of increasing $\frac{\sigma^2}{E}$ would decrease the surface energy.

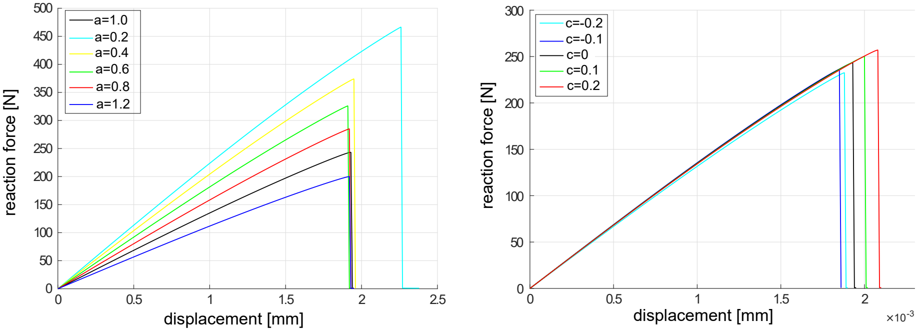

Figure 11: Load-displacement curves for (Left) change of crack length (Right) change of crack position.

Fig. 12 shows the reaction curves for different grading profiles. From this graph, it is easy to notice that, if the grading direction is along the x-axis (grading-6 as in 12) opposite to the crack propagation path, the reaction curves shows a gradual drop. Also, grading-1, grading-2, grading-3, and grading-4 profiles has different material properties at their crack tip and the corresponding reaction curves shows similar surface energies release rates but different elastic energy release rate.

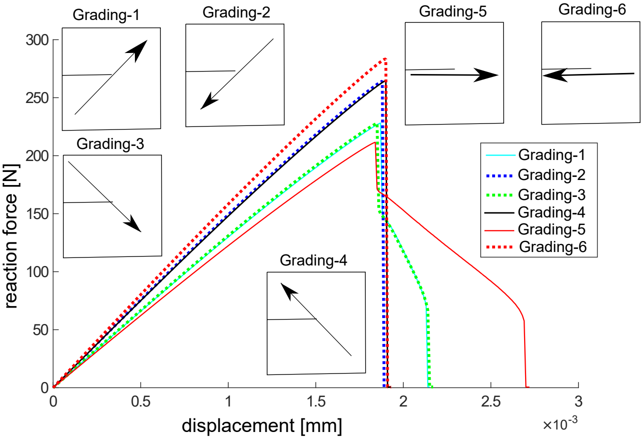

Figure 12: Load-displacement curves for different grading profiles.

Size-scale effects

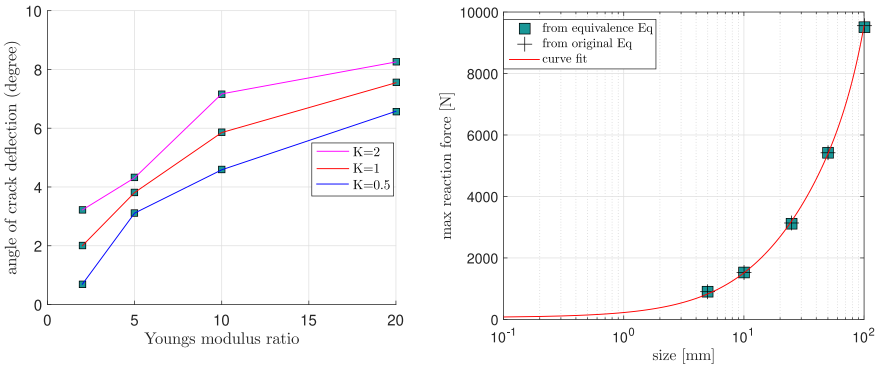

Figure 13: (Left) angle of crack deflection due to different Young's modulus ratio (Right) maximum reaction due to size effects.

In this subsection, we consider the size-scale effects for FGMs with linear grading and keeping the material properties as in Subsection 2.5.3, while change the dimensions w to account for a square specimen. If we scale the Fig. 6 including also the crack length, keeping the internal length scale constant, it is easy to see from Eq.(2.2) that the potential energy increases as the domain is expanded. Also, from the numerical viewpoint, the same conclusion holds for the reaction forces, whilst the elastic energy release rate is kept constant but the surface energy release becomes higher. Since the maximum reaction force is directly proportional to the maximum surface energy release rate, it is also interesting to see that the scaling factor follows a power law as in Fig. 13(b). This constitutes the main idea of the $\Gamma-$convergence proof presented in Section 2.3.

We emphasize on the equivalence relation that, from Eq. (2.7) and Eq. (2.12) it is easy to see that for every increase in size (of domain) of Eq. (2.7), there exists a ϵ in Eq. (2.12) such that the bulk and the surface energies are equal due to continuous mapping S_u. Meaning that, it is possible to find a ϵ value in Eq. (2.12) which mimics the size-scale effects of Eq. (2.7). This idea can have direct applications in engineering design and analysis.

Recalling this idea, let consider a problem of fracture on a large model, which is possible to reduce to model to a very small convenient size and find the ϵ such that the reduced model mimics the original one. For example, by setting $b = w = 10$, ϵ value for Eq. (2.12) using the following straightforward relation $b' = \frac{1}{2}(1+\frac{1}{\epsilon})b$, to mimic any value of b'. For $b' = 25, 50, 100$, the value of $\epsilon = 0.25, 0.110, 0.05263$ respectively are equivalent. Meaning that, it is possible to simulate the behaviour of the model $b' = 25$, with $\epsilon = 0.25$ and $b = 10$ from Eq. (2.12). As one expects, the comparison between numerical experiments done using Eq. (2.7) and Eq. (2.12) would give same results as in Fig. 13(b). For $b \neq w$, ϵ is calculated by the approximate area of the domain such that $b'w' = (\frac{1}{2}(1+\frac{1}{\epsilon}))^2 bw$ for some fixed b, w.

Also, it can be seen from the power law that as the scaling approaches infinity in Eq. (2.7) (or ϵ approaches zero from Eq. (2.12)), the maximum reaction force also approach infinity asymptotically, hence can be considered as the numerical evidence for $\Gamma-$Convergence.

2.5.4 Micromechanical application

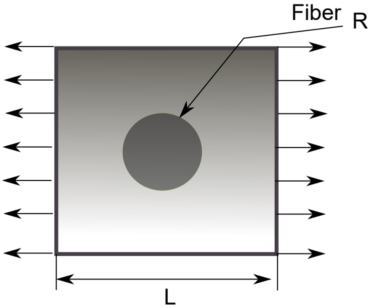

Figure 14: Micromechanics of fiber-reinforced FGM material under transverse tensile loading conditions: geometry and boundary conditions.

In this subsection, the proposed model is applied to a fiber-reinforced specimen with a functionally graded material matrix. This application intends to revisiting the cases presented in [95, 16] for homogeneous matrix. Nevertheless, differing from precedent investigations of the authors [95], we neglect the potential presence of fibre-matrix decohesion events (usually modelled via interface-like models) in order to preserve the main focus of the current investigation. In addition to the previous considerations, it is worth mentioning that the present application inherently incorporates different scale separations due to he homogenized FGM properties in the matrix (which implies a FGM microstructure) and the explicit discretization of the fiber. A more careful analysis scale separation assumptions could be investigated via the methodology developed in [128].

The baseline single-fiber domain is subjected to transverse loading conditions from micromechanical perspective is considered as in [95] and the reference therein. A squared 2D domain complying with a brittle response contains a circular fibre, see Fig. 14. The domain is meshed with 120000 first order plane-stress elements and 1000 steps are used to run the computations under displacement control.

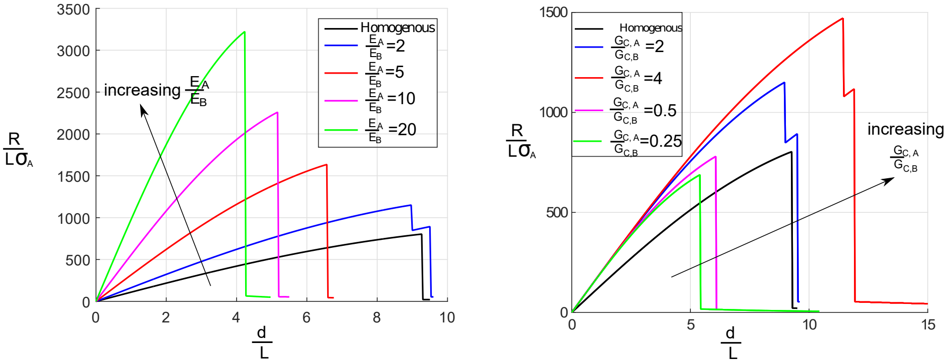

Figure 15: $\frac{R}{L\sigma_A}$ vs $\frac{L}{d}$ ratio for different (left) Young's modulus ratio (right) fracture toughness ratio.

The system properties consists of circular transverse section of side length vs radius $\frac{L}{R} = 4$. Both, the fiber and the matrix are considered to obey a linear elastic material behaviour with a FGM matrix. Without any loss of generality, the baseline properties for the present numerical investigations recall some standard values previously reported in the related literature [95]. In this regard, the properties of the fiber is taken to be $E_f = 78$ GPa and Poisson's ratio of $\nu_f = 0.22$. The FGM properties are $E_A = 2.8$ GPa, $\nu_A = 0.33$, $\mathcal{G}_{C,A} = 0.016$ $\frac{N}{mm}$. Keeping these properties constant, the material properties such as E_B, $\mathcal{G}_{C,B}$ are varied to understand the effects of different grading, and preserving the ratio $\frac{E_f}{E_A} = 27.8$ throughout the section in conjunction with varying $\frac{E_A}{E_B}$ ratio and $\frac{\mathcal{G}_{C,A}}{\mathcal{G}_{C,B}}$ ratio.

The dimensionless parameters $\frac{d}{L}$ for the applied displacement d is plotted against $\frac{R}{L\sigma_A}$ (R denoting the overall reaction forces at left edge of the system) for different Young's modulus ratio $\frac{E_A}{E_B}$ with $\frac{\mathcal{G}_{C,A}}{\mathcal{G}_{C,B}} = 2$, see Fig. 15 a). Similarly, the variation of fracture toughness ratio $\frac{\mathcal{G}_{C,A}}{\mathcal{G}_{C,B}}$, keeping $\frac{E_A}{E_B} = 2$ constant is plotted in Fig. 15b) for the comprehensive visualization of the spatial variability regarding the material properties. Analyzing these results, it is observed that, as the Young's modulus ratio increases, the asymmetry in the loading increases leading to asymmetrical crack propagation. Fig. 16 depicts the crack initiation and

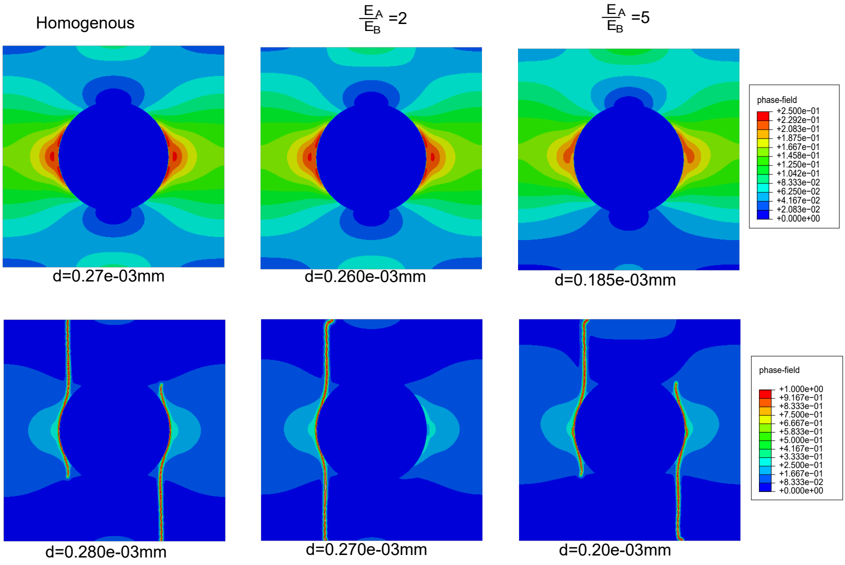

Figure 16: Crack initiation and crack propagation in single fiber reinforced composite due to different material conditions.

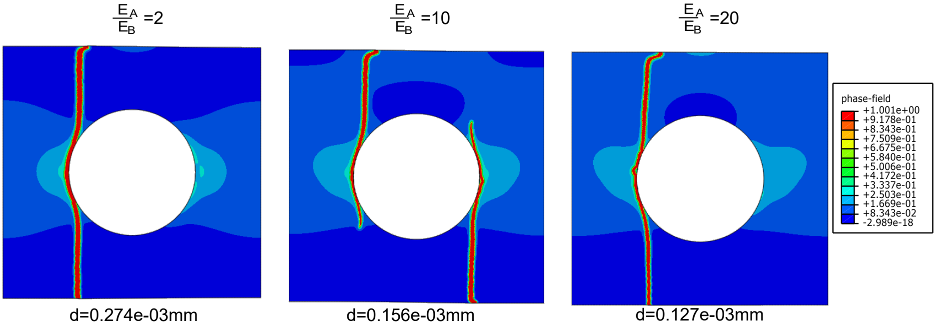

Figure 17: Crack propagation in single fiber reinforced composite.

propagation condition for the different ratio of Young's modulus. As mentioned earlier as in Theorem-3. The asymmetry is the case of single-fiber transverse loading starts towards the lowest Young's modulus side.

For $\frac{E_A}{E_B} = 2$, crack propagation happens from only one side and, in subsequent loading stages, a secondary crack starts appearing on the other side of the fibre-matrix edge, see Fig. 16. This behaviour is also reflected in the reaction force curve which displays two sudden drops, see Fig. 15a. For $\frac{E_A}{E_B} \geq 5$, crack propagation is asymmetrical, see Fig. 16.

The $\frac{\mathcal{G}_{C,A}}{\mathcal{G}_{C,B}}$ ratio plays a significant role in crack propagation, as the $\frac{\mathcal{G}_{C,A}}{\mathcal{G}_{C,B}}$ ratio increases, the reaction force also increases and delays the crack nucleation. Finally, with respect to the cracking pattern for different $\frac{E_A}{E_B}$ values (Fig. 17), we observe a general trend in this numerical experiment exhibiting a lower kinking angle towards the matrix of the main crack as $\frac{E_A}{E_B}$ decreases.

Chapter 3

A multi phase-field fracture model for long fiber reinforced composites based on the puck theory of failure

This chapter is mainly taken from [129, 130] and is organised as follows. In Section 3.2, a novel Multi Phase-Field (MPF) model relying on the Puck theory of failure for intra-laminar failure at ply level is coupled with a Cohesive Zone Model (CZM) for inter-laminar cracking. In Section 3.3, the model's variational formulation, along with the strong form, is outlined with a special focus on each failure mechanism's construction particular contribution. In Section 3.4, current computational method is numerically implemented as a system of non-linear partially coupled equations using the finite element method via user-defined `UMAT` and `UEL` subroutines in `ABAQUS`. The computational tool is applied to qualitatively predict delamination migration in long laminated fiber-reinforced polymers composites comprising 44 cross-ply laminates. The reliability of the current approach is examined via the correlation with experimental results. Finally, in Section 3.5 the present study is complemented with additional representative examples with the aim of providing further insight into the potential role of different aspects of the system in the delamination migration, including (i) the variation of the ply angle in the migration zone, (ii) the load application point, and (iii) initial crack length.

3.1 Introduction

The widespread use of Laminated Fiber Reinforced Composites (LFRCs) due to their high strength to weight ratios has paved their way into many practical applications in different industrial sectors, with remarkable impact in aerospace and aeronautics, and more recently in the automotive sector [131, 132], to quote a few of them. In the presence of ever-increasing demands of new technological advancements, load-bearing capabilities and failure modes of these materials are not yet fully understood, posing notable restrictions on their use and leading to the introduction of high safety factors.

Within this context, delamination failure can be conceived as one of the most critical failure mechanisms in Laminated Fiber Reinforced Composites (LFRCs). Such cracking events are generally associated with low through-thickness stiffness in layered disposals and can emerge from manufacturing defects, the occurrence of post-buckling phenomena [133, 134], among many others. From a modeling standpoint, delamination events in layered composites structures have been analyzed using linear elastic fracture mechanics (LEFM), enforcing initiation and growth along the ply interface with the use of strain energy-based methods to define the corresponding fracture toughness [135, 136]. Delamination can be found in low-velocity impact [137], skin debonding [138], defects from notches [139, 140], among many other practical cases. These phenomena have been extensively investigated based on cohesive-like cracking methods in pre-notched coupon configurations. An ad-hoc inter-laminar failure model can be inserted into the most critical locations of the specimen for triggering such cracking events [141, 142, 143, 144]. From a mechanical perspective, delamination can be seen as a result of the coalescence of micro-cracks at the ply interface, perpendicular to the tensile stress [145, 146, 147].

However, for some specific loading cases and configurations, it has been reported that mostly due to the sign of the change of shearing stresses, a pre-existing crack along the ply interface can kink out from such location, propagating into the adjacent ply. Matrix-cracking induced by delamination can further progress through the ply thickness and then ”propagates out” at another interface as reported in [145, 148, 149], leading to the so-called ”delamination migration” failure mode. Thus, following the terminologies used in [150], the turning of delamination crack front into one of the adjacent plies is referred to as ”kinking,” whereas, when a crack propagates across the thickness of plies and propagates out in adjacent interface is called ”migration” [151]. The main causes of such phenomena can be motivated by the analysis of the stress field around the interface crack tip, see the experimental studies conducted in [145, 152, 149] for a $0^\circ/90^\circ$ interface and [146] for a $0^\circ/\theta^\circ$ interface.

In the last decade, the advent of new numerical capabilities and modeling techniques has promoted the thorough analysis of the potential reasons for the driving mechanisms that provoke delamination migration failures. Note also that the migration phenomenon is also observed in the models without the presence of pre-existing cracks [152]. Numerical methods such a eXtended FEM (XFEM) [153], augmented finite element methods [154], floating node methods [155], cohesive-crack element methods [156] have been widely applied to study delamination migration. Moreover, delamination migration can be explained using micro-mechanics as reported by Arteiro and coauthors [157].

Concerning the different modeling methods for triggering intra-laminar failure in LFRCs, the use of continuum damage mechanics (CDM)-based methods have been of notable importance; see the phenomenological models proposed in [158, 159] and the references given therein. Notwithstanding, the local versions of CDM models generally suffer from mesh pathological issues that can be remedied using alternative methodologies. Nonlocal damage models [160, 6] have been used extensively, which also share as part of phase-field formalism while providing a detailed description of the damage behavior. On the other hand, theories such as crack band theory have been extensively used in the literature to mitigate spurious mesh sensitivity in the modeling location. Within this context, phase-field methods have become plausible nonlocal modeling alternatives that prevent most of the main limitations of alternative modeling tools for fracture in solids as explored in the sequel.

3.2 Multi Phase-Field-Cohesive Zone model (MPF-CZ)

In this section, the computational framework herein proposed for capturing delamination migration in layered composite structures is outlined. The current method relies on the combination of multiple phase-fields. Each phase-field based on different physically motivated failure mechanisms such as Puck failure criterion [130] driving the crack propagation in long fiber reinforced polymer composites along with the cohesive zone model.

Following the standard phase-field formulation, consider an arbitrary body in the general n_{dim} Euclidean space, occupying the placement $\mathcal{B} \in \mathbb{R}^{n_{dim}}$, with its external delimiting boundary $\partial\mathcal{B} \in \mathbb{R}^{n_{dim}-1}$, see Fig. 18. For any material point, the position vector is denoted by $\mathbf{x} \in \mathcal{B}$. The displacement field is identified by the vector $\mathbf{u} : \mathcal{B} \to \mathbb{R}^{n_{dim}}$, with infinitesimal stain tensor $\boldsymbol{\varepsilon} := \nabla^s \mathbf{u}$ for $\boldsymbol{\varepsilon} : \mathcal{B} \to \mathbb{R}^{n_{dim} \times n_{dim}}$. The displacement boundary conditions are prescribed as $\mathbf{u} = \overline{\mathbf{u}}$ on $\partial\mathcal{B}_u$ and traction conditions are given by $\overline{\mathbf{t}} = \boldsymbol{\sigma} \cdot \mathbf{n}$ on $\partial\mathcal{B}_t$ such that, kinematic and static boundary conditions satisfy: $\overline{\partial\mathcal{B}_t \cup \partial\mathcal{B}_u} = \partial\mathcal{B}$ and $\partial\mathcal{B}_t \cap \partial\mathcal{B}_u = 0$, where $\mathbf{n}$ is outward normal vector and $\boldsymbol{\sigma}$ is the Cauchy stress tensor.

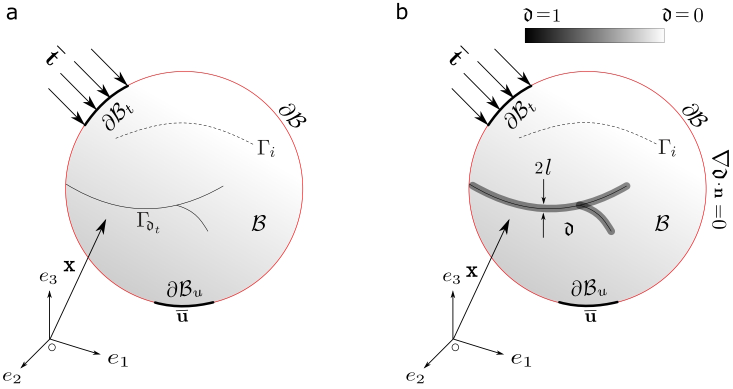

Figure 18: Body under consideration: (a) sharp crack representation and (b) Regularized crack topology.

In addition to the previous definitions, let Γ be a crack set incorporating interface cracks Γ_i arising from the cohesive interface and cracks in the bulk $\Gamma_{\mathfrak{d}_t}$ from the multi phase-field such that, $\Gamma_i \cup \Gamma_{\mathfrak{d}_t} = \Gamma$ and $\Gamma_i \cap \Gamma_{\mathfrak{d}_t} = \emptyset$ for each discrete $t \in [0, T]$ with $\Gamma_t \subseteq \Gamma_{t+1}$. The displacement jumps along the interface as the relative displacement between two homogeneous points at the flanks are denoted by $\mathfrak{g} = \mathbf{u}_i^+ - \mathbf{u}_i^-$, representing the difference between kinematic field along the interface Γ_i^+ and Γ_i^- in line with [161, 162]. On the other hand, $\Gamma_{\mathfrak{d}_t}$ is defined as the set of discontinuous points $\mathbf{x}$, where $\mathbf{u}$ has one sided approximate limits

$\mathbf{u}_{\mathfrak{d}}^{+} \neq \mathbf{u}_{\mathfrak{d}}^{-}$ with respect to a suitable direction $\mathfrak{v}_u$ normal to $\Gamma_{\mathfrak{d}_t}$ inline with [17, 20].

To account for multiple energies in the system, the total free energy functional describing the mechanics of body $\mathcal{B}$, is given as the sum total of internal and external energies acting on the system as follows

$$\Pi(\mathbf{u}, \Gamma) = \Pi_{\text{int}}(\mathbf{u}, \Gamma) + \Pi_{\text{ext}}(\mathbf{u}). \tag{3.1}$$

The consistent generalization of the isotropic damage formulation for the consideration of different failure mechanisms can be postulated by the additive decomposition of total internal energy into multiple contributions, in which each of them is associated with a certain failure mechanism. In such a postulation, a scalar damage variable $\mathfrak{d}_i$ $(i = 1, ..., n)$ is associated with each one of the n failure mechanisms, such that $\mathfrak{d}_i = 0$ for intact material state and $\mathfrak{d}_i = 1$ for fully broken state and so that $\mathfrak{d}_i \in [0, 1]$ for each $i = 1, ..., n$. Moreover, to account for non-local damage evolution, the respective gradients $\nabla_{\mathbf{x}}\mathfrak{d}_i$ are incorporated in the formulation. This additive decomposition postulation for intralaminar failure was successfully applied in [158] and later extended to incorporate failure criteria such as Puck failure theory so as to distinguish between the fiber and matrix dominated damage mechanisms in LFRPs [130, 159]. However, the consideration of dissipative energies stemming from debonding along the interface Γ_i, and crack propagation in the bulk $\Gamma_{\mathfrak{d}_t}$ is still a matter of investigation. The prediction of such crack topology becomes increasingly complex due to branching and coalescence phenomenons, as well as the interaction with diffusive cracks, which may induce the debonding process along the existing interface Γ_i. One possibility to achieve this is by employing a phase-field model incorporating multiple diffusive crack fields within the bulk and interface elements relying on cohesive zone methodologies at a prescribed interface inline with [162]. Hence, the total internal energy is now an amalgamation of (i) total elastic energy constituting from bulk (fiber and inter-fiber) energy, (ii) surface energy (crack energy) stemming from bulk (fiber and inter-fiber) failure, and (iii) cohesive interface energy obeying a bi-linear traction-separation law

$$\Pi_{\text{int}}(\mathbf{u}, \Gamma) = \Pi_{\text{int},b}(\mathbf{u}, \Gamma_{\mathfrak{d}_i}) + \Pi_{\text{int},c}(\Gamma_i), \tag{3.2}$$

where $\Pi_{int,b}(\mathbf{u}, \Gamma)$ is the internal energy stemming from the bulk (fiber and inter-fiber) and $\Pi_{int,C}(\Gamma_i)$ is the dissipative energy associated with cohesive debonding which are addressed in detail in the sequel. The bulk energy $\Pi_{int,b}(\mathbf{u}, \Gamma)$ is further decomposed into

$$\Pi_{\text{int},b}(\mathbf{u}, \Gamma_{\mathfrak{d}_i}) = \Pi_{\text{int},FF}(\mathbf{u}, \Gamma_{\mathfrak{d}_{FF}}) + \Pi_{\text{int},IFF}(\mathbf{u}, \Gamma_{\mathfrak{d}_{IFF}}), \tag{3.3}$$

where $\Pi_{\text{int},FF}(\mathbf{u}, \Gamma_{\mathfrak{d}_{FF}})$ and $\Pi_{\text{int},IFF}(\mathbf{u}, \Gamma_{\mathfrak{d}_{IFF}})$ correspond to the energies associated with fiber failure and inter-fiber failure, respectively.

With such decomposition at hand, the scheme herein used recalls that the dissipated energy arising from each of the individual failure mechanisms only affects their corresponding counterparts in the elasticity tensor, therefore precluding the coupling between fiber inter-fiber failures and each of these failures with respect to the cohesive debonding. Note that, due to this preclusion of interaction between the energies, the elastic energy is strongly coupled with the surface energies stemming from fiber, inter-fiber, and cohesive debonding. In contrast, surface energies among themselves are only weakly coupled.

The effective Helmholtz free energy function $\hat{\Psi}$ is defined as

$$\hat{\Psi}(\boldsymbol{\varepsilon}, \mathbf{A}) = \frac{1}{2}\boldsymbol{\varepsilon} : \mathbb{C}^e : \boldsymbol{\varepsilon},$$

where $\mathbb{C}^e$ is the undamaged elastic constitutive tensor defined as

$$\mathbb{C}^e := \partial_{\boldsymbol{\varepsilon}\boldsymbol{\varepsilon}}\hat{\Psi} = \lambda\mathbf{1} \otimes \mathbf{1} + 2\mu_T\mathbb{I} + \alpha(\mathbf{1} \otimes \mathbf{A} + \mathbf{A} \otimes \mathbf{1}) + 2(\mu_L - \mu_T)\mathbb{I}_A + \beta\mathbf{A} \otimes \mathbf{A},$$

where $\mathbf{1}$ is the second order identity tensor, $\mathbb{I}_{A,ijkl} = A_{im}\mathbb{I}_{jmkl} + A_{jm}\mathbb{I}_{mikl}$ represents the fourth-order identity matrix, and λ, α, β, μ_T and μ_L are to the elastic constants taking the form

$$\begin{gathered}
\lambda = E_{22}\left(\nu_{23} + \nu_{31}\nu_{13}\right)/D, \\
\alpha = E_{22}\left[\nu_{31}\left(1 + \nu_{32} - \nu_{13}\right) - \nu_{32}\right]/D, \\
\beta = E_{11}\left(1 - \nu_{32}\nu_{23}\right)/D - E_{22}\left[1 - \nu_{21}\left(\nu_{12} + 2(1 + \nu_{23})\right)\right]/D - 4G_{12}, \\
\mu_L = G_{12}; \quad \mu_T = G_{23},
\end{gathered}$$

with $D = 1 - \nu_{32}^2 - 2\nu_{13}\nu_{31} - 2\nu_{32}\nu_{13}\nu_{31}$. The material direction is denoted by $\mathbf{a}$ and $\mathbf{A} := \mathbf{a} \otimes \mathbf{a}$ is so called structural tensor.

Here, 1-direction corresponds to the fiber orientation, 2-direction is transverse in-plane orientation with respect to the fiber direction, and 3-direction stands for transverse out-of-plane orientation.

3.2.1 Bulk energies

In the light of previous developments, the total energy of the fiber can be established as the sum total of the elastic energy and fracture energy associated with the fiber as

$$\begin{aligned}
\Pi_{\text{int},FF}(\mathbf{u}, \Gamma_{\mathfrak{d}_{FF}}) \approx \Pi_{\text{int},FF}(\mathbf{u}, \mathfrak{d}_{FF}) = & \int_{\mathcal{B}} (1 - \mathfrak{d}_{FF})^2 \hat{\Psi}_{FF}(\boldsymbol{\varepsilon}, \mathbf{A}) \mathrm{dV} \\
& + \int_{\mathcal{B}} \mathcal{G}_{c,FF}\left[\frac{1}{2l_{FF}}\mathfrak{d}_{FF}^2 + \frac{l_{FF}}{2}|\nabla\mathfrak{d}_{FF}|^2\right] \mathrm{dV},
\end{aligned} \tag{3.4}$$

where $\hat{\Psi}_{FF}$ is the elastic contribution associated with the fiber: $\hat{\Psi}_{FF} = \frac{1}{2}\boldsymbol{\varepsilon} : \mathbb{C}^e_{FF} : \boldsymbol{\varepsilon}$, with

$$\mathbb{C}^e_{FF} = \begin{bmatrix} \mathbb{C}^e_{11} & 0 & 0 & 0 & 0 & 0 \\ 0 & 0 & 0 & 0 & 0 & 0 \\ 0 & 0 & 0 & 0 & 0 & 0 \\ 0 & 0 & 0 & 0 & 0 & 0 \\ 0 & 0 & 0 & 0 & 0 & 0 \\ 0 & 0 & 0 & 0 & 0 & 0 \end{bmatrix},$$

and $\mathcal{G}_{c,FF}$ is the fracture energy, and l_{FF} is the material characteristic length associated with fiber failure in phase-field related to the apparent material strength [163] as

$$l_{FF} = \frac{27}{256}\frac{E_{11}\mathcal{G}_{c,FF}}{\sigma_{s,FF}^2},$$

where $\sigma_{s,FF}$ is the apparent material strength associated with fiber failure.

Similarly, the inter-fiber contribution to the total internal energy can be expressed as

$$\begin{aligned}\Pi_{\text{int},IFF}(\mathbf{u},\Gamma_{\mathfrak{d}_{FF}}) \approx \Pi_{\text{int},IFF}(\mathbf{u},\mathfrak{d}_{IFF}) = &\int_{\mathcal{B}} (1-\mathfrak{d}_{IFF})^2 \hat{\Psi}_{IFF}(\boldsymbol{\varepsilon},\mathbf{A})\mathrm{dV} \\ &+ \int_{\mathcal{B}} \mathcal{G}_{c,IFF}\left[\frac{1}{2l_{IFF}}\mathfrak{d}^2_{IFF} + \frac{l_{IFF}}{2}|\nabla\mathfrak{d}_{IFF}|^2\right]\mathrm{dV},\end{aligned} \tag{3.5}$$

where $\hat{\Psi}_{IFF} = \frac{1}{2}\boldsymbol{\varepsilon} : \mathbb{C}^e_{IFF} : \boldsymbol{\varepsilon}$ is the elastic contribution associated with the inter-fiber failure, and

$$\mathbb{C}^e_{IFF} = \begin{bmatrix} 0 & \mathbb{C}^e_{12} & \mathbb{C}^e_{13} & 0 & 0 & 0 \\ \mathbb{C}^e_{21} & \mathbb{C}^e_{22} & \mathbb{C}^e_{23} & 0 & 0 & 0 \\ \mathbb{C}^e_{31} & \mathbb{C}^e_{32} & \mathbb{C}^e_{33} & 0 & 0 & 0 \\ 0 & 0 & 0 & \mathbb{C}^e_{44} & 0 & 0 \\ 0 & 0 & 0 & 0 & \mathbb{C}^e_{55} & 0 \\ 0 & 0 & 0 & 0 & 0 & \mathbb{C}^e_{66} \end{bmatrix},$$

where $\mathcal{G}_{c,IFF}$ and l_{IFF} are the fracture energy and corresponding length scale associated with inter-fiber failure, respectively. Similarly, the length scale parameter is estimated for the apparent material strength $\sigma_{s,IFF}$ of inter-fiber failure as

$$l_{IFF} = \frac{27}{256}\frac{E_{22}\mathcal{G}_{c,IFF}}{\sigma^2_{s,IFF}}.$$

Note that with these definitions at hand, the damaged constitutive matrix $\mathbb{C}$ renders

$$\mathbb{C}(\mathfrak{d}_{FF},\mathfrak{d}_{IFF}) = (1-\mathfrak{d}_{FF})^2\mathbb{C}^e_{FF} + (1-\mathfrak{d}_{IFF})^2\mathbb{C}^e_{IFF}, \tag{3.6}$$

with

$$\mathbb{C}(\mathfrak{d}_{FF},\mathfrak{d}_{IFF}) = \begin{bmatrix} \mathcal{P}_1\mathbb{C}^e_{11} & \mathcal{P}_2\mathbb{C}^e_{12} & \mathcal{P}_2\mathbb{C}^e_{13} & 0 & 0 & 0 \\ \mathcal{P}_2\mathbb{C}^e_{21} & \mathcal{P}_2\mathbb{C}^e_{22} & \mathcal{P}_2\mathbb{C}^e_{23} & 0 & 0 & 0 \\ \mathcal{P}_2\mathbb{C}^e_{31} & \mathcal{P}_2\mathbb{C}^e_{32} & \mathcal{P}_2\mathbb{C}^e_{33} & 0 & 0 & 0 \\ 0 & 0 & 0 & \mathcal{P}_{12}\mathbb{C}^e_{44} & 0 & 0 \\ 0 & 0 & 0 & 0 & \mathcal{P}_{12}\mathbb{C}^e_{55} & 0 \\ 0 & 0 & 0 & 0 & 0 & \mathcal{P}_2\mathbb{C}^e_{66} \end{bmatrix}, \tag{3.7}$$

where $\mathcal{P}_1 = (1-\mathfrak{d}_{FF})^2$, $\mathcal{P}_2 = (1-\mathfrak{d}_{IFF})^2$, and $\mathcal{P}_{12} = \min(\mathcal{P}_1,\mathcal{P}_2)$. Notice that $\mathcal{P}_{12}$ is not differentiable due to the existence of "min". Hence, we first take the minima so that, any minimum of $\mathcal{P}_{12}$ (i.e $\mathcal{P}_1$ or $\mathcal{P}_2$) is differentiable.

3.2.2 Interface energies

The energy stemming from the interface is governed by a bi-linear traction separation law which constitutes of a linear elastic stage characterized by an initial stiffness of K_n, K_{t1} and K_{t2} corresponding to the normal and shear components, respectively, followed by a linear softening as in Fig. 19. The irreversibility is accounted by introducing a damage variable $\mathfrak{d}_c$

depending on the relative kinematic critical normal and tangential openings, $\mathfrak{g}_n^f$ and $\mathfrak{g}_{t_j}^f$ (j=1 for 2D and j=1,2 for 3D), respectively [142, 143].

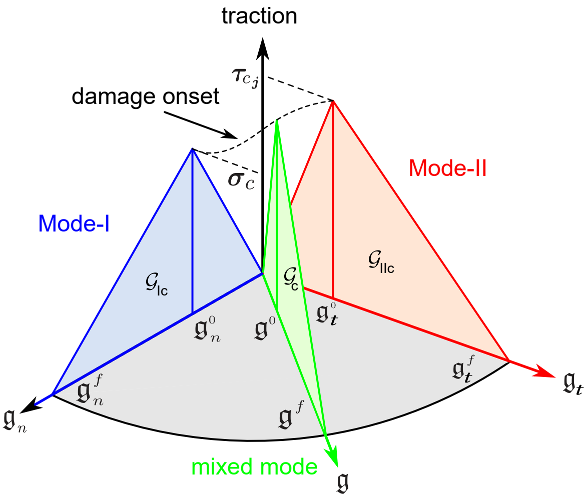

Figure 19: Schematic representation of the bi-linear cohesive zone model traction-separation law for mixed mode

The corresponding interface laws governing the normal and tangential tractions $\boldsymbol{\sigma}_n$ and $\boldsymbol{\tau}_{t_j}$, respectively, take the form

$$\boldsymbol{\sigma}_n = \begin{cases} k_n \mathfrak{g}_n & \text{if } \mathfrak{g}_n \leq \mathfrak{g}_n^0 \\ (1-\mathfrak{d}_c) k_n \mathfrak{g}_n & \text{if } \mathfrak{g}_n^0 < \mathfrak{g}_n < \mathfrak{g}_n^f \\ 0 & \text{otherwise} \end{cases},$$

$$\boldsymbol{\tau}_{t_j} = \begin{cases} k_{t_j} \mathfrak{g}_{t_j} & \text{if } \mathfrak{g}_{t_j} \leq \mathfrak{g}_{t_j}^0 \\ (1-\mathfrak{d}_c) k_{t_j} \mathfrak{g}_{t_j} & \text{if } \mathfrak{g}_{t_j}^0 < \mathfrak{g}_{t_j} < \mathfrak{g}_{t_j}^f \\ 0 & \text{otherwise} \end{cases},$$

for each $j = 1, 2$ to account for the tangential traction, whereas $\mathfrak{g}_n$ and $\mathfrak{g}_{t_j}$ are the relative normal and tangential displacements, respectively. The mixed-mode fracture energy of the interface reads

$$\mathcal{G}_C^i = \mathcal{G}_{IC} + (\mathcal{G}_{IIC} - \mathcal{G}_{IC}) \left(\frac{\mathcal{G}_{II} + \mathcal{G}_{III}}{\mathcal{G}_I + \mathcal{G}_{II} + \mathcal{G}_{III}} \right)^{\eta},$$

where $\mathcal{G}_{IC}$, $\mathcal{G}_{IIC}$, and $\mathcal{G}_{IIIC}$ represent the corresponding fracture toughness associated with normal (mode I) and shear (mode II and III), respectively, and computed as the area under the traction separation curve, η identifies an experimental fitting parameter elucidating the effects of fracture mode mixities [134]. Finally, $\mathcal{G}_I$, $\mathcal{G}_{II}$, and $\mathcal{G}_{III}$ are energy release rate associated with mode I, mode II, and III, respectively. Damage is initiated using the quadratic interaction function of nominal stress ratios. The damage is evolved using Benzeggagh-Kenane (BK) failure criterion based on cumulative energy such that mixed fracture toughness $\mathcal{G}_C^i$ reaches the critical energy.

Based on the energy considerations, the evolution of the damage variable $\mathfrak{d}_c$ is estimated based on the effective displacement of the cohesive element, where $\mathfrak{d}_c$ is evolving linearly with

$$\mathfrak{d}_c = \frac{\mathfrak{g}_m^f(\mathfrak{g}_m^{\max} - \mathfrak{g}_m^0)}{\mathfrak{g}_m^{\max}(\mathfrak{g}_m^f - \mathfrak{g}_m^0)}, \tag{3.8}$$

where $\mathfrak{g}_m^0$ is effective displacement at initiation and $\mathfrak{g}_m^f = \dfrac{2\mathcal{G}_C^i}{T_{eff}^0}$ is the effective displacement at failure. Here, T_{eff}^0 is the effective traction at damage initiation estimated using effective tractions $T_{eff} = \sqrt{(\boldsymbol{\sigma}_n)^2 + (\boldsymbol{\tau}_{t_1})^2 + (\boldsymbol{\tau}_{t_2})^2}$, as $T_{eff}^0 = \min\{T_{eff}(\mathfrak{d}_c > 0)\}$. And $\mathfrak{g}_m^{\max}$ refers to the maximum value of effective displacement during loading history estimated using $\mathfrak{g}_m^{\max} = \max_{[0,T]} \mathfrak{g}_m$, where $\mathfrak{g}_m := \sqrt{\mathfrak{g}_n^2 + (\mathfrak{g}_{t_1})^2 + (\mathfrak{g}_{t_2})^2}$. Finally, with this at hand, the corresponding total energy generated by the cohesive interface takes the form

$$\Pi_{\text{int},c}(\Gamma_i) \approx \Pi_{\text{int},c}(\mathfrak{d}_c) = \int_{\Gamma_i} \mathcal{G}_c^i(\mathfrak{g}, \mathfrak{d}_c)\text{dS} = \int_{\Gamma_i} \mathfrak{g}^T \mathcal{T}\text{dS}, \tag{3.9}$$

with $\mathfrak{g} = [\mathfrak{g}_n, \mathfrak{g}_{t_1}]$ and $\mathcal{T} = [\boldsymbol{\sigma}_n, \boldsymbol{\tau}_{t_1}]$.

3.2.3 Fundamentals of Puck failure criterion

Damage evolution in bulk relies on Puck failure theory [164] whose corresponding failure criterion accounts for the independent assessment of fiber and inter-fiber failure surfaces. For the fiber failure, with usual notations, that is $\|$ (subscript 1), $\perp$ (subscript 2 and subscript 3) representing fiber direction, normal to the fiber direction in-plane and, normal to the fiber direction out-of-plane, respectively, for the ply co-ordinates in a local setting $0 - \mathbf{e}_1 - \mathbf{e}_2 - \mathbf{e}_3$ as in Fig. 20.

According to the Puck theory, fiber failure is triggered based on energetic considerations that, the exposure factor (denoted $f_{E,FF+}$, for tensile only) reaches the value 1, where $f_{E,FF+}$ is given by

$$f_{E,FF+} = \frac{1}{R_{\|}^t}\left[\sigma_{11} - \left(\nu_{\perp\|} - \frac{E_{\|}}{E_{\|f}}\nu_{\perp\|f}\right)(\sigma_{22} + \sigma_{33})\,\mathcal{P}_2\right],$$

where $R_{\|}^t$ stands for the tensile longitudinal strength in fiber direction. $\nu_{\perp\|}$ and $\nu_{\perp\|f}$ identify the major Poisson's ratios of the ply and the fibers, respectively, and $E_{\|f}$ is the elastic modulus of the fibers. $FF+$ denotes the fiber failure in tension, whereas the compression is omitted for the sake of brevity but can easily be incorporated as in [130]. The incorporation of $\mathcal{P}_2$ is to scale the influence of the transverse stress components on the longitudinal stress (lateral contraction) with respect to the state of matrix damage. It is assumed that the contraction in the longitudinal direction due to transverse stress will vanish in a case $\mathcal{P}_2 \to 1$, i.e., matrix rupture parallel to the fibers. In the case of compressive longitudinal stress, reduced compressive longitudinal fracture resistance of the plies is assumed in the case of increasing shear stress.

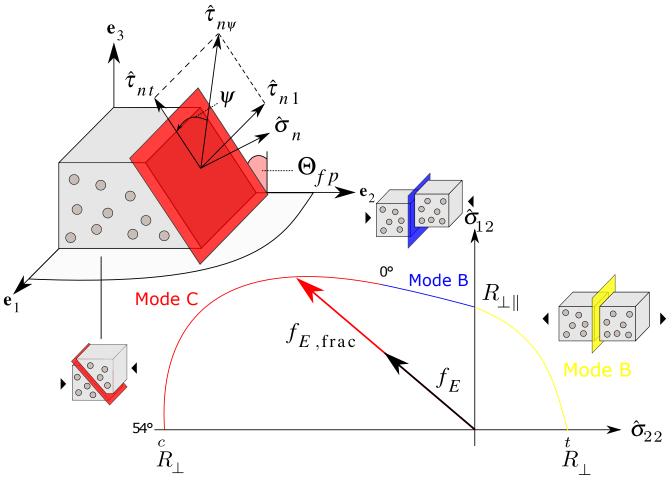

Figure 20: Puck failure theory: (a) definition of acting stresses on the fracture plane by θ_{fp} angle and (b) the exposure factor f_E, where $f_{E,(fr)}$ is the exposure factor at the failure point.

Puck theory also distinguishes the inter-fiber failure by introducing the so-called action plane [165, 164], which corresponds to identifying the potential fracture plane derived from the maximum stress states $\{\bar{\sigma}_n(\Theta), \bar{\tau}_{nt}(\Theta), \bar{\tau}_{n1}(\Theta)\}$, where $\bar{\sigma}_n(\Theta)$, $\bar{\tau}_{nt}(\Theta)$, and $\bar{\tau}_{n1}(\Theta)$ are the normal stress component, shear stress component transverse to the fiber, and the shear stress component plane parallel to the fiber, respectively, each on the action plane. The determination of the fracture plane is usually performed via the assessment of the most critical stress state in terms of the local components by calculating the value of inter-fiber exposure factor $F_{E,IFF}$ for all angles Θ within the interval of $-90^\circ \leq \Theta \leq +90^\circ$, using an increment of one degree. The transformation from the local ply setting to the action plane system yields

$$\begin{bmatrix} \sigma_n(\Theta) \\ \tau_{nt}(\Theta) \\ \tau_{n1}(\Theta) \end{bmatrix} = \begin{bmatrix} \cos^2\Theta & \sin^2\Theta & 2\cos\Theta\sin\Theta & 0 & 0 \\ -\cos\Theta\sin\Theta & \cos\Theta\sin\Theta & \cos^2\Theta - \sin^2\Theta & 0 & 0 \\ 0 & 0 & 0 & \sin\Theta & \cos\Theta \end{bmatrix} \begin{bmatrix} \sigma_{22} \\ \sigma_{33} \\ \sigma_{23} \\ \sigma_{13} \\ \sigma_{12} \end{bmatrix}.$$

In particular, the expression for inter-fiber failure under tensile conditions on the action plane takes the form

$$f_{E,IFF+}(\Theta) = \left[\sqrt{\left[\left(\frac{1}{R_{\perp}^{At}} - \frac{p_{\perp\psi}^{t}}{R_{\perp\psi}^{A}}\right)\sigma_n(\Theta)\right]^2 + \left(\frac{\tau_{nt}(\Theta)}{R_{\perp\perp}^{A}}\right)^2 + \left(\frac{\tau_{n1}(\Theta)}{R_{\parallel\perp}^{A}}\right)^2} + \frac{p_{\perp\psi}^{t}}{R_{\perp\psi}^{A}}\sigma_n(\Theta) \right]$$

$$\frac{1}{\eta_w} \text{ for } \sigma_n(\Theta) \geq 0,$$

where $R_{\perp}^{At}$ and $R_{\perp\perp}^{A}$ are transverse tensile strength and fracture strength respectively, whereas $R_{\perp\psi}^{A}$ is the transverse tensile strength at any ply angle ψ, with $f_{E,IFF+}$ representing the exposure factor and the failure is triggered when $f_{E,IFF+}$ reaches the value 1.

In the previous expression, $\cos^2\psi$ and $\sin^2\psi$ are

$$\cos^2\psi = \frac{\tau_{nt}^2}{\tau_{nt}^2 + \tau_{n1}^2} \text{ and } \sin^2\psi = \frac{\tau_{n1}^2}{\tau_{nt}^2 + \tau_{n1}^2}.$$

Finally, the definition of the inclination parameters $p_{\perp\psi}^{t}$ and $p_{\perp\psi}^{c}$ for any angle ψ renders

$$\frac{p_{\perp\psi}^{i}}{R_{\perp\psi}^{A}} = \frac{p_{\perp\perp}^{i}}{R_{\perp\perp}^{A}}\cos^2\psi + \frac{p_{\perp\parallel}^{i}}{R_{\perp\parallel}^{A}}\sin^2\psi, \;\; i = t, c;$$

with

$$R_{\perp\psi}^{A} = \left[\left(\frac{\cos\psi}{R_{\perp\perp}^{A}}\right)^2 + \left(\frac{\sin\psi}{R_{\perp\parallel}^{A}}\right)^2\right].$$

Due to the modelling assumptions herein made, the proposed model requires the following fracture energy values: (i) $\mathcal{G}_{c,FF}$ fiber fracture energy, (ii) $\mathcal{G}_{c,IFF}$ matrix dominated fracture energy, and (iii) $\mathcal{G}_c$ inter-laminar fracture energy. These properties can be determined via experimental procedures, see [166, 157, 167, 168] and the references therein.

3.3 Variational formulation

Relying on the considerations given in Section 3.2, the total energy functional of the solid body $\mathcal{B}$, along with the cracks Γ_i and $\Gamma_{\mathfrak{d}_i}$ at any arbitrary instance $t \in [0, T]$ takes the form

$$\Pi(\mathbf{u}, \Gamma) \approx \Pi(\mathbf{u}, \mathfrak{d}_i, \mathfrak{d}_c) = \Pi_{\text{int}}(\mathbf{u}, \mathfrak{d}_i, \mathfrak{d}_c) + \Pi_{\text{ext}}(\mathbf{u}), \tag{3.10}$$

where the internal and external contribution to the energy functional $\Pi(\mathbf{u}, \mathfrak{d}_i, \mathfrak{d}_c)$ read, respectively

$$
\begin{aligned}
\Pi_{\text{int}}(\mathbf{u}, \mathfrak{d}_i, \mathfrak{d}_c) = & \int_{\mathcal{B}} (1-\mathfrak{d}_{FF})^2 \hat{\Psi}_{FF}(\boldsymbol{\varepsilon}, \mathbf{A}) + (1-\mathfrak{d}_{IFF})^2 \hat{\Psi}_{IFF}(\boldsymbol{\varepsilon}, \mathbf{A}) \mathrm{dV} \\
& + \int_{\mathcal{B}} P_{FF} \mathcal{G}_{c,FF} \left[\frac{1}{2 l_{FF}} \mathfrak{d}_{FF}^2 + \frac{l_{FF}}{2} |\nabla \mathfrak{d}_{FF}|^2 \right] \mathrm{dV} \\
& + \int_{\mathcal{B}} P_{IFF} \mathcal{G}_{c,IFF} \left[\frac{1}{2 l_{IFF}} \mathfrak{d}_{IFF}^2 + \frac{l_{IFF}}{2} |\nabla \mathfrak{d}_{IFF}|^2 \right] \mathrm{dV} \\
& + \int_{\Gamma_i} \mathfrak{g}^T \mathcal{T} \mathrm{dS},
\end{aligned}
\tag{3.11}
$$

$$
\Pi_{\text{ext}}(\mathbf{u}) = - \int_{\mathcal{B}} \mathbf{f}_v \mathrm{dV} - \int_{\partial \mathcal{B}_t} \bar{\mathbf{t}} \mathrm{dS}, \tag{3.12}
$$

where $\mathbf{f}_v$ is the deformation-independent volume-specific loads.

In the above expression, Eq. (3.11), P_{FF} and P_{IFF} are the activation flags, which are activated when the corresponding pucks failure criterion is met. The approximate solution of the stated problem with MPF-CZ can be obtained as a quadruplet of the solution of the following minimization problem. Determine

$$
(\mathbf{u}^*,\, \mathfrak{d}_{FF}^*,\, \mathfrak{d}_{IFF}^*,\, \mathfrak{g}^*) = \operatorname{argmin}_{\mathcal{S}} \Pi(\mathbf{u}, \mathfrak{d}_i, \mathfrak{d}_c). \tag{3.13}
$$

where, $\mathcal{S} = \{\dot{\mathfrak{d}_{FF}}, \dot{\mathfrak{d}_{IFF}} \geq 0 \quad \text{for all } \mathbf{x} \in \mathcal{B} \diagdown \Gamma_i, \dot{\mathfrak{d}}_c \geq 0 \quad \text{for all } \mathbf{x} \in \Gamma_i\}$ enforcing irreversibility of the evolution parameters. One may also argue that $\mathfrak{g}^*$ should be replaced by the $\mathfrak{d}_c$ in the minimization problem, however, it is easy to see that the minimum value of $\mathfrak{g}^*$ also leads to a minimum value of $\mathfrak{d}_c$ from Eq. (3.8).

The quadruplet set $(\mathbf{u}^*,\, \mathfrak{d}_{FF}^*,\, \mathfrak{d}_{IFF}^*,\, \mathfrak{g}^*)$ in Eq. (3.13) is solved by taking a variational form of the total internal energy functional (Gateaux derivative) assuming enough regularity of the terms involved. In the infinitesimal setting, considering the irriversibility of the damage variables set $\mathcal{S}$ for any admissible test function $(\delta \mathbf{u},\, \delta \mathfrak{d}_{FF}, \delta\, \mathfrak{d}_{IFF},\, \delta \mathfrak{g})$ in the appropriate space of distribution, a strong form of the field equations can be reduced to the following

$$
\begin{aligned}
\operatorname{div} \left[(1-\mathfrak{d}_{FF})^2 \mathbb{C}_{FF}^e : \boldsymbol{\varepsilon} + (1-\mathfrak{d}_{IFF}) \mathbb{C}_{IFF}^e : \boldsymbol{\varepsilon} \right] + \mathbf{f}_v = & \mathbf{0} \quad \text{in } \mathcal{B} \diagdown \Gamma_i, \\
\text{and} \quad \boldsymbol{\sigma} \cdot \mathbf{n} = & 0 \quad \text{on } \partial \mathcal{B}_t,
\end{aligned}
\tag{3.14}
$$

$$
\begin{aligned}
2(1-\mathfrak{d}_{FF}) P_{FF} \mathcal{H}_{FF}(\mathbf{x}, t) = \mathcal{G}_{c,FF} \delta_{\mathfrak{d}_{FF}} \gamma(\mathfrak{d}_{FF}, \nabla_{\mathbf{x}} \mathfrak{d}_{FF}) \quad & \text{in } \mathcal{B} \diagdown \Gamma_i \\
\text{and} \quad \nabla_{\mathbf{x}} \mathfrak{d}_{FF} \cdot \mathbf{n} = 0 \quad & \text{in } \partial \mathcal{B},
\end{aligned}
\tag{3.15}
$$

$$
\begin{aligned}
2(1-\mathfrak{d}_{IFF}) P_{IFF} \mathcal{H}_{IFF}(\mathbf{x}, t) = \mathcal{G}_{c,IFF} \delta_{\mathfrak{d}_{IFF}} \gamma(\mathfrak{d}_{IFF}, \nabla_{\mathbf{x}} \mathfrak{d}_{IFF}) \quad & \text{in } \mathcal{B} \diagdown \Gamma_i \\
\text{and} \quad \nabla_{\mathbf{x}} \mathfrak{d}_{IFF} \cdot \mathbf{n} = 0 \quad & \text{in } \partial \mathcal{B},
\end{aligned}
\tag{3.16}
$$

$$
\operatorname{div}_{\mathfrak{g}} \left[\boldsymbol{\sigma}_n(\mathfrak{d}_c) + \tau_n(\mathfrak{d}_c) \right] = 0 \quad \text{in } \Gamma_i, \tag{3.17}
$$

wherein the previous expressions $\operatorname{div}_{\mathfrak{g}}[\bullet]$ represents the divergence operator taken with respect to $\mathfrak{g}$. The terms $\mathcal{H}_{FF}$ and $\mathcal{H}_{IFF}$ are the crack driving forces related to fiber and interfiber failure, respectively. In accordance with the Pucks failure criteria, the crack driving force of each $j = FF, IFF$ are given by

$$\mathcal{H}_j(\mathbf{x},t) = \xi_j \left[\left\langle \frac{\max\limits_{\tau\in[0,t]} \hat{\Psi}_j(\mathbf{x},\tau)}{\hat{\Psi}_{j,init}} - 1 \right\rangle_+ \right], \tag{3.18}$$

where ξ_j is a dimensionless fitting parameter that characterizes the damage activation and post peak behaviours from experimental results. $\hat{\Psi}_{j,init}$ is the effective elastic energy for damage initiation in each of $j = FF, IFF$.

The unilateral stationary condition of the total internal energy functional implies that $\delta\Pi_{int} = 0$ for all $(\delta\mathbf{u},\ \delta\mathfrak{d}_{FF}, \delta\,\mathfrak{d}_{IFF},\ \delta\mathfrak{g}) > 0$ and $\delta\Pi_{int} > 0$ for $(\delta\mathbf{u},\ \delta\mathfrak{d}_{FF}, \delta\,\mathfrak{d}_{IFF},\ \delta\mathfrak{g}) = 0$ along with the irriversibility and boundedness of $\mathfrak{d}_{FF}, \mathfrak{d}_{IFF}, \mathfrak{d}_c$ leads to the first-order optimality (KKT) conditions for the quasi-static evolution [16, 114]. $\Gamma-$ convergence of the multi phase-field problem in the absence of the interface can be easily derived following the results obtained in [24].

It is worth noting that the irreversible character of the phase-fields and cohesive zone can be reduced to $\mathcal{S}$, this is fulfilled by the history variable embedded by the history variable Eq. (3.18). The boundedness of the phase-field variables $\mathfrak{d}_{FF}, \mathfrak{d}_{IFF} \in [0,1]$ is ensured due to the choice of degradation function $(1-\mathfrak{d}_j)^2$ as in [28]. Also, it is important to note that, we have assumed $\nabla_{\mathbf{x}}\mathfrak{d}_j = 0$ due to the compactness property and $\delta\mathbf{u} = 0$ on $\partial\Omega_t$ and $\delta\mathfrak{d}_j = 0$ on $\partial\Omega$, from the variational form which are reflected in the choice of approximate spaces of test functions as in Section 3.4, see [17, 20].

3.4 Finite element implementation

In this section, details of the finite element implementation of the proposed model are outlined. A staggered solution scheme is used to solve the system of coupled Partial Differential Equations (PDEs) using an alternating minimization scheme [15]. Consider the discritization of the domain defined as $\mathcal{B} \to \mathcal{B}^e$, $\Gamma_i \to \Gamma_i^e$ such that the functions $\mathbf{u}^e \in \mathcal{U}_h$, $\mathfrak{d}_j^e \in \mathcal{U}_{\mathfrak{d}}(\mathfrak{d}_j)$ for $j = FF, IFF$ are well defined along with the space of approximate functions

$$\mathcal{U}_h(u) = \left\{ u \in H^1(\mathcal{B}) \,\middle|\, \nabla u \in L^2(\mathcal{B});\ u = u_d \,\text{on}\ \partial\mathcal{B}_d \right\}, \tag{3.19}$$

$$\mathcal{U}_{\mathfrak{d}}(\mathfrak{d}_j) = \left\{ \mathfrak{d}_j \in H^1(\mathcal{B}) \,\middle|\, \mathfrak{d}_j(\mathbf{x}) \in [0,1],\ \dot{\mathfrak{d}_j} \geq 0\ , \forall \mathbf{x} \in \mathcal{B} \right\} \tag{3.20}$$

Similarly, the approximate space for the test functions (distributional spaces) for $\delta\mathbf{u}^e \in \mathcal{V}_h$, $\delta\mathfrak{d}^e \in \mathcal{U}_{\delta\mathfrak{d}}(\mathfrak{d}_j)$ for $j = FF, IFF$ takes the form

$$\mathcal{V}_h(\delta u) = \left\{ \delta u \in H^1(\mathcal{B}) \,\middle|\, \nabla\delta u \in L^2(\mathcal{B});\ \delta u = 0 \,\text{on}\, \partial\mathcal{B}_d \right\}, \tag{3.21}$$

$$\mathcal{U}_{\delta\mathfrak{d}}(\delta\mathfrak{d}_j) = \left\{ \delta\mathfrak{d}_j \in H^1(\mathcal{B}) \,\middle|\, \delta\mathfrak{d}_j \geq 0\,, \forall \mathbf{x} \in \mathcal{B} \right\}. \tag{3.22}$$

At each element level, in the isoparametric space settings, the triplet of field variables $\{\mathbf{u}^e, \mathfrak{d}^e_{FF}, \mathfrak{d}^e_{IFF}\}$ as well as their variations $\{\delta\mathbf{u}^e, \delta\mathfrak{d}^e_{FF}, \delta\mathfrak{d}^e_{IFF}\}$ are approximated using linear first order Lagrangian triplet of shape functions $\left\{\mathbf{N}_i^u, \mathbf{N}_i^{\mathfrak{d}}, \mathbf{N}_i^{\mathfrak{d}}\right\}$ at i^{th} node of each element satisfying partition of unity is defined as

$$\mathbf{u}^e = \sum_{i=1}^{\mathbf{N}_{node}} \mathbf{N}_i^u \mathbf{u}_i^e, \qquad \mathfrak{d}_j^e = \sum_{i=1}^{\mathbf{N}_{node}} \mathbf{N}_i^{\mathfrak{d}} \mathfrak{d}_{j,i}^e,$$

$$\delta\mathbf{u}^e = \sum_{i=1}^{\mathbf{N}_{node}} \mathbf{N}_i^u \delta\mathbf{u}_i^e, \qquad \delta\mathfrak{d}_j^e = \sum_{i=1}^{\mathbf{N}_{node}} \mathbf{N}_i^{\mathfrak{d}} \delta\mathfrak{d}_{j,i}^e, \qquad \text{for each } j = FF, IFF.$$

The triplet of spatial derivatives $\{\nabla\mathbf{u}^e, \nabla\mathfrak{d}_{FF}^e, \nabla\mathfrak{d}_{IFF}^e\}$ are approximated using the gradients of the shape functions $\left\{\mathbf{B}_i^u, \mathbf{B}_i^{\mathfrak{d}}, \mathbf{B}_i^{\mathfrak{d}}\right\}$ at i^{th} node of each element takes the form

$$\boldsymbol{\varepsilon}^e = \sum_{i=1}^{\mathbf{N}_{node}} \mathbf{B}_i^u \mathbf{u}_i^e, \qquad \nabla\mathfrak{d}_j^e = \sum_{i=1}^{\mathbf{N}_{node}} \mathbf{B}_i^{\mathfrak{d}} \mathfrak{d}_{j,i}^e,$$

$$\delta\boldsymbol{\varepsilon}^e = \sum_{i=1}^{\mathbf{N}_{node}} \mathbf{B}_i^u \delta\mathbf{u}_i^e, \qquad \nabla\delta\mathfrak{d}_j^e = \sum_{i=1}^{\mathbf{N}_{node}} \mathbf{B}_i^{\mathfrak{d}} \delta\mathfrak{d}_{j,i}^e, \qquad \text{for each } j = FF, IFF.$$

Complying with the formulation of interface cohesive element, the displacement jump vector $\mathfrak{g}$ is represented in terms of local frames across the interface Γ_i [162]. Hence, the jump $\mathfrak{g}$ and its variation $\delta\mathfrak{g}$ is approximated using the kinematic jump-displacement operator $\mathbf{B}^{\mathfrak{g}} = R\mathbf{N}^{\mathfrak{g}}L$ as

$$\mathfrak{g}^e = \mathbf{B}^{\mathfrak{g}}\mathbf{u}^e L, \qquad \delta\mathfrak{g}^e = \mathbf{B}^{\mathfrak{g}}\delta\mathbf{u}^e L,$$

where L matrix estimates the difference between the displacement of the upper and lower interface points and R is a rotation matrix that converts integration points from global to the local frame, and $\mathbf{N}_{\mathfrak{g}}$ represents the standard cohesive shape function, see [143].

The discrete elemental residual vectors for the quadruplet $\{\mathbf{u}^e, \mathfrak{d}_{FF}^e, \mathfrak{d}_{IFF}^e, \mathfrak{g}^e\}$ can be reduced to the following system of equations

$$\begin{aligned}\mathbf{R}_e^{\mathbf{u}} = \int_{\mathcal{B}^e} \Big[(1-\mathfrak{d}_{FF})^2(\mathbf{B}^u)^T\bar{\boldsymbol{\sigma}}_{FF} + (1-\mathfrak{d}_{IFF})^2(\mathbf{B}^u)^T\bar{\boldsymbol{\sigma}}_{IFF}\Big]\,\mathrm{dV} \\ - \int_{\mathbf{B}^e} (\mathbf{N}^u)^T\mathbf{f}_v\mathrm{dV} - \int_{\partial\mathbf{B}_u^e} (\mathbf{N}^u)^T\overline{\mathbf{u}}\mathrm{dS} + \mathbf{R}_e^{\mathfrak{g}},\end{aligned} \tag{3.23}$$

$$\mathbf{R}_e^{\mathfrak{d}_{FF}} = \int_{\mathcal{B}^e} \left\{ \left[\frac{\mathcal{G}_{c,FF}}{l_{FF}}\mathfrak{d}_{FF} - 2(1-\mathfrak{d}_{FF})P_{FF}\mathcal{H}_{FF}(\mathbf{x},t)\right](\mathbf{N}^{\mathfrak{d}})^T + \mathcal{G}_{c,FF}l_{FF}(\mathbf{B}^{\mathfrak{d}})^T\nabla\mathfrak{d}_{FF}\right\}\mathrm{dV}, \tag{3.24}$$

$$\begin{aligned}\mathbf{R}_e^{\mathfrak{d}_{IFF}} = \int_{\mathcal{B}^e} \left[\frac{\mathcal{G}_{c,IFF}}{l_{IFF}}\mathfrak{d}_{IFF} - 2(1-\mathfrak{d}_{IFF})P_{IFF}\mathcal{H}_{IFF}(\mathbf{x},t)\right](\mathbf{N}^{\mathfrak{d}})^T + \\ \int_{\mathcal{B}^e} \left\{\mathcal{G}_{c,IFF}l_{IFF}(\mathbf{B}^{\mathfrak{d}})^T\nabla\mathfrak{d}_{IFF}\right\}\mathrm{dV}.\end{aligned} \tag{3.25}$$

where

$$\mathbf{R}_e^{\mathfrak{g}} = \int_{\Gamma_i^e} (\mathbf{R}\mathbf{B}^{\mathfrak{g}})^T \mathcal{T}(\mathfrak{g}, \mathfrak{d}_c)\mathrm{dS}, \tag{3.26}$$

is the residual vector associated with the cohesive interface. It is clear that the displacement field $\mathbf{u}$ is strongly coupled with the phase-fields $\mathfrak{d}_{FF}$, $\mathfrak{d}_{IFF}$ and the displacement jump $\mathfrak{g}$. Whereas, the phase-fields are among themselves and with jump $\mathfrak{g}$ are decoupled which are evident from Eq. (3.15), (3.16), (3.17) and from the assumption that $\Gamma_i \cap \Gamma_{\mathfrak{d}_t} = \emptyset$. Due to the existence of multiple phase-field and interface, the system of equations describing the fracture is non-linear. Hence, an iterative Newton-Raphson solver is used until the convergence in the sense of Cauchy sequence $[(\mathbf{u}_n^{t+1} - \mathbf{u}_n^t)]$ is reached. Here, $\mathbf{u}_n^t$ is the t^{th} iteration at n^{th} step. The corresponding Newton-Raphson iteration to estimate $(n+1)$ time step takes the form

$$\begin{bmatrix} \mathbf{u} \\ \mathfrak{d}_{FF} \\ \mathfrak{d}_{IFF} \end{bmatrix}_{n+1} = \begin{bmatrix} \mathbf{u} \\ \mathfrak{d}_{FF} \\ \mathfrak{d}_{IFF} \end{bmatrix}_{n} - \begin{bmatrix} K^{\mathbf{uu}} + K^{\mathfrak{g}\mathfrak{g}} & 0 & 0 \\ 0 & K^{\mathfrak{d}_{FF}\mathfrak{d}_{FF}} & 0 \\ 0 & 0 & K^{\mathfrak{d}_{IFF}\mathfrak{d}_{IFF}} \end{bmatrix}_{n+1}^{-1} \begin{bmatrix} \mathbf{R}^{\mathbf{u}} \\ \mathbf{R}^{\mathfrak{d}_{\mathbf{FF}}} \\ \mathbf{R}^{\mathfrak{d}_{\mathbf{IFF}}} \end{bmatrix}_{n}. \tag{3.27}$$

where the corresponding element stiffness matrices read

$$\mathcal{K}_e^{\mathbf{uu}} := \frac{\partial \mathcal{R}_e^{\mathbf{u}}}{\partial \mathbf{u}^e} = \int_{\mathcal{B}^e} (\mathbf{B}^u)^T \mathbb{C}^{ep\mathfrak{d}} \mathbf{B}^u \mathrm{dV}, \tag{3.28}$$

$$\mathcal{K}_e^{\mathfrak{g}\mathfrak{g}} := \frac{\partial \mathcal{R}_e^{\mathfrak{g}}}{\partial \mathbf{u}^e} = \int_{\Gamma_i^e} (\mathbf{B}^{\mathfrak{g}})^T \partial_{\mathfrak{g}} \tau \mathbf{B}^{\mathfrak{g}} \mathrm{dS},$$

$$\mathcal{K}_e^{\mathfrak{d}_{FF}\mathfrak{d}_{FF}} := \frac{\partial \mathcal{R}_e^{\mathfrak{d}_{FF}}}{\partial \mathfrak{d}_{FF}^e} = \int_{\mathcal{B}^e} \left[\frac{\mathcal{G}_{c,FF}}{l_{FF}} + 2\mathfrak{P}_{FF}\mathcal{H}_{IFF} \right] \mathbf{N}^{\mathfrak{d}} (\mathbf{N}^{\mathfrak{d}})^T + \mathcal{G}_{c,FF} l_{FF} (\mathbf{B}^{\mathfrak{d}})^T \mathbf{B}^{\mathfrak{d}} \mathrm{dV}, \tag{3.29}$$

$$\mathcal{K}_e^{\mathfrak{d}_{IFF}\mathfrak{d}_{IFF}} := \frac{\partial \mathcal{R}_e^{\mathfrak{d}_{IFF}}}{\partial \mathfrak{d}_{IFF}^e} = \int_{\mathcal{B}^e} \left[\frac{\mathcal{G}_{c,IFF}}{l_{IFF}} + 2\mathfrak{P}_{IFF}\mathcal{H}_{IFF} \right] \mathbf{N}^{\mathfrak{d}} (\mathbf{N}^{\mathfrak{d}})^T + \mathcal{G}_{c,IFF} l_{IFF} (\mathbf{B}^{\mathfrak{d}})^T \mathbf{B}^{\mathfrak{d}} \mathrm{dV}. \tag{3.30}$$

In the Eq. (3.28), $\mathbb{C}^{ep\mathfrak{d}}$ represents the material consistent tangent estimated using the finite difference method as

$$\mathbb{C}^{ep\mathfrak{d}} = \frac{d\boldsymbol{\sigma_{ij}}}{d\boldsymbol{\varepsilon}_{kl}} \approx \frac{\boldsymbol{\sigma_{ij}}(\hat{\varepsilon}^{kl}) - \boldsymbol{\sigma_{ij}}(\hat{\varepsilon})}{\Delta\varepsilon},$$

with $(\hat{\boldsymbol{\varepsilon}}^{kl}) = \varepsilon + \dfrac{\Delta\boldsymbol{\varepsilon}}{2}(e_k \otimes e_l + e_l \otimes e_k) = \boldsymbol{\varepsilon} + \Delta\boldsymbol{\varepsilon}^{kl}$. Here e_k and e_l are the k^{th} and l^{th} unit vectors, $\Delta\boldsymbol{\varepsilon}^{kl}$ is the strain perturbation with respect to the components kl and $\Delta\boldsymbol{\varepsilon}$ is the scalar perturbation parameter. Moreover, $\boldsymbol{\sigma}$ is estimated from Eq. (3.7) as $\boldsymbol{\sigma} = \mathbb{C} : \boldsymbol{\varepsilon}$.

The previous non-linear system of equations has been implemented in the finite element software `ABAQUS`. For this purpose, a user-defined `UMAT` to define the material behaviour is written for the solution of equilibrium equations associated with the displacement field. Whereas, `UEL` is utilized to create residual and stiffness matrix for each of the two phase-fields using the material behaviour from `UMAT` for solving the fracture-associated problem.

3.5 Virtual testing

In this section, modeling application to delamination migration is presented. A comprehensive numerical analysis is presented to validate the model against experimental results. In the sequel, a holistic sensitivity analysis is carried out utilizing the variation of the loading application point, ply angle, and initial pre-crack length to understand their effects on delamination migration.

3.5.1 Description of the numerical model

Fig. 21 depicts the baseline configuration under investigation herein. The corresponding numerical model consists of 44 cross-ply IM7/8552 laminates with the layup sequence $[90^\circ_4/0^\circ_3/(90^\circ/0^\circ)_{2s}/0^\circ_3/CL/90^\circ_4/CL/0^\circ/0^\circ/(90^\circ/0^\circ)_{2s}/0^\circ/0^\circ/90^\circ_3/0^\circ/90^\circ]$, where CL refers to a cohesive layer. Each ply has a thickness of 0.125mm. Compared with the experimental sequence as in [145], a PTFE (Polytetrafluoroethylene) layer is replaced by a cohesive layer and in addition, another cohesive layer is added at the interface between the 90°_4 and 0° sequence in order to account for delamination migration.

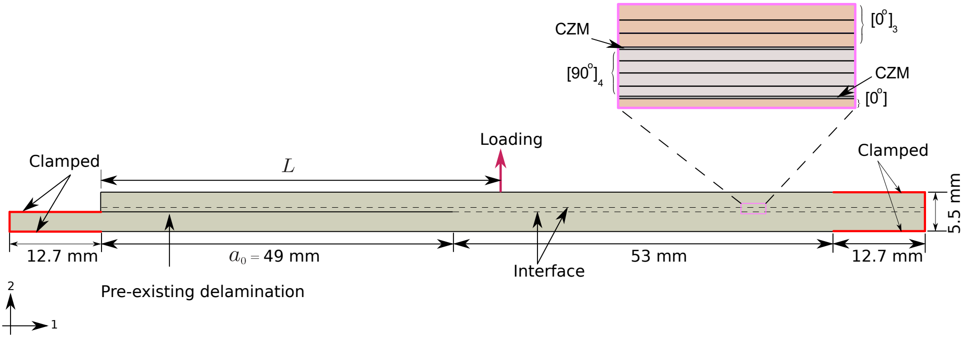

Figure 21: Schematic representation of the delamination migration model.

It is evident from the experimental results reported in [146] that, when shear stresses in the model change sign, migration/kinking occurs, and the crack propagates to the 90°_4 layers facilitating the inter-fiber failure.

For each of the numerical simulations conducted in the sequel, a 2D analysis is carried with an out-of-plane thickness of 8.37mm. Since, in order to resolve the gradient of the phase field, the mesh size $\bar{h}$ is restricted to $\bar{h} \approx l/4$. Hence, the domain is discretized by employing 960000 4-node quadrilateral plane stress elements with an average element size of 0.04mm. Each layer of the cross-ply contains at least four elements across its thickness.

The material properties of IM7/8552 ply are shown in Tab. 5 consistent with the experimental results in [145]. The fracture energy and length scale parameters for the phase-fields chosen according to the material fracture properties are shown in Tab. 6. The properties of the cohesive layer following [156] are listed in Tab. 10.

E_{11} (GPa)	E_{22} (GPa)	G_{12} (GPa)	ν_{12}	ν_{23}
161.0	11.38	5.17	0.03	0.43

Table 5: IM7/8552: Elastic properties.

$\mathcal{G}_{c,FF}$ (N/mm)	$\mathcal{G}_{c,IFF}$ (N/mm)	l_{FF} (mm)	l_{IFF} (mm)
81.5	0.2774	0.237	0.07

Table 6: IM7/8552: intra-laminar fracture properties and phase-field parameters.

Nominal stress (MPa)	Nominal stress in shear (MPa)	Nominal fracture energy (N/mm)	Fracture energy in shear (N/mm)	Power (BK law)
15	15	0.5	0.65	2.17

Table 7: Cohesive layer properties.

3.5.2 Model validation

The global failure response for the specimen under consideration is investigated for the load case $L = a_0 = 49$mm. The numerical-experimental correlation corresponding to the load-displacement curve is given in Fig. 22. As shown in this figure, the failure response can reasonably be divided into three main zones: (i) delamination of the cohesive zone, (ii) kinking followed by migration, and (iii) delamination of the top cohesive zone. Overall, a satisfactory agreement between the numerical and the experimental data can be observed.

As was previously discussed, based on postulations made in [145, 146] and the corresponding thorough discussion, delamination migration occurs due to a change of sign in the shear stress components. Negative shearing stresses promote delamination growth at the $0^\circ/90^\circ$ interface, and positive shearing stresses promote migration/kinking into 90° plies. The kinking happens at multiple sites across the specimen. Due to the diffusive nature of the bulk cracks, the shearing stress change can easily be noticed by the inter-fiber phase-field initiation as depicted in Fig. 23. Notice that, due to the negative sign initially, delamination propagates until a certain point until shearing stresses are positive. Meanwhile, inter-fiber failure is already initiated, but from the opposite direction, i.e., $90^\circ/0^\circ$ interface, but is not nucleated. Whereas, when the shear stresses become positive in the adjacent increments, the migration starts developing, with a crack front now migrating into the $90^\circ/0^\circ$ interface.

For a phenomenology of embodiment, in the cohesive layers, once the failure criterion is met, the cohesive layer starts delaminating. Similarly, when the Puck criterion is violated, the inter-fiber failure phase-field is activated due to shearing stresses in the model. As long as the P_{IFF} is active, the inter-fiber failure phase-field crack $\mathfrak{d}_{IFF}$ grows and migrates into the 90°

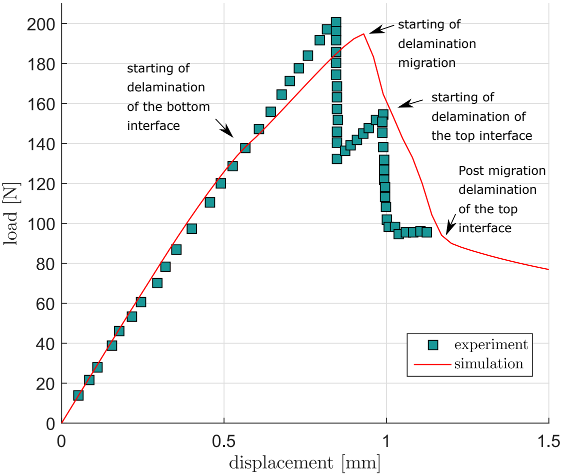

Figure 22: Numerical-experimental correlation corresponding to the load-displacement curve for $L = a_0$=49 mm.

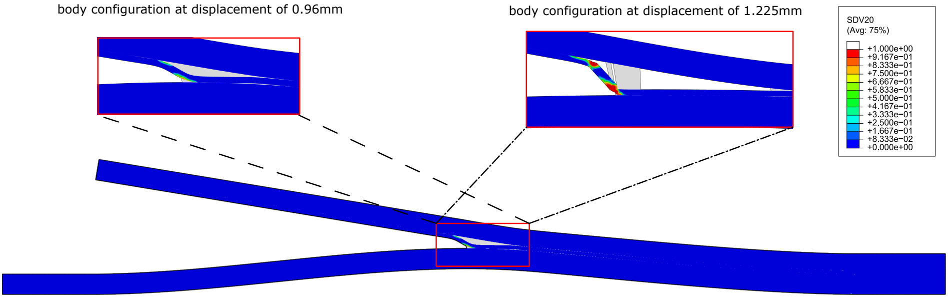

Figure 23: Phase-field indicating delamination migration

plies until the $90^\circ/0^\circ$ interface. Simultaneously, the top cohesive layer at the $90^\circ/0^\circ$ interface starts to delaminate. When the migration crack front crosses the $90^\circ/0^\circ$ interface, the crack front is again propagating due to the negative shear stress leading to the delamination of the top cohesive layer. Here onward, the residual stresses dominate crack propagation in the model as in Fig. 22. The discrepancies between the experimental and numerical results can be attributed to quasi-static load conditions and smooth initiation and propagation of phase-field approximations. However, a satisfactory agreement between the results can be observed.

3.5.3 Sensitivity analysis

This section aims at proving a further understanding with regard to the potential role of different design parameters that can favor delamination-migration events.

Effect of position of loading application

The first aspect under analysis concerns the variation of load application point along the specimen. This parameter in the experimental setting might have a strong influence on the activation of migration phenomena by simply inducing a different local stress field at critical locations. Moreover, from a global standpoint, this can have notable effects on the load-displacement curve as the shear stresses acting on the specimen are significantly different from one another. Keeping $a_0 = 49$ mm, the variation of load L for $L = 0.7a_0$, $0.8a_0$, $0.9a_0$, $1.0a_0$, $1.1a_0$ are plotted in Fig. 24.

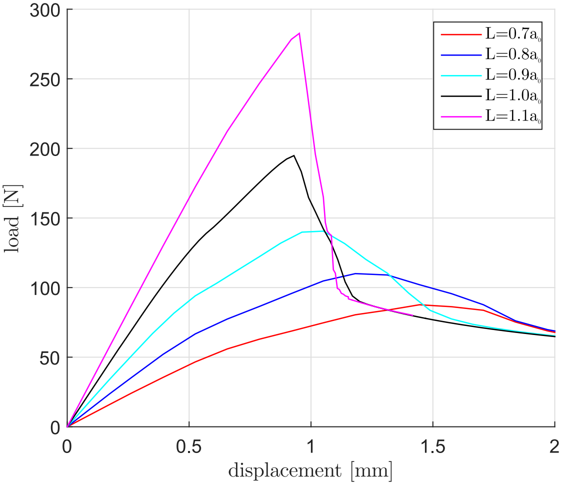

Figure 24: Variation of load across the specimen for $a_0 = 49$mm.

Based on the current results, it can be observed that for $a_0 > L$, all the cases exhibit delamination prior to migration and show a sudden drop in the load-carrying capacity when migration starts, see Fig. 25. Whereas, for $a_0 < L$, the shearing stress sign is favorable for migration at the beginning, and hence there is smooth migration, with delamination spreading over the whole experiment, see Fig. 25 which is consistent with [146]. It is also to notice that after delamination migration is finished, the residual stiffness for delamination converges to a single value for all the load variations.

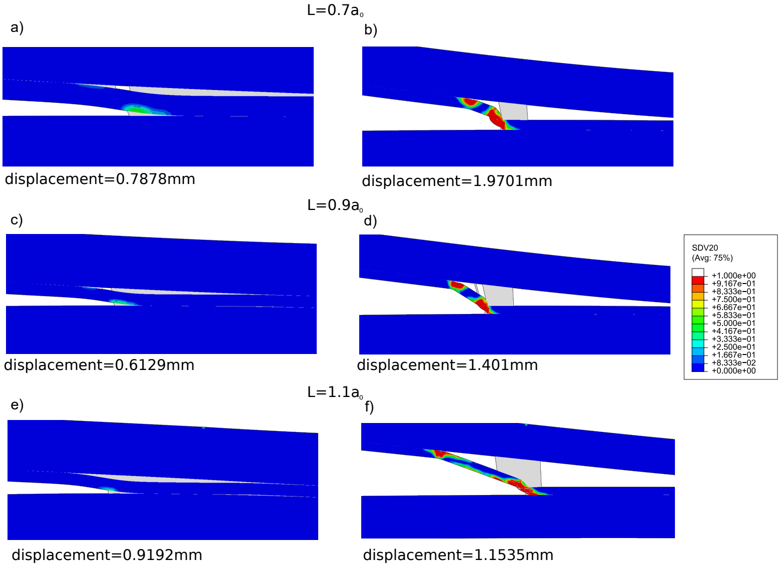

Figure 25: Inter-fiber crack field (SDV20) from 3 cases at $L = 0.7a_0$, $L = 0.9a_0$, $L = 1.1a_0$.

Effect of the variation of ply angle

The second aspect understudy has an inherent local effect since it focused on investigating the delamination migration at $0^\circ/\theta^\circ_4$ interface. For this purpose, the original stacking sequence is replaced by a new layup sequence near the cohesive zones as $0^\circ_3/CL/\theta^\circ_4/CL/0^\circ/0^\circ$. The fiber orientation, θ° of 30°, 45°, and 60° is studied along with 90°, and the results are shown in Fig. 26.

From this graph, it can be seen that the global pre-peak response is almost unaltered by the variation of the local orientation of the adjacent layers to the $0^\circ/\theta^\circ_4$ interface. However, this aspect has a notable influence on the post-peak response, delaying the delamination initiation and the subsequent delamination event of the top interface, according to the description given in Fig. 23, but however, the cracking migration is predicted to occur at almost the same loading level (along the post-peak evolution).

Effect of the variation of initial crack length

The last effect under consideration corresponds to the initial crack length. Focusing on very specific cases, we vary initial crack size from $a_0 = 49$ mm to $a_0 = 55$ mm.

The global load-displacement evolution curves for such cases are shown in Fig. 27. According to these data, it can be stated that a simple variation of the initial crack length has a very remarkable role in the specimen response. Thus, observing the pre-peak evolution, before any inelastic process commences, the large the initial crack length is set, the higher

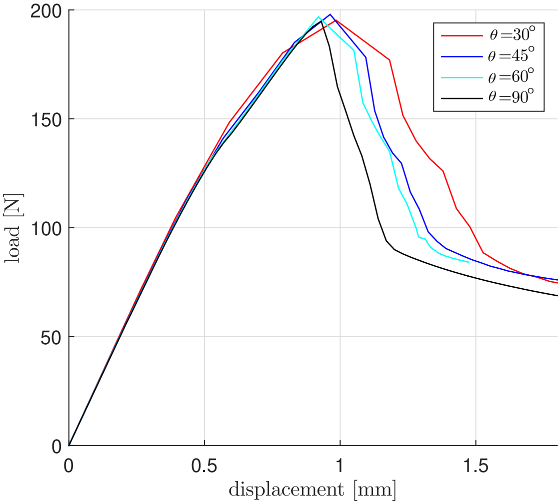

Figure 26: Variation of angle across the specimen for $L = a_0 = 49$mm.

the maximum load is achieved. Moreover, concerning the post-peak evolution, it is observable that while the shorter initial crack-length case evidence similar evolution with respect to those previously described, i.e., with the occurrence of delamination events and the posterior cracking migration to the adjacent layer, the response of $a_0 = 55$mm (and $a_0 > 55$mm) exhibited an entirely different evolution with no evidence of cracking migration, see Fig. 27, and 28 where the matrix-failure maps for both configurations are depicted. These differences in the response are directly associated with the local stress state's discrepancies at the crack tips at the interface and the intermediate layer. This is again in line with previous studies as in [146, 145].

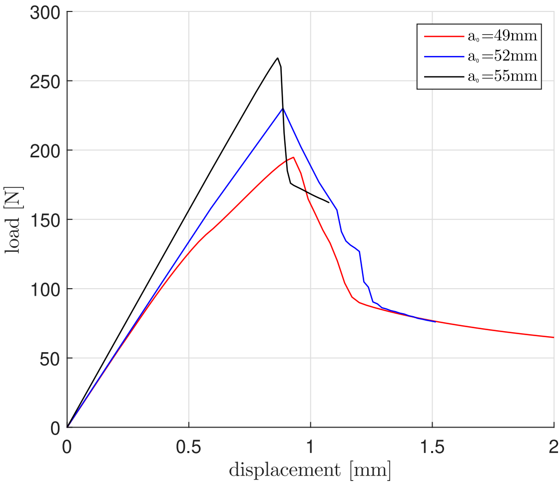

Figure 27: Variation of initial crack length across the specimen for $L = a_0$.

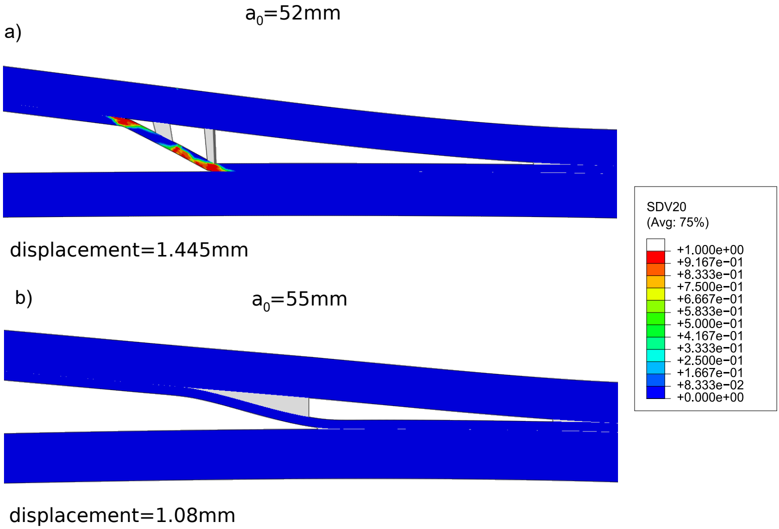

Figure 28: Inter-fiber crack field (SDV20) for initial crack length $a_0 = 52$mm, $a_0 = 55$mm with $L = 1.0a_0$.

Chapter 4

Nonlinear thermoelastic phase-field fracture for thin-walled structures relying on solid shell concepts

This chapter is mainly taken from [169, 170, 171]. With the aim of achieving reliable prediction of temperature-driven failures in thin-walled structures, this chapter is concerned with the development of a thermodynamically consistent framework for the coupled thermo-mechanical phase-field model for thin-walled structures using fully-integrated finite elements. This enables the use of three-dimensional constitutive thermo-mechanical models for the materials. The proposed thermo-mechanical phase-field models are equipped with the Enhanced Assumed Strain (EAS) to alleviate Poison and volumetric locking pathologies. This technique is further combined with the Assumed Natural Strain (ANS) method leading to a locking-free thermo-mechanical solid shell phase-field element. Special attention is also paid to evaluating the corresponding thermodynamic consistency and the variational formalism leading to the nonlinear coupled equations equipped with the coupled driving force. Moreover, the same degradation function is used for both displacement and thermal fields. The coupled equations are numerically solved with ad hoc efficient solution schemes for nonlinear problems.

The investigation is mainly categorized into three parts

1. Nonlinear thermoelastic analysis of thin walled structures combined with cohesive-like interfaces [169].
2. Nonlinear thermoelastic phase-field analysis [170].
3. Non-linear thermoelastic phase field analysis: Extension to Functionally Graded materials [171].

This chapter is organized as follows. Section 4.1 provides the general introduction of solid shells, the different models in the literature and throw some light on the thermo-mechanical formulations and non-linearity. A general mathematical formulation thermo-dynamically consistent framework to study coupled thermo-mechanical phase-field model for thin-walled structures using a fully integrated finite element is presented. Section 4.2 presents the fundamental concepts of coupled thermoelastic analysis along with the definition of the constitutive formulation herewith considered. Section 4.3 presents the variational formulation of the system as a minimization problem, finite element approximation of the problem, along with the linearization principles leading to a system of linear equations. In this regard, the Hu-Washizu principle is adopted for removing the locking pathologies through EAS and ANS methods. The weak form of the balance equations and the variational that leads to the corresponding finite element discretization is given in Section 4.3.1. The computational techniques employed for tackling the different locking pathologies, namely the EAS and the ANS methods, are covered in Section 4.3.3. Finally, Numerical examples for each of the analyses, as mentioned earlier is provided as the subclass of the presented formulation as

1. Section 4.4 provides the example with phase-field zero everywhere. This formulation is combined with a thermo-mechanical cohesive zone model. Comparison between the `ABAQUS` SC8RT element and the current formulation (with $\mathfrak{d} = 0$ everywhere) is made against the second Danilovskaya problem to ensure the validation of the current model. The response of this element is further examined in the application of a thin bar subjected to bending, crushing, and lifting and an annular ring subjected to line force to highlight the locking free capabilities of the thermo-mechanical solid shell (without interface). Several representative numerical examples are presented to establish the predictive capability of the current framework.

2. Section 4.5 provides the numerical examples of the formulation in the presence of phase-field. First, a benchmark test is proposed and passed. Then, problems characterized by temperature-assisted fracture are examined in relation to a technological phenomenon relevant for silicon solar cells. Finally, examples concerning coupled mechanical-temperature effects for small and large strain problems are shown for a series of structural issues with straight and curved shells.

3. Section 4.6 provides the extension of the formulation to accommodate FGM. First, the model is verified via a standard benchmark test. Using numerous examples of straight and curved beams, the effect of grading in terms of crack path and load-bearing capacity is explored thoroughly. Moreover, the thermo-mechanical interactions in the FGM are compared against the homogeneous materials. The effect of temperature on the load-bearing capacity of the FGM is pinpointed. The impact of material properties such as Young's modulus, thermal conductivity, fracture energy on the FGM performance is explored using three different FGM pairs (metal-metal, ceramic-ceramic, ceramic-polymer). The model is then modified to accommodate a three-phase/ double FGM, and their thermo-elastic behavior is explored.

4.1 Introduction

Engineering systems such as aircraft (fuselages, wings), automotive chassis, renewable energy (wind turbines, turbine/compressor blades, photovoltaic laminates [172, 173, 174, 175, 176], electronic systems [177, 178] (chips, laptop panels, screen, and protectors), thermal barrier coatings [179] are all based on thin-walled structures. Thermal interactions and the load-bearing capacity of these thin-walled structures are key aspects and thus regulate the design, analysis, and production of their engineering components. Due to intricate geometrical definitions, the use of analytical methods is rather limited and mostly confined to simplified scenarios. Therefore, numerical methods lead to a more general and versatile range of analysis.

The related literature regarding the computational procedures for triggering fracture in shell structures can be classified into 4 different categories:

1. Meshless crack approaches based on the partition of unity methods [180].
2. Discrete crack methods such as XFEM (eXtended FEM) [181, 182, 183, 184], phantom node models [185], meshless methods [186, 187], among many others, that were applied to thin walled structures based on classical shell theories such as Kirchhoff-Love [188, 189, 190, 191] (3 parameters), Reissner-Mindlin (5-parameters) [181, 183] and geometrically nonlinear continuum shell [192] for their kinematic description.
3. Cohesive zone models [193, 194, 195, 196] implemented via interface elements.
4. Continuum-based methods such as non-local or gradient enhanced damage approaches [197, 198, 7, 199], which use constitutive equations at the material point level describing damage in the bulk.

Within this context, it is worth mentioning that methodologies falling into the previous categories (1.), (2.) and (3.) generally require ad-hoc criteria for their initiation and propagation of the crack, and often it is necessary to know the crack path a priori. This issue can be circumvented via the exploitation of a new continuum-based technique denominated as the phase field (PF) approach of fracture due to its inherent incorporation of an evolution equation for the scalar-valued function for triggering stiffness degradation within the bulk.

Modeling thermo-mechanical effects in thin-walled structures necessitates the development of a consistent formulation that accounts for the coupled effects of the thermal and mechanical fields, as well as stress transfer and heat conduction across the internal interfaces. In this context, recent advances in shell modeling aim at incorporating three-dimensional effects into the corresponding numerical simulation, being possible the use of unmodified constitutive laws in the corresponding computations without further modifications. To do so, it has been amply addressed the necessity of developing shell models that embody at least a linear normal strain distribution along the thickness direction [200]. In the related literature, two main paths have been followed:

1. Shell formulations which model the reference surface of the body and include the previous linear distribution using either an enhancing strain method or a quadratic displacement distribution in thickness direction [201, 202, 203, 204, 205, 206, 207, 208].
2. Shell models relying on the so-called solid shell concept, which make use of the parametrization of the top and the bottom surfaces of the body [209, 210, 205, 207, 211].

This idea in (2.) has been extensively developed over the least years due to the complete avoidance of complex update procedure associated with the rotational tensor. However, up to now, the extension of shell models for coupled thermo-mechanical applications under large strains has been received a limited attention, see [202, 212, 213, 214, 215] for alternative formulations. Furthermore, finite element formulations of shells complying with a low-order of kinematic interpolation generally suffer from locking pathologies , which should be numerically alleviated. For this purpose, several numerical strategies have been proposed such as Reduced Integration (RI) schemes, the popular Enhanced Assumed Strain (EAS) [214, 216, 217, 218, 219] and the Assumed Natural Strain (ANS) [220, 221] methods, or combination of them [222, 223, 224]. Note also that these techniques have been accordingly employed in coupled the thermo-mechanical applications, see [225] and the references therein given.

Regarding the thermo-mechanical coupling, recently, R. G. Tangella et al [226] proposed the hybrid phase-field model to predict complex crack paths in quasi-static thermo-elastic brittle fracture. H. Badnava et al [227] suggested an h-adaptive thermo-mechanical phase-field model, T.-T. Nguyen et al [93] postulated the chemo-thermo-mechanical coupling for the phase-field to predict early age shrinkage in cement-based materials, whereas A. Dean at al [228, 229] proposed invariant-based anisotropic material models for short fiber-reinforced thermoplastics, to name a few of recent contributions. On the other hand, W. Shu et al [230] proposed a thermo-mechanical solid shell for reduced integration and with the Enhanced Assumed Strain (EAS) and Assumed Natural Strain (ANS) methods to avoid hourglass locking [230], and P.K.Asur Vijaya Kumar et al [231] proposed a thermo-mechanical solid shell formulation for geometric non-linearity having full integration, incorporating EAS and ANS methods to alleviate the locking pathologies. However, at present, the application of the PF approach of fracture to thermo-mechanical analysis of thin-walled structures relying on the solid shell concept is largely unexplored.

Different Cohesive Zone Models (CZM) were developed for engineering applications, mainly dealing with the fracture and delamination process. In the literature, there exist a wide variety of typologies of CZMs in line with the Kyoungsoo Park et al [232] can be arranged in (i) potential-derived laws and (ii) non-potential-derived laws. The difference between them lies in the constitutive response. On the one hand, potential-derived laws use fracture energy potential and whose derivatives with respect to displacement provide the traction vector, and their second derivative provides the constitutive tensor. On the other hand, non-potential derived models endow a comparative simplicity, where cohesive tractions are defined through the traction separation laws (constitutive relation between tractions and opening displacement vector), which are widely used. Some widely used examples of non-potential-based cohesive laws can be broadly categorized as (a) piece-wise linear cohesive laws, (b) trapezoidal cohesive laws, and (c) exponential cohesive laws are studied with great attention in the past few years. Tvergaad [233] introduces the notion of the mixed-mode fracture to separate the tangential and normal directions, Ortiz and Pandolfi [234] introduced the idea of reference mid surface. Recently, many authors have proposed the extension of cohesive zone models to thermoelastic material models. See, eg [235, 236, 237, 238] and the reference therein. Balzano and Wagner [239] modified the work of [234] to cover the compressive behavior in mode one. The effects of large displacements have been investigated in [240].

This work presents phase-field modeling of fracture fully coupled with thermo-mechanics for the failure analysis of thin-walled structures using the solid shell concept. In order to avoid the complex update of rotational tensor, the shell model presented exploits the solid shell concept aforementioned which parametrizes the top and bottom surface of the body [209, 210, 205, 207, 211]. By the virtue of this kinematic description, the solid shell approach features a discretization identical to that of 8 node brick element [210, 241, 242]. Within this framework, three-dimensional constitutive equations (such as) thermo-elastic Kirchhoff-Saint-Venant Material Model is considered and extended to accommodate phase-field degradation. Moreover, the elastic energy and the thermal energy are degraded using the same phase-field degradation function. The potential locking pathologies arising due to the intrinsic nature of a shell complying with lower-order kinematic displacement interpolation schemes is alleviated by the combination of EAS and ANS methods, in line with the advanced shell formulations discussed in [225, 222, 223, 224]. Hence, the volumetric and the Poisson's thickness locking effects are alleviated by EAS, whereas trapezoidal and transverse shear locking are alleviated using the ANS method. Furthermore, a fully coupled scheme between the phase-field and the mixed finite element formulation (particularly EAS) is accordingly condensed using static condensation of the enhancing strain at the element level [218] such that the original coupling is fully preserved.

4.2 Coupled thermo-mechanical formulation

The initial boundary value problem (IBVP) for coupled thermo mechanical solid shell with phase-field damage is characterised by: (i) the deformation field of the solid shell, (ii) the temperature field, and (iii) the scalar valued phase-field variable. In the sequel, the basic aspects and definitions are introduced for the sake of clarity.

4.2.1 Primary fields

Let $\mathcal{B}_0 \subset \mathbb{R}^{n_{dim}}$ denote a reference configuration of a continuum body in n_{dim} Euclidean space with its delimiting boundary $\partial\mathcal{B}_0 \subset \mathbb{R}^{n_{dim}-1}$. For every position vector $\mathbf{X} \in \mathcal{B}_0$, define the vector valued displacement field $\mathbf{u}(\mathbf{X}, t) : \mathcal{B}_0 \times [0, t] \to \mathbb{R}^3$, the smooth scalar valued temperature $T(\mathbf{X}, t) : \mathcal{B}_0 \times [0, t] \to \mathbb{R}_+$, and a smooth scalar valued function of damage (phase-field) $\mathfrak{d}(\mathbf{X}, t) : \mathcal{B}_0 \times [0, t] \to [0, 1]$, for time interval $[0, t]$, here $\mathfrak{d} = 0$ refers to intact material and $\mathfrak{d} = 1$ refers to a cracked material.

The fields in the reference configurations are assumed to be a consequence of prescribed: (i) displacement $\mathbf{u} = \bar{\mathbf{u}}$ on $\partial\mathcal{B}_{0,u}$, (ii) traction $\bar{\mathbf{t}} = \boldsymbol{\sigma} \cdot \mathbf{n}(\mathbf{X}, t)$ on $\partial\mathcal{B}_{0,\bar{t}}$ for the Cauchy stress $\boldsymbol{\sigma}$ and outwards normal $\mathbf{n}$, (iii) temperature T_0 on $\partial\mathcal{B}_{0,T}$, and (iv) heat flux vector $\boldsymbol{Q}_N$ on $\partial\mathcal{B}_{0,q}$ such that $\partial\mathcal{B}_0 = \overline{\partial\mathcal{B}_{0,u} \cup \partial\mathcal{B}_{0,\bar{t}} \cup \partial\mathcal{B}_{0,T} \cup \partial\mathcal{B}_{0,q}}$ and $\partial\mathcal{B}_{0,u} \cap \partial\mathcal{B}_{0,\bar{t}} = \emptyset$, $\partial\mathcal{B}_{0,T} \cap \partial\mathcal{B}_{0,q} = \emptyset$ as in Fig. 29.

For generalization purpose, $\mathcal{B}_0$ can be subdivided into $\mathcal{B}_0^i (i > 0)$, such that $\mathcal{B}_0 = \cup_i \mathcal{B}_0^i$. Each $\mathcal{B}_0^i$ is allowed to have different constitutive relationships that characterize their mechanical, fracture and thermal behaviour. The Γ_{int} characterises the presence of cohesive surface such that $\partial\mathcal{B}_0 = \cup_i \overline{\partial\mathcal{B}_{0,u}^i \cup \partial\mathcal{B}_{0,\bar{t}}^i \cup \partial\mathcal{B}_{0,T}^i \cup \partial\mathcal{B}_{0,q}^i \cup \Gamma_{int}^i}$, see Fig 29.

Define a single valued continuously differentiable function $\boldsymbol{\varphi}(\mathbf{X}, t) \in \mathcal{V}$ that maps the reference material point $\mathbf{X} \in \mathcal{B}_0$ onto the current reference configuration point $\mathbf{x} \in \mathcal{B}_t$, such that $\mathbf{x} = \boldsymbol{\varphi}(\mathbf{X}, t) = \mathbf{X} + \mathbf{u}(\mathbf{X}, t)$ for each time instant t throughout the deformation process.

Here $\mathcal{V}$ is a space of admissible functions defined as

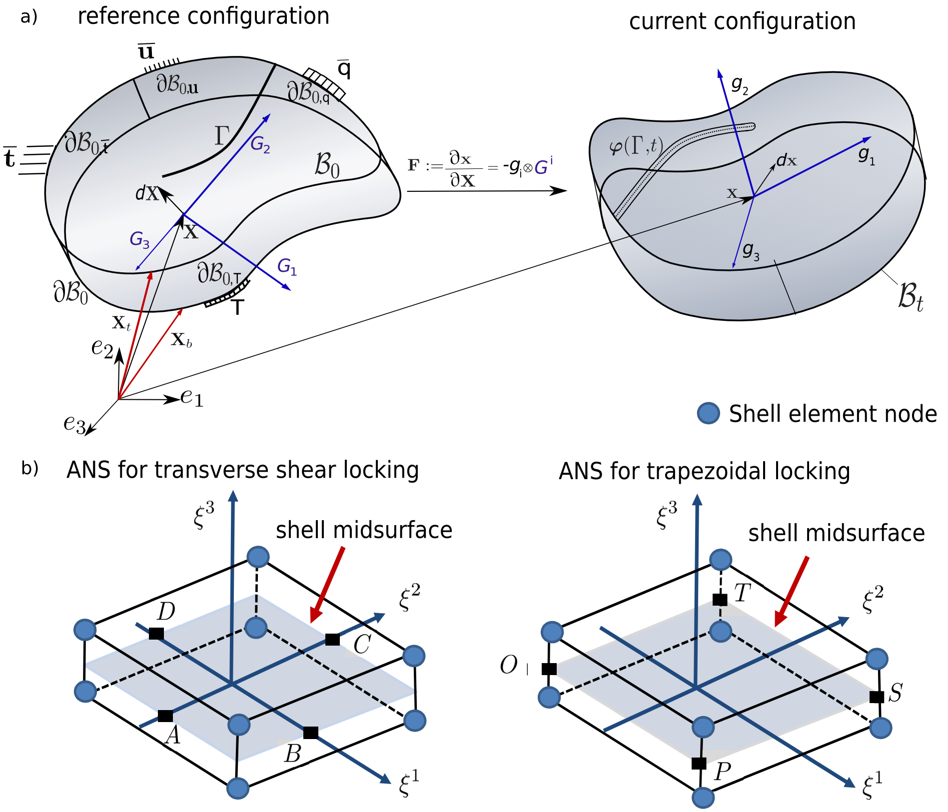

Figure 29: Finite deformation of a body: reference and current configurations. Deformation mapping $\varphi(\mathbf{X}, t)$, that transforms at time t the reference configuration $\mathcal{B}_0$ onto the current configuration $\mathcal{B}_t$, and the displacement-derived deformation gradient $\mathbf{F}^u := \partial_{\mathbf{X}}\varphi(\mathbf{X}, t)$.

$$\mathcal{V} = \left\{ \varphi : \mathcal{B}_0 \times [0,t] \to \mathbb{R}^{n_{dim}} | \varphi \in W^{1,p}(\mathcal{B}_0) \quad \text{and} \quad \varphi = \bar{\varphi} \quad \text{on} \quad \partial\mathbb{R}_u \quad \text{for} \;\; p \geq 2 \right\}.$$

A key kinematic quantity is the deformation gradient (derived from the displacement field), which is defined as gradient of the non-linear deformation map with respect to reference setting

$$\mathbf{F}^u := \partial_{\mathbf{X}} \boldsymbol{\varphi}(\mathbf{X}, t) = \nabla_{\mathbf{X}} \boldsymbol{\varphi}(\mathbf{X}, t) = 1 + \nabla \mathbf{u} = \frac{\partial \mathbf{x}}{\partial \mathbf{X}} \in \mathbb{R}^{n_{dim} \times n_{dim}}.$$

This operator represents a linear map between the unit reference line elements $d\mathbf{X}$ onto the current line elements $d\mathbf{x} = \mathbf{F}^u d\mathbf{X}$. In the following derivations $\nabla_{\mathbf{X}}[\bullet]$ and $\nabla_{\mathbf{x}}[\bullet]$ denote the Lagrangian and Eulerian gradient operators, respectively. The Jacobian of the transformation $\mathbf{F}^u$ satisfies

$$J^u := \det[\mathbf{F}^u] > 0.$$

where $\det[\cdot]$ stands for dominant operator.

The co-variant basis as in Fig. 29 in reference ($\mathbf{G}_i$) and the current configurations ($\mathbf{g}_i$) are defined as

$$\mathbf{G_i}(\xi) := \frac{\partial \mathbf{X}(\xi)}{\partial \xi^i}; \quad \mathbf{g_i}(\xi) := \frac{\partial \mathbf{x}(\xi)}{\partial \xi^i}, \qquad i = \{1, 2, 3\}.$$

The dual and contravariant base vector satisfy the following standard relations

$$\mathbf{G}_i \mathbf{G}^j = \delta_i^j; \qquad \mathbf{g}_i \mathbf{g}^j = \delta_i^j.$$

Then the metric tensor now takes the form in reference configuration

$$\mathbf{G} = G_{ij} \mathbf{G}^i \otimes \mathbf{G}^j = G^{ij} \mathbf{G}_i \otimes \mathbf{G}_j,$$

and in the reference configuration

$$\mathbf{g} = g_{ij} \mathbf{g}^i \otimes \mathbf{g}^j = g^{ij} \mathbf{g}_i \otimes \mathbf{g}_j.$$

Here, $\mathbf{G}^i$ and $\mathbf{g}^i$ are contravariant basis in reference and current configuration. With this at hand, the displacement-derived deformation gradient $\mathbf{F}^u$ in the curvilinear setting reads

$$\mathbf{F}^u := \mathbf{g}_i \otimes \mathbf{G}^i.$$

Furthermore, the displacement-derived left $\mathbf{C}^u$ Cauchy-Green deformation tensor takes the form

$$\mathbf{C}^u := [\mathbf{F}^u]^{\mathrm{T}} \mathbf{g} [\mathbf{F}^u] = g_{ij} \mathbf{G}^i \otimes \mathbf{G}^j,$$

whereas the displacement-derived Green-Lagrangian strain tensor takes the form

$$\mathbf{E}^u := \frac{1}{2} \left[\mathbf{C}^u - \mathbf{G} \right] = \frac{1}{2} \left[g_{ij} - G_{ij} \right] \mathbf{G}^i \otimes \mathbf{G}^j.$$

To avoid locking pathologies, the displacement derived Green-Lagrangian strain tensor is enhanced by the considering incompatible Green-Lagrangian tensor $\tilde{\mathbf{E}}$. This is achieved by additive decomposition of the total Green-Lagrangian strain tensor which constitutes the central idea of EAS, in line with [214], as

$$\mathbf{E} := \mathbf{E}^u + \tilde{\mathbf{E}}. \tag{4.1}$$

Consequently, the enhanced right Cauchy-Green tensor $\mathbf{C}$ is modified to accommodate the total Green-Lagrangian strain tensor and it takes the form

$$\mathbf{C} := \mathbf{C}^u + \tilde{\mathbf{C}} = 2(\mathbf{E}^u + \tilde{\mathbf{E}}) + \mathbf{G}. \tag{4.2}$$

In order to compute the enhanced right Cauchy-Green tensor, the displacement-derived deformation field can be decomposed into the rotation tensor $\mathbf{R}$ and the compatible right stretch tensor $\mathbf{U}^u$ as $\mathbf{F}^u = \mathbf{R}\mathbf{U}^u$ by applying the polar decomposition theorem. The modified right stretch tensor $\mathbf{U}$ is then estimated via Eq. (4.2) accounting for the enhanced strains, and it takes the form $\mathbf{U} := \mathbf{C}^{\frac{1}{2}}$. With this, the modified deformation gradient yields

$$\mathbf{F} := \mathbf{R}\mathbf{U},$$

with $J = \det[\mathbf{F}]$ being the corresponding modified Jacobian.

The second Piola-Kirchhoff stress tensor $\mathbf{S}$ (referred as PK2 in the related literature) in the reference configuration is estimated using the Cauchy stress tensor as

$$\mathbf{S} = \mathbf{F}^{-1} \cdot \mathbf{P} = J\mathbf{F}^{-1} \cdot \sigma \cdot \mathbf{F}^{-1} = S^{ij}\mathbf{G}_i \otimes \mathbf{G}_j,$$

where S^{ij} identifies its contravariant component.

Consider $\mathcal{P}_0 \subset \mathcal{B}_0$ from the continuum body $\mathcal{B}_0$ in the reference configuration surrounded by the boundary $\partial\mathcal{P}_0$, and its spatial counterpart $\mathcal{P}_t \subset \mathcal{B}_t$, being $\partial\mathcal{B}_t$ the boundary at the current configuration. The Cauchy's stress theorem postulates the linear dependency between Cauchy traction vector $\mathbf{t}$ and the normal $\mathbf{n}$ of $\partial\mathcal{P}_t$ through the Cauchy (true) stress tensor $\boldsymbol{\sigma}$ as

$$\mathbf{t} = \boldsymbol{\sigma} \cdot \mathbf{n}.$$

Similarly, the first Piola–Kirchhoff stress tensor $\mathbf{P}$ (PK1) is also defined via the Cauchy's stress theorem as

$$\hat{\mathbf{T}} = \mathbf{P} \cdot \mathbf{N}, \quad \text{with} \quad \mathbf{P} = \mathrm{J}\boldsymbol{\sigma} \cdot \mathbf{F}^{-1}.$$

where $\hat{\mathbf{T}}$ denotes first Piola–Kirchhoff traction vector presented by the force equality $\hat{\mathbf{T}}\mathrm{d}S = \mathbf{t}\mathrm{d}s$, and $\mathbf{N}$ refers to the normal of $\partial\mathcal{P}_0$ in the reference configuration.

Analogously to the Cauchy's stress theorem, Stokes heat flux theorem through the surface $\mathrm{d}\mathbf{a}$ on $\partial\mathcal{P}_t$ in the current configuration reads

$$q_n = \mathbf{q} \cdot \mathbf{n},$$

where q_n and $\mathbf{q}$ denote the scalar and vector (Cauchy) heat flux, respectively. The material heat flux $\mathbf{Q}$ relies on the equality $\mathbf{q} \cdot \mathbf{n}\mathrm{d}s = \mathbf{Q} \cdot \mathbf{N}\mathrm{d}S$, and therefore its definition yields to

$$\mathbf{Q} = \mathrm{J}\mathbf{F}^{-1} \cdot \mathbf{q} = Q^i\mathbf{G}_i,$$

where Q^i identifies its contravariant component.

4.2.2 Global equations of thermo-elasticity

The constitutive equations are derived such that they comply with the essential balance principle (conservation law) and second law of thermodynamics, which in its local material version is identified as the Clausius-Duhem inequality. Assuming a local theory, the constitutive law postulates that the Helmholtz free energy function Ψ depends on the modified Green-Lagrangian strain tensor $\mathbf{E}$, the temperature T and its spacial gradient $\nabla_{\mathbf{X}}T$, phase-field (excluded here) and a set of internal variables $\boldsymbol{\mathcal{I}}$ as

$$\rho_0\Psi = \hat{\Psi}(\mathbf{E}, T, \nabla_{\mathbf{X}}T, \boldsymbol{\mathcal{I}}), \tag{4.3}$$

for $\rho_0 = \rho_0(\mathbf{x})$ being the material density in reference configuration. For the isotropic Kirchhoff-Saint-Venant material model, the Helmholtz free energy reads

$$\Psi(\mathbf{E}, T) = \quad \tfrac{1}{2}\lambda\left(\mathrm{tr}[\mathbf{E}]\right)^2 + \mu\mathrm{tr}[\mathbf{E}^2] - 3\kappa\alpha\mathrm{tr}[\mathbf{E}]\left(T - T_0\right) \quad + c_p\left[(T - T_0) - T\log\frac{T}{T_0}\right] \tag{4.4}$$

where λ and μ are the Lamé constants, κ identifies the bulk modulus, and α is the coefficient of thermal expansion and T_0 is the initial reference temperature.

4.2.3 Extension to FGM

Within the context of functionally graded materials, material properties changes as a variation of spatial dimension across the domain. Let A and B be two materials compositions of a functionally graded materials, then the volume fraction of the material A in the domain $\mathcal{B}_0$ can be defined as

$$Vf_A(\mathbf{x}) := Vf_A(\mathbf{x},\ \zeta,\ \boldsymbol{\mathcal{I}}) : \mathcal{B}_0 \to [0, 1],$$

where ζ is the grading constant and $\boldsymbol{\mathcal{I}}$ is a set of internal variable that depends on the domain $\mathcal{B}_0$. Then, the volume fraction of the material B can be estimated as a function of material A. i.e $Vf_B(\mathbf{x}) = 1 - Vf_A(\mathbf{x})$. Based on the rule of mixtures, the material properties such as Young's Modulus E, Poisson's ratio ν, co-efficient of thermal expansion α, thermal conductivity k_0, heat capacity c_p and fracture energy $\mathcal{G}_C$ as a function of volume fraction of one of the material. i.e $\mathcal{G}_C = \mathcal{G}_C(Vf_A) = \mathcal{G}_C(Vf_B)$. Fixing $Vf_A(\mathbf{x})$ as a prime function, the material properties takes the form

$$E(\mathbf{x}) = E_A + (E_B - E_A)Vf_A(\mathbf{x}), \tag{4.5a}$$

$$\nu(\mathbf{x}) = \nu_A + (\nu_B - \nu_A)Vf_A(\mathbf{x}), \tag{4.5b}$$

$$\alpha(\mathbf{x}) = \alpha_A + (\alpha_B - \alpha_A)Vf_A(\mathbf{x}), \tag{4.5c}$$

$$k_0(\mathbf{x}) = k_{0,A} + (k_{0,B} - k_{0,A})Vf_A(\mathbf{x}), \tag{4.5d}$$

$$c_p(\mathbf{x}) = c_{p,A} + (c_{p,B} - c_{p,A})Vf_A(\mathbf{x}), \tag{4.5e}$$

$$\mathcal{G}_C(\mathbf{x}) = \mathcal{G}_{C,A} + (\mathcal{G}_{C,B} - \mathcal{G}_{C,A})Vf_A(\mathbf{x}). \tag{4.5f}$$

It can be argued that internal length scale l is largely considered as material parameters [37]. In particular, the length scale l can be estimated using the relation $l = \frac{27}{256}\frac{\mathcal{G}_C E}{\sigma_c^2}$ for σ_c being critical stress as in [24]. Moreover, many authors such as [90] considered l to be constant. In order to include the vast literature regarding the choice of the length scale l, here length scale is considered as a function of volume fraction i.e

$$l(\mathbf{x}) = l_{c,A} + (l_{c,B} - l_{c,A})Vf_A(\mathbf{x}). \tag{4.6}$$

Since Clausius-Duhem Inequality and the balance equations are defined locally, the Kirchoff-Saint-Venant in Eq. (4.4) is modified to accommodate FGM as

$$\begin{aligned}\Psi_0(\mathbf{E}, T; \mathbf{X}) = \quad & \tfrac{1}{2}\lambda(\mathbf{X})\left(\mathrm{tr}[\mathbf{E}]\right)^2 + \mu(\mathbf{X})\mathrm{tr}[\mathbf{E}^2] - 3\kappa(\mathbf{X})\alpha(\mathbf{X})\mathrm{tr}[\mathbf{E}]\left(T - T_0(\mathbf{X})\right) \\ & + c_p(\mathbf{X})\left[(T - T_0(\mathbf{X})) - T\log\tfrac{T}{T_0(\mathbf{X})}\right].\end{aligned} \tag{4.7}$$

Here, the material properties $\lambda(\mathbf{X})$, $\mu(\mathbf{X})$, $\kappa(\mathbf{X})$, $\alpha(\mathbf{X})$, $c_p(\mathbf{X})$, and $T_0(\mathbf{X})$ exhibit a variation in the spatial dimension. The material parameters from the surface energy, $\mathcal{G}_C$ and l are also written as $\mathcal{G}_C(\mathbf{X})$ and $l(\mathbf{X})$ Moreover, the Lamé constants, $\lambda(\mathbf{X})$, $\mu(\mathbf{X})$ and the bulk modulus $\kappa(\mathbf{X})$ can be estimated as

$$\lambda(\mathbf{X}) = \frac{E(\mathbf{X})\nu(\mathbf{X})}{(1+\nu(\mathbf{X}))(1-2\nu(\mathbf{X}))}; \qquad \mu(\mathbf{X}) = \frac{E(\mathbf{X})}{2(1+\nu(\mathbf{X}))}; \qquad \kappa(\mathbf{X}) = \frac{\nu(\mathbf{X})E(\mathbf{X})}{3(\nu(\mathbf{X})-2)}, \tag{4.8}$$

for each $\mathbf{X} \in \mathcal{B}_0$, whereas $E(\mathbf{X})$ and $\nu(\mathbf{X})$ are the spatial variations of Young's modulus and Poisson's ratio.

From here onward, we drop the $\mathbf{X}$ dependency on all the material properties. As mentioned earlier, the constitutive law follows the energy balance with respect to the reference configuration as

$$\begin{cases}\rho_0 = \mathrm{J}\rho : & \text{Local mass balance} \\ \rho_0\ddot{\boldsymbol{\varphi}} = \mathrm{DIV}\left[\mathbf{P}\right] + \rho_0\bar{\gamma} = \mathbf{0} : & \text{Linear Momentum balance} \\ \rho_0\dot{e} = \mathbf{S} : \dot{\mathbf{E}} + R - \mathrm{DIV}\left[\mathbf{Q}\right] : & \text{Energy balance}\end{cases} \tag{4.9}$$

Here, $\rho_0(\mathbf{X})$ and $\rho(\mathbf{X}, t)$ are the density fields in the reference and current configurations, respectively. Whilst, $\rho_0\bar{\gamma}$ identifies the prescribed body forces per unit of reference volume, e stands for the specific internal energy whose temporal rate given by $\dot{e}$, $\dot{\mathbf{E}}$ represents the rate of Green-Lagrange strain tensor, R is the internal heat source measured per unit reference volume.

The second law of thermodynamics which ensures the consistency of the formulation takes the form

$$\mathcal{D} = \mathcal{D}_{\mathrm{loc}} + \mathcal{D}_{\mathrm{cond}} = \left[\mathbf{S} : \dot{\mathbf{E}} - \rho_0\left(\dot{\Psi} + \dot{T}\eta\right)\right] - \left[\frac{1}{T}\mathbf{Q} \cdot \nabla_{\mathbf{X}} T\right] \geq 0, \tag{4.10}$$

which is referred as Clausius-Duhem inequality, with $\mathcal{D}$ representing the dissipated energy, $\mathcal{D}_{\mathrm{loc}}$ the energy due to the local actions and $\mathcal{D}_{\mathrm{cond}}$ is the energy due to heat conduction. It is easy to see that by enforcing

$$\mathcal{D}_{\text{loc}} \geq 0, \quad \text{and} \quad \mathcal{D}_{\text{cond}} \geq 0, \tag{4.11}$$

the Clausius-Duhem inequality in Eq. (4.10) is satisfied, leaving Clausius-Planck inequality Eq. $(4.11)_1$ and the Fourier inequality $(4.11)_2$.

Inserting the free energy function in Eq. (4.3), and Eq. (4.4) into Eq. (4.10) satisfies the Clausius-Duhem inequality by following the Coleman and Noll procedure [243] with

$$\mathcal{D}_{\text{loc}} = [\mathbf{S} - \partial_{\mathbf{E}}\Psi] : \dot{\mathbf{E}} - [\eta + \partial_T \Psi]\,\dot{T} - \partial_{\nabla_{\mathbf{X}} T}\Psi : \nabla_{\mathbf{X}}\dot{T} - \partial_{\boldsymbol{\mathcal{I}}}\Psi : \dot{\boldsymbol{\mathcal{I}}} \geq 0, \tag{4.12}$$

Accordingly, the constitutive equations corresponding to the second Piola-Kirchhoff tensor, and entropy reads

$$\mathbf{S} := \partial_{\mathbf{E}}\Psi = \lambda\,(\text{tr}[\mathbf{E}])\,\mathbf{1} + 2\mu\mathbf{E} - 3\kappa\alpha\,(T - T_0)\,\mathbf{1}, \tag{4.13}$$

$$\eta := -\partial_T\Psi = 3\kappa\alpha\text{tr}[\mathbf{E}] + c_p \log\frac{T}{T_0}, \tag{4.14}$$

Consequently, the internal dissipation reads

$$\mathcal{D}_{\text{loc}} := -\partial_{\boldsymbol{\mathcal{I}}}\Psi : \dot{\boldsymbol{\mathcal{I}}} \geq 0, \tag{4.15}$$

accounting for the evolution of inelastic processes such as visco-elastic, plastic effects, among others. Note that damage variable can be added here to the local action $\mathcal{D}_{\text{loc}}$ as $\partial_{\mathfrak{d}}\Psi : \dot{\mathfrak{d}}$, the irreversibility condition and Karush-Kuhn-Tucker (KKT) conditions can be readily obtained as a consequence of Eq.(4.15) and Eq.(4.12). In order to preserve the current derivation the similar format to that corresponding to the original phase-field formulation as in [16] i.e as a competition between the elastic (thermo-elastic) and the surface energy/crack energy, the phase-field variable is added at a later stage as in Section 4.3.

Based on the Legendre transformation, the evolution equation for entropy η takes the form

$$\rho_0\dot{\eta}T = -\partial_{\boldsymbol{\mathcal{I}}}\Psi : \dot{\boldsymbol{\mathcal{I}}} + R - \text{DIV}[\mathbf{Q}] = \mathcal{D}_{\text{loc}} + R - \text{DIV}[\mathbf{Q}]. \tag{4.16}$$

The left hand side of Eq.(4.16) can be expressed as:

$$\rho_0\eta\dot{T} = c_p\dot{T} - \rho_0\mathcal{S}_{\mathcal{H}}, \tag{4.17}$$

where the heat capacity, c_p, and the structural heating $\mathcal{S}_{\mathcal{H}}$ due to the rate of temperature reads

$$\begin{gathered} c_p := -\rho_0 T\partial^2_{TT}\Psi; \\ \mathcal{S}_{\mathcal{H}} := T\partial^2_{T\mathbf{E}}\Psi : \dot{\mathbf{E}} + T\partial^2_{T\boldsymbol{\mathcal{I}}}\Psi : \dot{\boldsymbol{\mathcal{I}}} = T\mathbf{Z} : \dot{\mathbf{E}} + T\boldsymbol{\mathcal{Q}} : \dot{\boldsymbol{\mathcal{I}}}, \end{gathered} \tag{4.18}$$

where $\mathbf{Z}$ is the second order tensor containing the thermal conductivity $\mathbf{k}$ in the curvilinear setting associated with the Helmholtz free energy, and $\boldsymbol{\mathcal{Q}}$ identifies the internal variable operator. For an adiabatic process, $\text{DIV}[\mathbf{Q}] \equiv 0$ and $R \equiv 0$. Since there is no irreversible evolution in interval variables (phase-field not included yet), $\partial^2_{T\boldsymbol{\mathcal{I}}}\Psi = 0$ in above equation and hereafter.

The constitutive operators in the curvilinear setting reads

$$\begin{aligned} \mathbb{C} = \partial_{\mathbf{EE}}\Psi = \left[\lambda G^{ij}G^{kl} + \mu\left(G^{ik}G^{jl} + G^{il}G^{jk}\right)\right] \mathbf{G}_i \otimes \mathbf{G}_j \otimes \mathbf{G}_k \otimes \mathbf{G}_l, \\ \mathbf{Z} = -3\kappa\alpha\left[G^{ij}\mathbf{G}_i \otimes \mathbf{G}_j\right], \end{aligned} \tag{4.19}$$

$$\mathbf{Q} = -J\mathbf{F}^{-1}\cdot\mathbf{k}\cdot\mathbf{F}^{-\mathrm{T}}\cdot\nabla_{\mathbf{X}}T = -Jk\left(\mathbf{G}_i \otimes \mathbf{g}^i\right)\left(g^{kl}\mathbf{g}_k \otimes \mathbf{g}_l\right)\left(\mathbf{g}^j \otimes \mathbf{G}_j\right)\nabla_{\mathbf{X}}T = -Jk\mathbf{C}^{-1}\cdot\nabla_{\mathbf{X}}T. \tag{4.20}$$

Here, the isotropic conductivity is written using the contravariant basis vector as $\mathbf{k} = kg^{ij}\mathbf{g}_i \otimes \mathbf{g}_i$, and $\mathbf{C}^{-1}$ stands for the inverse of the right Cauchy-Green strain tensor. By assuming a isotropic heat flux in the reference configuration, the formulation for the heat flux can be further simplified to $\mathbf{Q} = -k_0\mathbf{G}\nabla_{\mathbf{X}}T$, where k_0 identifies the thermal conductivity in the reference configuration.

4.2.4 Thermo-mechanical CZM

The first interface law under consideration is the cohesive zone model inspired by the work of Ortiz and Pandolfi [234], and later extended by Balzani and Wager [239] to enhance the model for Mode-I compression behaviour. The extension of Balzani exponential cohesive law to thermo-mechanical problems is developed according to the work of Turon et al [244], Walander et al [245], Willam et al [238], Wenyashu et al [246] and Fleischhauer et al [236, 237]. The cohesive zone model postulates the existence of a free energy density Φ per unit undeformed area. The thermo-mechanical coupling is achieved by making effective traction temperature dependent and the interface conductance dependent upon the cohesive damage variable. For this, define the displacement gaps in a 3-D modelling setting as: $\boldsymbol{\Delta} = (\Delta_n, \Delta_t, \Delta_s)$, where $\Delta_n, \Delta_s, \Delta_t$ identify normal, shear and tangential displacement gaps, respectively, and the temperature gap $\Delta_T = (T_+ - T_-)$ across the interface. In isothermal conditions, the free energy density reads

$$\Phi = \Phi(\boldsymbol{\Delta}, p), \tag{4.21}$$

where p is a suitable internal variable to describe the current decohesion state. Based on thermodynamic considerations, the cohesive tractions take the form

$$\boldsymbol{\sigma} := \frac{\partial\Phi(\boldsymbol{\Delta}, p)}{\partial\boldsymbol{\Delta}}. \tag{4.22}$$

In applications, where more than one fracture mode is predominant, the adoption of mixed mode fracture conditions are required. Following [247], the mixed mode conditions are herein accounted by introducing the effective/equivalent displacement Δ_m as

$$\Delta_m = \sqrt{\langle\Delta_n^2\rangle + \chi^2\left(\Delta_s^2 + \Delta_t^2\right)} = \sqrt{\boldsymbol{\Delta}^{\mathrm{T}}\mathcal{C}\boldsymbol{\Delta}} \quad \text{with} \quad \mathcal{C} = \begin{bmatrix} \chi^2 & 0 & 0 \\ 0 & \chi^2 & 0 \\ 0 & 0 & 1 \end{bmatrix}.$$

Here, $\langle\cdot\rangle = \dfrac{(|\cdot| + \cdot)}{2}$ is Macaulay brackets to avoid fracture events under compression normal actions, χ is the weighing factor between normal and shear fracture modes.

Assuming that the free energy depends upon the effective mechanical displacement Δ_m, under mixed mode conditions, the elastic tractions read

$$\boldsymbol{\sigma} = \frac{\sigma}{\Delta_m}\left[\Delta_n^2 \mathbf{n}_n + \chi^2\left(\Delta_s^2 \mathbf{n}_s + \Delta_t^2 \mathbf{n}_t\right)\right],$$

where $\mathbf{n}_i$ is the unit vector along i^{th} direction. Additionally, effective tractions $\boldsymbol{\sigma}_m$ takes the form

$$\boldsymbol{\sigma}_m = \frac{\partial \Phi}{\partial \Delta_m}.$$

The free energy function proposed in [239] takes the form

$$\Phi = e\sigma_c\Delta_c\left[1 - \left(1 + \frac{\Delta_m}{\Delta_c}\right)e^{\left(-\frac{\Delta_m}{\Delta_c}\right)}\right] + \frac{1}{2}K_c\Delta_n^2\frac{\langle -\Delta_n^2\rangle}{-\Delta_n^2}, \tag{4.23}$$

where σ_c and Δ_c are the initial effective limit traction and corresponding opening displacement gap. Here K_c identifies the penalty stiffness applied in compression and estimated as

$$K_c = \frac{e\sigma_c}{\Delta_c}.$$

In the presence of temperature, the critical energy release rate and the effective limit tractions are temperature dependent [245]. Hence, we herein assume that the peak traction is affected by temperature as

$$\sigma_c^* = \sigma_c(\boldsymbol{\Delta}, T, p) = \sigma_c\left(1 - \frac{\sum_{i=1}^{8} T_i - T_0}{T_0}\right). \tag{4.24}$$

Here, $\sum_{i=1}^{8} T_i$ represents the average temperature of all the nodes in an element. This leads to weakening of the interfaces at elevated temperatures by decreasing the total critical energy release rate of the system. Moreover, the constitutive assumption that the peak cohesive traction dependence on the temperature can be directly related to critical energy release rates for which the experimental results may be available for some specific materials.

As a consequence of thermodynamic considerations and the choice of the free energy function, the cohesive traction $\boldsymbol{\sigma}$ and the effective cohesive tractions $\boldsymbol{\sigma}_m$ render

$$\boldsymbol{\sigma} = \frac{e\sigma_c^*}{\Delta_c}e^{\left(-\frac{\Delta_m}{\Delta_c}\right)}\mathcal{C}\boldsymbol{\Delta} + K_c\mathcal{I}_c\boldsymbol{\Delta} = \mathcal{D}\boldsymbol{\Delta} \quad \text{with} \quad \mathcal{I}_c = \begin{bmatrix} 0 & 0 & 0 \\ 0 & 0 & 0 \\ 0 & 0 & \frac{\langle -\Delta_n\rangle}{-\Delta_n}. \end{bmatrix}, \tag{4.25}$$

and

$$\sigma_m = \frac{e\sigma_c^*\Delta_m}{\Delta_c}e^{\left(-\frac{\Delta_m}{\Delta_c}\right)}. \tag{4.26}$$

The linearized constitutive tensor for mechanical field is then directly obtained as

$$\mathbb{C} = \frac{\partial \boldsymbol{\sigma}}{\partial \boldsymbol{\Delta}} = \mathcal{D} + \frac{\partial \mathcal{D}}{\partial \boldsymbol{\Delta}}\boldsymbol{\Delta},$$

which follows that

$$\mathbb{C} = \frac{e\sigma_c^*}{\Delta_c} e^{\left(-\frac{\Delta_m}{\Delta_c}\right)} + K_c\mathcal{I}_c + \mathcal{F}e\frac{\sigma_c^*}{\Delta_c^2\Delta_m} e^{\left(-\frac{\Delta_m}{\Delta_c}\right)} (\mathcal{C}\boldsymbol{\Delta})(\mathcal{C}\boldsymbol{\Delta})^{\mathrm{T}}.$$

Here, the load function $\mathcal{F}$ is defined to distinguish between different cases of irreversibility. Additionally, the fracture toughness $\mathcal{G}_C$ is defined using the modified B-K criterion as

$$\mathcal{G}_C = \mathcal{G}_{Ic} + (\mathcal{G}_{IIc} - \mathcal{G}_{Ic})\left(\frac{\mathcal{G}_{II} + \mathcal{G}_{III}}{\mathcal{G}_I + \mathcal{G}_{II} + \mathcal{G}_{III}}\right)^{\eta}.$$

Additionally, the effective toughness relating $\mathcal{G}_C$ and the effective displacement Δ_m takes the form

$$\bar{\mathcal{G}_C} = \lim_{\Delta_m \to \infty}\{\Phi(\Delta_m, p)\} = e\sigma_c^*\Delta_c.$$

In order to track the extent of damage progression, the damage variable $\mathfrak{d}_{int}$ for mixed mode condition can be defined as the ratio between the dissipated energy and the effective fracture energy

$$\mathfrak{d}_{int} = \frac{\Phi(\Delta_m, p)}{\bar{\mathcal{G}_C}} = \left[1 - \left(1 + \frac{\Delta_m}{\Delta_c}\right) e^{\left(-\frac{\Delta_m}{\Delta_c}\right)}\right]. \tag{4.27}$$

Evidently, damage $\mathfrak{d}_{int} \in [0, 1]$ with $\mathfrak{d}_{int} = 0$ indicates no damage, whereas $\mathfrak{d}_{int} = 1$ indicates complete decohesion/damage.

The thermal flux across the interface $q_+ = \mathbf{q} \cdot \mathbf{n}_+$ occurs in the normal direction. Neglecting the effects of plasticity, convection, and radiation, the thermal flux now depends only on the interface conductance and the temperature jump $\Delta_T = (T_+ - T_-)$ across the interface. As a result, the heat flux across the interface renders

$$\bar{q_+}(h_{cz}) = h_{cz}\Delta_T, \tag{4.28}$$

where, h_{cz} is the thermal conductance of the interface. As a consequence of the opening gaps, the interface conductance decreases as the gap increases. Hence, the interface conductance is reduced with the help of the damage variable $\mathfrak{d}_{int}$ in line with the arguments of [235, 244]. With this, thermal conductance of the damaged surface takes the form

$$h_{cz} = (1 - \mathfrak{d}_{int})h_{int} \quad \text{for} \quad \Delta_n \geq 0. \tag{4.29}$$

Here h_{int} is the undamaged interface conductance. This way, the degradation of thermal and mechanical properties are controlled by a single damage variable. The FE implementation of the interface is detailed in Section 4.3.2

4.2.5 Extension of CZM to other models

The second interface model herewith examined recalls the exponential-like formulation given in [233]. Similarly to the previous section, we define the displacement gaps $\boldsymbol{\Delta} = (\Delta_n, \Delta_t, \Delta_s)$, where $\Delta_n, \Delta_s, \Delta_t$ identifies normal, shear and tangential displacement gaps respectively and the temperature gap $\Delta_T = (T_+ - T_-)$. Given the critical displacement δ_n, and γ, the ratio of normal to shear displacement, $\delta_s = \gamma\delta_n$, and $\delta_t = \gamma\delta_n$, define the non-dimensional, internal damage-like variable $\bar{\lambda} \in [0, 1]$ as

$$\bar{\lambda} = \sqrt{\left\{\left(\frac{\Delta_n}{\delta_n}\right)^2 + \left(\frac{\Delta_s}{\delta_s}\right)^2 + \left(\frac{\Delta_t}{\delta_t}\right)^2\right\}},$$

and a function $F(\bar{\lambda})$ is chosen as

$$F(\bar{\lambda}) = \frac{27}{4}\sigma_c(1 - 2\bar{\lambda} + \bar{\lambda}^2) \quad \text{for} \quad 0 \leq \bar{\lambda} \leq 1.$$

Then, for the monotonically increasing $\bar{\lambda}$, with $\bar{\lambda} = 0$ indicating no damage, and $\bar{\lambda} = 1$ indicating complete failure, the tractions are expressed as

$$\sigma = \left(\frac{\Delta_n}{\delta_n}\right) F(\bar{\lambda}); \quad \tau_s = \gamma\left(\frac{\Delta_s}{\delta_s}\right) F(\bar{\lambda}); \quad \tau_t = \gamma\left(\frac{\Delta_t}{\delta_t}\right) F(\bar{\lambda}).$$

Now, we assume that the effective limit traction σ_c (without renaming) affected by temperature $\sigma_c = \sigma_c\left(1 - \dfrac{\sum_{i=1}^{8} T_i - T_0}{T_0}\right)$. Here, $\sum_{i=1}^{8} T_i$ represents the average temperature of all the nodes in an element. Then as in Section 4.2.4, the interface conductance is reduced to

$$h_{cz} = (1 - \bar{\lambda})h_{int} \quad \text{for} \quad \Delta_n \geq 0.$$

with usual notations as in Section 4.2.4.

4.3 Variational basis and finite element formulation

Based on the previous considerations, and assuming a scalar isotropic degradation of the Helmholtz free energy function in Eq.(4.4) due to the evolution of fracture, the variational basis for the thermo-mechanical phase-field problem is herewith described. Within the framework of Hu-Washizu variational principle, the modified version of the Helmholtz free energy function incorporating the EAS method and the surface energy created due to fracture takes the form

$$\Pi(\mathbf{u}, \tilde{\mathbf{E}}, \mathfrak{d}, T, \mathfrak{d}_{int}) = \int_{\mathcal{B}_0} g(\mathfrak{d})\Psi(\mathbf{u}, \tilde{\mathbf{E}}, T)\mathrm{d}\Omega - \int_{\mathcal{B}_0} \mathbf{S} : \tilde{\mathbf{E}}\, \mathrm{d}\Omega + \int_{\mathcal{B}_0} \frac{\mathcal{G}_C}{2}\left[\frac{\alpha(\mathfrak{d})}{l} + l\,|\nabla\mathfrak{d}|^2\right] \mathrm{d}\Omega + \int_{\Gamma_{int}} \bar{q} \cdot \delta\Delta_T \; \mathrm{d}\partial\Omega + \Pi_{\text{ext}}. \tag{4.30}$$

Here, $\alpha(\mathfrak{d}) := \mathfrak{d}^2$ is a continuous monotonic function with $\alpha(0) = 0$ and $\alpha(1) = 1$, called the geometric crack function [29, 30, 31, 24]. The term $\frac{\alpha(\mathfrak{d})}{l}$ refers to the local part of the crack surface and $l\,|\nabla\mathfrak{d}|^2$ is the non local part. Moreover, $g(\mathfrak{d}) := [(1-\mathfrak{d})^2 + \mathfrak{k}_k]$ refers to the energetic degradation function that is used to deteriorate the initial coupled thermo-mechanical Helmholtz free energy function with $g(\mathfrak{d}) : [0,1] \rightarrow [1,0]$ and $\mathfrak{k}_k$ refers to a residual stiffness.

Recalling the additive decomposition of the strain field in Eq. (4.1), it is important to note that the orthogonality condition between the interpolation spaces of the stress and enhanced strain fields can be exploited from the subsequent derivations.

With this at hand, the solution of Eq.(4.30) can be obtained by solving it as a minimization problem.

Determine $(\mathbf{u}, \tilde{\mathbf{E}}, \mathfrak{d}, T, \mathfrak{d}_{int})$ from

$$(\mathbf{u}^*, \tilde{\mathbf{E}}^*, \mathfrak{d}^*, T^*, \mathfrak{d}^*_{int}) = \arg\min_{\mathcal{S}} \Pi(\mathbf{u}, \tilde{\mathbf{E}}, \mathfrak{d}, T, \mathfrak{d}_{int}) \tag{4.31}$$

with $\mathcal{S} = \{\dot{\mathfrak{d}} \geq 0 \text{ for all } \mathbf{x} \in \mathcal{B}_0|\Gamma_{int},\ \dot{\mathfrak{d}} \geq 0\ \forall \mathbf{x} \in \Gamma_i\}$. The set $(\mathbf{u}, \tilde{\mathbf{E}}, \mathfrak{d}, T, \boldsymbol{\Delta})$ in Eq. (4.31) is solved by taking a first variation of the total modified potential functional assuming enough regularity of the fields involved. Recalling the irriversibility of the damage variables $\mathfrak{d}$, for any admissible test function $(\delta\mathbf{u}, \delta\tilde{\mathbf{E}}, \delta\mathfrak{d}, \delta T, \delta\boldsymbol{\Delta})$ in the appropriate space of distribution (see below for details), this leads to the following residual of continuous multi-field problem:

$$\begin{aligned}
\mathcal{R}^u(\mathbf{u}, \tilde{\mathbf{E}}, \mathfrak{d}, T, \mathfrak{d}_{int}, \delta\mathbf{u}) = &\int_{\mathcal{B}_0} g(\mathfrak{d})\,[\mathbf{S} : \delta\mathbf{E}^u]\ \mathrm{d}\Omega - \int_{\mathcal{B}_0} \rho_0\bar{\gamma}\delta\mathbf{u}\ \mathrm{d}\Omega - \int_{\partial\mathcal{B}_{0,t}} \hat{\mathbf{t}}\cdot\delta\mathbf{u}\ \mathrm{d}\partial\Omega \\
&+ \int_{\Gamma_{int}} \boldsymbol{\sigma}\cdot\delta\boldsymbol{\Delta}\ \mathrm{d}\partial\Omega = 0, \\
\mathcal{R}^u = &\mathcal{R}^u_{\text{int}} - \mathcal{R}^u_{\text{ext}} + \mathcal{R}^u_{\text{coh}} = 0,
\end{aligned} \tag{4.32}$$

for all $\delta\mathbf{u} \in \mathfrak{B}^u$ with $\mathfrak{B}^u = \{\delta\mathbf{u} \in \mathbf{H}^1(\mathcal{B}_0),\ \delta\mathbf{u} = 0 \text{ on } \partial\mathcal{B}_{0,\mathbf{u}}\}$. Here, $\rho_0\bar{\gamma}$ denotes the external force applied per unit volume. The residual vector associated with the incompatible strain tensor takes the form

$$\mathcal{R}^{\tilde{E}}(\mathbf{u}, \tilde{\mathbf{E}}, \mathfrak{d}, T, \mathfrak{d}_{int}, \delta\tilde{\mathbf{E}}) = \int_{\mathcal{B}_0} g(\mathfrak{d}) \left[\mathbf{S} : \delta\tilde{\mathbf{E}}\right]\ \mathrm{d}\Omega = \mathcal{R}^{\tilde{E}}_{\text{int}} = 0, \tag{4.33}$$

for all $\delta\tilde{E} \in \mathfrak{B}^{\tilde{E}}$ with $\mathfrak{B}^{\tilde{E}} = \{\delta\tilde{E} \in \mathbf{L}^2(\mathcal{B}_0)\}$. The residual associated with the phase-field variable takes the form

$$\mathcal{R}^{\mathfrak{d}}(\mathbf{u}, \tilde{\mathbf{E}}, \mathfrak{d}, T, \mathfrak{d}_{int}, \delta\mathfrak{d}) = \int_{\mathcal{B}_0} \mathcal{G}_C \left[\frac{\mathfrak{d}}{l}\delta\mathfrak{d} + l\nabla\mathfrak{d}\cdot\nabla\delta\mathfrak{d}\right]\ \mathrm{d}\Omega - \int_{\mathcal{B}_0} 2(1-\mathfrak{d})\Psi(\mathbf{u}, \tilde{\mathbf{E}}, T)\delta\mathfrak{d}\ \mathrm{d}\Omega = 0, \tag{4.34}$$

for all $\delta\mathfrak{d} \in \mathfrak{B}^{\mathfrak{d}}$ with $\mathfrak{B}^{\mathfrak{d}} = \{\delta\mathfrak{d} \in H^1(\Omega)\Big|\delta\mathfrak{d} \geq 0\,\forall\ \mathbf{X} \in \mathcal{B}_0\}$. In the absence of other dissipative mechanisms and heat source ($R \equiv 0$), the residual for the coupled thermal field reads

$$\begin{aligned}\mathcal{R}^T(\mathbf{u},\tilde{\mathbf{E}},\mathfrak{d},T,\mathfrak{d}_{int},\delta T)=&\int_{\mathcal{B}_0} c_p\dot{T}\delta T\,\mathrm{d}\Omega-\int_{\mathcal{B}_0} g(\mathfrak{d})\left[T\mathbf{Z}:\dot{\mathbf{E}}\right]\delta T\,\mathrm{d}\Omega+\int_{\mathcal{B}_0} g(\mathfrak{d})\mathrm{DIV}[\mathbf{Q}]\delta T\,\mathrm{d}\Omega\\&+\int_{\Gamma_{int}}\bar{q}\cdot\delta\Delta_T\,\mathrm{d}\partial\Omega=0,\end{aligned}\tag{4.35}$$

for all $\delta T\in\mathfrak{B}^{\mathrm{T}}$ with $\mathfrak{B}^T=\{\delta T\in H^1(\Omega)\Big|\delta T=0\,\text{on}\,\partial\mathcal{B}_{0,q}\}$. The third term in Eq.(4.35) can be reformulated using the divergence theorem as

$$\int_{\mathcal{B}_0}\mathrm{DIV}[\mathbf{Q}]\delta T\,\mathrm{d}\Omega=\int_{\partial\mathcal{B}_{0,q}}Q_N\delta T\,\mathrm{d}\partial\Omega-\int_{\mathcal{B}_0}\mathbf{Q}\cdot\nabla_{\mathbf{X}}\delta T\,\mathrm{d}\Omega,$$

where $Q_N=\mathbf{Q}\cdot\mathbf{N}$ refers to the Neumann boundary condition on $\partial\mathcal{B}_{0,q}$. With this, the variational form of energy balance equation at the reference configuration takes the form

$$\begin{aligned}\mathcal{R}^T(\mathbf{u},\tilde{\mathbf{E}},\mathfrak{d},T,\mathfrak{d}_{int},\delta T)=&\int_{\mathcal{B}_0} c_p\dot{T}\delta T\,\mathrm{d}\Omega-\int_{\mathcal{B}_0} g(\mathfrak{d})\left[T\mathbf{Z}:\dot{\mathbf{E}}\right]\delta T\,\mathrm{d}\Omega+\int_{\partial\mathcal{B}_{0,q}}Q_N\delta T\,\mathrm{d}\partial\Omega\\&-\int_{\mathcal{B}_0}g(\mathfrak{d})\mathbf{Q}\cdot\nabla_{\mathbf{X}}\delta T\,\mathrm{d}\Omega+\int_{\Gamma_{int}}\bar{q}\cdot\delta\Delta_T\,\mathrm{d}\partial\Omega=0.\end{aligned}$$

Through the insertion of the Duhamel's law, Eq.(4.20)$_1$:

$$\begin{aligned}\mathcal{R}^T(\mathbf{u},\tilde{\mathbf{E}},\mathfrak{d},T,\mathfrak{d}_{int},\delta T)=&\int_{\mathcal{B}_0} c_p\dot{T}\delta T\,\mathrm{d}\Omega-\int_{\mathcal{B}_0} g(\mathfrak{d})\left[T\mathbf{Z}:\dot{\mathbf{E}}\right]\delta T\,\mathrm{d}\Omega+\int_{\partial\mathcal{B}_{0,q}}Q_N\delta T\,\mathrm{d}\partial\Omega\\&+\int_{\mathcal{B}_0}g(\mathfrak{d})\left[\nabla_{\mathbf{X}}\delta T\right]^{\mathrm{T}}\cdot J\mathbf{F}^{-1}\cdot\mathbf{k}\cdot\mathbf{F}^{-\mathrm{T}}\nabla_{\mathbf{X}}T\,\mathrm{d}\Omega\\&+\int_{\Gamma_{int}}\bar{q}\cdot\delta\Delta_T\,\mathrm{d}\partial\Omega=0.\end{aligned}\tag{4.36}$$

For isotropic thermal conductivity, Eq.(4.20)$_2$, the temperature residual finally reads

$$\begin{aligned}\mathcal{R}^T(\mathbf{u},\tilde{\mathbf{E}},\mathfrak{d},T,\mathfrak{d}_{int},\delta T)=&\int_{\mathcal{B}_0} c_p\dot{T}\delta T\,\mathrm{d}\Omega-\int_{\mathcal{B}_0} g(\mathfrak{d})\left[T\mathbf{Z}:\dot{\mathbf{E}}\right]\delta T\,\mathrm{d}\Omega+\int_{\Gamma_{int}}\bar{q}\cdot\delta\Delta_T\,\mathrm{d}\partial\Omega\\&+\int_{\partial\mathcal{B}_{0,q}}Q_N\delta T\,\mathrm{d}\partial\Omega+\int_{\mathcal{B}_0}g(\mathfrak{d})Jk\left[\nabla_{\mathbf{X}}\delta T\right]^{\mathrm{T}}\cdot\mathbf{C}^{-1}\cdot\nabla_{\mathbf{X}}[T]\,\mathrm{d}\Omega=0.\end{aligned}\tag{4.37}$$

Notice that, the degradation function $g(\mathfrak{d})$ is added in Eq. (4.36). Meaning that, the thermal conductivity k present in $\mathbf{Z}$ and $\boldsymbol{Q}$ (fourth term) is degraded. As the phase-field value reaches $\mathfrak{d}=1$, the thermal conductivity approaches zero acting as a potential barrier for the heat transfer across the cracked region Γ.

4.3.1 Finite element formulation

The finite element discretization is introduced on the reference configuration $\mathcal{B}_0$ (recalling a total Lagrangian formulation) with standard arguments of the isoparametric interpolation. The functional space $\mathcal{B}_0$ is discretized into n_e non-overlapping elements, such that $\mathcal{B}_0 \approx \bigcup_{e=1}^{n_e} \mathcal{B}_0^{(e)}$. Complying with the solid shell approach, for the natural coordinate system (ξ^1, ξ^2, ξ^3), the position vector at reference and current configuration $\mathbf{X}$ and $\mathbf{x}$ are expressed by the points of top and bottom surface $\mathbf{X}_t(\xi^1, \xi^2)$ and bottom surfaces $\mathbf{X}_b(\xi^1, \xi^2)$ of the shell as in Fig. 29. Accordingly, the position vector in the reference configuration can be expressed as

$$\mathbf{X}(\boldsymbol{\xi}) = \frac{1}{2}\left(1+\xi^3\right)\mathbf{X}_t(\xi^1,\xi^2) + \frac{1}{2}\left(1-\xi^3\right)\mathbf{X}_b(\xi^1,\xi^2), \tag{4.38}$$

whereas the position in the current configuration takes the form

$$\mathbf{x}(\boldsymbol{\xi}) = \frac{1}{2}\left(1+\xi^3\right)\mathbf{x}_t(\xi^1,\xi^2) + \frac{1}{2}\left(1-\xi^3\right)\mathbf{x}_b(\xi^1,\xi^2), \tag{4.39}$$

with the parametric space defined in natural co-ordinates as $\mathcal{A} := \{\boldsymbol{\xi} = (\xi^1, \xi^2, \xi^3) \in \mathbb{R}^3 \mid -1 \leq \xi^i \leq +1; i = 1, 2, 3\}$, with (ξ^1, ξ^2) being in plane and ξ^3 being thickness direction.

Regarding the phase-field variable embedded in the shell body, the definition of position vector is adopted in the reference and current configuration, a possible anszat yields to a linear interpolation between the top $(\mathfrak{d}_t)$ and bottom $(\mathfrak{d}_b)$ surfaces of the shell in line with [207], expressed as

$$\mathfrak{d}(\boldsymbol{\xi}) = \frac{1}{2}\left(1+\xi^3\right)\mathfrak{d}_t(\xi^1,\xi^2) + \frac{1}{2}\left(1-\xi^3\right)\mathfrak{d}_b(\xi^1,\xi^2). \tag{4.40}$$

The discrete reference (Lagrangian) and current (Eulerian) nodal position vectors are interpolated through standard trilinear shape functions N^I ($\mathbf{N}(\boldsymbol{\xi})$ in matrix notation) as

$$\mathbf{X} \approx \sum_{I=1}^{n_n} N^I(\boldsymbol{\xi})\mathbf{X}_I = \mathbf{N}(\boldsymbol{\xi})\widetilde{\mathbf{X}} \quad \text{and } \mathbf{x} \approx \sum_{I=1}^{n_n} N^I(\boldsymbol{\xi})\mathbf{x}_I = \mathbf{N}(\boldsymbol{\xi})\widetilde{\mathbf{x}},$$

with number of nodes $n_n = 8$ whose nodal values are collected into the respective global vectors $\widetilde{\mathbf{X}}$ and $\widetilde{\mathbf{x}}$.

The interpolation of the fields $(\mathbf{u}, \tilde{\mathbf{E}}, \mathfrak{d}, T)$, their respective variations $(\delta\mathbf{u}, \delta\tilde{\mathbf{E}}, \delta\mathfrak{d}, \delta T)$ and their increments $(\Delta\mathbf{u}, \Delta\tilde{\mathbf{E}}, \Delta\mathfrak{d}, \Delta T)$ in compact form reads

$$\mathbf{u} \approx \mathbf{N}(\boldsymbol{\xi})\mathbf{d}; \quad \delta\mathbf{u} \approx \mathbf{N}(\boldsymbol{\xi})\delta\mathbf{d}; \quad \Delta\mathbf{u} \approx \mathbf{N}(\boldsymbol{\xi})\Delta\mathbf{d},$$

$$\tilde{\mathbf{E}} \approx \mathbf{M}(\boldsymbol{\xi})\varsigma, \quad \delta\tilde{\mathbf{E}} \approx \mathbf{M}(\boldsymbol{\xi})\delta\varsigma, \quad \Delta\tilde{\mathbf{E}} \approx \mathbf{M}(\boldsymbol{\xi})\Delta\varsigma,$$

$$\mathfrak{d} \approx \mathbf{N}(\boldsymbol{\xi})\tilde{\mathfrak{d}}; \quad \delta\mathfrak{d} \approx \mathbf{N}(\boldsymbol{\xi})\delta\tilde{\mathfrak{d}}; \quad \Delta\mathfrak{d} \approx \mathbf{N}(\boldsymbol{\xi})\Delta\tilde{\mathfrak{d}}$$

$$T \approx \hat{\mathbf{N}}(\boldsymbol{\xi})\hat{\boldsymbol{T}}, \delta T \approx \hat{\mathbf{N}}(\boldsymbol{\xi})\delta\hat{\boldsymbol{T}}, \Delta T \approx \hat{\mathbf{N}}(\boldsymbol{\xi})\Delta\hat{\boldsymbol{T}}.$$

Here, the $\mathbf{M}(\boldsymbol{\xi})$ denotes the enhancing interpolation matrix and $\boldsymbol{\varsigma}$ is the vector collecting the EAS parameters. In particular, within the element space $\boldsymbol{\xi} = \{\xi^1, \xi^2, \xi^3\}$, the operator $\mathbf{M}(\boldsymbol{\xi})$ takes for form

$$\tilde{\mathbf{M}} = \begin{bmatrix} \xi^1 & 0 & 0 & 0 & 0 & 0 & 0 \\ 0 & \xi^1 & 0 & 0 & 0 & 0 & 0 \\ 0 & 0 & \xi^3 & \xi^1\xi^3 & \xi^2\xi^3 & 0 & 0 \\ 0 & 0 & 0 & 0 & 0 & \xi^1 & \xi^2 \\ 0 & 0 & 0 & 0 & 0 & 0 & 0 \\ 0 & 0 & 0 & 0 & 0 & 0 & 0 \end{bmatrix}. \tag{4.41}$$

is the operator with 7 parameter at each element level suitable to alleviate volumetric and Poison's thickness locking pathologies. Similarly

$$\tilde{\mathbf{M}} = \begin{bmatrix} \xi^1 & 0 & 0 & 0 & \xi^1\xi^2 & 0 & 0 & 0 & 0 & 0 & 0 \\ 0 & 0 & \xi^1 & \xi^2 & 0 & 0 & \xi^1\xi^2 & 0 & 0 & 0 & 0 \\ 0 & 0 & 0 & 0 & 0 & 0 & 0 & 0 & 0 & 0 & 0 \\ 0 & \xi^2 & 0 & 0 & 0 & \xi^1\xi^2 & 0 & 0 & 0 & 0 & 0 \\ 0 & 0 & 0 & 0 & 0 & 0 & 0 & 0 & 0 & 0 & 0 \\ 0 & 0 & 0 & 0 & 0 & 0 & 0 & 1 & \xi^1 & \xi^2 & \xi^1\xi^2 \end{bmatrix} \tag{4.42}$$

is the 11 parameter at each element level. Apart from the volumetric and Poison's, it can tackle the moderately distorted meshes.

In the current solid shell formulation, transverse shear and transverse normal strain components are modified in order to circumvent transverse shear and trapezoidal locking respectively using ANS interpolation method. The interpolation of the transverse shear strains E_{13} and E_{23} are performed at points $\boldsymbol{\xi}_A = (0, -1, 0)$, $\boldsymbol{\xi}_B = (1, 0, 0)$, $\boldsymbol{\xi}_C = (0, 1, 0)$ and $\boldsymbol{\xi}_D = (-1, 0, 0)$ as in Fig. 29. Accordingly, the transverse shear strain components reads

$$\begin{Bmatrix} 2E_{13}^{ANS} \\ 2E_{23}^{ANS} \end{Bmatrix} = \begin{Bmatrix} (1-\xi^2)2E_{13}(\boldsymbol{\xi}_A) + (1+\xi^2)2E_{13}(\boldsymbol{\xi}_C) \\ (1+\xi^1)2E_{23}(\boldsymbol{\xi}_B) + (1-\xi^1)2E_{23}(\boldsymbol{\xi}_D) \end{Bmatrix}.$$

Similarly, the interpolation of the transverse normal strain E_{33} are performed at points $\boldsymbol{\xi}_O = (-1, -1, 0)$, $\boldsymbol{\xi}_P = (1, -1, 0)$, $\boldsymbol{\xi}_S = (1, 1, 0)$ and $\boldsymbol{\xi}_T = (-1, 1, 0)$ as in Fig. 29. Based on this, the transverse normal strain takes the form

$$\begin{aligned} E_{33}^{ANS} &= \sum_{m=O,P,S,T} N^m(\xi^1, \xi^2) E_{33}; \\ N^m(\xi^1, \xi^2) &= \frac{1}{4}\left(1 + \xi^1_m \xi^1\right)\left(1 + \xi^2_m \xi^2\right), \\ &\text{with } \xi^1_m, \xi^2_m = \pm 1. \end{aligned}$$

The interpolation of displacement derived compatible strains are approximated using displacement strain operator $\mathbf{B}$ as

$$\mathbf{E}^u \approx \mathbf{B}(\mathbf{d})\mathbf{d}, \quad \delta\mathbf{E}^u \approx \mathbf{B}(\mathbf{d})\delta\mathbf{d}, \quad \Delta\mathbf{E}^u \approx \mathbf{B}(\mathbf{d})\Delta\mathbf{d}.$$

Similarly, the gradient of phase-field are interpolated using a suitable operator $\mathbf{B}^{\mathfrak{d}}$ as

$$\nabla_{\mathbf{x}}\mathfrak{d} \approx \mathbf{B}^{\mathfrak{d}}(\mathbf{d})\tilde{\mathfrak{d}}, \quad \nabla_{\mathbf{x}}\delta\mathfrak{d} \approx \mathbf{B}^{\mathfrak{d}}(\mathbf{d})\delta\tilde{\mathfrak{d}}, \quad \nabla_{\mathbf{x}}\Delta\mathfrak{d} \approx \mathbf{B}^{\mathfrak{d}}(\mathbf{d})\Delta\tilde{\mathfrak{d}}.$$

The interpolation of the spatial temperature gradient at current configuration ($\nabla_{\mathbf{X}}T$), and its associated variations can be expressed as

$$\nabla_{\mathbf{X}}T = \mathbf{G}^{-1}\nabla_{\boldsymbol{\xi}}T \approx \mathbf{G}^{-1}\nabla_{\boldsymbol{\xi}}\hat{\mathbf{N}}(\boldsymbol{\xi})\hat{\boldsymbol{T}}; \quad \nabla_{\mathbf{X}}\delta T \approx \mathbf{G}^{-1}\nabla_{\boldsymbol{\xi}}\hat{\mathbf{N}}(\boldsymbol{\xi})\delta\hat{\boldsymbol{T}}; \quad \nabla_{\mathbf{X}}\Delta T \approx \mathbf{G}^{-1}\nabla_{\boldsymbol{\xi}}\hat{\mathbf{N}}(\boldsymbol{\xi})\Delta\hat{\boldsymbol{T}}, \tag{4.43}$$

where $\nabla_{\boldsymbol{\xi}}$ is the gradient of temperature at each node with respect natural coordinate defines in the curvilinear setting.

4.3.2 FE implementation of interface

Regarding the internal cohesive interfaces, the contribution of the interface cohesive traction $\boldsymbol{\sigma}$ in Eq. (4.32) and heat flux $\bar{q}$ in Eq. (4.35), the total potential reads

$$\Pi_{int} = \int_{\Gamma_{int}} \tilde{\mathbf{T}} \cdot \mathbf{g}_{loc}^{\mathrm{T}} \, \mathrm{d}\partial\Omega, \tag{4.44}$$

where the gaps $\mathbf{g}_{loc} = (\delta_n, \delta_t, \delta_s, \delta_T)$ includes both mechanical and thermal gaps, $\tilde{\mathbf{T}} = (\boldsymbol{\sigma}, \bar{q}) = (\sigma, \tau_t, \tau_s, \bar{q})$.

The virtual variation of the Π_{int} according to principle of virtual work takes the form

$$\delta\Pi_{int} = \int_{\Gamma_{int}} \tilde{\mathbf{T}} \cdot \frac{\partial \mathbf{g}_{loc}}{\partial \mathbf{u}}^{\mathrm{T}} \, \mathrm{d}\partial\Omega. \tag{4.45}$$

At each element, four degrees of freedom for each node are specified for each node as

$$\hat{\mathbf{d}} = (\mathbf{d}, T)^{\mathrm{T}}. \tag{4.46}$$

The mid surface is specified such that the average value of the displacements are specified on the mid surface plane. Due to the geometrical non-linearity/large displacement, the updated coordinates of a generic point are given by $\mathbf{x} = \mathbf{X} + \mathbf{d}$. As in [207, 234], the collective traction to the middle surface can be determined by the average co-ordinates with respect to the natural co-ordinates ξ and η. The gap vector in the reference frame, $\mathbf{g}$ can be obtained by pre-multiplying the nodal displacement vector $\mathbf{d}$ and a suitable operator $\mathbf{L}$ which provides the difference between the top and bottom interface. Accordingly, the discritized gaps in the finite element framework reads

$$\mathbf{g} = \mathbf{N}\mathbf{L}\hat{\mathbf{d}}. \tag{4.47}$$

Here, $\mathbf{N}$ is the interpolation operator whose expression reads

$$\mathbf{N} = \left[N_1\mathcal{I}_4, N_2\mathcal{I}_4, N_3\mathcal{I}_4, N_4\mathcal{I}_4\right], \tag{4.48}$$

where $N_1 = \dfrac{1}{4}(1-\xi^1)(1-\xi^2)$, $N_2 = \dfrac{1}{4}(1+\xi^1)(1-\xi^2)$, $N_3 = \dfrac{1}{4}(1+\xi^1)(1+\xi^2)$ and $N_4 = \dfrac{1}{4}(1-\xi^1)(1+\xi^2)$, whereas $\mathcal{I}_4$ is the 4×4 identity vector. Moreover, the averaging operator reads $\mathbf{L} = [-\mathcal{I}_{16}, \mathcal{I}_{16}]$ with $\mathcal{I}_{16}$ identifies as 16×16 identity matrix.

The generalized displacement gaps in the local reference frame are computed by multiplying the gaps g in reference frame by a rotation operator R, i.e

$$\mathbf{g}_{loc} = \mathbf{R}(\hat{\mathbf{d}})\mathbf{g} = \mathbf{R}(\hat{\mathbf{d}})\mathbf{N}\mathbf{L}\hat{\mathbf{d}}. \tag{4.49}$$

It is important to observe that the rotation operator depends on the displacement $\hat{\mathbf{d}}$ due to the large displacements, see [240], for more details. The displacement dependent rotation operator $\mathbf{R}(\hat{\mathbf{d}})$ takes the form

$$\mathbf{R}(\hat{\mathbf{d}}) = \begin{bmatrix} t_x & s_x & n_x & 0 \\ t_y & s_y & n_y & 0 \\ t_y & s_z & n_z & 0 \\ 0 & 0 & 0 & 1 \end{bmatrix}. \tag{4.50}$$

On this impending event, $\dfrac{\partial \mathbf{g}_{loc}}{\partial \hat{\mathbf{d}}}$ in Eq. (4.45) can be estimated as

$$\frac{\partial \mathbf{g}_{loc}}{\partial \mathbf{u}} \approx \frac{\partial \mathbf{g}_{loc}}{\partial \hat{\mathbf{d}}} = \mathbf{R}(\hat{\mathbf{d}})\mathbf{N}\mathbf{L} + \frac{\partial \mathbf{R}(\hat{\mathbf{d}})}{\partial \hat{\mathbf{d}}}\mathbf{N}\mathbf{L}\hat{\mathbf{d}}. \tag{4.51}$$

Here, $\dfrac{\partial \mathbf{R}(\hat{\mathbf{d}})}{\partial \hat{\mathbf{d}}}$ is a third order tensor. Replacing $\mathbf{B} = \mathbf{N}\mathbf{L}$ in the above expression, and putting in Eq (4.45) leads to

$$\delta\Pi_{int} = \delta\hat{\mathbf{d}}^{\mathrm{T}} \int_{\Gamma_{int}} \left(\mathbf{R}\mathbf{B} + \frac{\partial \mathbf{R}}{\partial \hat{\mathbf{d}}}\mathbf{B}\hat{\mathbf{d}}\right)^{\mathrm{T}} \tilde{\mathbf{T}}\, \mathrm{d}\partial\Omega. \tag{4.52}$$

The solution of the variational equation $\delta\Pi_{int} = 0$ results in $\mathbf{f}_{int} = 0$ with

$$\mathbf{f}_{int} = \int_{\Gamma_{int}} \left(\mathbf{R}\mathbf{B} + \frac{\partial \mathbf{R}}{\partial \hat{\mathbf{d}}}\mathbf{B}\hat{\mathbf{d}}\right)^{\mathrm{T}} \tilde{\mathbf{T}}\, \mathrm{d}\partial\Omega. \tag{4.53}$$

A Newton-Raphson iterative scheme is used to find the corrector $\delta\tilde{\mathbf{d}}$ at each iteration until the convergence is achieved. At iteration k, the equation reads

$$\mathbf{K}^{e,k}\Delta\hat{\mathbf{d}} = -\mathbf{f}_{int}, \tag{4.54a}$$

$$\hat{\mathbf{d}}^{k+1} = \hat{\mathbf{d}}^{k} + \Delta\hat{\mathbf{d}}, \tag{4.54b}$$

where $\mathbf{K}^k$ is the elemental stiffness matrix obtained by the linearization of the residual. i,e $\mathbf{K}^{e,k} = \dfrac{\partial \mathbf{f}_{int}}{\partial \hat{\mathbf{d}}}$. Following the lines of derivation as in [240], the final stiffness matrix renders

$$\mathbf{K}^e = \mathbf{K}^e_{mat} + \mathbf{K}^e_{geom}, \tag{4.55}$$

with material contribution $\mathbf{K}^e_{mat}$ takes the form

$$\mathbf{K}^e_{mat} = \int_{\Gamma_{int}} \left(\mathbf{B}^{\mathrm{T}}\mathbf{R}^{\mathrm{T}}\mathbb{C}\mathbf{R}\mathbf{B}\right)\, \mathrm{d}\partial\Omega, \tag{4.56}$$

and the geometrical contribution $\mathbf{K}^e_{geom}$ to the stiffness matrix is

$$
\begin{aligned}
\mathbf{K}^{e}_{geom} = &\int_{\Gamma_{int}} \left(2\mathbf{B}^{\mathrm{T}} \frac{\partial \mathbf{R}}{\partial \hat{\mathbf{d}}}^{\mathrm{T}} \mathbf{T} + \hat{\mathbf{d}}^{\mathrm{T}} \mathbf{B}^{\mathrm{T}} \frac{\partial \mathbf{R}}{\partial \hat{\mathbf{d}}}^{\mathrm{T}} \mathbb{C} \frac{\partial \mathbf{R}}{\partial \hat{\mathbf{d}}} \mathbf{B} \hat{\mathbf{d}} \right) \\
&+ \int_{\Gamma_{int}} \left(\mathbf{B}^{\mathrm{T}} \mathbf{R}^{\mathrm{T}} \mathbb{C} \frac{\partial \mathbf{R}}{\partial \hat{\mathbf{d}}} \mathbf{B} \hat{\mathbf{d}} + \hat{\mathbf{d}}^{\mathrm{T}} \mathbf{B}^{\mathrm{T}} \frac{\partial \mathbf{R}}{\partial \hat{\mathbf{d}}} \mathbb{C} \mathbf{R} \mathbf{B} \right) \Bigg] \, \mathrm{d}\partial\Omega,
\end{aligned}
\tag{4.57}
$$

Here, $\mathbb{C} = \dfrac{\partial \tilde{\mathbf{T}}}{\partial \mathbf{g}_{loc}}$ is the tangent interface constitutive matrix whose computation is detailed in Section 4.2.4. In case of small displacement, the geometrical contribution yields $\dfrac{\partial \mathbf{R}}{\partial \mathbf{d}} = 0$.

4.3.3 Consistent linearization

Through the insertion of the previously discussed interpolation scheme, the residuals of the independent fields $(\mathbf{u}, \tilde{\mathbf{E}}, \mathfrak{d}, T)$ in the discrete form can be expressed as

$$
\hat{\mathcal{R}}^{u}_{\text{int}}(\mathbf{d}, \varsigma, \tilde{\mathfrak{d}}, \hat{\boldsymbol{T}}, \delta\mathbf{d}) = \delta\mathbf{d}^{\mathrm{T}} \left[\int_{\mathcal{B}_0} g(\mathfrak{d}) \mathbf{B}(\mathbf{d})^{\mathrm{T}} \mathbf{S} \, \mathrm{d}\Omega \right], \tag{4.58}
$$

$$
\hat{\mathcal{R}}^{\tilde{E}}_{\text{int}}(\mathbf{d}, \varsigma, \tilde{\mathfrak{d}}, \hat{\boldsymbol{T}}, \delta\varsigma) = \delta\boldsymbol{\varsigma}^{\mathrm{T}} \left[\int_{\mathcal{B}_0} g(\mathfrak{d}) \mathbf{M}(\boldsymbol{\xi})^{\mathrm{T}} \mathbf{S} \, \mathrm{d}\Omega \right], \tag{4.59}
$$

$$
\begin{aligned}
\hat{\mathcal{R}}^{\mathfrak{d}}(\mathbf{d}, \varsigma, \tilde{\mathfrak{d}}, \hat{\boldsymbol{T}}, \delta\mathfrak{d}) = \delta\mathfrak{d}^{\mathrm{T}} \Bigg[&\int_{\mathcal{B}_0} \mathcal{G}_C \left[\frac{1}{l} \mathbf{N}(\boldsymbol{\xi})^{\mathrm{T}} \mathfrak{d} + l \mathbf{B}^{\mathfrak{d}}(\boldsymbol{\xi})^{\mathrm{T}} \nabla_{\mathbf{x}} \mathfrak{d} \right] \, \mathrm{d}\Omega \\
&- \int_{\mathcal{B}_0} 2(1-\mathfrak{d}) \mathbf{N}^{\mathrm{T}}(\boldsymbol{\xi}) \mathcal{H} \delta\mathfrak{d} \, \mathrm{d}\Omega \Bigg],
\end{aligned}
\tag{4.60}
$$

$$
\begin{aligned}
\hat{\mathcal{R}}^{T}_{\text{int}}(\mathbf{d}, \varsigma, \tilde{\mathfrak{d}}\hat{\boldsymbol{T}}, \delta\hat{\boldsymbol{T}}) = \delta\hat{\boldsymbol{T}}^{\mathrm{T}} \Bigg[&\int_{\mathcal{B}_0} \hat{\mathbf{N}}(\boldsymbol{\xi})^{\mathrm{T}} c_p \dot{T} \, \mathrm{d}\Omega - \int_{\mathcal{B}_0} g(\mathfrak{d}) \hat{\mathbf{N}}(\boldsymbol{\xi})^{\mathrm{T}} \left(\mathbf{Z}^{\mathrm{T}} \dot{\mathbf{E}} \right) T \, \mathrm{d}\Omega + \\
&\int_{\mathcal{B}_0} J \mathbf{B}_T^{\mathrm{T}} \mathbf{F}^{-1} \cdot \mathbf{k} \cdot \mathbf{F}^{-\mathrm{T}} \cdot \nabla_{\mathbf{X}} T \, \mathrm{d}\Omega \Bigg].
\end{aligned}
\tag{4.61}
$$

Here,

$$
\mathcal{H} = \max_{\tau \in [0,t]} \left[\Psi(\mathbf{u}, \tilde{\mathbf{E}}, T) \right], \tag{4.62}
$$

is the crack driving force (history variable) as defined in [207] to ensure the irreversibility of the phase-field variable $\mathfrak{d}$ and $\mathbf{B}_T$ defines a suitable operator to compute the gradient of the temperature field.

Due to the existence of non-linearity in the multi-field Eqs.(4.58)- (4.61), an incremental iterative quasi Newton-Raphson scheme is adopted (details are omitted for the sake of brevity). This is achieved by linearization of the residual in Eq.(4.58), (4.59), (4.60), (4.61) using directional Gateaux derivatives [231, 24, 207].

For this, consider a finite time increment $\Delta t := t_{n+1}^{(k)} - t_n > 0$, where the fields $(\mathbf{u}, \tilde{\mathbf{E}}, \mathfrak{d}, T)$ at step t_n is assumed to be known. The temporal variation of the fields are expressed as

$$\dot{\boldsymbol{T}} = \frac{\boldsymbol{T}_{n+1} - \boldsymbol{T}_n}{\Delta t}; \dot{\mathbf{E}} = \frac{\mathbf{E}_{n+1} - \mathbf{E}_n}{\Delta t}; \dot{\mathbf{d}} = \frac{\mathbf{d}_{n+1} - \mathbf{d}_n}{\Delta t}; \dot{\boldsymbol{\varsigma}} = \frac{\boldsymbol{\varsigma}_{n+1} - \boldsymbol{\varsigma}_n}{\Delta t}, \tag{4.63}$$

constituting a backward Euler scheme.

The independent fields $(\mathbf{u}, \tilde{\mathbf{E}}, \mathfrak{d}, T)$ are computed at current time step t_{n+1} via consistent linearization of the residual functions which can be expressed as

$$\begin{aligned} \hat{L}[\hat{\mathcal{R}}^u] &= \hat{\mathcal{R}}^u(\mathbf{d}, \boldsymbol{\varsigma}, \tilde{\mathfrak{d}}, \hat{\boldsymbol{T}}, \delta\mathbf{d}) + \Delta\hat{\mathcal{R}}^u(\mathbf{d}, \boldsymbol{\varsigma}, \tilde{\mathfrak{d}}, \hat{\boldsymbol{T}}, \delta\mathbf{d}, \Delta\mathbf{d}, \Delta\boldsymbol{\varsigma}, \Delta\tilde{\mathfrak{d}}, \Delta\hat{\boldsymbol{T}}) \\ &= \hat{\mathcal{R}}^u + \Delta_{\mathbf{d}}\hat{\mathcal{R}}^u\Delta\mathbf{d} + \Delta_{\varsigma}\hat{\mathcal{R}}^u\Delta\boldsymbol{\varsigma} + \Delta_{\mathfrak{d}}\hat{\mathcal{R}}^u\Delta\tilde{\mathfrak{d}} + \Delta_T\hat{\mathcal{R}}^u\Delta\hat{\boldsymbol{T}}, \end{aligned} \tag{4.64}$$

$$\begin{aligned} \hat{L}[\hat{\mathcal{R}}^{\tilde{E}}] &= \hat{\mathcal{R}}^{\tilde{E}}(\mathbf{d}, \boldsymbol{\varsigma}, \tilde{\mathfrak{d}}, \hat{\boldsymbol{T}}, \delta\boldsymbol{\varsigma}) + \Delta\hat{\mathcal{R}}^{\tilde{E}}(\mathbf{d}, \boldsymbol{\varsigma}, \tilde{\mathfrak{d}}, \hat{\boldsymbol{T}}, \delta\mathbf{d}, \Delta\mathbf{d}, \Delta\boldsymbol{\varsigma}, \Delta\tilde{\mathfrak{d}}, \Delta\hat{\boldsymbol{T}}) \\ &= \hat{\mathcal{R}}^{\tilde{E}} + \Delta_{\mathbf{d}}\hat{\mathcal{R}}^{\tilde{E}}\Delta\mathbf{d} + \Delta_{\varsigma}\hat{\mathcal{R}}^{\tilde{E}}\Delta\boldsymbol{\varsigma} + \Delta_{\mathfrak{d}}\hat{\mathcal{R}}^{\tilde{E}}\Delta\tilde{\mathfrak{d}} + \Delta_T\hat{\mathcal{R}}^{\tilde{E}}\Delta\hat{\boldsymbol{T}} \end{aligned} \tag{4.65}$$

$$\begin{aligned} \hat{L}[\hat{\mathcal{R}}^{\tilde{\mathfrak{d}}}] &= \hat{\mathcal{R}}^{\tilde{\mathfrak{d}}}(\mathbf{d}, \boldsymbol{\varsigma}, \tilde{\mathfrak{d}}, \hat{\boldsymbol{T}}, \delta\boldsymbol{\varsigma}) + \Delta\hat{\mathcal{R}}^{\tilde{\mathfrak{d}}}(\mathbf{d}, \boldsymbol{\varsigma}, \tilde{\mathfrak{d}}, \hat{\boldsymbol{T}}, \delta\mathbf{d}, \Delta\mathbf{d}, \Delta\boldsymbol{\varsigma}, \Delta\tilde{\mathfrak{d}}, \Delta\hat{\boldsymbol{T}}) \\ &= \hat{\mathcal{R}}^{\tilde{\mathfrak{d}}} + \Delta_{\mathbf{d}}\hat{\mathcal{R}}^{\tilde{\mathfrak{d}}}\Delta\mathbf{d} + \Delta_{\varsigma}\hat{\mathcal{R}}^{\tilde{\mathfrak{d}}}\Delta\boldsymbol{\varsigma} + \Delta_{\mathfrak{d}}\hat{\mathcal{R}}^{\tilde{\mathfrak{d}}}\Delta\tilde{\mathfrak{d}} + \Delta_T\hat{\mathcal{R}}^{\tilde{\mathfrak{d}}}\Delta\hat{\boldsymbol{T}} \end{aligned} \tag{4.66}$$

$$\begin{aligned} \hat{L}[\hat{\mathcal{R}}^T] &= \hat{\mathcal{R}}^T(\mathbf{d}, \boldsymbol{\varsigma}, \tilde{\mathfrak{d}}, \hat{\boldsymbol{T}}, \delta\hat{\boldsymbol{T}}) + \Delta\hat{\mathcal{R}}^T(\mathbf{d}, \boldsymbol{\varsigma}, \tilde{\mathfrak{d}}, \hat{\boldsymbol{T}}, \delta\mathbf{d}, \Delta\mathbf{d}, \Delta\boldsymbol{\varsigma}, \Delta\tilde{\mathfrak{d}}, \Delta\hat{\boldsymbol{T}}) \\ &= \hat{\mathcal{R}}^T + \Delta_{\mathbf{d}}\hat{\mathcal{R}}^T\Delta\mathbf{d} + \Delta_{\varsigma}\hat{\mathcal{R}}^T\Delta\boldsymbol{\varsigma} + \Delta_{\mathfrak{d}}\hat{\mathcal{R}}^T\Delta\tilde{\mathfrak{d}} + \Delta_T\hat{\mathcal{R}}^T\Delta\hat{\boldsymbol{T}} \end{aligned} \tag{4.67}$$

where $\Delta_{\mathfrak{b}}[\mathfrak{a}]$ denotes the tangent matrices calculated as a directional derivative of the residual form $\mathfrak{a}$ with respect to the field $\mathfrak{b}$. In particular $\Delta_{\mathfrak{b}}[\mathfrak{a}] = \mathbf{k}_{\mathfrak{a}\mathfrak{b}}$ with $\{\, \mathfrak{a}, \mathfrak{b}\} = \{\mathbf{d}, \boldsymbol{\varsigma}, \tilde{\mathfrak{d}}, \hat{\boldsymbol{T}}\}$. Following the standard finite element procedure, Eq.(4.64), (4.65), (4.66), (4.67) can be expressed as a system of linear equations as

$$\begin{bmatrix} \mathbf{K}_{\mathbf{dd}} & \mathbf{K}_{\mathbf{d}\varsigma} & \mathbf{K}_{\mathbf{d}\tilde{\mathfrak{d}}} & \mathbf{K}_{\mathbf{d}T} \\ \mathbf{K}_{\varsigma\mathbf{d}} & \mathbf{K}_{\varsigma\varsigma} & \mathbf{K}_{\varsigma\tilde{\mathfrak{d}}} & \mathbf{K}_{\varsigma T} \\ \mathbf{K}_{\tilde{\mathfrak{d}}\mathbf{d}} & \mathbf{K}_{\tilde{\mathfrak{d}}\varsigma} & \mathbf{K}_{\tilde{\mathfrak{d}}\tilde{\mathfrak{d}}} & \mathbf{K}_{\tilde{\mathfrak{d}}T} \\ \mathbf{K}_{T\mathbf{d}} & \mathbf{K}_{T\varsigma} & \mathbf{K}_{T\tilde{\mathfrak{d}}} & \mathbf{K}_{TT} \end{bmatrix} \begin{bmatrix} \Delta\mathbf{d} \\ \Delta\boldsymbol{\varsigma} \\ \Delta\mathfrak{d} \\ \Delta\hat{\boldsymbol{T}} \end{bmatrix} = \begin{bmatrix} \hat{\mathcal{R}}^u_{\text{ext}} \\ \mathbf{0} \\ \mathbf{0} \\ \hat{\mathcal{R}}^T_{\text{ext}} \end{bmatrix} - \begin{bmatrix} \hat{\mathcal{R}}^u_{\text{int}} \\ \hat{\mathcal{R}}^{\varsigma}_{\text{int}} \\ \hat{\mathcal{R}}^{\tilde{\mathfrak{d}}}_{\text{int}} \\ \hat{\mathcal{R}}^T_{\text{int}} \end{bmatrix}. \tag{4.68}$$

The different elements of the tangent stiffness matrix takes the form

$$\mathbf{K}_{\mathbf{dd}} = \int_{\mathcal{B}_0} g(\mathfrak{d}) \left(\mathbf{B}(\mathbf{d})^{\mathrm{T}}\mathbb{C}\mathbf{B}(\mathbf{d}) + \left[\frac{\partial\mathbf{B}(\mathbf{d})}{\partial\mathbf{d}}\right]^{\mathrm{T}} \mathbf{S} \right) \mathrm{d}\Omega = \mathbf{K}_{\mathbf{dd},\text{mat}} + \mathbf{K}_{\mathbf{dd},\text{geom}} \tag{4.69a}$$

$$\mathbf{K}_{\mathbf{d}\varsigma} = \int_{\mathcal{B}_0} g(\mathfrak{d})\mathbf{M}(\boldsymbol{\xi})^{\mathrm{T}}\mathbb{C}\mathbf{B}(\mathbf{d})\,\mathrm{d}\Omega; \tag{4.69b}$$

$$\mathbf{K}_{\mathbf{d}\tilde{\mathfrak{d}}} = \int_{\mathcal{B}_0} -2(1-\mathfrak{d})\mathbf{B}(\mathbf{d})^{\mathrm{T}}\mathbf{S}\mathbf{N}(\boldsymbol{\xi})\,\mathrm{d}\Omega, \tag{4.69c}$$

$$\mathbf{K}_{\mathbf{d}T} = \int_{\mathcal{B}_0} g(\mathfrak{d})\mathbf{B}(\mathbf{d})^{\mathrm{T}}\mathbf{Z}\hat{\mathbf{N}}(\boldsymbol{\xi})\,\mathrm{d}\Omega, \tag{4.69d}$$

$$\mathbf{K}_{\varsigma u} = \int_{\mathcal{B}_0} g(\mathfrak{d})\mathbf{M}(\boldsymbol{\xi})^{\mathrm{T}}\mathbb{C}\mathbf{B}(\mathbf{d})\,\mathrm{d}\Omega; \tag{4.70a}$$

$$\mathbf{K}_{\varsigma\varsigma} = \int_{\mathcal{B}_0} g(\mathfrak{d})\mathbf{M}(\boldsymbol{\xi})^{\mathrm{T}}\mathbb{C}\mathbf{M}(\boldsymbol{\xi})\,\mathrm{d}\Omega, \tag{4.70b}$$

$$\mathbf{K}_{\varsigma\tilde{\mathfrak{d}}} = \int_{\mathcal{B}_0} -2(1-\mathfrak{d})\mathbf{M}(\boldsymbol{\xi})^{\mathrm{T}}\mathbf{S}\mathbf{N}(\boldsymbol{\xi})\,\mathrm{d}\Omega; \tag{4.70c}$$

$$\mathbf{K}_{\varsigma T} = \int_{\mathcal{B}_0} \mathbf{M}(\boldsymbol{\xi})^{\mathrm{T}}\mathbf{Z}\hat{\mathbf{N}}(\boldsymbol{\xi})\,\mathrm{d}\Omega \tag{4.70d}$$

$$\mathbf{K}_{\tilde{\mathfrak{d}}\mathbf{d}} = \int_{\mathcal{B}_0} -2(1-\mathfrak{d})\mathbf{N}(\boldsymbol{\xi})^{\mathrm{T}}\mathbf{S}\mathbf{B}(\mathbf{d})\,\mathrm{d}\Omega; \tag{4.71a}$$

$$\mathbf{K}_{\tilde{\mathfrak{d}}\varsigma} = \int_{\mathcal{B}_0} -2(1-\mathfrak{d})\mathbf{N}(\boldsymbol{\xi})^{\mathrm{T}}\mathbf{S}\mathbf{M}(\boldsymbol{\xi})\,\mathrm{d}\Omega, \tag{4.71b}$$

$$\mathbf{K}_{\tilde{\mathfrak{d}}\tilde{\mathfrak{d}}} = \int_{\mathcal{B}_0} \left[2\frac{G_c}{l}\mathcal{H}\right]\mathbf{N}(\boldsymbol{\xi})^{\mathrm{T}}\mathbf{N}(\boldsymbol{\xi})\,\mathrm{d}\Omega + \int_{\mathcal{B}_0} 2G_c l\mathbf{B}^{\mathfrak{d}}(\boldsymbol{\xi})^{\mathrm{T}}\mathbf{B}^{\mathfrak{d}}(\boldsymbol{\xi})\,\mathrm{d}\Omega, \tag{4.71c}$$

$$\mathbf{K}_{\tilde{\mathfrak{d}}T} = \int_{\mathcal{B}_0} -2(1-\mathfrak{d})\mathbf{N}(\boldsymbol{\xi})\mathbf{B}^{T}(\mathbf{d})\hat{\mathbf{N}}(\boldsymbol{\xi})\,\mathrm{d}\Omega, \tag{4.71d}$$

$$\begin{aligned}\mathbf{K}_{T\mathbf{d}} = &\int_{\mathcal{B}_0} g(\mathfrak{d})\Delta_{\mathbf{d}}[J]\mathbf{B}_T^{\mathrm{T}}\mathbf{F}^{-1}\cdot\mathbf{k}\cdot\mathbf{F}^{-\mathrm{T}}\cdot\nabla_{\mathbf{X}}T\ \mathrm{d}\Omega\\ &+\int_{\mathcal{B}_0} g(\mathfrak{d})J\mathbf{B}_T^{\mathrm{T}}\left(\Delta_{\mathbf{d}}[\mathbf{F}^{-1}]\cdot\mathbf{k}\cdot\mathbf{F}^{-\mathrm{T}}+\mathbf{F}^{-1}\cdot\mathbf{k}\cdot\Delta_{\mathbf{d}}[\mathbf{F}^{-\mathrm{T}}]\right)\cdot\nabla_{\mathbf{X}}T\ \mathrm{d}\Omega\\ &-\int_{\mathcal{B}_0} \hat{\mathbf{N}}^{\mathrm{T}}\frac{T}{\Delta t}\mathbf{Z}^{\mathrm{T}}\mathbf{B}\,\mathrm{d}\Omega,\end{aligned} \tag{4.72a}$$

$$\mathbf{K}_{T\varsigma} = -\int_{\mathcal{B}_0} \hat{\mathbf{N}}(\boldsymbol{\xi})^{\mathrm{T}}\frac{T}{\Delta t}\mathbf{Z}^{\mathrm{T}}\mathbf{M}(\boldsymbol{\xi})\,\mathrm{d}\Omega; \tag{4.72b}$$

$$\mathbf{K}_{T\mathfrak{d}} = \int_{\mathcal{B}_0} 2(1-\mathfrak{d})\hat{\mathbf{N}}(\boldsymbol{\xi})^{\mathrm{T}}(\mathbf{Z}^{\mathrm{T}}\dot{\mathbf{E}})\mathbf{N}(\boldsymbol{\xi})\,\mathrm{d}\Omega + \int_{\mathcal{B}_0} 2(1-\mathfrak{d})J\mathbf{B}_T^{\mathrm{T}}\mathbf{F}^{-1}\cdot\mathbf{k}\cdot\mathbf{F}^{-\mathrm{T}}\cdot\nabla_{\mathbf{X}}T\ \mathrm{d}\Omega, \tag{4.72c}$$

$$\begin{aligned}\mathbf{K}_{TT} = &\int_{\mathcal{B}_0} \hat{\mathbf{N}}(\boldsymbol{\xi})^{\mathrm{T}}\frac{c_p}{\Delta t}\hat{\mathbf{N}}(\boldsymbol{\xi})\,\mathrm{d}\Omega - \int_{\mathcal{B}_0} g(\mathfrak{d})\hat{\mathbf{N}}(\boldsymbol{\xi})^{\mathrm{T}}(\mathbf{Z}^{\mathrm{T}}\dot{\mathbf{E}})\hat{\mathbf{N}}(\boldsymbol{\xi})\,\mathrm{d}\Omega\\ &+\int_{\mathcal{B}_0} g(\mathfrak{d})J\mathbf{B}_T^{\mathrm{T}}\mathbf{F}^{-1}\cdot\mathbf{k}\cdot\mathbf{F}^{-\mathrm{T}}\mathbf{B}_T\ \mathrm{d}\Omega.\end{aligned} \tag{4.72d}$$

Here, $\mathbf{K}_{\mathbf{dd},\mathrm{geom}}$ refers to the geometric contribution and the $\mathbf{K}_{\mathbf{dd},\mathrm{mat}}$ is the material contribution. Also, $\Delta_{\mathbf{d}}[J]$ and $\Delta_{\mathbf{d}}[\mathbf{F}^{-1}]$ and $\Delta_{\mathbf{d}}[\mathbf{F}^{-\mathrm{T}}]$ represents the linearization with respect to the kinematic field of the Jacobian J of the transformation $\mathbf{F}$, the inverse of the modified deformation gradient and its transpose, respectively, which lead to additional geometrical terms. The overall algorithm of the implementation can be found in our recent article [231] (without phase-field).

Since inter-element continuity is not required for enhanced strains, as in [207], they can be condensed out at the element level via a standard condensation process. Thus, the condensed version of the stiffness matrix given in Eq.(4.68) reads

$$\begin{bmatrix} \mathbf{K}^*_{\mathbf{d}\mathbf{d}} & \mathbf{K}^*_{\mathbf{d}\tilde{\mathfrak{d}}} & \mathbf{K}^*_{\mathbf{d}T} \\ \mathbf{K}^*_{\tilde{\mathfrak{d}}\mathbf{d}} & \mathbf{K}^*_{\tilde{\mathfrak{d}}\tilde{\mathfrak{d}}} & \mathbf{K}^*_{\tilde{\mathfrak{d}}T} \\ \mathbf{K}^*_{T\mathbf{d}} & \mathbf{K}^*_{T\tilde{\mathfrak{d}}} & \mathbf{K}^*_{TT} \end{bmatrix} \begin{bmatrix} \Delta\mathbf{d} \\ \Delta\mathfrak{d} \\ \Delta\hat{\boldsymbol{T}} \end{bmatrix} = \begin{bmatrix} \tilde{\mathcal{R}}^{\mathbf{d}} \\ \tilde{\mathcal{R}}^{\mathfrak{d}} \\ \tilde{\mathcal{R}}^{T} \end{bmatrix} \tag{4.73}$$

where the element stiffness contribution takes the form

$$\begin{aligned} \mathbf{K}^*_{\mathbf{d}\mathbf{d}} = \mathbf{K}_{\mathbf{d}\mathbf{d}} - \mathbf{K}_{\mathbf{d}\varsigma}\mathbf{K}^{-1}_{\varsigma\varsigma}\mathbf{K}_{\varsigma\mathbf{d}};\;\; \mathbf{K}^*_{\mathbf{d}\tilde{\mathfrak{d}}} = \mathbf{K}_{\mathbf{d}\tilde{\mathfrak{d}}} - \mathbf{K}_{\mathbf{d}\varsigma}\mathbf{K}^{-1}_{\varsigma\varsigma}\mathbf{K}_{\varsigma\tilde{\mathfrak{d}}}, \\ \mathbf{K}^*_{\mathbf{d}T} = \mathbf{K}_{\mathbf{d}T} - \mathbf{K}_{\mathbf{d}\varsigma}\mathbf{K}^{-1}_{\varsigma\varsigma}\mathbf{k}_{\varsigma T};\;\; \mathbf{K}^*_{\tilde{\mathfrak{d}}\mathbf{d}} = \mathbf{K}_{\tilde{\mathfrak{d}}\mathbf{d}} - \mathbf{K}_{\tilde{\mathfrak{d}}\varsigma}\mathbf{K}^{-1}_{\varsigma\varsigma}\mathbf{k}_{\varsigma\tilde{\mathfrak{d}}}, \\ \mathbf{K}^*_{\tilde{\mathfrak{d}}\tilde{\mathfrak{d}}} = \mathbf{K}_{\tilde{\mathfrak{d}}\tilde{\mathfrak{d}}} - \mathbf{K}_{\tilde{\mathfrak{d}}\varsigma}\mathbf{K}^{-1}_{\varsigma\varsigma}\mathbf{K}_{\varsigma\tilde{\mathfrak{d}}};\;\; \mathbf{K}^*_{\mathbf{d}T} = \mathbf{K}_{\tilde{\mathfrak{d}}T} - \mathbf{K}_{\tilde{\mathfrak{d}}\varsigma}\mathbf{K}^{-1}_{\varsigma\varsigma}\mathbf{K}_{\varsigma T}, \\ \mathbf{K}^*_{T\mathbf{d}} = \mathbf{K}_{T\mathbf{d}} - \mathbf{K}_{T\varsigma}\mathbf{K}^{-1}_{\varsigma\varsigma}\mathbf{k}_{\varsigma\mathbf{d}};\;\; \mathbf{K}^*_{T\tilde{\mathfrak{d}}} = \mathbf{K}_{T\tilde{\mathfrak{d}}} - \mathbf{K}_{T\varsigma}\mathbf{K}^{-1}_{\varsigma\varsigma}\mathbf{K}_{\varsigma\tilde{\mathfrak{d}}}, \\ \mathbf{K}^*_{TT} = \mathbf{K}_{TT} - \mathbf{K}_{T\varsigma}\mathbf{K}^{-1}_{\varsigma\varsigma}\mathbf{K}_{\varsigma T}, \end{aligned} \tag{4.74}$$

along with the residual force vectors

$$\begin{aligned} \tilde{\mathcal{R}}^{\mathbf{d}} &= \hat{\mathcal{R}}^{u}_{\text{ext}} - \hat{\mathcal{R}}^{u}_{\text{int}} + \mathbf{K}_{\mathbf{d}\varsigma}\mathbf{K}^{-1}_{\varsigma\varsigma}\hat{\mathcal{R}}^{\varsigma}_{\text{int}} \\ \tilde{\mathcal{R}}^{\mathfrak{d}} &= -\hat{\mathcal{R}}^{\mathfrak{d}}_{\text{int}} + \mathbf{K}_{\mathfrak{d}\varsigma}\mathbf{K}^{-1}_{\varsigma\varsigma}\hat{\mathcal{R}}^{\varsigma}_{\text{int}} \\ \tilde{\mathcal{R}}^{T} &= \hat{\mathcal{R}}^{T}_{\text{ext}} - \hat{\mathcal{R}}^{T}_{\text{int}} + \mathbf{K}_{T\varsigma}\mathbf{K}^{-1}_{\varsigma\varsigma}\hat{\mathcal{R}}^{\varsigma}_{\text{int}} \end{aligned} \tag{4.75}$$

The resulting system of algebraic equations in Eq. (4.73) can be solved using monolithic/staggered solution scheme using different types of solvers such as nonlinear Newton-Raphson, quasi-Newton based solvers such as Broyden–Fletcher–Goldfarb–Shanno (BFGS), coupled displacement solvers, etc.

Regarding the numerical implementation, a staggered scheme is used for the solution of the coupled problem. The coupled terms with respect to the damage variable $\mathfrak{d}$ are suppressed owing to the staggered scheme implementation. i.e, $\mathbf{K}_{d\varsigma}, \mathbf{K}_{dT}, \mathbf{K}_{T\varsigma}, \mathbf{K}_{T\tilde{\mathfrak{d}}}, \mathbf{K}_{\tilde{\mathfrak{d}}T}, \mathbf{K}_{\tilde{\mathfrak{d}}\varsigma}\mathbf{K}_{\varsigma T}$. Moreover, it was noticed that the standard Newton solver of `ABAQUS` performs in a satisfactory manner in terms of achieving convergence equilibrium states at each time step for thermo-mechanical coupled applications. Note also that for the problem without non-linearity (geometric), BFGS leads to very efficient computations, reducing the number of equilibrium iteration at each time step. However, in the current computations and when the geometric non-linearity is involved, BFGS computation times significantly increase for the achievement of equilibrium solutions at each time step. The comparison between the solvers in terms of CPU times or iteration is out of scope for this article. In the following numerical application section, temperature assisted fracture in Section 4.5.2, plate with notch and many holes in Section 4.5.4, plate with two edge notch in Section 4.6.2, plate with notch Section 4.6.5, and 4.6.6 are solved using BFGS scheme, whereas, the other examples are solved using the standard Newton solver of `ABAQUS`. The numerical examples in section 4.4 are performed using the coupled temperature-displacement solver. Note that, the choice of solution scheme mentioned above is just to show that both solvers can be used in the solution scheme.

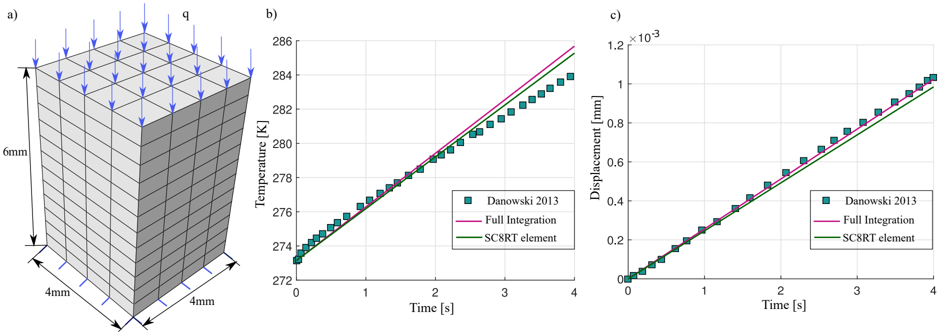

Figure 30: a)Initial and boundary conditions for second Danilovskaya problem. b) Comparison of temperature between Danowski, current model (Full Integration) and `ABAQUS` SC8RT element. c) Comparison of displacement between Danowski, current model and `ABAQUS` SC8RT element.

4.4 Virtual testing: thermo-elastic applications

This section presents the numerical simulations to evaluate the 11 parameter non-linear thermo-mechanical solid shell model with the presence of cohesive-like interfaces to simulate decohesion events. When $\mathfrak{d} = 0$ in all the residual functions in Eqs. (4.32), (4.33), (4.34), (4.36) vanish leading to $\mathcal{R}^{\mathfrak{d}} = 0$. Similarly, the stiffness matrix in the Eq. (4.68) changes as a consequence, only $\Delta \mathbf{d}$, and ΔT in the Eq. (4.73) has to be solved.

First, we verify the current model by taking the second Danoilovskaya problem as in [248] and compare the temperature and displacement distribution with the original experiment and the in-build `ABAQUS` SC8RT element. The second application recalls the benchmark example as in [249] to assess the implementation of the current solid shell element for thermo-elastic applications. The response of this element is further examined in the application of a thin bar subjected to bending, crushing, and lifting to highlight the capabilities of the thermo-mechanical solid shell (without interface). Subsequently, we incorporate two different cohesive zone models, the Tveergard [233], and the exponential one [239] to model decohesion phenomena, which are first employed for the case of a plate under tensile conditions with the presence of a cohesive layer. Finally, a peeling test is shown to exploit the principal capabilities of the present formulation fully. Different effects such as temperature, displacement, material, and cohesive properties on the simulations are discussed.

4.4.1 Model verification

The second Danilovskaya problem is often used for verification of a fully coupled thermo-mechanical model, see [248, 246] and the references therein. A cuboid with dimensions as in Fig. 30a) is subjected to a uniform temperature change due to the heat flux $q = \bar{h}(T_0 - T_\infty)$ applied on one surface, with $\bar{h}$ being heat transfer coefficient. The y-direction and z-directions are fixed on other surface of the cuboid so that problem essential becomes one dimensional. The thermal properties are considered according to [248] as: i) ambient temperature $T_\infty = 373.15$K, ii) the surface initial temperature $T_0 = 273.15$K, iii) Young's modulus $E = 210$GPa, iv) Poisson's ratio $\nu = 0.3$, v) density $\rho = 7850$ kg/m^3, vi) co-efficient of linear thermal expansion $\alpha = 1.1 \times 10^{-5}/^o$ K, vii) thermal conductivity $k_0 = 1.03$ N/s^o K, and viii) mean specific heat capacity $c_p = 0.896$ m^2/s^2 ^{o}K. The cuboid is discritized with $12 \times 4 \times 4$ elements. Fig. 30b) and Fig. 30c) shows the comparison of temperature and the displacement between Danowski (2013) [248], `ABAQUS` SC8RT element and the proposed model (named as full integration), leading to a very satisfactory agreement.

4.4.2 Slit annular plate subjected to lifting line force

An annular plate with a slit cut along the radial direction is considered, see Fig. 31a). The ring is clamped at one side whereas the other side, a distributed force of 0.01 N/mm is applied. A temperature of 100^o C is applied on both the inner and outer radius of the annular plate. Both the temperature and the line force are applied linearly for a duration of $t = 1$. The geometric parameters considered in this example are: i) inner radius $R_i = 6$mm, ii) outer radius $R_o = 10$ mm and thickness $h = 0.05$ mm. The mechanical properties of the solid shell are assumed homogeneous: Young's modulus $E = 68$ GPa, Poisson's ratio $\nu = 0.32$, co-efficient of linear thermal expansion $\alpha = 22 \times 10^{-6}/^o$C, thermal conductivity $k_0 = 0.205$ W/mm^{o}C and mean specific heat capacity $c_p = 0.896$ KJ/Kg ^{o}C.

These structures usually suffer from transverse shear locking as a consequence of the large characteristic radius to thickness ratio (> 100). The solid element proposed alleviates the underpinned issue as seen in Fig. 31. The Fig. 31b) shows the displacement field at time step $t = 0.025$ and the temperature distribution can be seen in Fig. 31c). At the end of the full load application, i.e., $t = 1$, the large displacement and temperature distribution can be seen in Fig. 31d). The reaction force at the point A (also for other points along the clamped edge) increases if material parameters and the mechanical load are kept constant and only change the temperature boundary condition.

4.4.3 Bending, buckling and pulling of a thin plate

The problem under analysis consists of a square plate of thickness $h = 0.2$ mm with different loading conditions. The material properties considered are coincident with those used for the annular ring. The thin plate under bending usually suffers from shear locking. The plate dimensions are presented in Fig. 32a), and the same is maintained throughout. A temperature of 50^oC is applied on both ends of the plate, where the plate is fixed in Fig. 32a). The displacement of 30 mm is applied in the middle line to simulate a large displacement. The displacement field can be seen in Fig. 32a). Moreover, the crushing type load of 10 mm is applied on one edge of the square plate, restricting all degrees of freedom movement apart from the load applied so that the square plate is forced to undergo buckling. The temperature boundary conditions replicate those corresponding to the previous case. The current results are presented in Fig. 32b), where a clear central buckling shape is depicted. In an alternative experiment, a bending load of 5 mm is applied to one end, and fully restraining the opposite edge. The displacement field at of the bending is registered in Fig. 32c). The reaction forces for all three examples are plotted in Fig. 32d). The reactions forces are taken at the respective load application points and restricted only to a displacement magnitude of 10 mm so that a quantitative analysis can be made. It can be observed that for buckling (crushing), the

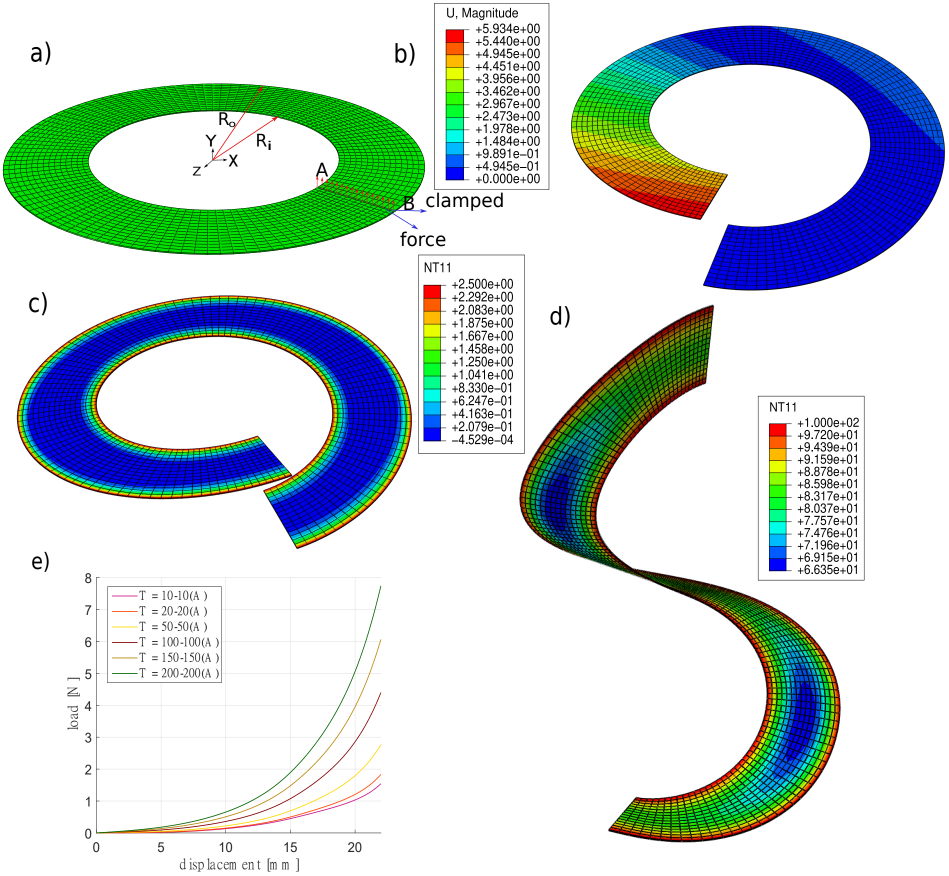

Figure 31: Slit annular ring subjected to line force. a) Geometry and load data. b) Displacement field distribution at the time step $t = 0.0025$. c) Temperature distribution at time step $t = 0.0025$. d) Temperature distribution at time step $t = 1$. e) Load displacement evolution cures at point A for various temperature boundary conditions.

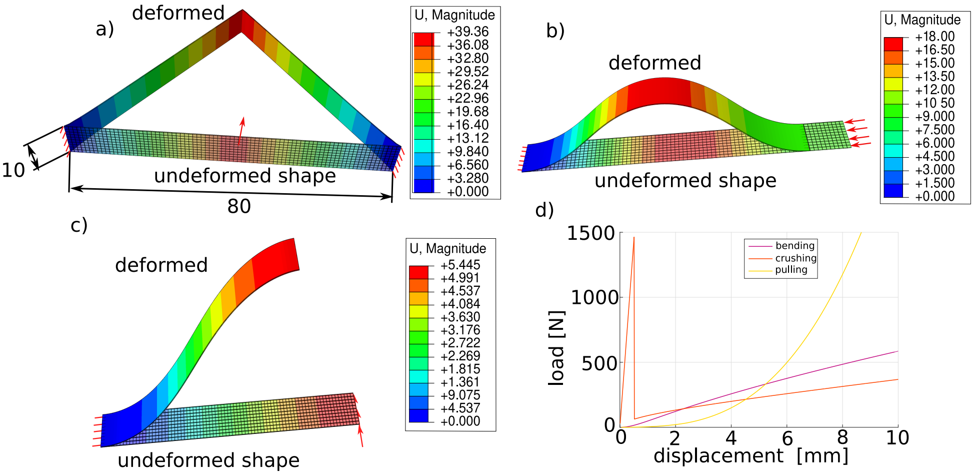

Figure 32: a) Pulling the bar from middle. b) Buckling of the bar. c) Bending thickness of 0.2 mm.

E (GPa)	ν	$\alpha_1(10^{-6}/^o\text{C})$	$\alpha_2(10^{-6}/^o\text{C})$	$\alpha_3(10^{-6}/^o\text{C})$	$k_0^1(\text{W/mm}^o\text{C})$	$k_0^2(\text{ W/mm}^o\text{C})$	$k_0^3(\text{W/mm}^o\text{C})$	$c_p(\text{KJ/Kg}^o\text{C})$
1.2	0.3	28	28	28	0.230	0.230	0.230	0.01

Table 8: Properties of the solid shell.

reactions increase very quickly during the initial loading. Once buckling starts to occur, a sudden drop in the reaction force is observed. Later, the reactions keep increasing steadily. In the pulling example, the initial slope of the reaction is the highest and it keeps decreasing throughout. In case of the bending example, the reaction forces increase steadily.

4.4.4 Plate under tensile loading

This example considers a plate with a cohesive interface as a benchmark example to understand the effects of variation of different model, structural, and temperature parameters. The structure as in Fig. 33 is subjected to tension at one end, while the opposite end is fixed. An initial temperature of zero degree Celsius is assumed at time $t = 0$ and the temperature of T_1^oC and T_2^oC is applied on the fixed and loaded ends, respectively. The orientation of the solid elements and the cohesive layer is shown in Fig. 33. The cohesive zone model parameters have been selected so that normal tractions are dominant in the cohesive layer. Hence, the cohesive layer is oriented towards the direction of the applied force.

As a baseline example, the model as in Fig. 33 with thickness of $h = 0.1$ mm is considered. The temperature boundary conditions of $T_1 = 50^o$C and $T_2 = 100^o$C is applied on the prescribed ends with reference temperature $T_0 = 100^o$C . The displacement load of $\bar{u} = 0.5$ mm are applied to one side as in Fig. 33. The properties of the solid shell and the cohesive zone model are listed in Tab. 8 and 9, respectively.

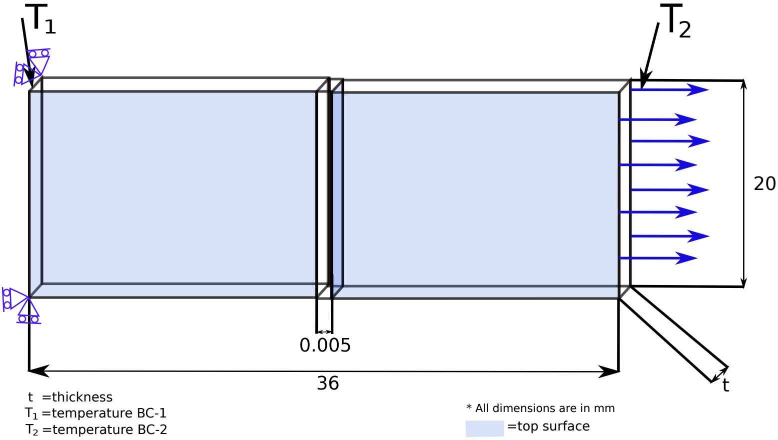

Figure 33: Plate with a cohesive interface.

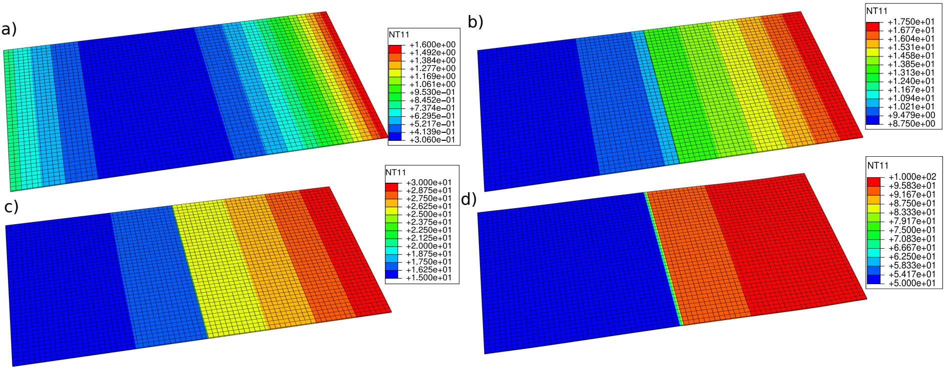

Figure 34: Variation of temperature (NT11) for $T_1 = 50^o$C and $T_2 = 100^o$C for thickness of 0.1 mm. a) At time $t = 0.0016$. b) At time $t = 0.175$. c)At time $t = 0.3$. d) At time $t = 1$.

Cohesive Model	σ_c (MPa)	τ_{1c} (MPa)	τ_{2c} (Mpa)	$\mathcal{G}_{Ic}$(N/mm)	$\mathcal{G}_{IIc}$ (N/mm)	$\mathcal{G}_{IIIc}$(N/mm)	k_0(W/mm^{o}C)
Exponential	1	0.5	0.5	0.2	0.1	0.1	0.230

Table 9: Properties of the cohesive zone model.

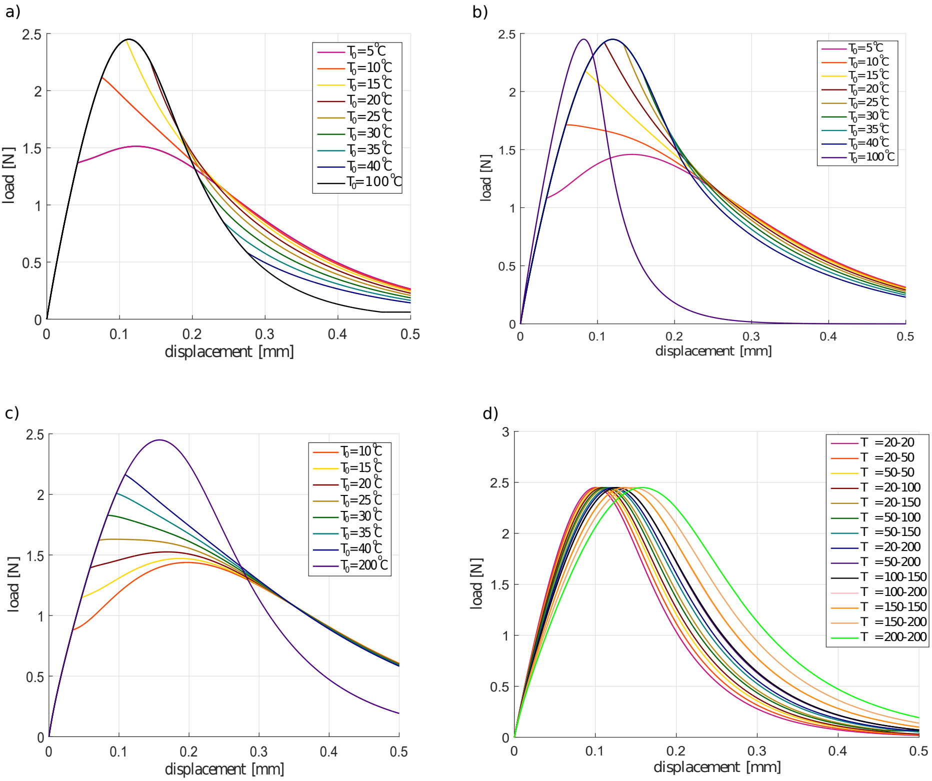

Figure 35: Variation of the reaction forces for different temperature boundary conditions. a) Model-A with $T_1 = 50^o\text{C}, T_2 = 100^o\text{C}$. b) Model-B with $T_1 = T_2 = 100^o\text{C}$. c) Model-C with $T_1 = T_2 = 200^o\text{C}$. d) Change of temperature.

Fig. 34 shows the variation of the temperature at different time t. Here, both displacement and temperature are applied linearly, with increments $\bar{u} = 0.0005$ mm $T_1 = 0.05^o$C and $T_2 = 0.1^o$C at each time step of $\Delta t = 0.001$s at each step so that 1000 steps are taken to reach the time step 1s and applied the load fully. All the experiments in this section follow a similar procedure, unless otherwise specified. At time ($t = 0.016$s), it can be seen from Fig. 34a) that the temperature diffuses and the cohesive interface is still are intact and perfectly conducting. At $t = 0.175$s, the cohesive zone model starts developing damage. From Eq. (4.29), the conductance of the interface starts reducing depending on damage, which can be observed in Fig. 34b). At $t = 0.3$s, the interface is fully separated, $\mathfrak{d} = 1$ and the interface conductance is $h_{cz} = 0$, see the final temperature distribution with a sudden jump across the interface in Fig. 34c) and Fig. 34d). In addition, notice that, due to the exponential decay of the cohesive traction, the damage variable never reaches 1. In such a case, the thermal conductance of the interface is never zero but it is extremely small.

Keeping the material parameters as in Tab. 8 and 9, changing only the temperature boundary conditions and reference temperature $T_0 = \max(T_1, T_2)$, the resulting reaction forces are shown in Fig. 35d). As the cumulative temperature increases, the reaction curves shift right, preserving the total fracture energy required for the system to break. Notice that, T_0 represents the environment temperature, and hence, it appears that the energy requires to break the interface changes little, which is contradicting, the reason for the shift can be explained as T_0 is kept changing as the cumulative temperature increases. In order to understand this more clearly, three cases are considered in Figs. 35a) b) c). The model-A considers temperature boundary conditions $T_1 = 50^o$C and $T_2 = 100^o$C. Similarly model-B and model-C consider temperature boundary conditions $T_1 = T_2 = 100^o$C and $T_1 = T_2 = 200^o$C respectively. The change of reference temperature in each of the model-A, B, C are presented in Fig. 35 a), b), c) respectively. In each of the reaction curves, the reference temperature T_0 indicates the temperature at which the interface starts to lose the peak critical traction. This T_0 also can be considered as the reference environmental temperature, meaning that, if the material is placed at different temperatures (other than room temperature), the material properties change. For the part of the solid shell, the reference temperature is directly given in Kirchhoff-Saint-Venant material model as in Eq. (4.4). For the corresponding cohesive zone, the reference temperature is added to the material model via Eq. (4.24). As the reference temperature decreases, the reaction curves can be seen shifting downwards, decreasing the total fracture energy required for fracture. This trend can be observed in all the considered models in Fig. 35 a), b), c). In conclusion, any material law that includes the variation of peak cohesive tractions depending on temperature can accommodate the reference temperature.

Similarly, keeping all the parameters constant with temperature boundary conditions $T_1 = T_2 = 100^o$C and reference temperature $T_0 = 100^o$C. i.e., assuming that the peak cohesive traction does not decrease as the temperature increases until 100^oC, keeping the ratio $\dfrac{\sigma_c}{\tau_c} = \dfrac{\mathcal{G}_{Ic}}{\mathcal{G}_{IIc}} = 2$, the reaction curves for the variation of σ_c and $\mathcal{G}_{Ic}$ are plotted in Fig. 36 a). As the σ_c, the fracture energy also increases. As the $\mathcal{G}_{Ic}$ increases, the cumulative fracture energy also increases. The main feature of the solid shell formulation is that these can be applied for both thin and thick models. This has been illustrated in Fig. 36b), where, reaction curves for change of thickness are plotted.

The properties for the exponential-like interface model [234] for initial temperatures of

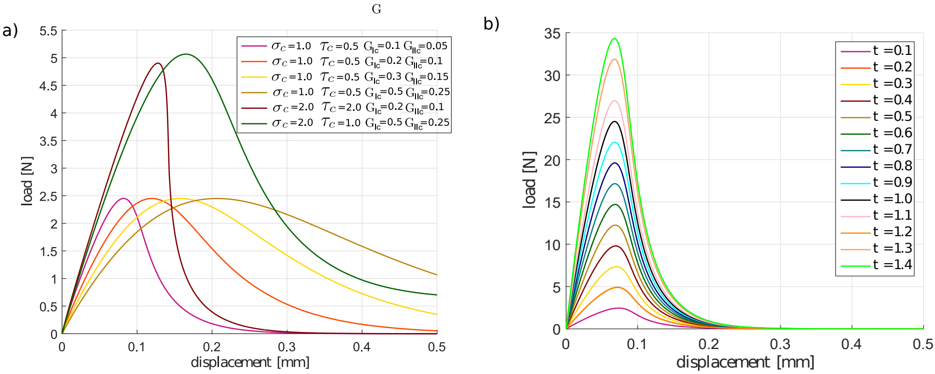

Figure 36: a)Variation of σ_c and $\mathcal{G}_C$. b) Variation of thickness.

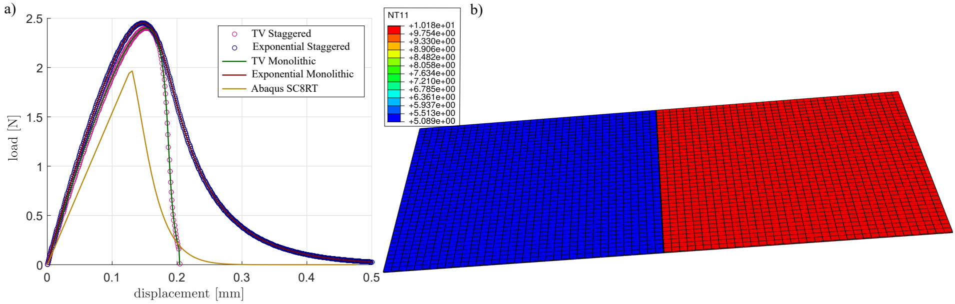

Figure 37: a) Comparison between TV model and exponential model, and comparison between staggered scheme and monolithic scheme and ABAQUS SC8RT. b) Temperature distribution for $T_1 = 50^0$C, $T_2 = 100^0$C at displacement $\bar{u} = 0.1$mm.

$T_1 = T_2 = 50^o$C are listed in Tab. 9. The corresponding properties for the the polynomial-like cohesive model [233] and keeping the maximum traction constants leads to $\sigma_c = 1$ (MPa), maximum normal displacement $\delta_n = 0.1$ mm, and $\gamma = 0.5$. The reactions are shown in Fig. 37. Even though the paper presents a fully monolithic scheme while describing the finite element implementation, a solution via a staggered scheme could also be used to solve the model. The reactions for the differences between fully monolithic and staggered scheme implementation (details omitted for brevity reasons) can be seen in Fig 37a). No observable differences have been noticed in this example that stems from the choice of solution scheme. Although, the exponential model tends to be asymptotic towards zero, where damage is tending to unity. In terms of temperature field, this means the thermal conductance is asymptotically going to zero. In contrast, the the polynomial-like cohesive model tends to a more abrupt decay after the thermal conductance is zero during the decohesion.

On the contrary, the ABAQUS SC8RT element combined with the ABAQUS built-in cohe-

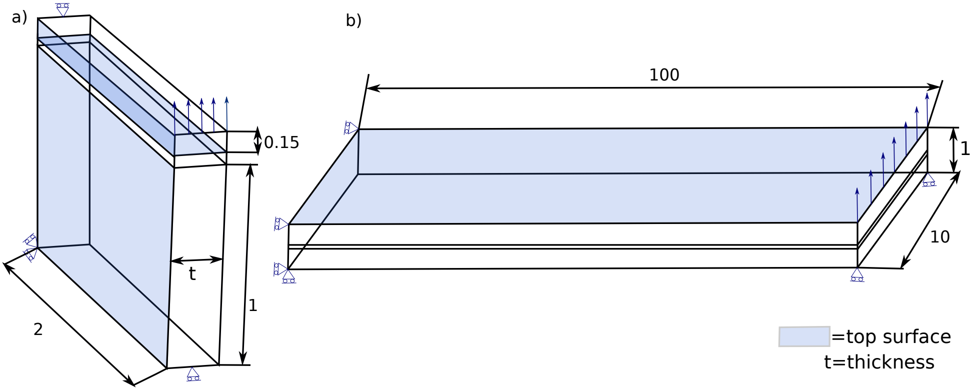

Figure 38: a) Model-A with thickness of $t = 0.1$ mm. b) Model-B with cohesive layer thickness of 0.2 mm.

sive zone element COH3D8 (with no thermal effect) is used to perform the same experiment with properties as in Tab. 10. The corresponding results show that the reaction curves features a similar evolution with respect to that of the polynomial-like cohesive model [233] and exponential-like interface model [234] without temperature. Moreover, Fig. 37b) shows the distribution of shell temperature at the displacement of 0.1mm before the failure. It is observed that the two shells connected by the interface behave like two different shells without any thermal interaction/heat transfer, which leads to a nonphysical solution. Change of temperature boundary conditions T_1 and T_2 is observed to have no impact on the reaction curves in this case. This pinpoints the importance of considering the thermal effect in the decohesion evolution, which is not incorporated in most of the available FE packages.

Nominal stress (MPa)	Nominal stress in shear (MPa)	Nominal fracture energy (N/mm)	Fracture energy in shear (N/mm)	Power (BK law)
1	0.5	0.1	0.05	2.15

Table 10: Cohesive layer properties.

4.4.5 Peeling application

This example concerns the performance of the new element for the large displacement and interplay between geometric and material nonlinearity. In the exponential model proposed, damage is not initiated by compression. These models work very well for models where compression is not desirable. It is observed that, Tvergaard Cohesive Zone model has a faster convergence rate during the strong nonlinear problem in the presence of mechanical and geometrical nonlinearities. Hence, for this reason, we adopt, for this example, the extension of the Tvergaard model to include temperature coupling in Sec. 4.2.5 using the same idea as in Sec. 4.2.4. It is noticed that both models give similar results, whereas the Tvergaard model

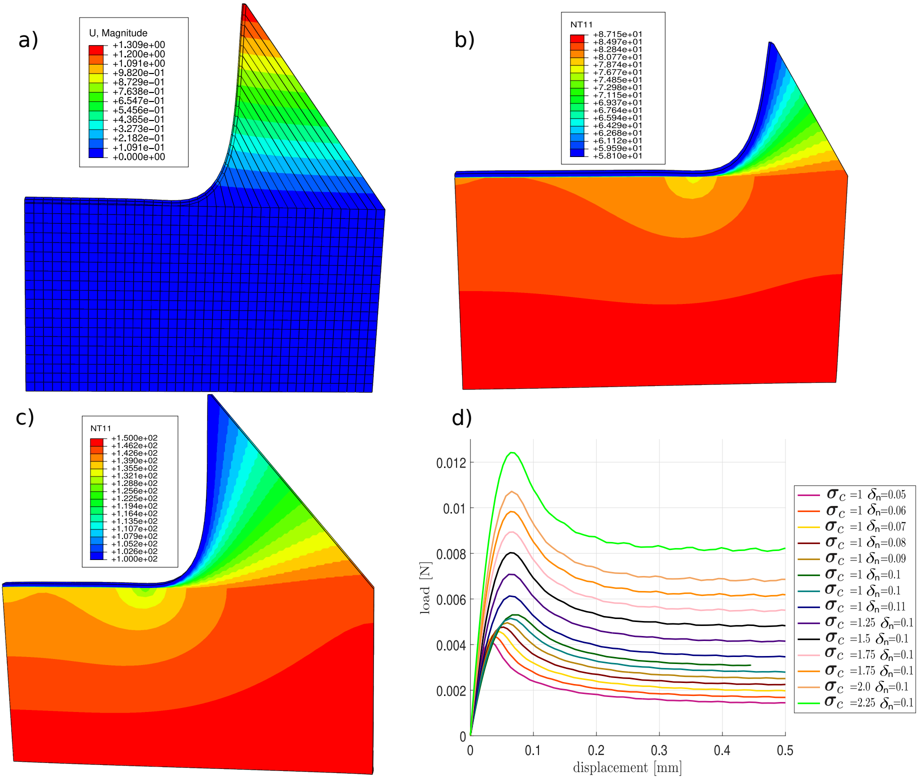

Figure 39: a) Displacement of model-A at time $\tau = 1$ for load $\bar{u} = 1$ mm. b) Temperature field for displacement of $\bar{u} = 0.07$mm. c) Temperature field for $\bar{u} = 1.0$ mm. d) Force v/s displacement curves of model-A for the variation of σ_c and maximum allowed gaps δ_n.

Cohesive Model	σ_c (MPa)	δ_n mm	γ	k_0(W/mm ^{o}C)
Tvergaard	1	0.1	0.2	0.230

Table 11: Properties of the cohesive zone model for peeling model-A.

Cohesive Model	σ_c (MPa)	δ_n mm	γ	k_0(W/mm ^{o}C)
Tvergaard	20	0.8	0.1	0.230

Table 12: Properties of the cohesive zone model for peeling model-B.

converges faster in this case.

We consider two different models for peeling motivated from the peeling of adhesive tapes as in [250] where the thin layer combined with a thin adhesive is peeled upon the substrate. Hereafter, this example is called model-A. The details of the model and the mesh orientation required for meshing are in Fig. 39a).

Model-B is motivated by the classic example of peeling the bonded thin plate. See, Fig. 39b) for the orientation of the top surface. More importantly, model-A has only one layer of cohesive layer along with the width, whereas model-B is allowed to have a multiple layer cohesive element along the width.

Model-A with the properties as in Tab. 8 for solid shell and Tab. 11 for the cohesive interface is considered with thickness $t = 0.1$ mm and temperature boundary condition of 150^{o}C is applied on the load side, and the 100^{o}C is applied on the bottom. Fig. 39a) illustrates the displacement field, including the non-linear effects. As in the exponential model, the Tvergaard model exhibits identical properties as that of the exponential model in terms of the temperature field at the interface. Fig. 39b) and Fig. 39c) illustrates the interplay of the temperature field (NT11) of the solid shell and the interface at displacement of $\bar{u} = 0.07$ mm and $\bar{u} = 1$ mm. It is observed that, as the interface starts peeling off, the heat conduction across the interface almost vanishes, and heat conduction takes place only in the undamaged interface portion ahead of the interface crack tip. Variation of the temperature boundary conditions for this model closely resembles that of the previous example, hence, omitted here for brevity. As an example keeping $T_0 = 150^o$C, the reactions for the variation of σ_c and normal gaps δ_n are presented in Fig. 39d).

The general properties of model-B are assumed as shown in Tab. 8 and Tab. 12. A total displacement of $\bar{u} = 30$mm is applied along with the boundary condition of 100^{o}C on one side (invisible side in the Fig. 39) and 100^{o}C on the other side. The displacement field and the temperature field are shown in Fig. 40a) and Fig. 40b). Fig. 40c) shows the variation of temperature field for temperature boundary $150 - 100^o$C. Model-B also exhibits similar properties as in model-A. As an example, the reaction curves for the variation of σ_c is presented in Fig. 40d). Note that after the applied displacement of $\bar{u} = 5$ mm, the behavior of the reactions are similar and repetitive. Hence, reaction forces until the applied displacement of $\bar{u} = 10$ mm is presented to have comprehensibility of the reaction forces.

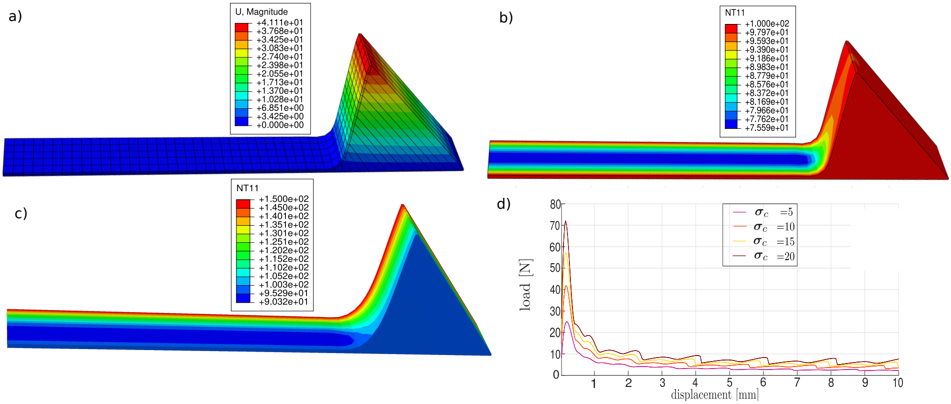

Figure 40: a) Displacement field for model-B along with mesh details. b) Distribution of temperature field for model-B with BC $100-100^o$C after displacement of $\bar{u} = 30$ mm. c) Distribution of temperature field for model-B with BC $150-100^o$C after displacement of $\bar{u} = 30$ mm. d) Force v/s displacement curves for variation of σ_c.

Material	E (MPa)	ν	$\alpha(10^{-6}/^o\text{K})$	$k_0(\text{W}/\text{mm}^o\text{K})$	$c_p(\text{kJ}/\text{kg}^o\text{K})$	$\mathcal{G}_C$ (MPa$\sqrt{\text{mm}}$)	l (mm)
Silicon	1.69×10^5	0.16	1.1	0.114	0.715	0.014394	0.05
Alumina	2.1×10^5	0.31	10.1	5.05	0.4	0.32	0.2
Zirconia	3.8×10^5	0.26	7.7	25	0.880	0.06634	0.2
Alluminium	8.84×10^4	0.32	22.0	0.205	0.896	0.545	0.06

Table 13: Properties of the simulated materials.

4.5 Thermo-mechanics with phase-field

In this section, the capabilities of the proposed phase-field model for thermo-mechanical solid shell formulation are assessed according to several representative examples. First, a benchmark test is proposed and passed. Then, problems characterized by temperature-assisted fracture are examined in relation to a technological phenomenon relevant for Silicon solar cells. Finally, examples concerning coupled mechanical-temperature effects, for small and large strain problems are shown for a series of structural problems with plates and curved shells. In order to show examples spanning the wide range of material behaviour (especially temperature effects), three different materials are considered in Tab. 13. There, E is the Young's Modulus, ν is the Poisson's ratio, α is the co-efficient of thermal expansion, k_0 is the thermal conductivity, c_p is heat capacity, $\mathcal{G}_C$ is the fracture energy, and l is the length scale of the phase field model.

4.5.1 Model validation

This example concerned with the application of the proposed model to a double-edged notched specimen. Fig. 41 shows the sketch of the model with an initial notch length $a = 0.1$

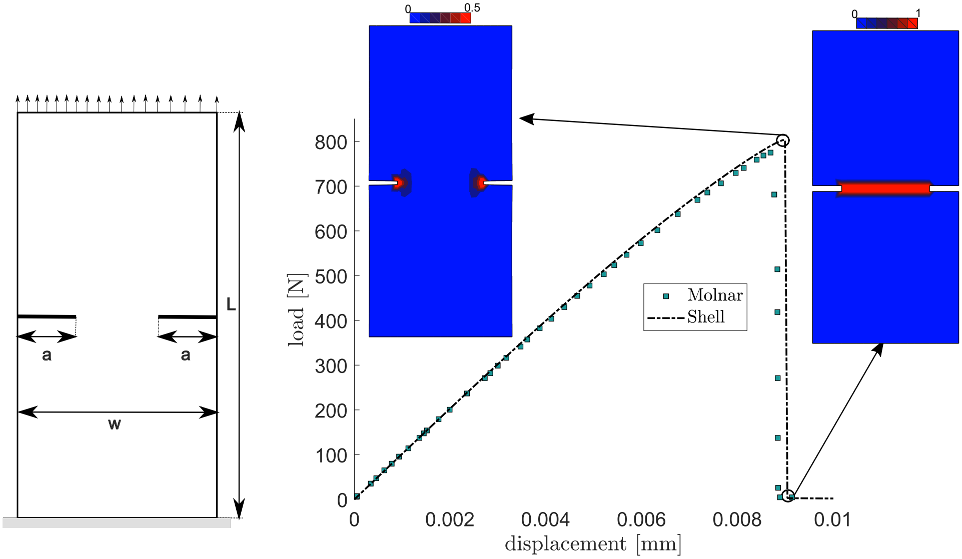

Figure 41: Verification example: geometry and force reaction-displacement evolution curve.

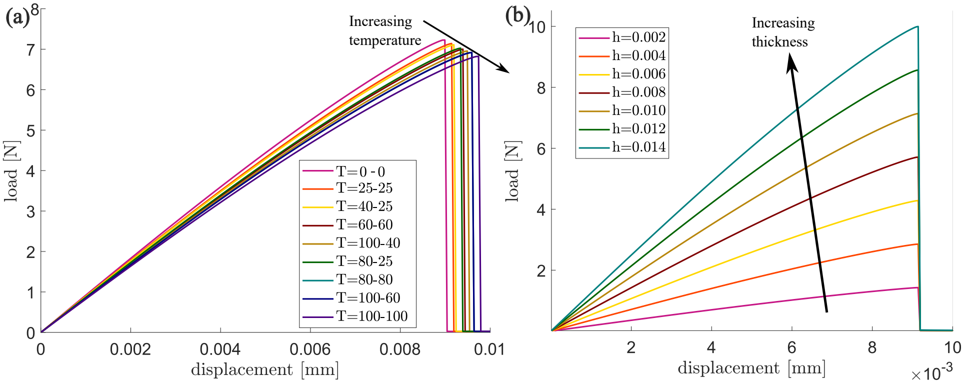

Figure 42: Double-edged notch specimen with (a) reactions for variation of temperatures, (b) reactions for variation of thickness.

mm, axial length $L = 1$ mm, width $w = 0.5$ mm and thickness $h = 0.01$ mm in line with the numerical experiment of [251] and has been studied by [252] by considering the alumina whose material properties are given in Tab. 13 Here, we used the length scale $l = 0.0075$ mm in line with the experiments in [251]. The model was discretized with 812 elements such that element size of $2l$ was kept along the crack path.

The displacement load of $\Delta = 0.01$ mm was applied in 1000 steps on the top surface, and the bottom surface was fully restrained as in Fig 41. The EAS and ANS are included in the whole domain but were turned off locally when the damage variable reaches $\mathfrak{d} = 0.5$ due to unstable crack propagation in the system.

Note that, due to the scarcity of thermo-mechanical crack propagation experiments, the comparison has been made based on standard examples proposed in [251]. In line with the numerical example reported in [251], where the temperature dependency was neglected, the temperature of the whole model was kept at $T = 0^o$C, which means that no external boundary temperature was inflicted upon the model. It can be argued that the local temperature T_0 is different from zero. Still, it is noticed that, numerically, the difference arises due to the difference between the initial temperature and the externally applied temperature rather than the absolute values. Hence, the all local temperatures are kept at T_0 for comparison.

The load-displacement curve for the evolution of the simulation shows a satisfactory agreement with the experimental results as in Fig. 41. The numerical experiments conducted in [251] consider the plane strain condition whose thickness is 1 mm. To match that, the reactions forced are multiplied by a factor of 100 since the thickness considered here is $h = 0.01$ mm.

The evolution of the phase-field variable $\mathfrak{d}$ at displacement just before and after the damage is shown in Fig. 41. This example is complemented by adding the thermal effect. For doing that, we select a temperature gradient within the domain, see the corresponding load-displacement evolution curves corresponding in Fig. 42(a). It can be readily seen that as the temperature increases, the maximum load-bearing capacity of the model decreases. Keeping the temperature boundary conditions ($T = 25^0 - 25^0$C) and the material properties constants, the thickness variation in the plate is considered. It is noticed that, as the thickness increases, the load-bearing capacity of the specimen increases, as shown in Fig. 42(b). It can be seen from Fig. 42(b) that there exists a direct linear mapping between the different variations of thickness. Meaning that, if load-displacement (say $F_1(t)$) curve for thickness h_1 is known, then for any thickness h_2, the load-displacement curve can be obtained from h_1 as $F_2(t) = F_1(t)\dfrac{h_2}{h_1}$.

4.5.2 Application to photo-voltaic panels

In this example, the proposed model is used to investigate the effects of cracking in silicon used for solar cells. Experimental results [253] and the numerical investigation [254] show that silicon defects may induce hot spots in solar cells. This phenomenon may enhance cracking, degrade the photovoltaic performance of the device, and eventually lead to safety issues.

Following [176, 254], it is discussed that during the manufacturing of a solar cell module, crack-free cells made of mono/poly-crystalline silicon are laminated inside a stack formed of an encapsulating polymer and a cover glass at a temperature around $T_0 = 150^o$C. Later, the

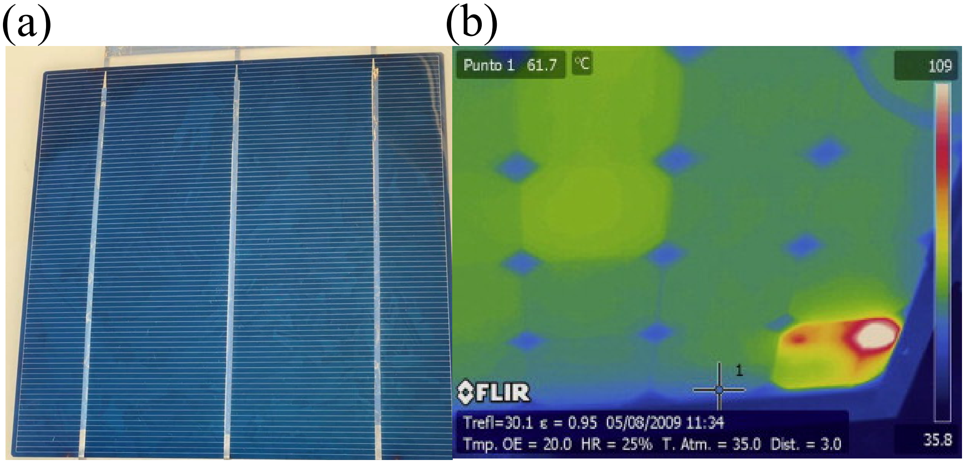

Figure 43: (a) Solar panel with bus bar. (b) Thermal images from thermal camera showing the local temperature rises (hot spots) in silica cells in case of cracks, adopted from [253].

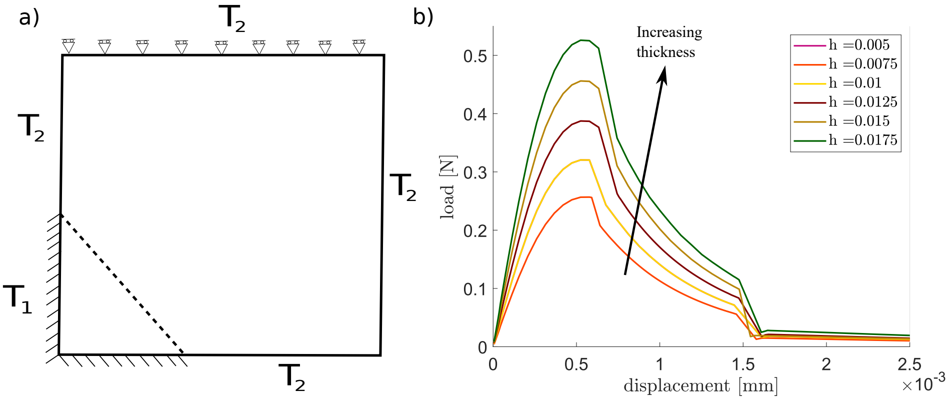

Figure 44: (a) Model under consideration. (b) Load-displacement curve for different solar cell thickness.

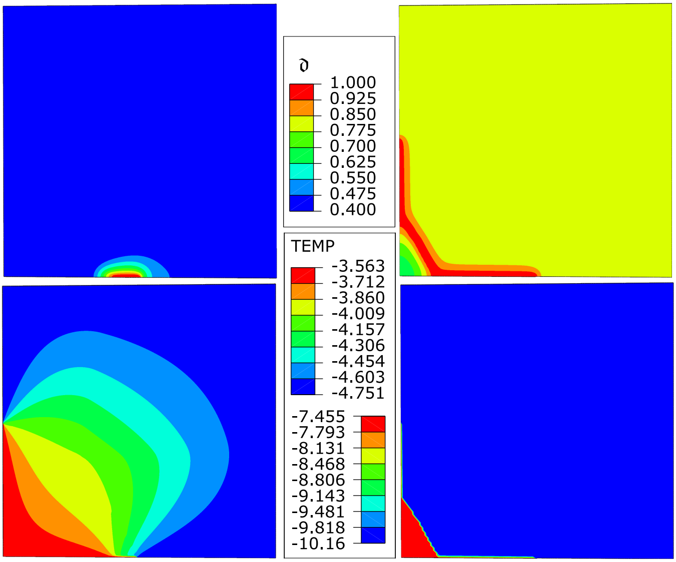

Figure 45: Temperature assisted fracture. (left) Figure on left represents phase-field and temperature distribution during initiation of fracture at step 118. (right) Fig on right represents phase-field and temperature distribution after the fracture at step 251.

module is cooled down to the ambient temperature with a final state with residual compressive stresses. Fig. 43(a) represents the solar cell with the glass laminate. A local temperature increase in thermal images, see Fig. 43(b) (adapted from [253]). The thermo-elastic displacement caused by these conditions Fig. 43(a) in the solar cells can induce fracture.

As an model example, a mono-crystalline silicon solar cell without any pre-existing crack is considered with properties as in Tab 13. The model is discretized with 16512 equidistant elements. The cell boundary $\partial\Omega$ is subdivided into $\partial\Omega_1$ and $\partial\Omega_2$, restrained as in Fig. 44(a). A temperature excursion $\Delta T_1 = -30^o$C is herein considered along $\partial\Omega_1$ to depict a temperature raise as compared to the other portion of the boundary, $\partial\Omega_2$, where we set $\Delta T_2 = -20^o$C as for normal operative conditions. The temperatures are applied over 1000 steps linearly. The reference temperature is in both cases the stress-free lamination temperature T_0.

The above non-linear heat conduction problem is solved using the proposed model, to simulate temperature-assisted fracture induced by the thermo-mechanical displacement field. The evolution of the phase-field variable along with the temperature distribution inside the cell is shown in Fig. 45(right). When the crack is fully propagated, it acts as a thermal barrier for heat transfer across the solar cell and the temperature becomes uniform in the two separated regions of the material. The load-displacement curve for the evolution of the damage is shown in Fig. 44(b) for different thicknesses of the solar cell. Analogous to the verification example, as the thickness increases, the load-bearing capacity increases. Moreover, it can be noticed that there exists a direct linear mapping of the load-displacement

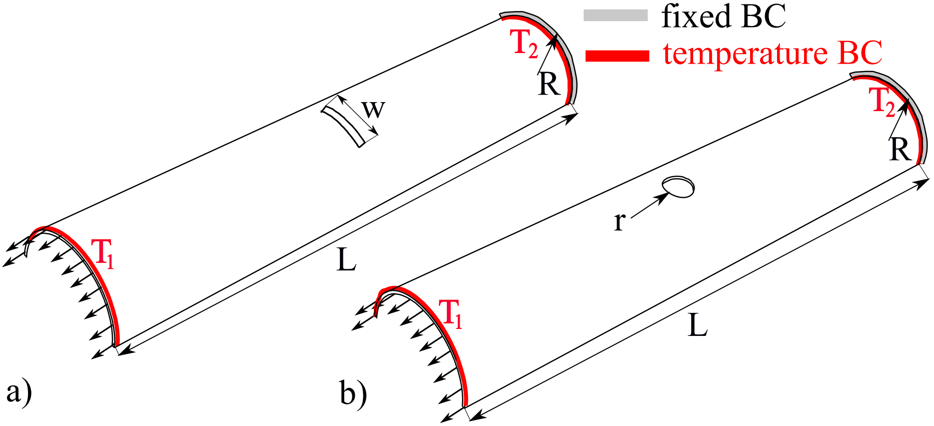

Figure 46: (a) plate with notch along with applied boundary conditions, (b) plate with the hole with the applied boundary conditions.

curves with the thickness as in the verification example.

4.5.3 Notched cylinder under tensile loading

In this example, a cylindrical shell is considered. In particular, two cases are considered (a) a cylindrical shell with an initial notch and (b) a cylindrical shell with a hole for sheets of alumina with material properties as detailed in Tab 13.

For the cylindrical shells with a notch, the geometrical description of the model considers a radius of the cylinder $R = 2$ mm, length $L = 10$ mm, thickness $h = 0.01$ mm with notch in the centre whose arc length is $w = 1.5$ mm such that the notch spans $\theta = 21.5^o$ each side as shown in Fig. 46a). The model is discretized with 24339 elements with maximum element size is at least $2l$.

One axial end of the cylinder is fixed, whereas a monotonic prescribed axial displacement is applied on the opposite end. Temperatures of $T_1 = 25^o$C and $T_2 = 50^o$C are applied on loaded end and on the fixed ends, respectively as in Fig. 46a). The ambient temperature is kept at $T_0 = 0^o$C. Fig. 47(a) shows the evolution of the phase-field ($\mathfrak{d}$) and temperature corresponding to the displacement $\Delta = 0.016$ mm. It can be observed that the temperature is linearly distributed along the cylinder length, until it breaks in two parts due to fracture, which again leads to heat flux insulation across the corresponding generated crack surface.

Along with the base model, Fig. 48(a) shows the variation of load-displacement curves for various temperature boundary conditions. It can be seen from Fig. 48(a) that as the temperature increases, the load-carrying capacity of the model decreases.

For the case of the cylinder including the central hole, the geometrical description of the model follows the radius of $R = 2$ mm, length $L = 20$ mm with thickness $h = 0.01$ mm with hole in the centre with radius $r = 0.15$ mm as shown in Fig. 46b) The model is discretized with 12491 elements with maximum element size is at least $2l$. For similar

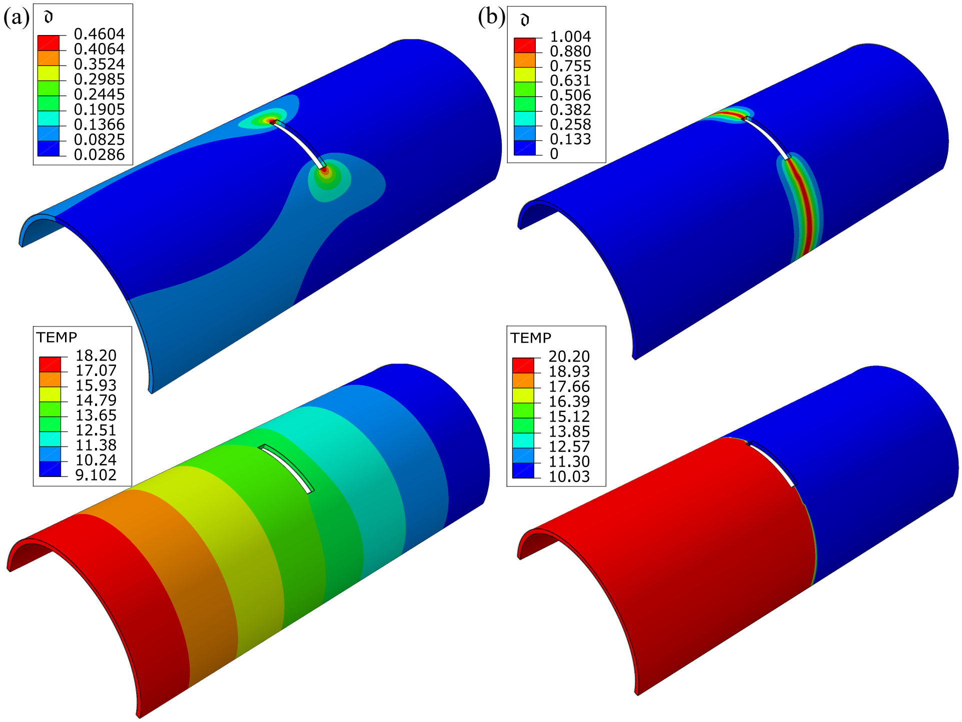

Figure 47: (a) Phase-field and temperature distribution for a cylindrical shell with a notch before crack at displacement load of $\Delta = 2.9 \times 10^{-3}$mm, (b) phase-field and temperature distribution after crack propagation at displacement load of $\Delta = 3.2 \times 10^{-3}$mm.

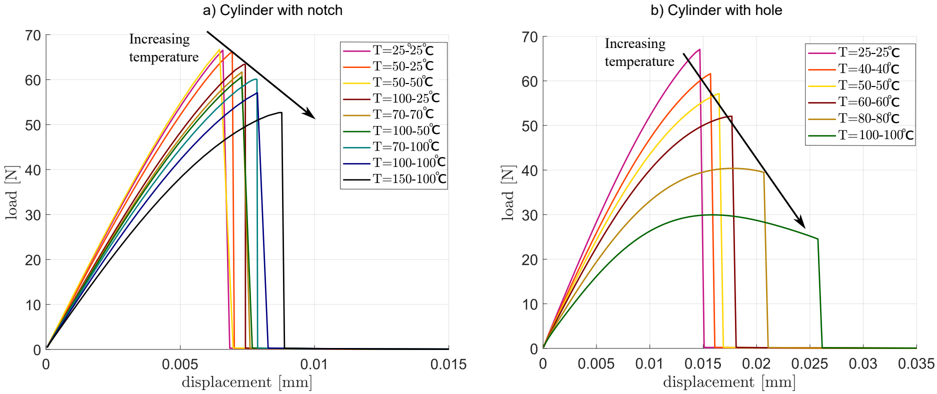

Figure 48: Force vs displacement curve for (a) cylinder with notch, and (b) cylinder with hole.

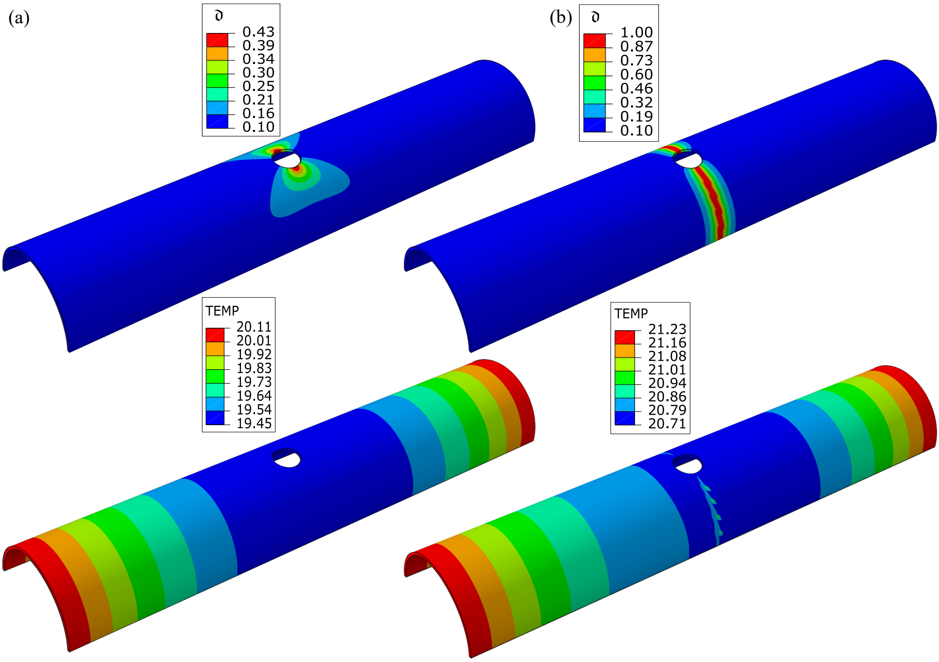

Figure 49: (a) Phase-field and temperature distribution for a cylindrical shell with a hole before crack at displacement load of $\Delta = 1.4 \times 10^{-2}$mm, (b) phase-field and temperature distribution after crack propagation at displacement load of $\Delta = 1.5 \times 10^{-2}$mm.

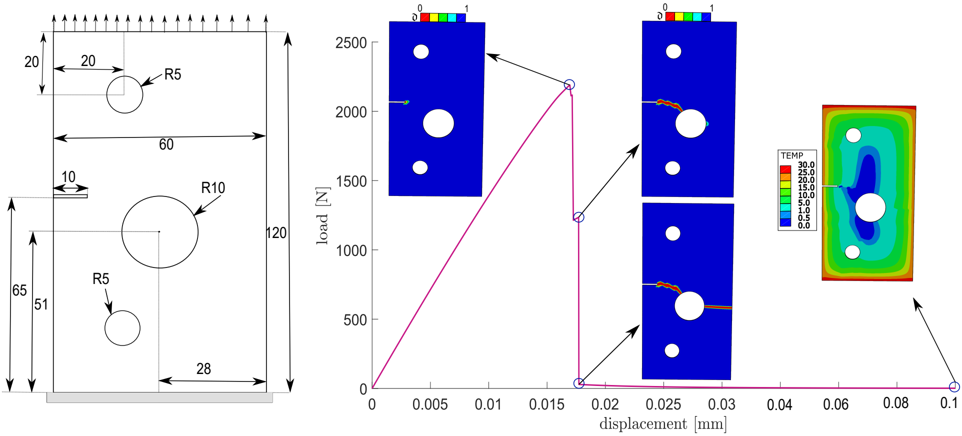

Figure 50: Phase-field and temperature distribution for plate with notch and hole along with reactions.

boundary conditions as before, but with $T_1 = T_2 = 25^o$C (base model), the phase-field and the temperature distribution before ($\Delta = 0.016$ mm) and after the fracture ($\Delta = 0.016$ mm) are shown in Fig. 49(a) and Fig. 49(b) respectively. Along with the base model, the load-displacement curve for the variation of different boundary conditions $T_1 = T_2$ are shown in Fig. 48(b). As in the case with cylinder with notch, as the temperature increases, the load carrying capacities of the cylinder decreases.

4.5.4 Plate with notch and multiple holes

In this example, a plate with multiple holes and an eccentric notch is considered to show stable crack propagation. A zirconia plate (with properties as in Tab. 13) of length $L = 120$ mm, width $w = 60$ mm and thickness $h = 1$ mm is considered as shown in Fig. 50(a). The bottom surface is fully restrained, whereas the displacement boundary of $\Delta = 0.1$mm is applied on the top surface as shown in Fig. 50(a). The temperature of 30^oC is applied on the top and bottom surfaces, whereas a temperature of 25^oC is applied on both sides of the plate. The evolution of the temperature and the phase-field along with the reactions are presented in Fig. 50(b). The phase-field evolution during the initiation, propagation (snapback), and the complete damage is shown in 50(b). The temperature distribution at the end of time step ($t = 1$, $\Delta = 0.1$mm) is shown in 50(b). It can be seen that, due to the existence of centre hole, the crack starts from the notch, and propagate only until centre hole. The temperature starts to diffuse inwards whereas at the path of crack, temperature is higher. Later, as the load increases, the crack travel further leading to complete failure. Temperature distribution reflects the applied temperature and the crack propagation.

Material	E (MPa)	ν	$\alpha(10^{-6}/^o\mathrm{K})$	$k_0(\mathrm{W/mm}^o\mathrm{K})$	$c_p(\mathrm{kJ/kg}^o\mathrm{K})$	$\mathcal{G}_C$ (MPa$\sqrt{\mathrm{mm}}$)	l (mm)
Copper	120×10^3	0.34	16.5	150	0.372	11.968	0.1
Titanium	116×10^3	0.34	8.90	17	0.72	5.9973	0.1267
Zirconia	210×10^3	0.31	10.1	5.05	0.4	0.32	0.06
Alumina	380×10^3	0.26	7.7	25	0.880	0.06634	0.08
Silicon carbide	410×10^3	0.35	4	120	0.750	0.045643	0.003
Polymer Glass	85×10^3	0.21	5.1	1.35	0.805	0.007197	0.008

Table 14: Properties of the simulated materials.

4.6 Virtual testing: Application to FGM

With regards to the formulation mentioned in Section 4.2.3, in this section, the predictive capability of the proposed thermo-mechanical solid shell formulation with phase-field for functionally graded materials is assessed using several representative examples. First, a benchmark test is proposed. Then, the numerical aspects concerning the grading are discussed by introducing a volume fraction that can describe the change of material properties. The examples of a plate with two notches and a plate with many holes are examined to study the deflection of cracks due to material properties grading and temperature effects. Later, a thin cylindrical shell is analyzed to show the applicability of the proposed model to complex structures. The classic benchmark examples concerning a plate with a notch is considered to study the effects of Young's modulus on crack propagation and temperature distribution using metal-metal, ceramic-polymer, and ceramic-ceramic FGM specimens. A three-phase FGM is finally considered to pinpoint the influence grading on the material behavior.

The details on the function Vf_A and the discussion on grading are provided for each example for more clarity. In order to show examples spanning the wide range of material behavior, six material parameters are considered spanning metals, ceramic, and polymers, namely: copper (metal), titanium (metal), alumina (ceramic), zirconia (ceramic), silicon carbide (ceramic) and polymer glass (polymer) whose material properties are given in Tab. 14.

4.6.1 Verification example

This example concerns the verification of the proposed model. Due to the scarce experiment concerning thermo-mechanical FGMs, and especially for FGMs, current numerical results are been compared against the 2D solution reported in [90]. Equal temperature is applied everywhere throughout the analysis in order to eliminate the thermal effects. Fig. 51a) shows the sketch of the model under consideration with grading in $y-$direction such that alumina (material-A) occupies the top surface, and zirconia (material-B) occupies the bottom surface. The material properties of alumina and zirconia are shown in Tab. 14. The volume fraction function is defined as

$$Vf_A = \left(\frac{y}{1}\right)^{\zeta} \quad \text{for} \quad 0 \leq y \leq L. \tag{4.76}$$

The force vs. displacement curve for homogeneous material (material-A) and the FGM with $\zeta = 1$, and $\zeta = 3$ with $l = 0.006$ are compared against the experiments in [90] as in Fig. 51b). A satisfactory agreement between the two formulations can be observed. The small discrepancy in the results might stem from the fact that numerical simulations in [90] were

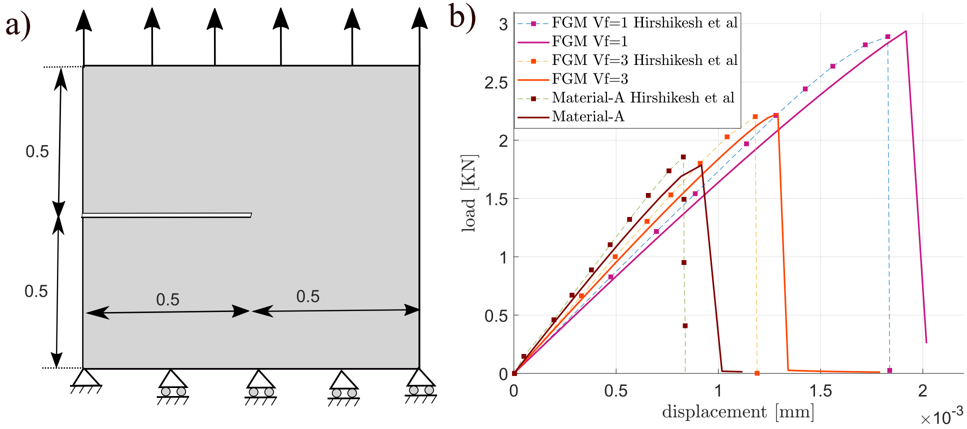

Figure 51: (a) Geometric description of the model, (b) force vs. displacement plots comparison with Hrishikesh et al [90].

performed in plane strain conditions, whereas the developed model in this article considers three-dimensional constitutive law.

4.6.2 Plate with two edge notches

This example concerns the application of the proposed model to functionally graded double edged asymmetrical notched specimen comprising alumina (Al_2O_3) and zirconia (ZrO_2) with grading in $y-$direction, with alumina on the top and zirconia on the bottom. Fig. 52 shows the sketch of the model under consideration with $L = 2$ mm, $a = 0.3$ mm, $w = 1$ mm, $\tilde{L} = 0.9$ mm, and thickness $h = 0.028$ mm. The model is discritized with 4896 elements. The bottom of the specimen is fully restrained whereas the displacement of $\Delta = 0.005$ mm is applied on the top edge. The properties of alumina and zirconia are reported in Tab. 14. With alumina being considered as material-A, the volume fraction function is defined as

$$Vf_A = \left(\frac{y}{2}\right)^{\zeta} \quad \text{for} \quad 0 \leq y \leq L. \tag{4.77}$$

The evolution force vs. displacement curves of the homogeneous materials and of the FGM with $\zeta = 1$ (linear) are shown in Fig. 52. In these examples, a temperature of $T_1 = T_2 = 25^o$C is applied on the left and right edges, respectively. Due to the thermo-elastic mismatch, the maximum load-bearing capacity and the thermal distributions are different in FGM compared to its homogeneous constituents.

Since the thermal conductivity of the alumina is five times larger than zirconia, the temperature distribution in FGM is unequal, and high temperatures are largely concentrated towards the top surface (alumina). The difference in temperature distributions between the homogeneous material (alumina) and the FGM are shown in Fig. 54 along with the crack propagation at different time instances. Notice that from Eq. (5.22), the degradation func-

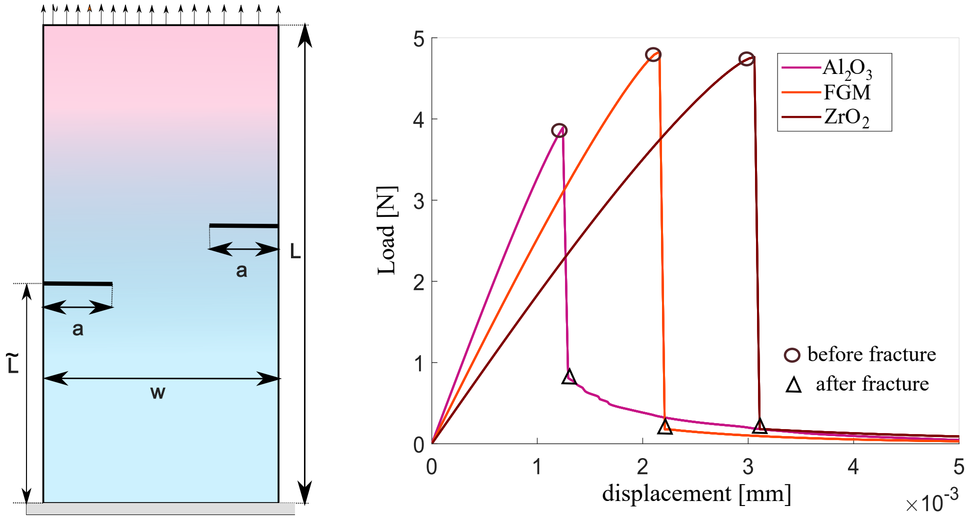

Figure 52: (left) Geometric description of the model, (right) force vs. displacement plots with $\zeta = 1$ in Eq. (4.77) and its homogeneous components.

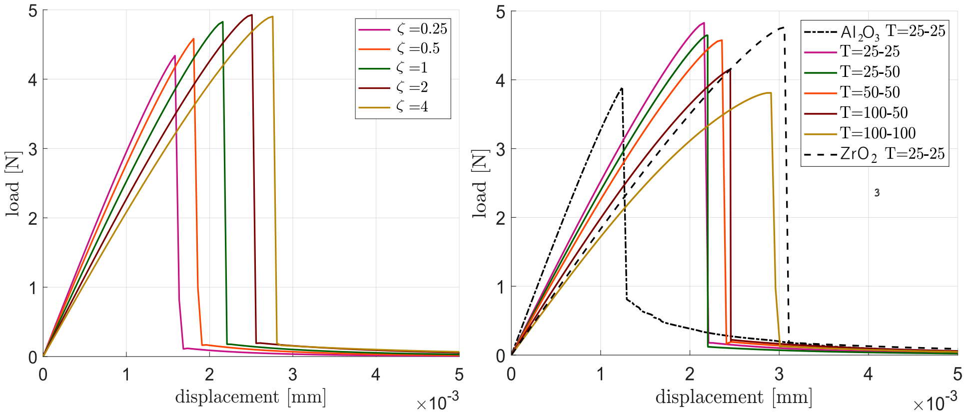

Figure 53: Force vs displacement curve for (left) variation of grading function ζ and (right) variation of temperature boundary conditions for double notched plate.

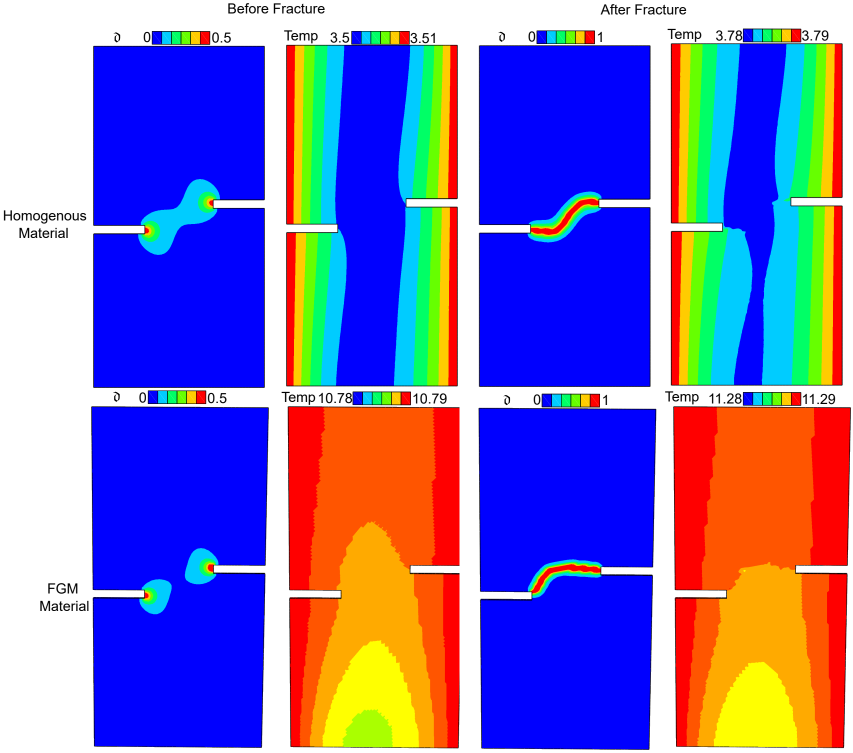

Figure 54: Double edge notched plate: phase-field and temperature distribution during initiation of fracture, and at failure.

tion $g(\mathfrak{d})$ is applied on the $\mathbf{Z}$ and $\boldsymbol{Q}$ matrix which contains the thermal conductivity $\mathbf{k}$. As the $\mathfrak{d}$ approaches 1, $\mathbf{k}$ tends to 0. In the region of crack propagation, $\mathbf{k}$ is almost zero and acts as a thermal barrier which can be observed in Fig. 54. Moreover, Fig. 53(Right) shows the force vs. displacement curve for the variation of temperature boundary condition with $\zeta = 1$. It can be noticed that, as the temperature increases, the load-bearing capacity decreases.

Referring to the other material properties' mismatch, the Young's modulus E and the fracture energy $\mathcal{G}_C$, and subsequently the characteristic length scale l, they play a vital role in determining the load-bearing capacity. It can be observed from Fig. 52 that, as expected, the initial slope depends on Young's modulus, whereas the peak response (load-bearing capacity) depends on the $\mathcal{G}_C$ and l (that are related to the apparent strength). Due to the fact that the alumina has the highest value of E and the lowest value of $\mathcal{G}_C$ among the two materials herein considered, the slope of alumina is higher, and the maximum load-bearing capacity is lower than zirconia. Since the properties of FGM are a linear/nonlinear combination of its homogeneous materials, the crack deflection of the FGM is different compared to the homogeneous materials as shown in Fig. 54 and qualitatively in line with the numerical-experimental correlation performed in [90]. Moreover, Fig. 53 (left panel) shows the evolution of force vs. displacement curve for the variation of grading parameter ζ with the same temperature boundary condition as before. Naturally, as ζ goes to infinity, the load-bearing capacity approaches the corresponding one to the zirconia.

For the pure elastic analysis (without temperature imposed), the maximum load-bearing capacity of the FGM is always bounded between its homogeneous constituents as in Section 2 for more details. When the temperature effects are considered, this is partially true. For the same boundary temperatures, the maximum load-bearing capacity of the FGM is bounded between its homogeneous constitutes, whose mathematical proof is a simple extension of Theorem- 3 in Section 2. In contrast, the peak load cannot be predicted accurately based on the energy bounds when different boundary temperatures are applied between FGM and its homogeneous materials.

4.6.3 Plate with multiple holes

In this example, the proposed model investigates crack deflection in FGMs. For this, a square plate of length $L = 2.5$ mm and thickness $h = 0.056$ mm is considered. The square plate contains 12 holes of radius $r = 0.125$ mm randomly placed across the plate. The model is discritized with 11209 elements. Similar to the previous example, the plate consists of FGM made up of alumina-zirconia graded in $y-$direction. In this example, a constant length scale $l = 0.06$ mm is considered for both homogeneous and FGM. See also [90]. The bottom surface made of zirconia (material-B) is restrained, and a vertical displacement is applied on the top surface made of alumina (material-A). The temperature of 25^oC is applied on both lateral sides. The volume fraction is defined as

$$Vf_A = \left(\frac{y}{2.5}\right)^{\zeta} \quad 0 \leq y \leq L; \qquad \Longrightarrow Vf_B = (1 - Vf_A). \tag{4.78}$$

Fig. 55 shows the evolution of force vs. displacement curve for the FGM with $\zeta = 1$ and is compared to its homogeneous constituents. Owing to the lower fracture of alumina, it can be seen that the crack initiation and propagation in FGM occur near the top surface compared to the central crack in the homogeneous surrogate.

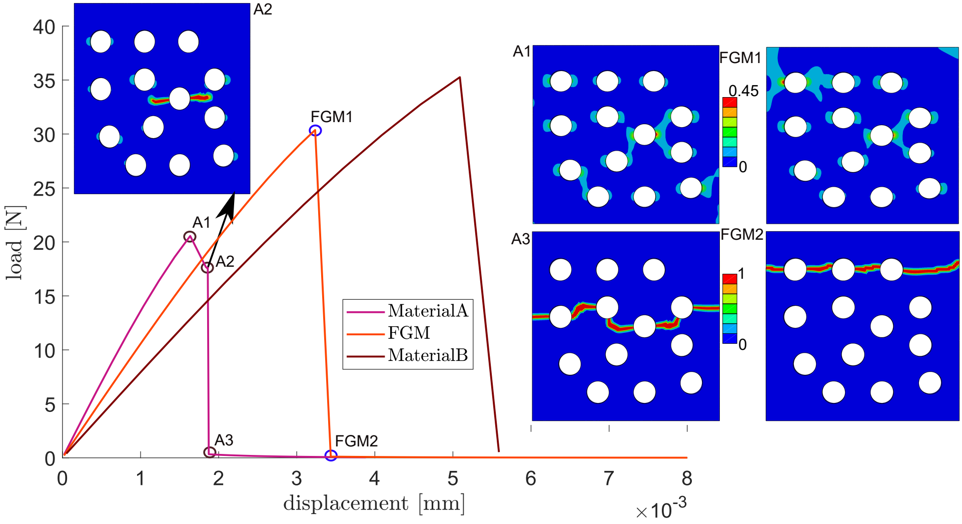

Figure 55: Plate with holes: force vs. displacement curves and the differences in crack propagation between FGM and homogeneous case.

The temperature distribution is very similar to the previous example where the temperature is concentrated towards the top surface. Recalling the reduction of thermal conductance due to crack propagation, the thermal insulation of the crack path can be observed in Fig. 56.

4.6.4 Cylinder with grading

In this example, a curved cylinder of radius $R = 2$ mm and length $L = 20$ mm with a central hole of radius $r = 0.15$ mm is made of FGM (alumina-zirconia) is considered. The model is discritized with 12491 elements. One axial end of the cylinder is restrained, whereas an axial displacement is prescribed on the opposite end. The initial temperature of $T = 25^oC$ is applied on both axial ends. The grading is done along its axial length ($z-$direction) such that the function Vf takes the form

$$Vf_A = \left(\frac{|z-10|}{10}\right)^{\zeta}, \qquad 0 \leq y \leq \text{Ł}. \tag{4.79}$$

Meaning that, alumina occupies both the axial ends (i.e $z = 0$, and $z = 20$) and zirconia occupies the centre ($z = 10$). The grading profiles for different ζ, and the change of material properties due to the function Vf_A is shown in Fig. 57 (left panel). The force vs. displacement curves for the FGM, along with its homogeneous constituents, are shown in Fig. 58 (left panel). On the other hand, Fig. 57 (right panel) shows the variation of force vs displacement curve for different grading parameter ζ. It is evident that as $\zeta \rightarrow \infty$, the load-bearing capacity of the FGM approaches alumina (material-A) since the volume fraction of alumina

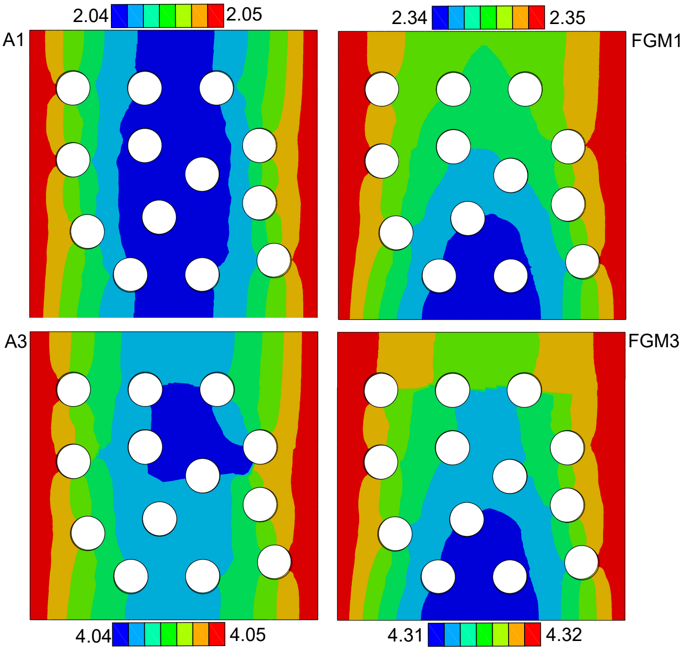

Figure 56: Plate with holes: temperature distribution in FGM as compared with that of the homogeneous model, before and after failure.

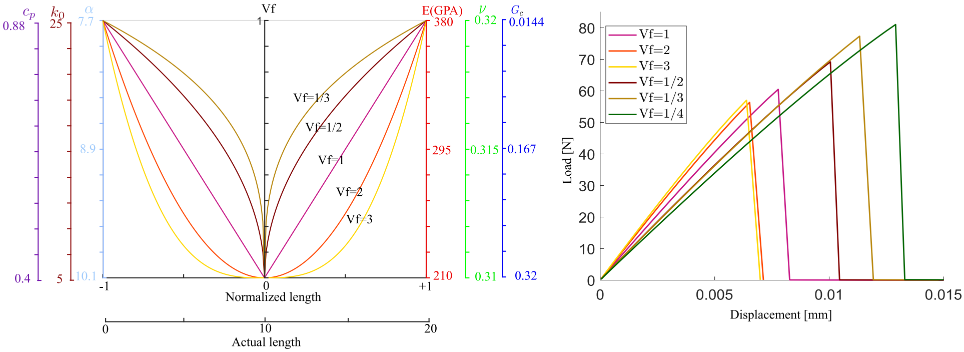

Figure 57: Cylinder with hole: properties of the materials and force vs displacement curve for change of grading function ζ.

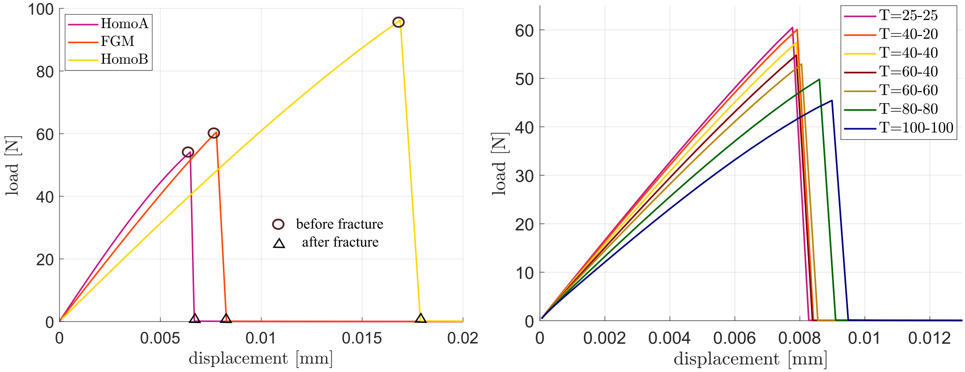

Figure 58: Cylinder with hole: force vs displacement curve FGM ($\zeta = 1$) and the homogeneous surrogates and variation of temperature boundary conditions.

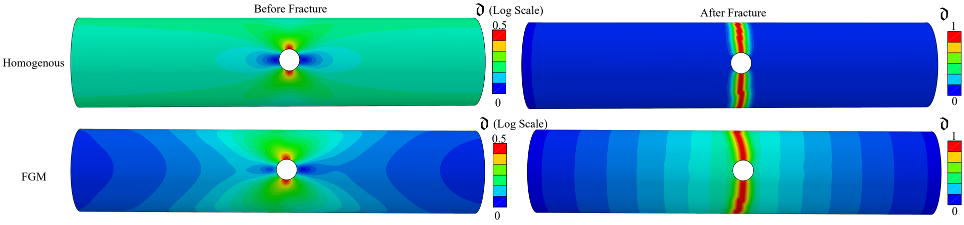

Figure 59: Cylinder with hole: phase-field and temperature distribution in FGM compared with homogeneous model before and after fracture.

is dense in the region of crack propagation.

Figure. 59 shows the comparison between crack paths for FGM and the homogeneous material (zirconia) and shows that the crack is deflected approximately 8^o towards the load end. The variation of the temperature boundary conditions shows that as the temperature increases, the load-bearing capacity of the specimen decreases as in Fig. 58 (right panel).

Note that total energy can be fairly split into elastic, thermal, and crack energy constituents. Numerical experiments show that elastic energy is driven mainly by Young's Modulus, whereas a combination of $\mathbf{k}$ and α primarily drives thermal energy. In contrast, crack energy is largely driven by $\mathcal{G}_C$ and l in line with [24]. When the length scale of FGM is considered constant as in plate with double notch example, the crack energy is driven by $\mathcal{G}_C$. The crack propagation is usually towards the lowest $\mathcal{G}_C$ side (for example, alumina in the previous example). In the presence of stress concentrators such as a notch, hole, etc., the crack initiation and propagation also depends on the material properties at the stress concentration zones (crack tip). Since the variational formulation is considered as a competition between the thermo-elastic energy and the crack energy, the following conclusions can be readily drawn.

1. As the grading parameters increase, i.e ($\zeta \geq 1$) or decrease ($\zeta \leq 1$), the FGM tends to behave like its homogeneous constituents.
2. As the temperature increases, the maximum load bearing capacity decreases.
3. The slope of the force vs. displacement curve depends strongly on the Young's modulus E.
4. The maximum load bearing capacity depends largely on $\mathcal{G}_C$, and it is directly proportional to l (or to the apparent tensile strength σ_c).
5. Since the thermal conductance is degraded as a function of $\mathfrak{d}$, and the maximum load bearing capacity is a function of applied temperature and $g(\mathfrak{d})$.

4.6.5 Plate with notch

This example concerns with the effect of grading and their subsequent temperature effects by considering three different FGM pairs. As an example, (i) Copper-Titanium (Cu-Ti), (ii) Alumina-Zirconia (A-Z), and (iii) Silicon Carbide- Polymer Glass (SiC-G), representing (i) metal-metal, (ii) ceramic-ceramic, and (iii) ceramic polymer pairs respectively are considered. In each of the example, the model is discritized with 4476 elements.

The properties of materials mentioned above are given in Tab. 14, whereas the ratio of Young's modulus, fracture energy, thermal conductivity, and length scale are given in Tab. 15. Here, material-A has the highest Young's modulus among the FGM pairs. i.e $E_A = \max(E_A, E_B)$, i.e copper, alumina and SiC is their respective FGM pairs.

Note that the ratio of chosen pairs represents vastly different mechanical and thermal properties, each of them is discussed in the sequel. A plate of length $L = 10$ mm and width $w = 10$ mm with initial notch of 3 mm at the centre are considered with the displacement boundary conditions applied as in Fig. 60a) to simulate stable crack propagation. A temperature $T = 25^o$C is applied on both sides for the numerical simulations in this example. The grading is done along the $y-$direction such that grading happens from the bottom (material-B) to top (material-A), whose function is defined as

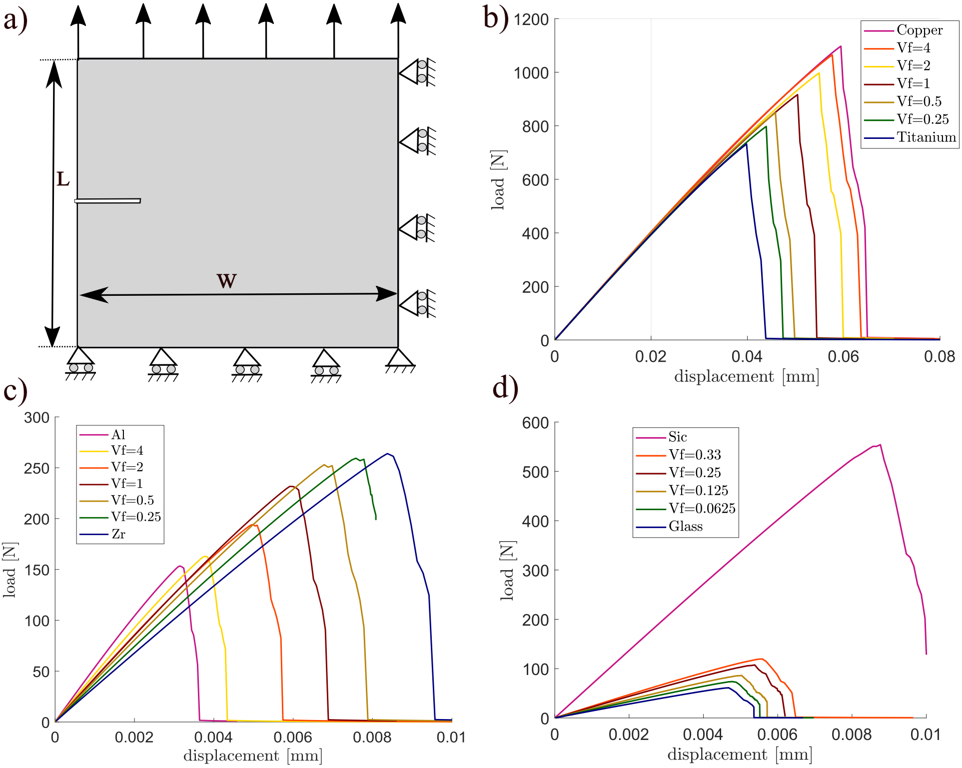

Figure 60: a) Model under consideration, force vs displacement curve with variation of ζ in b) copper-titanium FGM pair, c) alumina-zirconia FGM pair, d) silicon carbide-epoxy glass FGM pair.

FGM pair	$\frac{E_A}{E_B}$	$\frac{\mathcal{G}_{c,A}}{\mathcal{G}_{c,B}}$	$\frac{k_{0,A}}{k_{o,B}}$	$\frac{l_{c,A}}{l_{c,B}}$
Copper-Titanium (Cu-Ti)	1.03	2	8.82	0.754
Alumina-Zirconia (A-Z)	1.8	0.207	4.95	1.33
Silicon Carbide- Polymer Glasss (SiC-G)	4.8	6.34	88.88	0.375

Table 15: Ratio of the simulated materials.

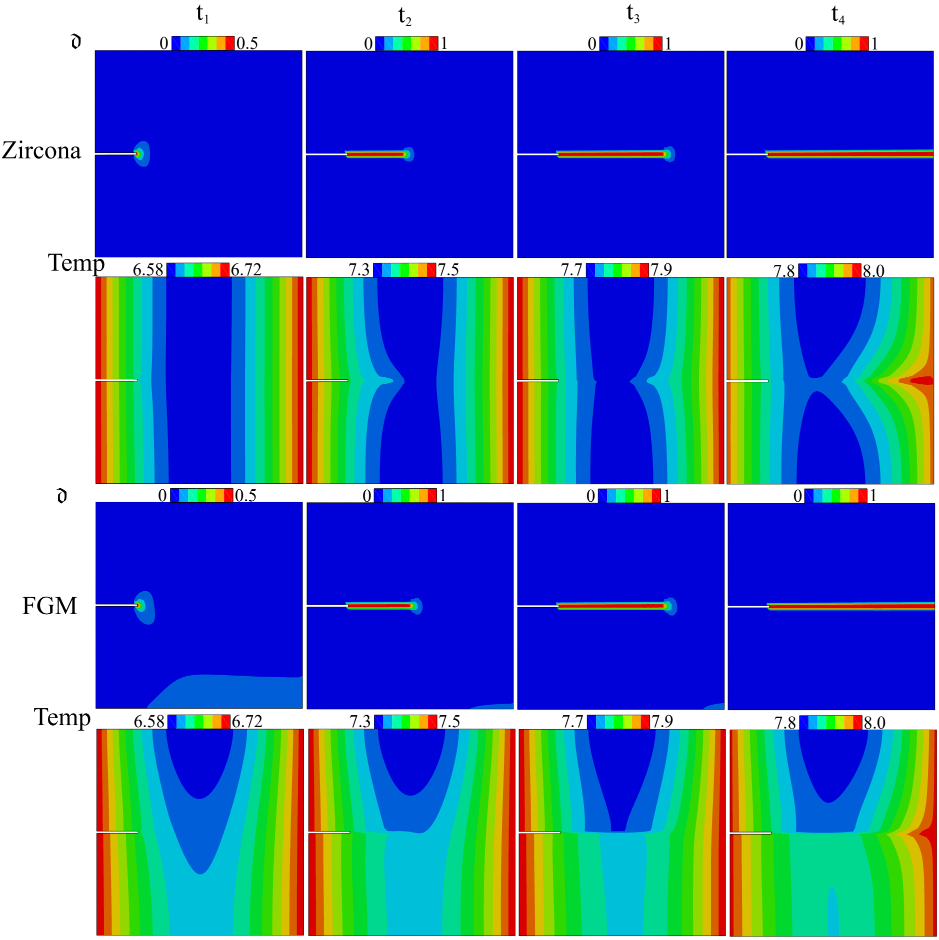

Figure 61: Phase-field and temperature distributions comparison between FGM and homogeneous material during (t_1) initiation, (t_2) crack propagation until $1/2$ of plate (t_3) crack propagation until $3/4$ of plate (t_4) after complete failure.

$$Vf_A = \left(\frac{y}{10}\right)^{\zeta} \quad 0 \leq y \leq L. \tag{4.80}$$

For the copper-titanium FGM pair with copper as material-A, Young's modulus ratio $\frac{E_A}{E_B}$ is approximately 1. The force vs. displacement curve for the FGM with different grading parameters ζ along with its homogeneous constituents are presented in Fig. 60(b). It is clear that the slope of all the curves is similar due to the similarity in the Young's moduli. Then, the peak load-bearing capacity of the model is driven by the $\mathcal{G}_C$ and l. In fact, using the expression, $l = \frac{27}{256}\frac{\mathcal{G}_C E}{\sigma_c^2}$, $\mathcal{G}_C$ and l can be directly related with σ_c. Note that both copper and titanium are highly conductive metals with a thermal conductance ratio $\frac{k_{0,A}}{k_{o,B}} = 8.82$, meaning that the temperature distribution is highly concentrated towards the Copper end.

For the alumina-zirconia pair, the Young's modulus ratio $\frac{E_A}{E_B}$ is approximately 2, whereas $\frac{k_{0,A}}{k_{o,B}} = 4.95$, Fig. 60(c) shows the force vs displacement curve for different grading parameters ζ. Moreover, Fig. 61 presents the crack propagation and temperature distribution of the homogeneous material (zirconia as an example) and FGM (with $\zeta = 1$) during four stages, namely (i) crack initiation, (ii) crack propagating approximately half the plate, (iii) crack propagating approximately $\frac{3}{4}^{th}$ of the plate, and finally (iv) fully cracked model. The temperature distribution at each of these stages is shown in Fig. 61 to comprehend the differences. As the crack propagates, the temperature around the crack increases, leaving a trail around the crack tips. Meanwhile, thermal conductance in the crack region approaches 0, hence creating thermal insulation around the region. Temperature distribution in all the FGM's are similar owing to the conductivity ratio always higher than 1 in all the pairs. See Fig. 61 for more details.

For the Silicon carbide and polymer glass FGM, the Young's Modulus ratio $\frac{E_A}{E_B}$ is approximately 5, whereas the $\frac{k_{0,A}}{k_{o,B}} = 88.88$, notice that, due to very high $\frac{\mathcal{G}_{C,A}}{\mathcal{G}_{C,B}}$ ratio, the FGM with $\zeta \geq 1$ gave a nonphysical boundary cracks, hence only $\zeta \leq 1$ is considered for the analysis. Fig. 60(d) shows the force vs. displacement curve for the FGM Sic-G along with its homogeneous constituents. From Fig. 60(a), (b), and (c), it is apparent that as Young's modulus ratio increases, the peak load-bearing capacity of the FGM changes drastically as a linear/nonlinear combination of their homogeneous constitutes.

4.6.6 Double FGM (three-phase FGM)

Double FGM is a three-phase functionally graded material where the material is graded with three different materials. This can also be considered as two functionally graded materials combined together at a point, see, [255] for more details. In order to accommodate such a model, the material parameters in Eq. (4.2.3) and (4.5) have to be modified accordingly.

Consider three materials, Mat-A, Mat-B and Mat-C. The volume fraction of each material at any position $\mathbf{x} \in \mathcal{B}_0$ can be written as Vf_A, Vf_B and Vf_C such that $Vf_A + Vf_B + Vf_C = 1$ for each $\mathbf{x} \in \mathcal{B}_0$. Introduce two grading parameters ζ_1 and ζ_2 that controls the behaviours of

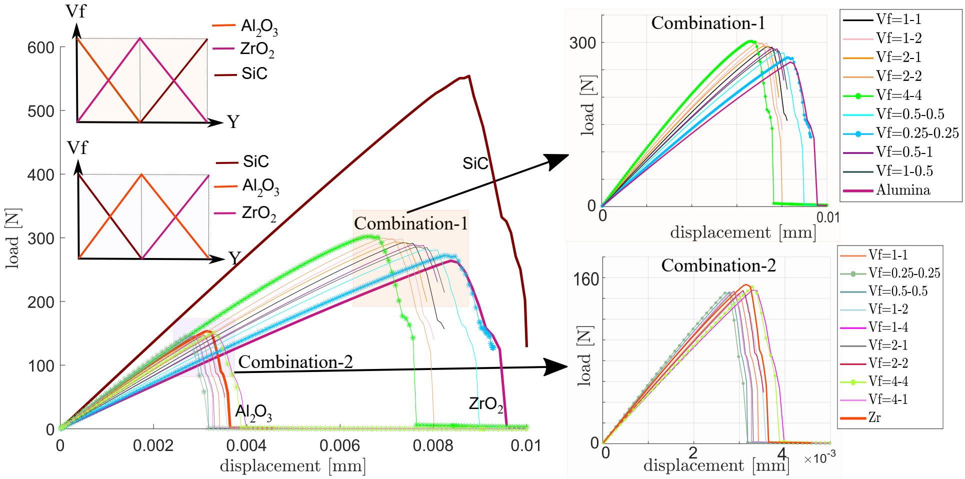

Figure 62: Force vs displacement curve for double FGM.

the grading in the materials. Then the volume fraction function for the FGM at any position vector can be defined as

$$Vf = \begin{cases} Vf_1(\mathbf{x}) & 0 \le \mathbf{x} \le (L_1, w_1, h_1) \\ Vf_2(\mathbf{x}) & (L_1, w_1, h_1) \le \mathbf{x} \le (L_2, w_2, h_2), \end{cases} \tag{4.81}$$

for some length $(L_1, L_2) \le L$, width $(w_1, w_2) \le w$, and thickness $(h_1, h_2) \le h$. The material properties now can be written as a function of Vf. As an example, we consider the square plate with an initial notch as in Sec. 4.6.5 with the same dimensions and boundary conditions. Alumina, zirconia, and silicon carbide are considered for the double FGM, where two combinations of grading of each of these materials to form a double FGM are considered in the $y-$direction are shown in Fig. 62.

The volume fraction functions can be defined as

$$Vf = \begin{cases} \left(\frac{y}{5}\right)^{\zeta_1} & 0 \le y \le 5 \\ \left(-\frac{y}{5} + 2\right)^{\zeta_2} & 5 \le y \le 10. \end{cases} \tag{4.82}$$

The material properties now takes the form

$$\Xi = \begin{cases} \Xi_A + (\Xi_B - \Xi_A)\left(\frac{y}{5}\right)^{\zeta_1} & 0 \le y \le 5 \\ \Xi_C + (\Xi_B - \Xi_C)\left(-\frac{y}{5} + 2\right)^{\zeta_2} & 5 \le y \le 10, \end{cases}$$

for each $\Xi = \{E, \nu, \alpha, k_0, \mathcal{G}_C, l\}$. Two combinations of the material properties are considered to explore the thermo-elastic behaviours of the double FGM's. In combination-1, zirconia is considered to exist everywhere across the model (coined as primary material). Meaning that,

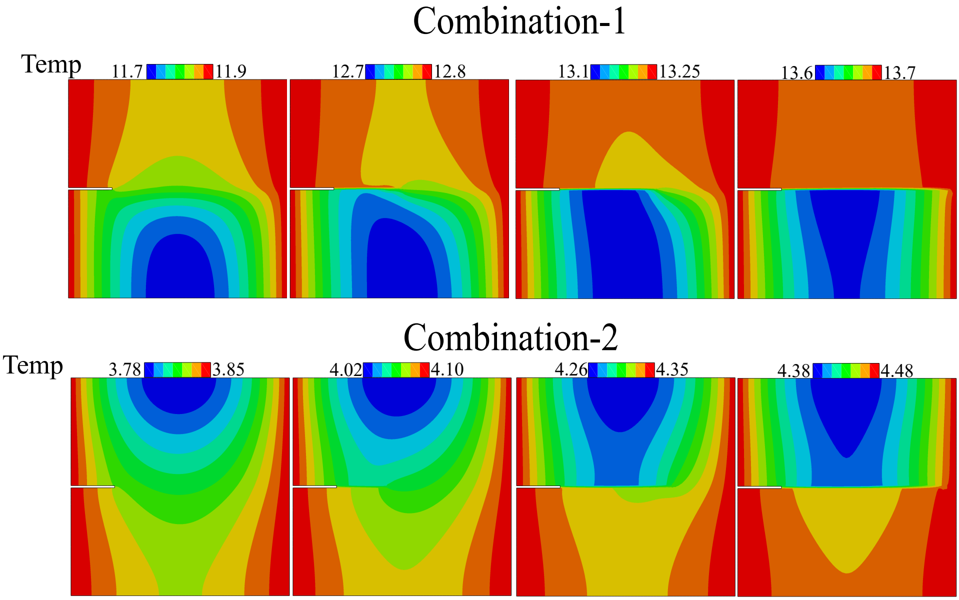

Figure 63: Temperature distribution between in combination-1 and combination-2 on different time instances for $\zeta = 1 - 2$ both.

combination-1 can be considered as a two pairs of FGM of alumina-zirconia, zirconia-silicon carbide combined together with zirconia in both pairs. Similarly, combination-2, consists of silicon carbide-alumina, alumina-zirconia with alumina as a primary material. The choice of the materials is motivated by the fact that the E and k_0 ranges in the order of magnitude 1, whereas $\mathcal{G}_C$ ranges in the order of magnitude 2. The material properties of combination-1 can be written as

$$\Xi = \begin{cases} \Xi_{Alumina} + (\Xi_{zirconia} - \Xi_{Alumina})\left(\dfrac{y}{5}\right)^{\zeta_1} & 0 \leq y \leq 5 \\ \Xi_{SiC} + (\Xi_{zirconia} - \Xi_{SiC})\left(-\dfrac{y}{5} + 2\right)^{\zeta_2} & 5 \leq y \leq 10, \end{cases}$$

whereas the material properties of combination-2 takes the form

$$\Xi = \begin{cases} \Xi_{SiC} + (\Xi_{Alumina} - \Xi_{SiC})\left(\dfrac{y}{5}\right)^{\zeta_1} & 0 \leq y \leq 5 \\ \Xi_{Alumina} + (\Xi_{Alumina} - \Xi_{zirconia})\left(-\dfrac{y}{5} + 2\right)^{\zeta_2} & 5 \leq y \leq 10. \end{cases}$$

Fig. 62 presents the pictorial representation of the combination-1 and combination-2 for $\zeta_1, \zeta_2 = 1$. For the different variations of the grading function ζ_1 and ζ_2 and the two combinations, the force vs. displacement curves can be seen in Fig. 62. It can be noticed that since the combination-1 is dominant with zirconia, the peak load response accumulates between the zirconia and the SiC. For combination-2, since alumina is dominant, the peak load responses are accumulated between alumina and zirconia. The temperature distribution for the combination-1 and combination-2 during the (i) crack initiation, (ii) crack propagating approximately half the plate, (iii) crack propagating approximately $3/4$ of the plate, and finally (iv) fully cracked model is presented in Fig. 63. It is noticed that combination-2 has a faster rate of heat transfer compared to combination-1 owing to the thermal conductivity of alumina. And the temperature distributions are inclined towards the SiC in both combinations.

Chapter 5

Phase-field model for fatigue induced fracture: application to thin walled structures

This chapter mainly concerns with developing thermodynamically consistent framework for phase-field fatigue damage model for thin walled structures using solid shell approach. This chapter is organised as follows. In Section 5.1, the energy based approach is used to derive the variational formulation eventually leading to the governing equations. In Section 5.2, a finite element implementation of the variational structures is discussed. Section 5.3 is complimented with representative examples to show the predictive capability of the model.

5.1 Variational formulation

Recalling the phase-field derivation put-forth in Section 1.3.1 and the choice the functions in Section 1.3.2. Taking into consideration the solid shell formulation using multi-field-Hu-Washizu variational principle and for some fatigue degradation function $f(\bar{\alpha})$ function, Eq. (4.30) is modified as

$$\Pi(\mathbf{u}, \tilde{\mathbf{E}}, \mathfrak{d}) = \int_{\mathcal{B}_0} g(\mathfrak{d})\Psi_0(\mathbf{u}, \tilde{\mathbf{E}})\mathrm{d}\Omega - \int_{\mathcal{B}_0} \mathbf{S} : \tilde{\mathbf{E}}\,\mathrm{d}\Omega + \int_{\mathcal{B}_0} f(\bar{\alpha}(t))\frac{\mathcal{G}_C}{4c_w}\left[\frac{\alpha(\mathfrak{d})}{l} + l\,|\nabla\mathfrak{d}|^2\right]\mathrm{d}\Omega + \Pi_{\mathrm{ext}}. \tag{5.1}$$

where $\Psi_0(\mathbf{u}, \tilde{\mathbf{E}})$ is the intact elastic energy density function which involves incompatible strains, and $\bar{\alpha}(t)$ is a suitable function that defines a suitable cumulative history variable to be defined.

The thermodynamic consistency of the total energy functional can be ensured by considering rate dissipation density potential

$$\dot{\mathcal{D}} = [\mathbf{S} - \partial_{\mathbf{E}}\Pi] : \dot{\mathbf{E}} - \partial_{\mathfrak{d}}\Pi : \dot{\mathfrak{d}} \geq 0. \tag{5.2}$$

Expanding the Second term $\partial_{\mathfrak{d}}\Pi : \dot{\mathfrak{d}}$ leads to

$$\partial_{\mathfrak{d}}\Pi : \dot{\mathfrak{d}} = \frac{dg}{d\mathfrak{d}}\Psi_0(\mathbf{u}, \tilde{\mathbf{E}}) : \dot{\mathfrak{d}} + f(\bar{\alpha}(t))\frac{\mathcal{G}_C}{4c_w}\left[\frac{d\alpha(\mathfrak{d})}{d\mathfrak{d}}\frac{\dot{\mathfrak{d}}}{l} + 2l\nabla\mathfrak{d}\cdot\nabla\dot{\mathfrak{d}}\right].$$

Integrating by parts the second term leads to

$$-\partial_{\mathfrak{d}}\Pi : \dot{\mathfrak{d}} = \frac{dg}{d\mathfrak{d}}\Psi_0(\mathbf{u}, \tilde{\mathbf{E}}) : \dot{\mathfrak{d}} - \frac{\mathcal{G}_C}{4c_w}l\left[\left(\Delta\mathfrak{d} - \frac{d\alpha}{d\mathfrak{d}}\frac{1}{2l^2}\right)f(\bar{\alpha}) + \nabla f(\bar{\alpha})\cdot\nabla\mathfrak{d}\right]\dot{\mathfrak{d}}.$$

In order for Eq. (5.2) to to hold, $\frac{dg}{d\mathfrak{d}}\Psi_0(\mathbf{u}, \tilde{\mathbf{E}}) \geq 0$, $\dot{\mathfrak{d}} \geq 0$, $f_d(\mathfrak{d}, \Delta\mathfrak{d}, f(\bar{\alpha})) \geq 0$ leading to

$$f_d(\mathfrak{d}, \Delta\mathfrak{d}, f(\bar{\alpha})) = \frac{\mathcal{G}_C}{4c_w}l\left[\left(\Delta\mathfrak{d} - \frac{d\alpha}{d\mathfrak{d}}\frac{1}{2l^2}\right)f(\bar{\alpha}) + \nabla f(\bar{\alpha})\cdot\nabla\mathfrak{d}\right] \geq 0,$$

$$\frac{dg}{d\mathfrak{d}}\Psi_0(\mathbf{u}, \tilde{\mathbf{E}}) \geq 0; \qquad \dot{\mathfrak{d}} \geq 0; \qquad f_d(\mathfrak{d}, \Delta\mathfrak{d}, f(\bar{\alpha}))\dot{\mathfrak{d}} = 0; \qquad f(\bar{\alpha})\cdot\nabla\mathfrak{d}\cdot\boldsymbol{n} \geq 0. \tag{5.3}$$

Notice that, due to choice of $g(\mathfrak{d})$, $\frac{dg}{d\mathfrak{d}}\Psi_0(\mathbf{u})$ naturally holds, and the first order stability conditions or KKT conditions are refereed as

$$\dot{\mathfrak{d}} \geq 0; \qquad f_d(\mathfrak{d}, \Delta\mathfrak{d}, f(\bar{\alpha})) \geq 0; \qquad f_d(\mathfrak{d}, \Delta\mathfrak{d}, f(\bar{\alpha}))\dot{\mathfrak{d}} = 0 \tag{5.4}$$

Notice from Eq. (5.1) that fatigue degradation function $f(\bar{\alpha})$ should be locally integrable, and from Eq. (5.4) to be true, $0 \leq f(\bar{\alpha}) \leq 1$. Since $f(\bar{\alpha})$ degrades the crack energy (to be specific fracture toughness $\mathcal{G}_C$), $f(\bar{\alpha})$ should be also monotonically decreasing function. i.e $f'(\bar{\alpha}) \leq 0$ for $f(\bar{\alpha}) \in [0, 1]$.

Keeping the choice of functions such as geometric crack function, and energy degradation function as in Chapter 4.3, we define the stored energy function $\Psi_0(\mathbf{E})$, cumulative history variable $\bar{\alpha}(t)$, and fatigue degradation function $f(\bar{\alpha})$ are defined as follows:

Stored energy function

The stored energy function describes the equilibrium state that defines the behaviour of a solid in the unbroken state (i.e $\mathfrak{d} = 0$). In this section, we consider isotropic elastic body whose stored energy is defined as

$$\Psi_0(\mathbf{E}) = \frac{1}{2}\mathbf{E} : \mathbb{C} : \mathbf{E} = \frac{1}{2}\lambda tr^2(\mathbf{E}) + \mu\mathbf{E} : \mathbf{E}. \tag{5.5}$$

Here, $\mathbb{C}$ defines the linear elasticity tensor whose particular expression in the curvilinear co-ordinates takes the form

$$\mathbb{C} = \partial_{\mathbf{EE}}\Psi = \left[\lambda G^{ij}G^{kl} + \mu\left(G^{ik}G^{jl} + G^{il}G^{jk}\right)\right]\mathbf{G}_i \otimes \mathbf{G}_j \otimes \mathbf{G}_k \otimes \mathbf{G}_l, \tag{5.6}$$

where λ and μ denotes the Lame's constant.

Cumulative history variable

The term $\bar{\alpha}(t)$ in Eq. (5.1) describes the cumulative history effects due to fatigue. We adopt the function described by Carrara et al [50] where

1. $\bar{\alpha}(t)$ is independent of the mean load defined as

$$\bar{\alpha}(\mathbf{x}, t) = \int_0^t H(\alpha\dot{\alpha})|\dot{\alpha}| d\tau. \tag{5.7}$$

2. For a normalization parameter α_N, mean load dependent cumulative history variable can be defined as

$$\bar{\alpha}(\mathbf{x}, t) = \frac{1}{\alpha_N} \int_0^t H(\alpha\dot{\alpha}) \alpha\dot{\alpha} d\tau, \tag{5.8}$$

   for $\alpha = \Psi(\mathbf{E}, \mathfrak{d})$ is the total degraded strain energy which ensures that the model is not affected by crack tip singularity. Here $H(\alpha\dot{\alpha})$ is heavy-side function defined as

$$H(\alpha\dot{\alpha}) = \begin{cases} 1 & \alpha\dot{\alpha} \geq 0 \quad \text{(Loading)} \\ 0 & \text{Otherwise (Unloading)} \end{cases}. \tag{5.9}$$

Fatigue degradation function

The function $f(\bar{\alpha})$ describes the degradation of the material property due to repeated loading. Based on the functions described in Section 1.4, the following fatigue degradation functions are considered:

The generalized asymptotic degradation function is defined as

$$f(\bar{\alpha}) = \begin{cases} 1 & \text{if } \bar{\alpha}(t) \leq \alpha_T \\ \left(\dfrac{2\alpha_T}{\bar{\alpha}(t) + \alpha_T} \right)^a & \text{if } \bar{\alpha}(t) \geq \alpha_T \end{cases}, \tag{5.10}$$

for some threshold α_T before which the fatigue degradation is not triggered. In all the numerical experiments section, the threshold of $\alpha_T = \dfrac{\mathcal{G}_C}{12l}$ is considered as defined in [54, 50]. The symptomatic degradation function is defined as

$$f(\bar{\alpha}) = \begin{cases} 1 & \text{if } \bar{\alpha}(t) \leq \alpha_T \\ \left[1 - k \, log \dfrac{\bar{\alpha}(t)}{\alpha_T} \right]^2 & \text{if } \alpha_T \leq \bar{\alpha}(t) \leq \alpha_T 10^{\frac{1}{k}} \\ 0 & \text{if } \bar{\alpha}(t) \geq \alpha_T 10^{\frac{1}{k}} \end{cases}. \tag{5.11}$$

Here, a and k are the material constant that can be used to control the fatigue degradation.

5.2 Finite element implementation

For any admissible test functions $\delta\mathbf{u} \in \mathfrak{B}^u$, $\delta\tilde{\mathbf{E}} \in \mathfrak{B}^{\tilde{E}}$, $\delta\mathfrak{d} \in \mathfrak{B}^{\mathfrak{d}}$, with functional space defined as

$$
\begin{aligned}
\mathfrak{B}^u &= \quad \{\delta\mathbf{u} \in \mathbf{H}^1(\mathcal{B}_0),\ \delta\mathbf{u} = 0 \text{ on } \partial\mathcal{B}_{0,\mathbf{u}}\}, && \text{(5.12a)}\\
\mathfrak{B}^{\tilde{E}} &= \qquad\qquad \{\delta\tilde{E} \in \mathbf{L}^2(\mathcal{B}_0)\}, && \text{(5.12b)}\\
\mathfrak{B}^{\mathfrak{d}} &= \quad \{\delta\mathfrak{d} \in H^1(\Omega)\Big|\delta\mathfrak{d} \geq 0\,\forall\ \mathbf{X} \in \mathcal{B}_0\}. && \text{(5.12c)}
\end{aligned}
$$

The set $(\mathbf{u}, \tilde{\mathbf{E}}, \mathfrak{d})$ is obtained by taking first variation of Eq. (5.1) leads to following multi-physics problems

$$
\mathcal{R}^u(\mathbf{u}, \tilde{\mathbf{E}}, \mathfrak{d}, \delta\mathbf{u}) = \int_{\mathcal{B}_0} g(\mathfrak{d})\,[\mathbf{S} : \delta\mathbf{E}^u]\ \mathrm{d}\Omega - \mathcal{R}^u_{\text{ext}} = 0 \tag{5.13a}
$$

$$
\mathcal{R}^{\tilde{E}}(\mathbf{u}, \tilde{\mathbf{E}}, \mathfrak{d}, \delta\tilde{\mathbf{E}}) = \int_{\mathcal{B}_0} \left[\mathbf{S} : \delta\tilde{\mathbf{E}}\right]\ \mathrm{d}\Omega = \mathcal{R}^{\tilde{E}}_{\text{int}} = 0, \tag{5.13b}
$$

$$
\mathcal{R}^{\mathfrak{d}}(\mathbf{u}, \tilde{\mathbf{E}}, \mathfrak{d}, \delta\mathfrak{d}) = \int_{\mathcal{B}_0} f(\bar{\alpha}(t))\mathcal{G}_C\left[\frac{\mathfrak{d}}{l}\delta\mathfrak{d} + l\nabla\mathfrak{d}\cdot\nabla\delta\mathfrak{d}\right]\ \mathrm{d}\Omega - \int_{\mathcal{B}_0} 2(1-\mathfrak{d})\Psi(\mathbf{u}, \tilde{\mathbf{E}})\delta\mathfrak{d}\ \mathrm{d}\Omega = 0. \tag{5.13c}
$$

The functional space $\mathcal{B}_0$ is discretized into n_e non-overlapping elements such that partition of unity holds. i.e $\mathcal{B}_0 \approx \bigcup_{e=1}^{n_e} \mathcal{B}_0^{(e)}$ for n_e.

The position vectors in reference and current configuration are interpolated using standard tri-linear shape function $\mathbf{N}(\boldsymbol{\xi})$ in natural co-ordinates $\boldsymbol{\xi} = \{\xi^1, \xi^2, \xi^3\}$ as

$$
\mathbf{X} \approx \sum_{I=1}^{8} N^I(\boldsymbol{\xi})\mathbf{X}_I = \mathbf{N}(\boldsymbol{\xi})\widetilde{\mathbf{X}} \quad \text{and } \mathbf{x} \approx \sum_{I=1}^{8} N^I(\boldsymbol{\xi})\mathbf{x}_I = \mathbf{N}(\boldsymbol{\xi})\widetilde{\mathbf{x}},
$$

for global vectors $\widetilde{\mathbf{X}}$ and $\widetilde{\mathbf{x}}$ in reference and current configuration respectively. Similarly, the unknown fields $(\mathbf{u}, \tilde{\mathbf{E}}, \mathfrak{d})$ and their variations $(\delta\mathbf{u}, \delta\tilde{\mathbf{E}}, \delta\mathfrak{d})$ are interpolated as

$$
\mathbf{u} \approx \mathbf{N}(\boldsymbol{\xi})\mathbf{d};\quad \tilde{\mathbf{E}} \approx \mathbf{M}(\boldsymbol{\xi})\varsigma;\quad \mathfrak{d} \approx \mathbf{N}(\boldsymbol{\xi})\tilde{\mathfrak{d}};\quad \delta\mathbf{u} \approx \mathbf{N}(\boldsymbol{\xi})\delta\mathbf{d};\quad \delta\tilde{\mathbf{E}} \approx \mathbf{M}(\boldsymbol{\xi})\delta\varsigma;\quad \delta\mathfrak{d} \approx \mathbf{N}(\boldsymbol{\xi})\delta\tilde{\mathfrak{d}}.
$$

Here, $\mathbf{M}(\boldsymbol{\xi})$ is so called enhancing interpolation matrix in the natural co-ordinates takes the form

$$
\tilde{\mathbf{M}} = \begin{bmatrix}
\xi^1 & 0 & 0 & 0 & 0 & 0 & 0\\
0 & \xi^1 & 0 & 0 & 0 & 0 & 0\\
0 & 0 & \xi^3 & \xi^1\xi^3 & \xi^2\xi^3 & 0 & 0\\
0 & 0 & 0 & 0 & 0 & \xi^1 & \xi^2\\
0 & 0 & 0 & 0 & 0 & 0 & 0\\
0 & 0 & 0 & 0 & 0 & 0 & 0
\end{bmatrix}. \tag{5.14}
$$

The $\boldsymbol{\varsigma}$ denotes the collection of EAS parameters. The transverse shear strains (E_{13}, E_{23} and transverse normal strain (E_{33}) are modified in line with ANS interpolation method to avoid transverse and trapezoidal locking. The interpolation of transverse shear are performed as in Fig 29 using points (A, B,C,D) as

$$\begin{Bmatrix} E_{13}^{ANS} \\ E_{23}^{ANS} \end{Bmatrix} = \begin{Bmatrix} (1-\xi^2)E_{13}(\boldsymbol{\xi}_A) + (1+\xi^2)E_{13}(\boldsymbol{\xi}_C) \\ (1+\xi^1)E_{23}(\boldsymbol{\xi}_B) + (1-\xi^1)E_{23}(\boldsymbol{\xi}_D) \end{Bmatrix}, \tag{5.15}$$

and transverse normal strains using (O,P,S,T) as

$$E_{33}^{ANS} = \sum_{m=E,F,G,H} \frac{1}{4}\left(1+\xi_m^1\xi^1\right)\left(1+\xi_m^2\xi^2\right)E_{33}; \qquad \text{with } \xi_m^1, \xi_m^2 = \pm 1. \tag{5.16}$$

The gradient quantities such as displacement derived Green-Lagrangian strain $\mathbf{E}^u$, $\nabla_{\mathbf{x}}\mathfrak{d}$ and their variations are interpolated as

$$\mathbf{E}^u \approx \mathbf{B}(\mathbf{d})\mathbf{d}; \;\; \delta\mathbf{E}^u \approx \mathbf{B}(\mathbf{d})\delta\mathbf{d}; \;\; \nabla_{\mathbf{x}}\mathfrak{d} \approx \mathbf{B}^{\mathfrak{d}}(\mathbf{d})\tilde{\mathfrak{d}}, \;\; \nabla_{\mathbf{x}}\delta\mathfrak{d} \approx \mathbf{B}^{\mathfrak{d}}(\mathbf{d})\delta\tilde{\mathfrak{d}},$$

for the standard gradient operator $\mathbf{B}(\mathbf{d})$ and $\mathbf{B}^{\mathfrak{d}}(\mathbf{d})$.

For each pseudo increment $\Delta t := t_{n+1}^{(k)} - t_n > 0$, and assuming that $(\mathbf{u}, \tilde{\mathbf{E}}, \mathfrak{d})_{t_n}$ is known, the cumulative fatigue history reads

$$\bar{\alpha}_{t+1} = \bar{\alpha}_t + \int_{t_n}^{t_{n+1}} \dot{\bar{\alpha}}\,\mathrm{d}\tau = \bar{\alpha}_t + \Delta\bar{\alpha}, \tag{5.17}$$

where $\Delta\bar{\alpha}$ is approximated as

$$\Delta\bar{\alpha} = |\alpha_{n+1} - \alpha_n| H\left(\frac{\alpha_{n+1}-\alpha_n}{\Delta t}\right). \tag{5.18}$$

Moreover, following the standard finite element procedure, the residual equations in Eq. (5.13) are written as system of linear equations

$$\begin{bmatrix} \mathbf{K}_{\mathbf{dd}} & \mathbf{K}_{\mathbf{d}\varsigma} & \mathbf{K}_{\mathbf{d}\tilde{\mathfrak{d}}} \\ \mathbf{K}_{\varsigma\mathbf{d}} & \mathbf{K}_{\varsigma\varsigma} & \mathbf{K}_{\varsigma\tilde{\mathfrak{d}}} \\ \mathbf{K}_{\tilde{\mathfrak{d}}\mathbf{d}} & \mathbf{K}_{\tilde{\mathfrak{d}}\varsigma} & \mathbf{K}_{\tilde{\mathfrak{d}}\tilde{\mathfrak{d}}} \end{bmatrix} \begin{bmatrix} \Delta\mathbf{d} \\ \Delta\boldsymbol{\varsigma} \\ \Delta\mathfrak{d} \end{bmatrix} = \begin{bmatrix} \hat{\mathcal{R}}_{\text{ext}}^{u} \\ \mathbf{0} \\ \mathbf{0} \end{bmatrix} - \begin{bmatrix} \hat{\mathcal{R}}_{\text{int}}^{u} \\ \hat{\mathcal{R}}_{\text{int}}^{\varsigma} \\ \hat{\mathcal{R}}_{\text{int}}^{\tilde{\mathfrak{d}}} \end{bmatrix}. \tag{5.19}$$

The components of stiffness matrix reads

$$\begin{aligned} \mathbf{K}_{\mathbf{dd}} &= \int_{\mathcal{B}_0} g(\mathfrak{d})\left(\mathbf{B}(\mathbf{d})^{\mathrm{T}}\mathbb{C}\mathbf{B}(\mathbf{d}) + \left[\frac{\partial\mathbf{B}(\mathbf{d})}{\partial\mathbf{d}}\right]^{\mathrm{T}}\mathbf{S}\right)\mathrm{d}\Omega = \mathbf{K}_{\mathbf{dd},\text{mat}} + \mathbf{K}_{\mathbf{dd},\text{geom}} \\ \mathbf{K}_{\mathbf{d}\varsigma} &= \int_{\mathcal{B}_0} g(\mathfrak{d})\mathbf{M}(\boldsymbol{\xi})^{\mathrm{T}}\mathbb{C}\mathbf{B}(\mathbf{d})\,\mathrm{d}\Omega; \qquad \mathbf{K}_{\mathbf{d}\tilde{\mathfrak{d}}} = \int_{\mathcal{B}_0} -2(1-\mathfrak{d})\mathbf{B}(\mathbf{d})^{\mathrm{T}}\mathbf{S}\mathbf{N}(\boldsymbol{\xi})\,\mathrm{d}\Omega, \end{aligned} \tag{5.20}$$

$$\begin{aligned} \mathbf{K}_{\varsigma u} &= \int_{\mathcal{B}_0} g(\mathfrak{d})\mathbf{M}(\boldsymbol{\xi})^{\mathrm{T}}\mathbb{C}\mathbf{B}(\mathbf{d})\,\mathrm{d}\Omega; \qquad \mathbf{K}_{\varsigma\varsigma} = \int_{\mathcal{B}_0} g(\mathfrak{d})\mathbf{M}(\boldsymbol{\xi})^{\mathrm{T}}\mathbb{C}\mathbf{M}(\boldsymbol{\xi})\,\mathrm{d}\Omega, \\ \mathbf{K}_{\varsigma\tilde{\mathfrak{d}}} &= \int_{\mathcal{B}_0} -2(1-\mathfrak{d})\mathbf{M}(\boldsymbol{\xi})^{\mathrm{T}}\mathbf{S}\mathbf{N}(\boldsymbol{\xi})\,\mathrm{d}\Omega; \end{aligned} \tag{5.21}$$

$$\begin{aligned}\mathbf{K}_{\tilde{\mathfrak{d}}\mathbf{d}} &= \int_{\mathcal{B}_0} -2(1-\mathfrak{d})\mathbf{N}(\boldsymbol{\xi})^{\mathrm{T}}\mathbf{S}\mathbf{B}(\mathbf{d})\,\mathrm{d}\Omega; \qquad \mathbf{K}_{\tilde{\mathfrak{d}}\varsigma} = \int_{\mathcal{B}_0} -2(1-\mathfrak{d})\mathbf{N}(\boldsymbol{\xi})^{\mathrm{T}}\mathbf{S}\mathbf{M}(\boldsymbol{\xi})\,\mathrm{d}\Omega, \\ \mathbf{K}_{\tilde{\mathfrak{d}}\tilde{\mathfrak{d}}} &= \int_{\mathcal{B}_0} \left[2f(\bar{\alpha}(t))\frac{\mathcal{G}_C}{l}\mathcal{H}\right]\mathbf{N}(\boldsymbol{\xi})^{\mathrm{T}}\mathbf{N}(\boldsymbol{\xi})\,\mathrm{d}\Omega + \int_{\mathcal{B}_0} 2f(\bar{\alpha}(t))\mathcal{G}_C l\mathbf{B}^{\mathfrak{d}}(\boldsymbol{\xi})^{\mathrm{T}}\mathbf{B}^{\mathfrak{d}}(\boldsymbol{\xi})\,\mathrm{d}\Omega,\end{aligned} \tag{5.22}$$

with crack driving force $\mathcal{H}$ takes the form

$$\mathcal{H} = \max_{\tau\in[0,t]}\left[\Psi(\mathbf{u},\tilde{\mathbf{E}})\right]. \tag{5.23}$$

Due to inter-element continuity of the enhanced strains, the above system of linear equation can be condensed via standard static condensation process as

$$\begin{bmatrix}\mathbf{K}^*_{\mathbf{d}\mathbf{d}} & \mathbf{K}^*_{\mathbf{d}\tilde{\mathfrak{d}}} \\ \mathbf{K}^*_{\tilde{\mathfrak{d}}\mathbf{d}} & \mathbf{K}^*_{\tilde{\mathfrak{d}}\tilde{\mathfrak{d}}}\end{bmatrix}\begin{bmatrix}\Delta\mathbf{d} \\ \Delta\mathfrak{d}\end{bmatrix} = \begin{bmatrix}\tilde{\hat{\mathcal{R}}}^{\mathbf{d}} \\ \tilde{\hat{\mathcal{R}}}^{\mathfrak{d}}\end{bmatrix}, \tag{5.24}$$

where $\mathbf{K}^*_{ij} = \mathbf{K}_{ij} - \mathbf{K}_{i\varsigma}\mathbf{K}^{-1}_{\varsigma\varsigma}\mathbf{K}_{\varsigma j}$ and $\tilde{\hat{\mathcal{R}}}^{j} = \mathcal{R}^{j}_{ext} - \mathcal{R}^{j}_{int} + \mathbf{K}_{i\varsigma}\mathbf{K}^{-1}_{\varsigma\varsigma}\mathcal{R}^{\varepsilon}_{int}$ for each $i, j = \{\mathbf{d}, \mathfrak{d}\}$.

The resulting system of linear algebraic equations in Eq. (5.24) is solved using the newton solver as detailed in Section 4.3.3.

5.3 Virtual testing

In this section, the predictive capabilities of the proposed fatigue model based on phase field model is assessed using several representative examples. The fatigue effects in the plate with notch under cyclic loads are examined for low cycle and moderately high cycle fatigue. Later, an example with half cylinder is considered to explore the capabilities of the shell structures.

5.3.1 Plate with notch

This example concerns with the application of the proposed model to plate with a notch specimen. Fig 64 a) shows the sketch of the model with an initial notch length of 0.5 mm, length of $L = 1$ mm, width of $w = 1$ mm and thickness $h = 0.05$ mm. This examples have been studies by considering Young's modulus $E = 210$ (GPa), Poisson's ratio $\nu = 0.3$, fracture energy $\mathcal{G}_C = 2.7$ (MPa$\sqrt{\text{mm}}$) and the length scale $l = 0.024$ mm is considered (unless specified).

A cyclic load of N number of cycles consisting of maximum amplitude $P = 0.002$mm and minimum of 0 is applied on the top surface, whereas the bottom surface is fixed. Similar to the previous examples in Chapter 4, EAS and ANS are included in the whole domain but are turned off locally when the phase field $\mathfrak{d} > 0.5$. Here, fatigue degradation function in Eq. (5.10) with $a = 2$ and the cumulative history variable independent of the mean load, is considered. In line with the example in [50], the Fig. 65a) represents the crack extension vs. number of cycles for the variation of maximum amplitude. Notice that, as the maximum amplitude decreases, the number of cycles taken to failure increases. Also, as the maximum amplitude decreases, the number of cycles taken to start the nucleation also increases which is well reflected in Fig. 65a). For P_{mon} being the amplitude required for full damage of the

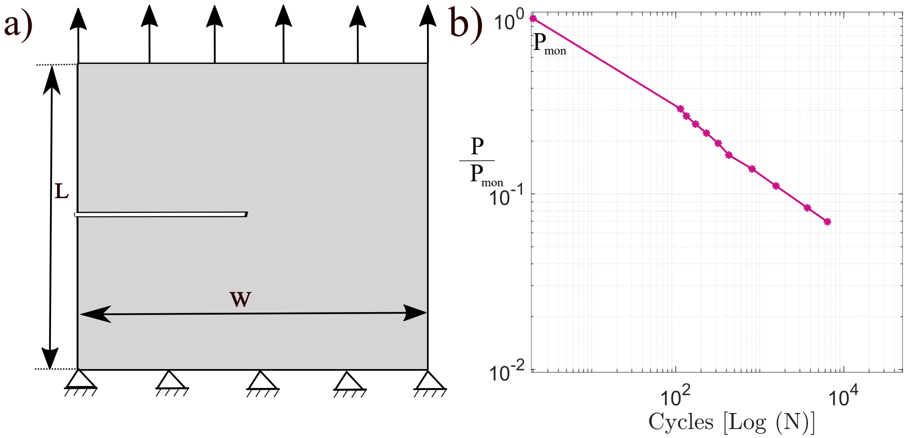

Figure 64: (a) Geometry and, (b) modified SN curve

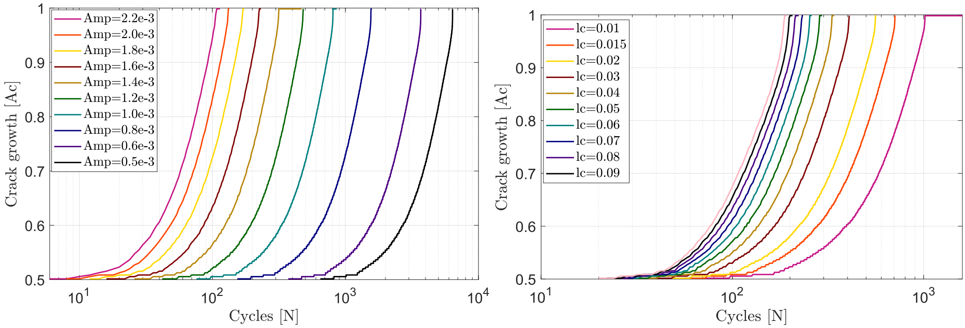

Figure 65: Crack extension vs. number of cycles (N) (a) for variation of maximum load amplitude P and, (b) for variation of characteristic length scale l.

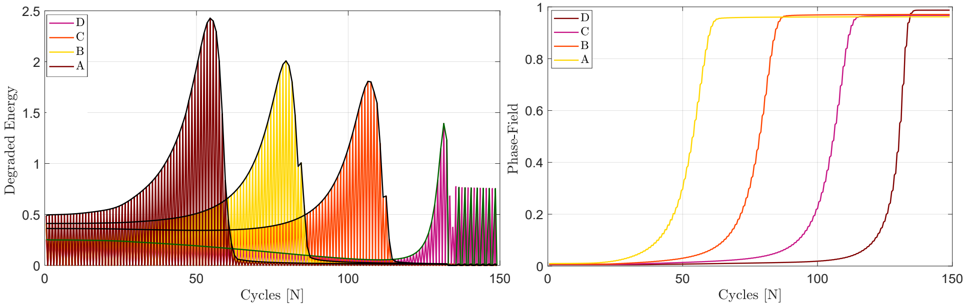

Figure 66: (a) Degraded Energy vs. N and, (b) phase-field vs. N at points (A,B,C,D).

specimen in monotonic condition, the Fig. 64 b) shows the modified SN curve where the ratio of maximum load P and P_{mon} is plotted against the number of cycles in the log-log scale. It can be clearly seen that as the $\dfrac{P}{P_{mon}}$ ratio decreases, the number of cycles increases. Generally, after $N = 10^7$, the specimen is considered to have infinite life. In other words, in the sense of numerical approximations, there exists a threshold of $\dfrac{P}{P_{mon}}$ such that the specimen will have an infinite life. Based on the Fig. 64 b), it is clear that for each load variation, a small difference in the load amplitude can have large change in the number of cycle (as an exponential functions) making the SN curve dense as the number of cycle increases.

Upon considering the variation of characteristics length scale l and keeping the maximum load amplitude $P = 0.0024$ constant, the crack extension vs. number of cycles are shown in Fig. 65b). Complying with the idea of $\Gamma-$convergence, as the length scale decreases, the number of cycles required for failure increases. Moreover, it can be observed from Fig. 65b) that variation of N for a linear variation of l is exponential in nature.

Fig. 66 shows the degraded energy and the phase-field values vs. number of cycles for $l = 0.0024$ mm and $P = 0.002$ mm at four different instances (A,B,C,D) which are equidistant from each other with distance approximately $(0.125, 0.25, 0.375, 0.5)$ from the notch tip. It can be seen from the energy degradation in Fig 66a) as the crack propagates, the bulk energy keeps decreasing until the fracture. Moreover, Fig 66b) shows the increase of phase-field at points (A,B,C,D) whose crack initiation, propagation and failure happens at different time instances. The crack propagation until the points (A, B, C, D) are shown in Fig. 67 showing a stable crack propagation.

For the fatigue degradation function as in Eq. (5.11), and cumulative history variable mean load independent, Fig. 68 shows the crack extension vs. number of cycles for variation of the k. It is observed that, for the $k < 0.26$, the crack propagation is stable resembling the Model-1, whereas for $k > 0.26$, the crack nucleation is stable whereas the crack propagation becomes unstable as in Fig. 68. This can be attributed to the fact that, the threshold of the fatigue function degradation is dependent on k in Eq. (5.11) making $f(\bar{\alpha}) = 0$ (symtotic). Moreover, as the $k \to 0$, number of cycles required for failure increases ($N \to \infty$).

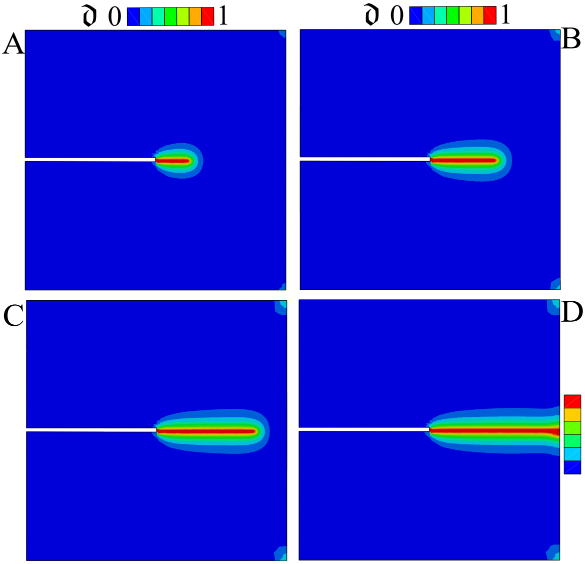

Figure 67: Phase-field crack propagation upto points (A, B, C, D).

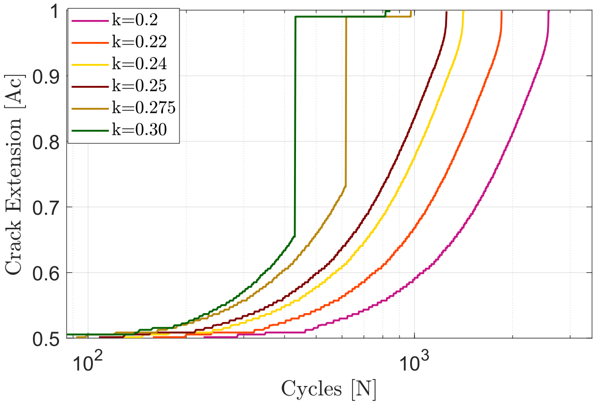

Figure 68: (a) Crack Extension in Model-2

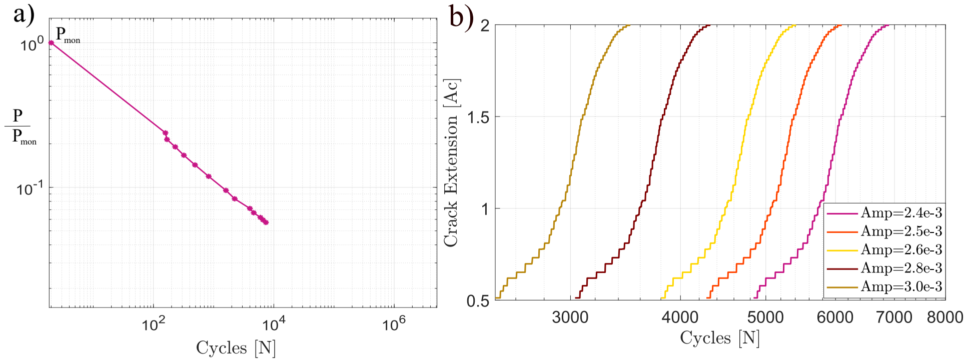

Figure 69: (a) SN Curve and, (b) Crack extension vs. number of cycles for cylindrical shells.

5.3.2 Curved shells

In this example, a curved half cylindrical shell with a hole is considered. For geometrical description of the model considers a radius of cylinder $R = 2$ mm, length $L = 10$mm , thickness $h = 0.01$ mm with an hole in the centre with radius $r = 0.15$mm. One axial end of the cylinder is fixed whereas the other axial end is loaded with N number of cycles of amplitude $(P, 0)$ is applied. The material properties with Young's modulus $E = 210$ (GPa), Poisons ratio $\nu = 0.3$, fracture energy $\mathcal{G}_C = 2.7$ (MPa$\sqrt{\text{mm}}$) and the length scale $l = 0.2$ mm is considered.

For the fatigue degradation function in Eq. (5.10), the crack extension vs. number of cycles for different load maximum load amplitude P is shown in Fig. 69 b), whereas the modified SN curve is shown in Fig. 69 a). With the usual notation, as the P decreases, the number of cycles N required for fracture increases. Also, It can also be seen that modified SN curve is dense at the number of number of cycles increases. Similar trends as Plate with notch are observed for the curved shells. For $P = 2.4 \times 10^{-3}$ mm and $l = 0.2$ mm, Fig. 70 shows the phase-field crack at cycles $N = 5000, 5500, 6000, 7500$ showing stable crack propagation.

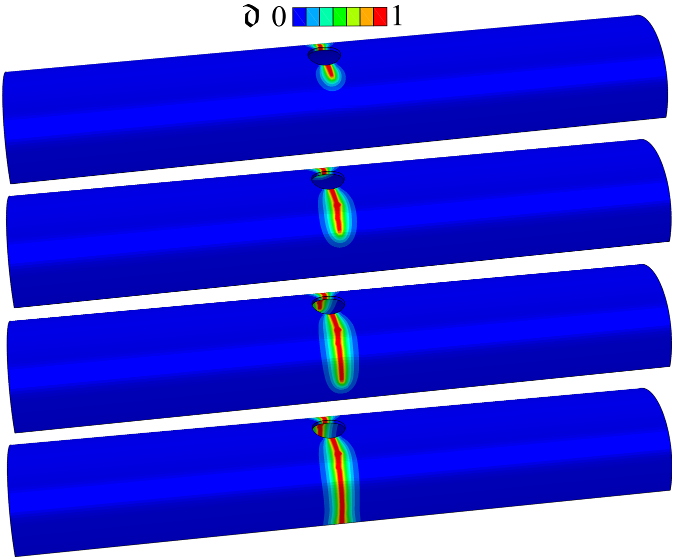

Figure 70: (a) Phase-field crack propagation for cylindrical shell.

Chapter 6

Conclusion and future developments

6.1 Conclusions

The research work conducted in this thesis deals with development of variational and cohesive methods for multi-physics problems in static and fatigue applications.

6.1.1 Conclusions on FGMs

With regard to the multi-physics developments, in Chapter 2 the phase field approximation of fracture in FGMs has been proposed by considering the internal length scale of the phase field as a characteristic property of the material. The proof of Γ-Convergence has been provided when the characteristics internal length scale l is constant or is a bounded function. It can be seen from the power law that as the scaling function approaches infinity in Eq. (2.7) (or ϵ approaches zero from Eq. (2.12)), the maximum reaction force also approach infinity asymptotically, hence can be considered as the numerical evidence for $\Gamma-$Convergence.

As an engineering application, it is possible to exploit the theoretical results upon size-scale effects to design experiments on scaled down specimens which do reproduce the behaviour of the real (full-scale) ones, by varying material properties. Moreover, it is shown that $\frac{\sigma^2}{E}$, and position of the initial crack tip affects the crack propagation and not only $E(\mathbf{x})$.

6.1.2 Conclusions on multi-failure modelling of fracture in long fibre reinforced composites

In Chapter 3, a consistent multi-phase field-cohesive zone model relying on phenomenological failure criterion has been proposed for matrix-dominated cracking in the presence of interfaces. Fiber failure, inter-fiber failure, and interface debonding mechanisms are accommodated into this model by considering a multi-phase field, each characterized by their failure phenomena with corresponding fracture energy and internal length scale, in conjunction to a cohesive zone model for the simulation of delamination events.

The computational framework has been carefully derived via multi-field variational formulation with multiple dissipative mechanisms within the spirit of phase-field and cohesive zone models such that thermodynamics consistency is preserved. The model has been applied to the study of delamination migration in composite materials to illustrate the capabilities of the model. The variation of the design parameters, such as the load application point, the angle between the plies, and the initial crack length, have been presented to assess the model response's sensitivity to such design parameters.

6.1.3 Conclusions on thermo-mechanical fracture in thin-walled structures

In Chapter 4, a consistent derivation of the thermo-mechanical locking free and fully integrated solid shell model for large displacement has been proposed. Locking effects have been remedied using the combination of 7 or 11 EAS parameters and the ANS method. The interface element, along its the thermo-mechanical extension, has been presented. Fully coupled thermo-mechanical extension for both the solid shell and the cohesive interface have been accounted for, as a major novelty with respect to the state-of-the-art literature. The details of the finite element implementation of the solid shell have been addressed. The thermo-mechanical coupling proposed can be easily modified to any of the existing cohesive which are distinct from the previous literature. The thermal conductivity degradation and the elastic energy degradation are done using the same function $g(\mathfrak{d})$.

In Section 4.4, numerical examples concerning slit annular rings with line forces showed the absence of locking. The large displacement arising from the solid shell has been addressed in specific examples with pulling, buckling, and bending of the bar, offering the alleviation of locking pathologies.

The interplay between the thermal and mechanical field and the effects of the interface on the solid shell have been discussed in reference to a plate with an internal cohesive interface. Through the peeling model, large displacements arising from the cohesive interface have been simulated, as well as coupling with heat conduction. This problem can be extremely relevant to simulate peeling tests performed inside climate chambers, to assess the behaviour of structural adhesives under different temperature conditions, which is noteworthy.

In Section 4.5, with phase field, the numerical predicting capabilities of the model are explored with three different materials having extremely different thermal and mechanical properties, namely: (a) silicon, (b) alumina, and (c) zircona.

A double-edged notch of allumina is provided to demonstrate the predictive capabilities of the model in comparison with the previous phase-field approaches. Furthermore, the model has been shown to predict temperature-assisted fractures and it has been shown that the presence of phase field cracks induces insulated barriers to heat flux. Correspondingly, the examples have shown that temperature distributions may lead to fracture and, conversely, cracks may affect the temperature distribution.

It can be emphasized that the developed model is particularly promising in addressing a wide range of industrial problems in automotive (body, chassis), aerospace (wings, turbines blades, rudder), renewable energy (photovoltaics, electronic chips, screen protectors, etc.) and thermal barrier coatings involving thick/thin plates (straight and curved) where temperature effects are significant.

In Section 4.6, an asymmetrical double-edge notched plate or with many holes have been analyzed to investigate the crack deflection in such complex FGM with all thermo-mechanical and fracture mechanics material properties function of space. The cylindrical shell example showed that the method can be effectively simulate crack deflection in FGM curved shells stemming from the material definition. The thermo-mechanical interaction and the difference between the elastic and temperature distribution between the FGM and homogeneous materials have been highlighted.

The plate with notch example is provided to show the thermo-elastic behavior, and the effect of the ratio of material properties such as Young's modulus, fracture energy, and thermal conductivity is explored using three different FGM pairs of (i) copper-titanium, (ii) alumina-zirconia, (iii) ailicon carbide- polymer glass.

Furthermore, based on the representative examples, the model has been shown to predict that the temperature distributions affect crack growth patterns and, conversely, cracks do affect heat transfer since they create thermally insulated zones in the material. A double FGM example has been provided to further show the possibility of combining two different FGM materials, which might be significant for material science.

Based on the FGMs, it can be emphasized that the proposed model is promising in addressing a wide range of industrial applications dealing with thermo-elastic applications involving thin/thick (straight or curved) plates such as heat ex-changers, cutting tools, turbine blades, biomedical implants, heat-resisting elements in space crafts, sports equipment, etc., where FGMs are extensively used.

6.1.4 Conclusions on phase field model for fatigue crack in thin-walled structures

In Chapter 5, a consistent derivation of locking free phase field fatigue has been proposed. The interplay between the fatigue effects on the fracture initiation and propagation have been explored thoroughly. The SN curves and the crack extension curves are naturally recovered as a consequence of the proposed model. Using representative examples, the predictive capability of the model is explored.

Finally, it can be emphasized that the proposed fatigue model is promising in addressing issues of industrial importance especially involving fatigue of thin sheets such as car chassis, turbine blades, solar panels, electronic chips etc.,

6.2 Conclusiones

El trabajo de investigación realizado en esta tesis trata sobre el desarrollo de métodos variacionales y cohesivos para problemas multifísicos en aplicaciones estáticas y de fatiga.

6.2.1 Conclusiones sobre las FGMs

Con respecto a los desarrollos multifísicos, en el Capítulo 2 se ha propuesto la aproximación del campo de fase de la fractura en FGM considerando la escala de longitud interna del campo de fase como una propiedad característica del material. La prueba de Γ-

Convergencia se proporciona cuando la escala de longitud interna de las características l es constante o es una función acotada. Se puede ver a partir de la ley de potencia que a medida que la función de escala se acerca al infinito en la ecuación. (2.7) (o ϵ se acerca a cero a partir de la ecuación (2.12)), la fuerza de reacción máxima también se acerca al infinito asintóticamente, por lo que puede considerarse como la evidencia numérica de $\Gamma-$Convergencia. Como una aplicación de ingeniería, es posible explotar los resultados teóricos sobre los efectos de escala de tamaño para diseñar experimentos en especímenes reducidos que reproduzcan el comportamiento de los reales (escala completa), variando las propiedades del material. Además, se muestra que $\frac{\sigma^2}{E}$, y la posición de la punta de la grieta inicial afecta la propagación de la grieta y no solo $E(\mathbf{x})$.

6.2.2 Conclusiones sobre el modelado de fallas múltiples de fractura en materiales compuestos reforzados con fibras largas

En el Capítulo 3, se ha propuesto un modelo consistente de zona cohesiva de campo multifásico que se basa en el criterio de falla fenomenológica para el agrietamiento dominado por la matriz en presencia de interfases. Los mecanismos de falla de fibra, falla entre fibras y desprendimiento de interfaz se acomodan en este modelo al considerar un campo multifásico, cada uno caracterizado por sus fenómenos de falla con la energía de fractura correspondiente y la escala de longitud interna, junto con un modelo de zona cohesiva para la simulación. de eventos de delaminación. El marco computacional se ha derivado cuidadosamente a través de una formulación variacional de múltiples campos con múltiples mecanismos disipativos dentro del espíritu de los modelos de fase-campo y zona cohesiva de modo que se preserva la consistencia termodinámica. El modelo se ha aplicado al estudio de la migración de la delaminación en materiales compuestos para ilustrar las capacidades del modelo. La variación de los parámetros de diseño, como el punto de aplicación de la carga, el ángulo entre las capas y la longitud inicial de la fisura, se han presentado para evaluar la sensibilidad de la respuesta del modelo a dichos parámetros de diseño.

6.2.3 Conclusiones sobre fractura termomecánica en estructuras de paredes delgadas

En el Capítulo 4, se ha propuesto una derivación consistente del modelo de capa sólida totalmente integrado y libre de bloqueo termomecánico para grandes desplazamientos. Los efectos de bloqueo se han solucionado utilizando la combinación de 7 u 11 parámetros EAS y el método ANS. Se ha presentado el elemento interfaz, junto con su extensión termomecánica. Se ha tenido en cuenta la extensión termomecánica completamente acoplada tanto para la capa sólida como para la interfaz cohesiva, como una gran novedad con respecto a la literatura de vanguardia. Se han abordado los detalles de la implementación de elementos finitos de la capa sólida. El acoplamiento termomecánico propuesto se puede modificar fácilmente a cualquiera de los cohesivos existentes que son distintos de la literatura anterior. La degradación de la conductividad térmica y la degradación de la energía elástica se realizan utilizando la misma función $g(\mathfrak{d})$.

En la Sección 4.4, los ejemplos numéricos relacionados con anillos anulares ranurados con fuerzas lineales mostraron la ausencia de bloqueo. El gran desplazamiento que surge de la cubierta sólida se ha abordado en ejemplos específicos tirando, pandeando y doblando la barra, lo que ofrece el alivio de las patologías de bloqueo.

La interacción entre el campo térmico y mecánico y los efectos de la interfaz en la capa sólida se han discutido en referencia a una placa con una interfaz cohesiva interna. Mediante el modelo de pelado se han simulado grandes desplazamientos derivados de la interfase cohesiva, así como el acoplamiento con la conducción de calor. Este problema puede ser sumamente relevante para simular ensayos de pelado realizados dentro de cámaras climáticas, para evaluar el comportamiento de adhesivos estructurales bajo diferentes condiciones de temperatura, lo cual es digno de mención.

En la Sección 4.5, con campo de fase, se exploran las capacidades de predicción numérica del modelo con tres materiales diferentes que tienen propiedades térmicas y mecánicas extremadamente diferentes, a saber: (a) silicio, (b) alúmina y (c) circona.

Se proporciona una muesca de alúmina de doble filo para demostrar las capacidades predictivas del modelo en comparación con los enfoques de campo de fase anteriores. Además, se ha demostrado que el modelo predice fracturas asistidas por temperatura y se ha demostrado que la presencia de grietas de campo de fase induce barreras aisladas al flujo de calor. En consecuencia, los ejemplos han demostrado que las distribuciones de temperatura pueden conducir a la fractura y, por el contrario, las grietas pueden afectar la distribución de temperatura.

Se puede enfatizar que el modelo desarrollado es particularmente prometedor para abordar una amplia gama de problemas industriales en automoción (carrocería, chasis), aeroespacial (alas, palas de turbinas, timón), energías renovables (fotovoltaica, chips electrónicos, protectores de pantalla, etc.).) y recubrimientos de barrera térmica que involucran placas gruesas/delgadas (rectas y curvas) donde los efectos de la temperatura son significativos.

En la Sección 4.6, se analizó una placa asimétrica con muescas de doble filo o con muchos orificios para investigar la deflexión de grietas en un FGM tan complejo con todas las propiedades del material termomecánicas y mecánicas de fractura en función del espacio. El ejemplo de capa cilíndrica mostró que el método puede simular de manera efectiva la deflexión de grietas en capas curvas FGM derivadas de la definición del material. Se ha destacado la interacción termomecánica y la diferencia entre la distribución elástica y de temperatura entre la FGM y los materiales homogéneos. Se proporciona el ejemplo de la placa con muesca para mostrar el comportamiento termoelástico, y se explora el efecto de la proporción de las propiedades del material, como el módulo de Young, la energía de fractura y la conductividad térmica, utilizando tres pares FGM diferentes de (i) cobre-titanio, (ii) alúmina-zirconia, (iii) vidrio de polímero de carburo de silicio.

Además, según los ejemplos representativos, se ha demostrado que el modelo predice que las distribuciones de temperatura afectan los patrones de crecimiento de grietas y, por el contrario, las grietas sí afectan la transferencia de calor, ya que crean zonas térmicamente aisladas en el material. Se ha proporcionado un ejemplo de doble FGM para mostrar aún más la posibilidad de combinar dos materiales de FGM diferentes, lo que podría ser significativo para la ciencia de los materiales.

Con base en los FGM, se puede enfatizar que el modelo propuesto es prometedor para abordar una amplia gama de aplicaciones industriales relacionadas con aplicaciones termoelásticas que involucran placas delgadas/gruesas (rectas o curvas) como intercambiadores de calor, herramientas de corte, turbinas. cuchillas, implantes biomédicos, elementos resistentes al calor en naves espaciales, equipos deportivos, etc., donde las MGF se utilizan ampliamente.

6.2.4 Conclusiones sobre el modelo de campo de fase para grietas por fatiga en estructuras de paredes delgadas

En el Capítulo 5, se ha propuesto una derivación consistente de la fatiga de campo de fase libre de bloqueo. La interacción entre los efectos de la fatiga en el inicio y la propagación de la fractura se ha explorado a fondo. Las curvas SN y las curvas de extensión de fisura se recuperan naturalmente como consecuencia del modelo propuesto. Usando ejemplos representativos, se explora la capacidad predictiva del modelo.

Finalmente, se puede enfatizar que el modelo de fatiga propuesto es prometedor para abordar problemas de importancia industrial, especialmente relacionados con la fatiga de láminas delgadas como chasis de automóviles, álabes de turbinas, paneles solares, chips electrónicos, etc.

6.3 Future developments

Along this line of research, several research areas can be potentially identified. In order for a comprehensive outlook, the future developments can be broadly divided into four categories (i) Fundamental issues, (ii) mathematical issues, (iii) multi-physics issues, and (iv) industrial relevance.

(i). Fundamental issues

The major drawback of the phase-field approximation to fracture is its inability to predict crack nucleation in the absence of pre-existing notch or crack. In this regard, some authors have suggested stress-based criteria, where predicting crack propagation is at stake. Recently these approaches have been presented in the sense of Phase-field. (1) Modification to the energy functional to accommodate nucleation either by adding the strength of the material or via the introduction of the strength through characteristic length scale [110]. (2) Implicitly account for defects at a microscopic level, so that the macroscopic manifestation defines the strength of material by modification of the crack driving force via ad hoc criteria [256].

Both partially solve the issue of crack nucleation. In the case of (1), since length scale l is considered to be constant, the $\Gamma-$convergence of the approximation function is not guaranteed. Note that, in this research, it has been proved that when l is constant, the approximation $\Gamma-$Convergence but only in two dimensions. Moreover, the technique used is very typical of two dimensions; hence it cannot be considered the general proof. In the case of (2), the variational structure of the phase-field formulation is lost. Even though the nucleation problem holds, the model cannot be based on either Griffith's theory or a proper modification of it.

In this regard, a theory that can combine the Dugdale/Barenblat theory of cohesive zone models and phase-field approximation to fracture can be valuable and possibly solve this issue in the current state of the art. Such a theory would nucleate the crack, coalescence, and propagate the crack. This poses two significant challenges (a) since phase-field approximation is based on the variational structures, the Dugdale/Barenblat theory needs to be also variational, (b) There are infinitely many possibilities of making the cohesive zone model consistent with phase-field since the problem reduces to finding a projection of hyper-surface onto a surface leading to the curse of dimensionality. It would be interesting to work towards unifying different models without loss of generality and sense of $\Gamma-$Convergence.

(ii). Mathematical aspects

Regarding $\Gamma-$Convergence, the space GSBD has shown promising results in the recent decade. Density results for $\mathrm{GSBD}^p(\Omega)$ for $\Omega \in \mathrm{R}^n$ is available now whose applications can be extended to plasticity-based models, tension/compression split, fatigue effects models. Moreover, it would be interesting to investigate the convergence for models based on solid shells and multiple phase fields formulations.

Concerning the discretization schemes, finite element (FE)-based methods approximated the functional space inducing an error. Moreover, the phase-field functional approximates Griffith's energy leading to multiplication of error. Research in this direction towards finding priori and posteriori error estimation for the coupled phase-field functional in the sense of FEM would be worth to be developed. The reason for not much research towards this area seems to be stemming from the fact that phase-field methods are neither fully elliptical (static) functionals nor fully parabolic (dynamic), but quasi-static. Moreover, a significant improvement in the simulation accuracy can be achieved by using the error estimate to compute the solution. Consequently, the total error between the approximated FEM and Griffith's energy can be reduced.

Powerful methods such as (ENO) Essentially Non-Oscillatory, spectral or pseudo-spectral methods, multigrid methods, infinite element methods could be interesting to see and access the performance of these methods with the existing ones.

Only a few solvers such as BFGS, newton, and quasi-newton solvers have been used to solve the linear equations arising from the phase field. Research towards using solvers such as GMRES, CR (conjugate residual), CG (conjugate gradient), GCR (Generalized Conjugate Residual), Newton-Krylov, Krylov subspace solvers could be interesting. In this regard, machine learning techniques such as physics-informed neural networks already showed great potential in solving partial differential equations. Adopting those methods and combining them with different solvers for the solution of phase-field, especially for the multi-physics problems, can be extremely useful to reduce the computational time.

(iii). Multi-Physics applications

Since the content of this thesis is devoted to developing multi-physics models, the reasonable step towards future can be summarised as follows. Based on the solid shell approach, it can be noticed that long reinforced composites are usually thin-walled structures. The development of a solid shell-based approach for composites could be exciting. The multi-physics related to composited such as thermo-mechanical interactions fatigue effects would be highly beneficial for industrial applications. Moreover, fatigue-based phase-field models are still in their infancy but have great potential to tackle industrial applications. The major drawback in the phase-field fatigue is its inability to predict nucleation and unstable crack propagation before and after Paris law, respectively. Research towards this direction could be interesting. Combining these models with cycle skipping methods and introducing multi-physics interaction could eventually lead to robust industrial designs. Specifically, fretting fatigue, hydrogen embrittlement, chemical deposition effects, moisture effects, porosity effects, etc., on the design and their interaction would provide a complete physics of the design issues.

(iv). Industrial Relevance

With moving parts in every engineering system, the interactions and exchange of energies between the moving parts cause the material to change (wear and tear) and sometimes develop a fracture. In this regard, contact problems are of most industrial relevance. Boundary element methods have shown to be most helpful and very well approximates the experimental results. Due to the micro-mechanics approach, these simulations' computational cost is high restricting it to small problems. The research concerning fracture development due to contact provides a tool for better design of moving parts. Such models can be developed by combining phase-field methods with BEM methods for different contact geometry. An extension to multi-physics problems involving heat transfer, friction wear, and micro-mechanics could render useful.

Non-destructive testing methods can determine defects in the material structures. This data can then be introduced into a phase-field method for realistic crack nucleation and propagation using stochastic-based phase-field models to accurately predict the crack and prevent the already existing crack from propagating. Fluid-structure interactions using phase-field method to access the possibility as a failure mechanism using phase-field methods could be helpful in applications such as turbine/compressor blades, engines, channels, high-pressure pipes, and high-pressure chambers, etc.,

Regarding direct applications of the industrial relevance, the already existing models can be used to study meta-materials, degradation of solar cells due to multi-physics, solid-state batteries via combining CZM and phase-field approaches, wings/components of aircraft using solid shell approach to name a few.

Furthermore, an engineering design is complete only if the design is neither over-optimized, leading to failure, nor under optimized leading underperformance. In this regard, topology optimization methods can be combined with the multi-physics phase-field approach to enhance the design for optimal performance.

Bibliography

[1] A. A. Griffith. "The Phenomena of Rupture and Flow in Solids". In: *Philosophical Transactions of the Royal Society of London. Series A, Containing Papers of a Mathematical or Physical Character* 221 (1921), pp. 163–198. ISSN: 02643952. URL: `http://www.jstor.org/stable/91192`.

[2] G. R. Irwin. "Analysis of Stresses and Strains Near the End of a Crack Traversing a Plate". In: *Journal of Applied Mechanics* 24.3 (June 2021), pp. 361–364. ISSN: 0021-8936. DOI: `10.1115/1.4011547`.

[3] Lazar M Kachanov. "Rupture Time Under Creep Conditions". In: *International Journal of Fracture* 97.1 (1999), pp. 11–18. ISSN: 1573-2673. DOI: `10.1023/A:1018671022008`. URL: `https://doi.org/10.1023/A:1018671022008`.

[4] J.C. Simo and J.W. Ju. "Strain- and stress-based continuum damage models—I. Formulation". In: *International Journal of Solids and Structures* 23.7 (1987), pp. 821–840. ISSN: 0020-7683. DOI: `https://doi.org/10.1016/0020-7683(87)90083-7`.

[5] R. de Borst and L.J. Sluys. "Localisation in a Cosserat continuum under static and dynamic loading conditions". In: *Computer Methods in Applied Mechanics and Engineering* 90.1 (1991), pp. 805–827. ISSN: 0045-7825. DOI: `https://doi.org/10.1016/0045-7825(91)90185-9`.

[6] Zdeněk P. Bažant and Gilles Pijaudier-Cabot. "Nonlocal Continuum Damage, Localization Instability and Convergence". In: *J. Appl. Mech.* 55(2) (1988), pp. 287–293. DOI: `https://doi.org/10.1115/1.3173674`.

[7] R. H. J. PEERLINGS et al. "GRADIENT ENHANCED DAMAGE FOR QUASI-BRITTLE MATERIALS". In: *International Journal for Numerical Methods in Engineering* 39.19 (1996), pp. 3391–3403. DOI: `https://doi.org/10.1002/(SICI)1097-0207(19961015)39:19<3391::AID-NME7>3.0.CO;2-D`.

[8] R. H. J. PEERLINGS et al. "GRADIENT ENHANCED DAMAGE FOR QUASI-BRITTLE MATERIALS". In: *International Journal for Numerical Methods in Engineering* 39.19 (1996), pp. 3391–3403. DOI: `10.1002/(SICI)1097-0207(19961015)39:19<3391::AID-NME7>3.0.CO;2-D`.

[9] Kim Pham et al. "Gradient Damage Models and Their Use to Approximate Brittle Fracture". In: *International Journal of Damage Mechanics* 20.4 (2011), pp. 618–652. DOI: `10.1177/1056789510386852`.

[10] D.S. Dugdale. "Yielding of steel sheets containing slits". In: *Journal of the Mechanics and Physics of Solids* 8.2 (1960), pp. 100–104. ISSN: 0022-5096. DOI: `https://doi.org/10.1016/0022-5096(60)90013-2`.

[11] G.I. Barenblatt. "The Mathematical Theory of Equilibrium Cracks in Brittle Fracture". In: ed. by H.L. Dryden et al. Vol. 7. Advances in Applied Mechanics. Elsevier, 1962, pp. 55–129. DOI: `https://doi.org/10.1016/S0065-2156(08)70121-2`.

[12] F. Erdogan and G. C. Sih. "On the Crack Extension in Plates Under Plane Loading and Transverse Shear". In: *Journal of Basic Engineering* 85.4 (Dec. 1963), pp. 519–525. ISSN: 0021-9223. DOI: `10.1115/1.3656897`.

[13] G.C. Sih. "Energy-density concept in fracture mechanics". In: *Engineering Fracture Mechanics* 5.4 (1973), pp. 1037–1040. ISSN: 0013-7944. DOI: `https://doi.org/10.1016/0013-7944(73)90072-6`.

[14] G.A. Francfort and J.-J. Marigo. "Revisiting brittle fracture as an energy minimization problem". In: *Journal of the Mechanics and Physics of Solids* 46.8 (1998), pp. 1319–1342. ISSN: 0022-5096. DOI: `https://doi.org/10.1016/S0022-5096(98)00034-9`.

[15] Blaise Bourdin, Gilles A. Francfort, and Jean-Jacques Marigo. "The Variational Approach to Fracture". In: *Journal of Elasticity* 91.1 (Apr. 2008), pp. 5–148. ISSN: 1573-2681. DOI: `10.1007/s10659-007-9107-3`.

[16] B. Bourdin, G.A. Francfort, and J-J. Marigo. "Numerical experiments in revisited brittle fracture". In: *Journal of the Mechanics and Physics of Solids* 48.4 (2000), pp. 797–826. ISSN: 0022-5096. DOI: `https://doi.org/10.1016/S0022-5096(99)00028-9`.

[17] Antonin Chambolle. "An approximation result for special functions with bounded deformation". In: *Journal de Mathématiques Pures et Appliquées* 83.7 (2004), pp. 929–954. ISSN: 0021-7824. DOI: `https://doi.org/10.1016/j.matpur.2004.02.004`. URL: `http://www.sciencedirect.com/science/article/pii/S0021782404000285`.

[18] David Mumford and Jayant Shah. "Optimal approximations by piecewise smooth functions and associated variational problems". In: *Communications on Pure and Applied Mathematics* 42.5 (1989), pp. 577–685. DOI: `https://doi.org/10.1002/cpa.3160420503`.

[19] Luigi Ambrosio and Andrea Braides. *Energies in SBV and variational models in fracture mechanics.* 1997.

[20] Luigi Ambrosio and Andrea Braides. *Energies in SBV and variational models in fracture mechanics.* 1997.

[21] Luigi Ambrosio and Vincenzo Maria Tortorelli. "ON THE APPROXIMATION OF FREE DISCONTINUITY PROBLEMS". In: 1992.

[22] Andrea Braides. "Gamma-convergence for beginners". In: *of Oxford Lecture Series in Mathematics and its Applications*. University Press, 2002.

[23] Luigi Ambrosio and Vincenzo Maria Tortorelli. "Approximation of functional depending on jumps by elliptic functional via t-convergence". In: *Communications on Pure and Applied Mathematics* 43.8 (1990), pp. 999–1036. DOI: `https://doi.org/10.1002/cpa.3160430805`.

[24] P.K. Asur Vijaya Kumar et al. "Phase field modeling of fracture in Functionally Graded Materials: Gamma-convergence and mechanical insight on the effect of grading". In: *Thin-Walled Structures* 159 (2021), p. 107234. ISSN: 0263-8231. DOI: `https://doi.org/10.1016/j.tws.2020.107234`.

[25] M. Negri and M. Paolini. "Numerical minimization¶of the Mumford–Shah functional". In: *CALCOLO* 38.2 (June 2001), pp. 67–84. ISSN: 1126-5434. DOI: `10.1007/s100920170004`.

[26] Crismale Chambolle A. "A Density Result in GSBDp with Applications to the Approximation of Brittle Fracture Energies." In: *Arch Rational Mech Anal 232,* (Aug. 2019), pp. 1329–1378. DOI: `https://doi.org/10.1007/s00205-018-01344-7`.

[27] Luigi Ambrosio, Alessandra Coscia, and Gianni Dal Maso. "Fine Properties of Functions with Bounded Deformation". In: *Arch. Rational Mech. Anal.* 139 (1997), pp. 201–238.

[28] Christian Miehe, Martina Hofacker, and Fabian Welschinger. "A phase field model for rate-independent crack propagation: Robust algorithmic implementation based on operator splits". In: *Computer Methods in Applied Mechanics and Engineering* 199.45 (2010), pp. 2765–2778. ISSN: 0045-7825. DOI: `https://doi.org/10.1016/j.cma.2010.04.011`.

[29] Charlotte Kuhn, Alexander Schlüter, and Ralf Müller. "On degradation functions in phase field fracture models". In: *Computational Materials Science* 108 (2015). Selected Articles from Phase-field Method 2014 International Seminar, pp. 374–384. ISSN: 0927-0256. DOI: `https://doi.org/10.1016/j.commatsci.2015.05.034`.

[30] Charlotte Kuhn and Ralf Müller. "A continuum phase field model for fracture". In: *Engineering Fracture Mechanics* 77.18 (2010), pp. 3625–3634. ISSN: 0013-7944. DOI: `https://doi.org/10.1016/j.engfracmech.2010.08.009`.

[31] A. Mesgarnejad, B. Bourdin, and M.M. Khonsari. "Validation simulations for the variational approach to fracture". In: *Computer Methods in Applied Mechanics and Engineering* 290 (2015), pp. 420–437. ISSN: 0045-7825. DOI: `https://doi.org/10.1016/j.cma.2014.10.052`.

[32] Roberto Alessi, Jean-Jacques Marigo, and Stefano Vidoli. "Gradient damage models coupled with plasticity: Variational formulation and main properties". In: *Mechanics of Materials* 80 (2015). Materials and Interfaces, pp. 351–367. ISSN: 0167-6636. DOI: `https://doi.org/10.1016/j.mechmat.2013.12.005`.

[33] J.Y. Wu. "A unified phase-field theory for the mechanics of damage and quasi-brittle failure". In: *Journal of the Mechanics and Physics of Solids* 103 (2017), pp. 72–99.

[34] Alain Karma, David A. Kessler, and Herbert Levine. "Phase-Field Model of Mode III Dynamic Fracture". In: *Phys. Rev. Lett.* 87 (4 July 2001), p. 045501. DOI: `10.1103/PhysRevLett.87.045501`. URL: `https://link.aps.org/doi/10.1103/PhysRevLett.87.045501`.

[35] C. Miehe, F. Welschinger, and M. Hofacker. "Thermodynamically consistent phase-field models of fracture: Variational principles and multi-field FE implementations". In: *International Journal for Numerical Methods in Engineering* 83.10 (2010), pp. 1273–1311. DOI: `10.1002/nme.2861`.

[36] Giovanni Lancioni and Gianni Royer-Carfagni. "The Variational Approach to Fracture Mechanics. A Practical Application to the French Panthéon in Paris". In: *Journal of Elasticity* 95.1 (2009), pp. 1–30. ISSN: 1573-2681. DOI: `10.1007/s10659-009-9189-1`. URL: `https://doi.org/10.1007/s10659-009-9189-1`.

[37] Hanen Amor, Jean-Jacques Marigo, and Corrado Maurini. "Regularized formulation of the variational brittle fracture with unilateral contact: Numerical experiments". In: *Journal of the Mechanics and Physics of Solids* 57.8 (2009), pp. 1209–1229. DOI: `https://doi.org/10.1016/j.jmps.2009.04.011`.

[38] Michael J. Borden et al. "A phase-field formulation for fracture in ductile materials: Finite deformation balance law derivation, plastic degradation, and stress triaxiality effects". In: *Computer Methods in Applied Mechanics and Engineering* 312 (2016). Phase Field Approaches to Fracture, pp. 130–166. ISSN: 0045-7825. DOI: `https://doi.org/10.1016/j.cma.2016.09.005`.

[39] Charlotte Kuhn, Alexander Schlüter, and Ralf Müller. “On degradation functions in phase field fracture models”. In: *Computational Materials Science* 108 (2015), pp. 374–384. ISSN: 0927-0256. DOI: `https://doi.org/10.1016/j.commatsci.2015.05.034`.

[40] Eric Lorentz. “A nonlocal damage model for plain concrete consistent with cohesive fracture”. In: *International Journal of Fracture* 207.2 (2017), pp. 123–159. ISSN: 1573-2673. DOI: `10.1007/s10704-017-0225-z`. URL: `https://doi.org/10.1007/s10704-017-0225-z`.

[41] A. Wohler. “Über die festigkeitsversuche mit eisen und stahl”. In: (1870).

[42] P. Paris and F. Erdogan. “A Critical Analysis of Crack Propagation Laws”. In: *Journal of Basic Engineering* 85.4 (Dec. 1963), pp. 528–533. ISSN: 0021-9223. DOI: `10.1115/1.3656900`. URL: `https://doi.org/10.1115/1.3656900`.

[43] P. C. Paris. “A rational analytic theory of fatigue”. In: 1961.

[44] L F Coffin Jr. “A STUDY OF THE EFFECTS OF CYCLIC THERMAL STRESSES ON A DUCTILE METAL”. In: (June 1953). URL: `https://www.osti.gov/biblio/4363016`.

[45] S. S. Manson. “Behavior of materials under conditions of thermal stress”. In: 1953.

[46] A Palmgren. “The service life of ball bearing”. In: *Z.Ver. Dtsch.Ing* 2 (1924), pp. 339–341.

[47] Milton A. Miner. “Cumulative Damage in Fatigue”. In: *Journal of Applied Mechanics* 12.3 (Mar. 2021), A159–A164. ISSN: 0021-8936. DOI: `10.1115/1.4009458`. URL: `https://doi.org/10.1115/1.4009458`.

[48] J.L. Boldrini et al. “A non-isothermal thermodynamically consistent phase field framework for structural damage and fatigue”. In: *Computer Methods in Applied Mechanics and Engineering* 312 (2016). Phase Field Approaches to Fracture, pp. 395–427. ISSN: 0045-7825. DOI: `https://doi.org/10.1016/j.cma.2016.08.030`. URL: `https://www.sciencedirect.com/science/article/pii/S0045782516310660`.

[49] Christoph Schreiber, Ralf Müller, and Charlotte Kuhn. “Phase field simulation of fatigue crack propagation under complex load situations”. In: *Archive of Applied Mechanics* 91.2 (2021), pp. 563–577. ISSN: 1432-0681. DOI: `10.1007/s00419-020-01821-0`.

[50] “A framework to model the fatigue behavior of brittle materials based on a variational phase-field approach”. In: *Computer Methods in Applied Mechanics and Engineering* 361 (2020), p. 112731. ISSN: 0045-7825. DOI: `https://doi.org/10.1016/j.cma.2019.112731`. URL: `https://www.sciencedirect.com/science/article/pii/S0045782519306218`.

[51] Roberto Alessi, Vito Crismale, and Gianluca Orlando. “Fatigue Effects in Elastic Materials with Variational Damage Models: A Vanishing Viscosity Approach”. In: *Journal of Nonlinear Science* 29.3 (2019), pp. 1041–1094. ISSN: 1432-1467. DOI: `10.1007/s00332-018-9511-9`. URL: `https://doi.org/10.1007/s00332-018-9511-9`.

[52] Karlo Seleš et al. “A general phase-field model for fatigue failure in brittle and ductile solids”. In: *Computational Mechanics* 67.5 (2021), pp. 1431–1452. ISSN: 1432-0924. DOI: `10.1007/s00466-021-01996-5`.

[53] Martha Seiler et al. “An efficient phase-field model for fatigue fracture in ductile materials”. In: *Engineering Fracture Mechanics* 224 (2020), p. 106807. ISSN: 0013-7944. DOI: `https://doi.org/10.1016/j.engfracmech.2019.106807`. URL: `https://www.sciencedirect.com/science/article/pii/S0013794419303200`.

[54] Zeyad Khalil, Ahmed Y. Elghazouli, and Emilio Martínez-Pañeda. “A generalised phase field model for fatigue crack growth in elastic–plastic solids with an efficient monolithic solver”. In: *Computer Methods in Applied Mechanics and Engineering* 388 (2022), p. 114286. ISSN: 0045-7825. DOI: `https://doi.org/10.1016/j.cma.2021.114286`.

[55] Roberto Alessi, Stefano Vidoli, and Laura De Lorenzis. “A phenomenological approach to fatigue with a variational phase-field model: The one-dimensional case”. In: *Engineering Fracture Mechanics* 190 (2018), pp. 53–73. ISSN: 0013-7944. DOI: `https://doi.org/10.1016/j.engfracmech.2017.11.036`.

[56] A Jaubert and J -J. Marigo. “Justification of Paris-type Fatigue Laws from Cohesive Forces Model via a Variational Approach”. In: *Continuum Mechanics and Thermodynamics* 18.1 (2006), pp. 23–45. ISSN: 1432-0959. DOI: `10.1007/s00161-006-0023-8`. URL: `https://doi.org/10.1007/s00161-006-0023-8`.

[57] Niino.M, Hirai.T, and Watanabe.R. “The functionally gradient materials”. In: *Jap Soc Compos Mat 13: 257-64.* (1987).

[58] Neubrand.A Rödel.J. “Gradient Materials: An Overview of a Novel Concept”. In: *Zeit Metall 88: 358-71.* (1997).

[59] H.A Bahr et al. “Cracks in functionally graded materials”. In: *Materials Science and Engineering: A* 362.1 (2003). Papers from the German Priority Programme (Functionally Graded Materials), pp. 2–16. DOI: `10.1016/S0921-5093(03)00582-3`.

[60] A. Moro, Y. Kuroda, and K. Kusaka. “Development status of the reusable high-performance engines with functionally graded materials”. In: *Acta Astronautica* 50 (Apr. 2002), pp. 427–432. DOI: `10.1016/S0094-5765(01)00174-6`.

[61] Chenglin Chu et al. "Structure optimization and properties of hydroxyapatite-Ti symmetrical functionally graded biomaterial". In: *Materials Science and Engineering: A* 316.1 (2001), pp. 205–210. ISSN: 0921-5093. DOI: `https://doi.org/10.1016/S0921-5093(01)01239-4`.

[62] T. Guillén-Hernández, J. Reinoso, and M. Paggi. "Phase field model for fracture analysis of functionally graded power-based shell structures". In: *Mechanics of Advanced Materials and Structures* 0.0 (2020), pp. 1–11. DOI: `10.1080/15376494.2020.1751354`.

[63] F. Delale and F. Erdogan. "The Crack Problem for a Nonhomogeneous Plane". In: *Journal of Applied Mechanics* 50.3 (Sept. 1983), pp. 609–614. ISSN: 0021-8936. DOI: `10.1115/1.3167098`.

[64] Noboru Konda and F. Erdogan. "The mixed mode crack problem in a nonhomogeneous elastic medium". In: *Engineering Fracture Mechanics* 47.4 (1994), pp. 533–545. ISSN: 0013-7944. DOI: `https://doi.org/10.1016/0013-7944(94)90253-4`.

[65] Matthew T. Tilbrook. "Fatigue Crack Propagation in Functionally Graded Materials". PhD thesis. School of Materials Science & Engineering, University of New South Wales, 2005.

[66] F. Erdogan. "Fracture mechanics of functionally graded materials". In: *Composites Engineering* 5.7 (1995), pp. 753–770. ISSN: 0961-9526. DOI: `https://doi.org/10.1016/0961-9526(95)00029-M`.

[67] Z.-H. Jin and R.C. Batra. "Some basic fracture mechanics concepts in functionally graded materials". In: *Journal of the Mechanics and Physics of Solids* 44.8 (1996), pp. 1221–1235. ISSN: 0022-5096. DOI: `https://doi.org/10.1016/0022-5096(96)00041-5`.

[68] Pei Gu and R.J. Asaro. "Cracks in functionally graded materials". In: *International Journal of Solids and Structures* 34.1 (1997), pp. 1–17. ISSN: 0020-7683. DOI: `https://doi.org/10.1016/0020-7683(95)00289-8`.

[69] Pei Gu and R.J. Asaro. "Crack deflection in functionally graded materials". In: *International Journal of Solids and Structures* 34.24 (1997), pp. 3085–3098. ISSN: 0020-7683. DOI: `https://doi.org/10.1016/S0020-7683(96)00175-8`.

[70] J.E. Dolbow and J.C. Nadeau. "On the use of effective properties for the fracture analysis of microstructured materials". In: *Engineering Fracture Mechanics* 69.14 (2002), pp. 1607–1634. ISSN: 0013-7944. DOI: `https://doi.org/10.1016/S0013-7944(02)00052-8`.

[71] Jeong-Ho Kim and Glaucio H. Paulino. "Simulation of Crack Propagation in Functionally Graded Materials Under Mixed-Mode and Non-Proportional Loading". In: *Mechanics and Materials in Design* 1.1 (Mar. 2004), pp. 63–94. ISSN: 1573-8841. DOI: `10.1023/B:MAMD.0000035457.78797.c5`.

[72] Matthew T. Tilbrook, Robert J. Moon, and Mark Hoffman. "Crack propagation in graded composites". In: *Composites Science and Technology* 65.2 (2005), pp. 201–220. ISSN: 0266-3538. DOI: `https://doi.org/10.1016/j.compscitech.2004.07.004`.

[73] Emilio Martínez-Pañeda. "On the Finite Element Implementation of Functionally Graded Materials." In: *Materials (Basel, Switzerland)* 12(2) (Jan. 2019), p. 287. DOI: `10.3390/ma12020287`.

[74] J. Reinoso, M. Paggi, and R. Rolfes. "A computational framework for the interplay between delamination and wrinkling in functionally graded thermal barrier coatings". In: *Computational Materials Science* 116 (2016). Articles from EUROMECH Colloquium 577 "Micromechanics of Metal Ceramic Composites", pp. 82–95. ISSN: 0927-0256. DOI: `https://doi.org/10.1016/j.commatsci.2015.08.031`. URL: `http://www.sciencedirect.com/science/article/pii/S0927025615005406`.

[75] M. Steigemann et al. "Simulation of crack paths in functionally graded materials". In: *Engineering Fracture Mechanics* 77.11 (2010), pp. 2145–2157. ISSN: 0013-7944. DOI: `https://doi.org/10.1016/j.engfracmech.2010.03.022`.

[76] J. W. Eischen. "Fracture of nonhomogeneous materials". In: *International Journal of Fracture* 34.1 (May 1987), pp. 3–22. ISSN: 1573-2673. DOI: `10.1007/BF00042121`.

[77] P. Gu, M. Dao, and R. J. Asaro. "A Simplified Method for Calculating the Crack-Tip Field of Functionally Graded Materials Using the Domain Integral". In: *Journal of Applied Mechanics* 66.1 (Mar. 1999), pp. 101–108. ISSN: 0021-8936. DOI: `10.1115/1.2789135`.

[78] G. Anlas, M.H. Santare, and J. Lambros. "Numerical Calculation of Stress Intensity Factors in Functionally Graded Materials". In: *International Journal of Fracture* 104.2 (July 2000), pp. 131–143. ISSN: 1573-2673. DOI: `10.1023/A:1007652711735`.

[79] G. Bao and L. Wang. "Multiple cracking in functionally graded ceramic/metal coatings". In: *International Journal of Solids and Structures* 32.19 (1995), pp. 2853–2871. ISSN: 0020-7683. DOI: `https://doi.org/10.1016/0020-7683(94)00267-Z`.

[80] Jeong-Ho Kim and Glaucio H. Paulino. "Finite element evaluation of mixed mode stress intensity factors in functionally graded materials". In: *International Journal for Numerical Methods in Engineering* 53.8 (2002), pp. 1903–1935. DOI: `10.1002/nme.364`.

[81] Claudia Comi and Stefano Mariani. “Extended finite element simulation of quasi-brittle fracture in functionally graded materials”. In: *Computer Methods in Applied Mechanics and Engineering* 196.41 (2007), pp. 4013–4026. ISSN: 0045-7825. DOI: `https://doi.org/10.1016/j.cma.2007.02.014`. URL: `http://www.sciencedirect.com/science/article/pii/S0045782507001697`.

[82] Hamid Bayesteh and Soheil Mohammadi. “XFEM fracture analysis of orthotropic functionally graded materials”. In: *Composites Part B: Engineering* 44.1 (2013), pp. 8–25. ISSN: 1359-8368. DOI: `https://doi.org/10.1016/j.compositesb.2012.07.055`. URL: `http://www.sciencedirect.com/science/article/pii/S1359836812005100`.

[83] Martínez-Pañeda and E. Gallego. “Numerical analysis of quasi-static fracture in functionally graded materials”. In: *Int J Mech Mater Des* 11 (2015), pp. 405–424. DOI: `https://doi.org/10.1007/s10999-014-9265-y`. URL: `https://link.springer.com/article/10.1007/s10999-014-9265-y#citeas`.

[84] S. Song Ooi E.T. Natarajan. “Crack propagation modelling in functionally graded materials using scaled boundary polygons”. In: *International journal of fracture* 192 (2015), pp. 87–105. DOI: `https://doi.org/10.1007/s10704-015-9987-3`.

[85] Z.-H. Jin, G.H. Paulino, and R.H. Dodds Jr. “Finite element investigation of quasi-static crack growth functionally graded materials using a novel cohesive zone fracture model”. In: *Journal of Applied Mechanics, Transactions ASME* 69.3 (2002), pp. 370–379. DOI: `10.1115/1.1467092`.

[86] S.S.V. Kandula et al. “Cohesive modeling of dynamic fracture in functionally graded materials”. In: *Int J Fract* 132.3 (2005), pp. 275–296.

[87] Chunyu Li, Zhenzhu Zou, and Zhuping Duan. “Multiple isoparametric finite element method for nonhomogeneous media”. In: *Mechanics Research Communications* 27.2 (2000), pp. 137–142. ISSN: 0093-6413. DOI: `https://doi.org/10.1016/S0093-6413(00)00073-2`.

[88] J.-H. Kim and G.H. Paulino. “Isoparametric graded finite elements for nonhomogeneous isotropic and orthotropic materials”. In: *Journal of Applied Mechanics, Transactions ASME* 69.4 (2002), pp. 502–514. DOI: `10.1115/1.1467094`.

[89] Zhengyu (Jenny) Zhang and Glaucio H. Paulino. “Cohesive zone modeling of dynamic failure in homogeneous and functionally graded materials”. In: *International Journal of Plasticity* 21.6 (2005). Plasticity of Multiphase Materials, pp. 1195–1254. ISSN: 0749-6419. DOI: `https://doi.org/10.1016/j.ijplas.2004.06.009`.

[90] Hirshikesh et al. “Phase field modelling of crack propagation in functionally graded materials”. In: *Composites Part B: Engineering* 169 (2019), pp. 239–248. ISSN: 1359-8368. DOI: `https://doi.org/10.1016/j.compositesb.2019.04.003`.

[91] Hossein Saberi et al. “FRP-confined concrete model based on damage-plasticity and phase-field approaches”. In: *Composite Structures* 244 (2020), p. 112263. ISSN: 0263-8223. DOI: `https://doi.org/10.1016/j.compstruct.2020.112263`.

[92] Thanh-Tung Nguyen, Danièle Waldmann, and Tinh Quoc Bui. “Role of interfacial transition zone in phase field modeling of fracture in layered heterogeneous structures”. In: *Journal of Computational Physics* 386 (2019), pp. 585–610. ISSN: 0021-9991. DOI: `https://doi.org/10.1016/j.jcp.2019.02.022`.

[93] Thanh-Tung Nguyen, Danièle Waldmann, and Tinh Quoc Bui. “Computational chemo-thermo-mechanical coupling phase-field model for complex fracture induced by early-age shrinkage and hydration heat in cement-based materials”. In: *Computer Methods in Applied Mechanics and Engineering* 348 (2019), pp. 1–28. ISSN: 0045-7825. DOI: `https://doi.org/10.1016/j.cma.2019.01.012`.

[94] Peng Zhang et al. “Modelling distinct failure mechanisms in composite materials by a combined phase field method”. In: *Composite Structures* 232 (2020), p. 111551. ISSN: 0263-8223. DOI: `https://doi.org/10.1016/j.compstruct.2019.111551`.

[95] T. Guillén-Hernández et al. “A micromechanical analysis of inter-fiber failure in long reinforced composites based on the phase field approach of fracture combined with the cohesive zone model”. In: *International Journal of Fracture* (2019). ISSN: 1573-2673. DOI: `10.1007/s10704-019-00384-8`. URL: `https://doi.org/10.1007/s10704-019-00384-8`.

[96] A. Quintanas-Corominas et al. “A phase field approach to simulate intralaminar and translaminar fracture in long fiber composite materials”. In: *Composite Structures* (2019). ISSN: 0263-8223. DOI: `10.1016/j.compstruct.2019.02.007`.

[97] J. Reinoso et al. “Strength prediction of notched thin ply laminates using finite fracture mechanics and the phase field approach”. In: *Composites Science and Technology* 150 (2017), pp. 205–216.

[98] V. Carollo, J. Reinoso, and M. Paggi. “A 3D finite strain model for intralayer and interlayer crack simulation coupling the phase field approach and cohesive zone model”. In: *Composite Structures* 182 (2017), pp. 636–651. ISSN: 0263-8223.

[99] Emilio Martínez-Pañeda, Alireza Golahmar, and Christian F. Niordson. "A phase field formulation for hydrogen assisted cracking". In: *Computer Methods in Applied Mechanics and Engineering* 342 (2018), pp. 742–761. ISSN: 0045-7825. DOI: https://doi.org/10.1016/j.cma.2018.07.021. URL: http://www.sciencedirect.com/science/article/pii/S0045782518303529.

[100] M. Dittmann et al. "Variational phase-field formulation of non-linear ductile fracture". In: *Computer Methods in Applied Mechanics and Engineering* 342 (2018), pp. 71–94. ISSN: 0045-7825. DOI: https://doi.org/10.1016/j.cma.2018.07.029. URL: http://www.sciencedirect.com/science/article/pii/S0045782518303621.

[101] T. Guillén-Hernández et al. "In-situ strength effects in long fibre reinforced composites: A micro-mechanical analysis using the phase field approach of fracture". In: *Theoretical and Applied Fracture Mechanics* 108 (2020), p. 102621. ISSN: 0167-8442. DOI: https://doi.org/10.1016/j.tafmec.2020.102621. URL: http://www.sciencedirect.com/science/article/pii/S016784422030197X.

[102] Osman Gültekin, Hüsnü Dal, and Gerhard A. Holzapfel. "Numerical aspects of anisotropic failure in soft biological tissues favor energy-based criteria: A rate-dependent anisotropic crack phase-field model". In: *Computer Methods in Applied Mechanics and Engineering* 331 (2018), pp. 23–52. ISSN: 0045-7825. DOI: https://doi.org/10.1016/j.cma.2017.11.008. URL: http://www.sciencedirect.com/science/article/pii/S0045782517307132.

[103] Duc Hong Doan et al. "Hybrid phase field simulation of dynamic crack propagation in functionally graded glass-filled epoxy". In: *Composites Part B: Engineering* 99 (2016), pp. 266–276. ISSN: 1359-8368. DOI: https://doi.org/10.1016/j.compositesb.2016.06.016.

[104] Duc Hong Doan et al. "A rate-dependent hybrid phase field model for dynamic crack propagation". In: *Journal of Applied Physics* 122.11 (2017), p. 115102. DOI: 10.1063/1.4990073.

[105] Tinh Quoc Bui et al. "Analysis of transient dynamic fracture parameters of cracked functionally graded composites by improved meshfree methods". In: *Theoretical and Applied Fracture Mechanics* 96 (2018), pp. 642–657. ISSN: 0167-8442. DOI: https://doi.org/10.1016/j.tafmec.2017.10.005.

[106] René de Borst and Clemens V. Verhoosel. "Gradient damage vs phase-field approaches for fracture: Similarities and differences". In: *Computer Methods in Applied Mechanics and Engineering* 312 (2016). Phase Field Approaches to

Fracture, pp. 78–94. ISSN: 0045-7825. DOI: `https://doi.org/10.1016/j.cma.2016.05.015`.

[107] J. Abanto-Bueno and J. Lambros. “An Experimental Study of Mixed Mode Crack Initiation and Growth in Functionally Graded Materials”. In: *Experimental Mechanics* 46.2 (Apr. 2006), pp. 179–196. ISSN: 1741-2765. DOI: `10.1007/s11340-006-6416-6`.

[108] M.T. Tilbrook et al. “Crack propagation paths in layered, graded composites”. In: *Composites Part B: Engineering* 37.6 (2006), pp. 490–498. ISSN: 1359-8368. DOI: `https://doi.org/10.1016/j.compositesb.2006.02.012`.

[109] T.T. Nguyen et al. “A phase-field method for computational modeling of interfacial damage interacting with crack propagation in realistic microstructures obtained by microtomography”. In: *Computer Methods in Applied Mechanics and Engineering* 312 (2016). Phase Field Approaches to Fracture, pp. 567–595. ISSN: 0045-7825. DOI: `https://doi.org/10.1016/j.cma.2015.10.007`.

[110] E. Tanné et al. “Crack nucleation in variational phase-field models of brittle fracture”. In: *Journal of the Mechanics and Physics of Solids* 110 (2018), pp. 80–99. ISSN: 0022-5096. DOI: `https://doi.org/10.1016/j.jmps.2017.09.006`.

[111] M. Paggi and J. Reinoso. “Revisiting the problem of a crack impinging on an interface:A modeling framework for the interaction between the phase field approach for brittle fracture and the interface cohesive zone model”. In: *Computer Methods in Applied Mechanics and Engineering* 321 (2017), pp. 145–172. ISSN: 0045-7825. DOI: `https://doi.org/10.1016/j.cma.2017.04.004`.

[112] Blaise Bourdin, Christopher J. Larsen, and Casey L. Richardson. “A time-discrete model for dynamic fracture based on crack regularization”. In: *International Journal of Fracture* 168.2 (2011), pp. 133–143. DOI: `10.1007/s10704-010-9562-x`.

[113] Gilles A. Francfort and Christopher J. Larsen. “Existence and convergence for quasi-static evolution in brittle fracture”. In: *Communications on Pure and Applied Mathematics* 56.10 (2003), pp. 1465–1500. DOI: `10.1002/cpa.3039`.

[114] Michael J. Borden et al. “A higher-order phase-field model for brittle fracture: Formulation and analysis within the isogeometric analysis framework”. In: *Computer Methods in Applied Mechanics and Engineering* 273 (2014), pp. 100–118. ISSN: 0045-7825. DOI: `https://doi.org/10.1016/j.cma.2014.01.016`.

[115] Flaviana Iurlano. “A density result for GSBD and its application to the approximation of brittle fracture energies”. In: *Calculus of Variations* 51 (Apr. 2014), pp. 315–. DOI: `10.1007/s00526-013-0676-7`.

[116] Antonin Chambolle and Vito Crismale. *Compactness and lower semicontinuity in $GSBD$*. 2018. arXiv: `1802.03302 [math.FA]`.

[117] A. Dean et al. “A phase field approach for ductile fracture of short fibre reinforced composites”. In: *Theoretical and Applied Fracture Mechanics* 106 (2020), p. 102495. ISSN: 0167-8442. DOI: `https://doi.org/10.1016/j.tafmec.2020.102495`.

[118] A. Dean et al. “A multi phase-field fracture model for long fiber reinforced composites based on the Puck theory of failure”. In: *Composite Structures* 251 (2020), p. 112446. ISSN: 0263-8223. DOI: `https://doi.org/10.1016/j.compstruct.2020.112446`.

[119] Luigi Ambrosio and Vincenzo Maria Tortorelli. “Approximation of functional depending on jumps by elliptic functional via Γ-convergence”. In: *Communications on Pure and Applied Mathematics* 43.8 (), pp. 999–1036. DOI: `10.1002/cpa.3160430805`.

[120] G. Alberti. “Variational models for phase transitions, an approach via Γ-convergence”. In: *Calculus of Variations and Partial Differential Equations: Topics on Geometrical Evolution Problems and Degree Theory*. Berlin, Heidelberg: Springer Berlin Heidelberg, 2000, pp. 95–114. DOI: `10.1007/978-3-642-57186-2_3`.

[121] L. Evans. “Measure Theory and Fine Properties of Functions.” In: 1992. DOI: `https://doi.org/10.1201/9780203747940`.

[122] Jian-Ying Wu et al. “Phase field modelling of fracture”. In: *Advances in Applied Mechanics* 53 (Sept. 2019).

[123] A. Simone et al. “Interpolation requirements for implicit gradient-enhanced continuum damage models”. In: *Communications in Numerical Methods in Engineering* 19.7 (2003), pp. 563–572. DOI: `10.1002/cnm.597`.

[124] Jian-Ying Wu, Yuli Huang, and Vinh Phu Nguyen. “On the BFGS monolithic algorithm for the unified phase field damage theory”. In: *Computer Methods in Applied Mechanics and Engineering* 360 (2020), p. 112704. ISSN: 0045-7825. DOI: `https://doi.org/10.1016/j.cma.2019.112704`. URL: `http://www.sciencedirect.com/science/article/pii/S0045782519305924`.

[125] Philip K. Kristensen and Emilio Martínez-Pañeda. "Phase field fracture modelling using quasi-Newton methods and a new adaptive step scheme". In: *Theoretical and Applied Fracture Mechanics* 107 (2020), p. 102446. ISSN: 0167-8442. DOI: `https://doi.org/10.1016/j.tafmec.2019.102446`. URL: `http://www.sciencedirect.com/science/article/pii/S0167844219305580`.

[126] G.V. Galvez J. Elices M. Guinea and Planas J. "Crack trajectories under mixed mode and non-proportional loading." In: *International Journal of Fracture* (1996), pp. 171–193.

[127] Jin-Rae Cho. "Evaluation of stress intensity factors in functionally graded materials by natural element method". In: *Journal of Mechanical Science and Technology* 33.1 (Jan. 2019), pp. 299–306. DOI: `10.1007/s12206-018-1229-y`.

[128] F. Fantoni et al. "A phase field approach for damage propagation in periodic microstructured materials". In: *International Journal of Fracture* 223 (2029), pp. 53–76. ISSN: 0263-8223.

[129] P.K. Asur Vijaya Kumar et al. "A multi phase-field-cohesive zone model for laminated composites: Application to delamination migration". In: *Composite Structures* 276 (2021), p. 114471. ISSN: 0263-8223. DOI: `https://doi.org/10.1016/j.compstruct.2021.114471`. URL: `https://www.sciencedirect.com/science/article/pii/S0263822321009338`.

[130] A. Dean et al. "A multi phase-field fracture model for long fiber reinforced composites based on the Puck theory of failure". In: *Composite Structures* 251 (2020), p. 112446. ISSN: 0263-8223. DOI: `https://doi.org/10.1016/j.compstruct.2020.112446`.

[131] A. Dean et al. "Finite deformation model for short fibre reinforced composites: Application to hybrid metal-composite clinching joints". In: *Composite Structures* 150 (2016), pp. 162–171.

[132] A. Dean et al. "An invariant-based anisotropic material model for short fiber-reinforced thermoplastics: Coupled thermo-plastic formulation". In: *Composites Part A: Applied Science and Manufacturing* 90 (2016), pp. 186–199.

[133] J. Reinoso et al. "Postbuckling behaviour of a pressurized stiffened composite panel – Part I: Experimental study". In: *Composite Structures* 94.5 (2012), pp. 1533–1543. ISSN: 0263-8223. DOI: `https://doi.org/10.1016/j.compstruct.2011.12.014`. URL: `http://www.sciencedirect.com/science/article/pii/S026382231100482X`.

[134] J. Reinoso et al. “A composite runout specimen subjected to tension–compression loading conditions: Experimental and global–local finite element analysis”. In: *Composite Structures* 101 (2013), pp. 274–289. ISSN: 0263-8223. DOI: https://doi.org/10.1016/j.compstruct.2012.12.056. URL: http://www.sciencedirect.com/science/article/pii/S0263822313000883.

[135] J Andersons and M König. “Dependence of fracture toughness of composite laminates on interface ply orientations and delamination growth direction”. In: *Composites Science and Technology* 64.13 (2004), pp. 2139–2152. ISSN: 0266-3538. DOI: https://doi.org/10.1016/j.compscitech.2004.03.007. URL: http://www.sciencedirect.com/science/article/pii/S0266353804000752.

[136] P. Robinson and D.Q. Song. “A Modified DCB Specimen for Mode I Testing of Multidirectional Laminates”. In: *Journal of Composite Materials* 26.11 (1992), pp. 1554–1577. DOI: 10.1177/002199839202601101. eprint: https://doi.org/10.1177/002199839202601101. URL: https://doi.org/10.1177/002199839202601101.

[137] Derek Hull and Yi Bing Shi. “Damage mechanism characterization in composite damage tolerance investigations”. In: *Composite Structures* 23.2 (1993), pp. 99–120. ISSN: 0263-8223. DOI: https://doi.org/10.1016/0263-8223(93)90015-I. URL: http://www.sciencedirect.com/science/article/pii/026382239390015I.

[138] Ronald Krueger et al. “Testing and Analysis of Composite Skin/Stringer Debonding under Multi-Axial Loading”. In: *Journal of Composite Materials* 34.15 (2000), pp. 1263–1300. DOI: 10.1177/002199830003401502. eprint: https://doi.org/10.1177/002199830003401502. URL: https://doi.org/10.1177/002199830003401502.

[139] Emile Greenhalgh and Sus Singh. “INVESTIGATION OF THE FAILURE MECHANISMS FOR DELAMINATION GROWTH FROM EMBEDDED DEFECTS”. In: (Apr. 2020).

[140] S.R. Hallett et al. “An experimental and numerical investigation into the damage mechanisms in notched composites”. In: *Composites Part A: Applied Science and Manufacturing* 40.5 (2009), pp. 613–624. ISSN: 1359-835X. DOI: https://doi.org/10.1016/j.compositesa.2009.02.021. URL: http://www.sciencedirect.com/science/article/pii/S1359835X09000499.

[141] J Reinoso, M Paggi, and A Blázquez. “A nonlinear finite thickness cohesive interface element for modeling delamination in fibre-reinforced composite laminates”. In: *Composites Part B: Engineering* 109 (2017), pp. 116–128.

[142] A. Turon et al. "A damage model for the simulation of delamination in advanced composites under variable-mode loading". In: *Mechanics of Materials* 38.11 (2006), pp. 1072–1089. ISSN: 0167-6636. DOI: `10.1016/j.mechmat.2005.10.003`.

[143] A. Turon et al. "An engineering solution for mesh size effects in the simulation of delamination using cohesive zone models". In: *Engineering Fracture Mechanics* 74.10 (2007), pp. 1665–1682. ISSN: 0013-7944. DOI: `10.1016/j.engfracmech.2006.08.025`.

[144] A. Turon et al. "Accurate simulation of delamination growth under mixed-mode loading using cohesive elements: Definition of interlaminar strengths and elastic stiffness". In: *Composite Structures* 92.8 (2010), pp. 1857–1864. ISSN: 0263-8223.

[145] James G. Ratcliffe, Michael W. Czabaj, and T. Kevin Obrien. "A Test for Characterizing Delamination Migration in Carbon/Epoxy Tape Laminates". In: 2012.

[146] M F Pernice et al. "Experimental Study on Delamination Migration in Composite Laminates". English. In: *Composites Part A: Applied Science and Manufacturing* 73 (2015), pp. 20–34. ISSN: 1359-835X. DOI: `10.1016/j.compositesa.2015.02.018`.

[147] D. Purslow. "Matrix fractography of fibre-reinforced epoxy composites". In: *Composites* 17.4 (1986), pp. 289–303. ISSN: 0010-4361. DOI: `https://doi.org/10.1016/0010-4361(86)90746-9`. URL: `http://www.sciencedirect.com/science/article/pii/0010436186907469`.

[148] Emile S. Greenhalgh, Charlotte Rogers, and Paul Robinson. "Fractographic observations on delamination growth and the subsequent migration through the laminate". In: *Composites Science and Technology* 69.14 (2009). The Sixteenth International Conference on Composite Materials with Regular Papers, pp. 2345–2351. ISSN: 0266-3538. DOI: `https://doi.org/10.1016/j.compscitech.2009.01.034`. URL: `http://www.sciencedirect.com/science/article/pii/S0266353809000499`.

[149] Maria Francesca Pernice et al. "Investigating Delamination Migration in Multidirectional Tape Laminates." In: June 2014.

[150] Ming-Yuan He and John W. Hutchinson. "Kinking of a Crack Out of an Interface". In: *Journal of Applied Mechanics* 56.2 (June 1989), pp. 270–278. ISSN: 0021-8936. DOI: `10.1115/1.3176078`. eprint: `https://asmedigitalcollection.asme.org/appliedmechanics/article-pdf/56/2/270/5460738/270\_1.pdf`. URL: `https://doi.org/10.1115/1.3176078`.

[151] L.F. Varandas et al. “Micromechanical analysis of interlaminar crack propagation between angled plies in mode I tests”. In: *Composite Structures* 220 (2019), pp. 827–841. ISSN: 0263-8223. DOI: `https://doi.org/10.1016/j.compstruct.2019.04.050`. URL: `http://www.sciencedirect.com/science/article/pii/S0263822318343605`.

[152] Carla Canturri et al. “Delamination growth directionality and the subsequent migration processes – The key to damage tolerant design”. In: *Composites Part A: Applied Science and Manufacturing* 54 (2013), pp. 79–87. ISSN: 1359-835X. DOI: `https://doi.org/10.1016/j.compositesa.2013.07.004`. URL: `http://www.sciencedirect.com/science/article/pii/S1359835X13001887`.

[153] Ted Belytschko, Robert Gracie, and Giulio Ventura. “A Review of Extended/Genera
Finite Element Methods for Material Modelling”. In: *Modelling and Simulation in Materials Science and Engineering* 17 (Apr. 2009), p. 043001. DOI: `10.1088/0965-0393/17/4/043001`.

[154] Ted Belytschko, Robert Gracie, and Giulio Ventura. “A review of extended/general
finite element methods for material modeling”. In: *Modelling and Simulation in Materials Science and Engineering* 17.4 (Apr. 2009), p. 043001. DOI: `10.1088/0965-0393/17/4/043001`.

[155] B.Y. Chen et al. “A floating node method for the modelling of discontinuities in composites”. In: *Engineering Fracture Mechanics* 127 (2014), pp. 104–134. ISSN: 0013-7944. DOI: `https://doi.org/10.1016/j.engfracmech.2014.05.018`. URL: `http://www.sciencedirect.com/science/article/pii/S0013794414001829`.

[156] Xiaole Li and Jiye Chen. “A highly efficient prediction of delamination migration in laminated composites using the extended cohesive damage model”. In: *Composite Structures* 160 (Oct. 2016). DOI: `10.1016/j.compstruct.2016.10.098`.

[157] A. Arteiro et al. “Micro-mechanical analysis of the effect of ply thickness on the transverse compressive strength of polymer composites”. In: *Composites Part A: Applied Science and Manufacturing* 79 (2015), pp. 127–137. ISSN: 1359-835X. DOI: `https://doi.org/10.1016/j.compositesa.2015.09.015`. URL: `http://www.sciencedirect.com/science/article/pii/S1359835X1500336X`.

[158] P Maimí et al. “A continuum damage model for composite laminates: {Part I} - Constitutive model”. In: *Mechanics of materials* 39 (2007), pp. 897–908.

[159] J. Reinoso et al. “A consistent anisotropic damage model for laminated fiber-reinforced composites using the 3D-version of the Puck failure criterion”. In: *International Journal of Solids and Structures* (2017), pp. 37–53. DOI: `10.1016/j.ijsolstr.2017.07.023`.

[160] Gilles Pijaudier-Cabot and Zdeněk P. Bažant. "Nonlocal Damage Theory". In: *Journal of Engineering Mechanics* 113.10 (1987), pp. 1512–1533. DOI: `10.1061/(ASCE)0733-9399(1987)113:10(1512)`.

[161] A. Quintanas-Corominas et al. "A phase field approach enhanced with a cohesive zone model for modeling delamination induced by matrix cracking". In: *Computer Methods in Applied Mechanics and Engineering* 358 (2020), p. 112618. ISSN: 0045-7825. DOI: `https://doi.org/10.1016/j.cma.2019.112618`. URL: `http://www.sciencedirect.com/science/article/pii/S0045782519304943`.

[162] M. Paggi and J. Reinoso. "Revisiting the problem of a crack impinging on an interface:A modeling framework for the interaction between the phase field approach for brittle fracture and the interface cohesive zone model". In: *Computer Methods in Applied Mechanics and Engineering* 321 (2017), pp. 145–172. ISSN: 0045-7825. DOI: `https://doi.org/10.1016/j.cma.2017.04.004`. URL: `http://www.sciencedirect.com/science/article/pii/S0045782516317066`.

[163] E. Tanné et al. "Crack nucleation in variational phase-field models of brittle fracture". In: *Journal of the Mechanics and Physics of Solids* 110 (2018), pp. 80–99. ISSN: 0022-5096. DOI: `10.1016/j.jmps.2017.09.006`.

[164] A. Puck and H. Schürmann. "Failure analysis of FRP laminates by means of physically based phenomenological models". In: *Composites Science and Technology* 62.12 (2002), pp. 1633–1662. ISSN: 0266-3538. DOI: `https://doi.org/10.1016/S0266-3538(01)00208-1`. URL: `http://www.sciencedirect.com/science/article/pii/S0266353801002081`.

[165] H Matthias Deuschle and Bernd-H Kröplin. "Finite element implementation of Puck's failure theory for fibre-reinforced composites under three-dimensional stress". In: *Journal of Composite Materials* 46.19-20 (2012), pp. 2485–2513. DOI: `10.1177/0021998312451480`.

[166] "Measurement of the compressive crack resistance curve of composites using the size effect law". In: *Composites Part A: Applied Science and Manufacturing* 56 (2014), pp. 300–307. ISSN: 1359-835X. DOI: `https://doi.org/10.1016/j.compositesa.2013.10.017`. URL: `http://www.sciencedirect.com/science/article/pii/S1359835X13002923`.

[167] G. Catalanotti and J. Xavier. "Measurement of the mode II intralaminar fracture toughness and R-curve of polymer composites using a modified Iosipescu specimen and the size effect law". In: *Engineering Fracture Mechanics* 138 (2015), pp. 202–214. ISSN: 0013-7944. DOI: `https://doi.org/10.1016/j.engfracmech.2015.03.005`. URL: `http://www.sciencedirect.com/science/article/pii/S0013794415000776`.

[168] Pedro Camanho et al. "Prediction of in situ strengths and matrix cracking in composites under transverse tension and in-plane shear". In: *Composites Part A: Applied Science and Manufacturing* 37 (Feb. 2006), pp. 165–176. DOI: `10.1016/j.compositesa.2005.04.023`.

[169] Pavan Kumar Asur Vijaya Kumar et al. "Non-linear thermoelastic analysis of thin-walled structures with cohesive-like interfaces relying on the solid shell concept". In: *Finite Elements in Analysis and Design* 202 (2022), p. 103696. ISSN: 0168-874X. DOI: `https://doi.org/10.1016/j.finel.2021.103696`.

[170] Pavan Kumar Asur Vijaya Kumar et al. "Nonlinear thermoelastic phase-field fracture of thin-walled structures relying on solid shell concepts: Theory and applications". In: *Submitted to CMAME* - (-), pp. -. ISSN: -.

[171] Pavan Kumar Asur Vijaya Kumar et al. "Thermo-elastic solid shell formulation with phase field fracture for thin-walled FGMs". In: *Submitted to Composites: Part-B Engineering* - (-), pp. -. ISSN: -.

[172] Francesca Fantoni, Andrea Bacigalupo, and Marco Paggi. "Design of thermo-piezoelectric microstructured bending actuators via multi-field asymptotic homogenization". In: *International Journal of Mechanical Sciences* 146-147 (2018), pp. 319–336. ISSN: 0020-7403. DOI: `https://doi.org/10.1016/j.ijmecsci.2018.07.019`.

[173] P Lenarda and M Paggi. "A geometrical multi-scale numerical method for coupled hygro-thermo-mechanical problems in photovoltaic laminates". In: *Computational Mechanics* 57.6 (2016), pp. 947–963. ISSN: 1432-0924. DOI: `10.1007/s00466-016-1271-5`.

[174] S.O. Ojo and M. Paggi. "A 3D coupled thermo-visco-elastic shear-lag formulation for the prediction of residual stresses in photovoltaic modules after lamination". In: *Composite Structures* 157 (2016), pp. 348–359. ISSN: 0263-8223. DOI: `https://doi.org/10.1016/j.compstruct.2016.08.036`.

[175] M Paggi, S Kajari-Schröder, and U Eitner. "Thermomechanical deformations in photovoltaic laminates". In: *The Journal of Strain Analysis for Engineering Design* 46.8 (2011), pp. 772–782. DOI: `10.1177/0309324711421722`.

[176] Marco Paggi and Alberto Sapora. "Numerical Modelling of Microcracking in PV Modules Induced by Thermo-mechanical Loads". In: *Energy Procedia* 38 (2013). Proceedings of the 3rd International Conference on Crystalline Silicon Photovoltaics (SiliconPV 2013), pp. 506–515. ISSN: 1876-6102. DOI: `https://doi.org/10.1016/j.egypro.2013.07.310`.

[177] Marco Paggi, Mauro Corrado, and Maria Alejandra Rodriguez. "A multiphysics and multi-scale numerical approach to microcracking and powerloss in photovoltaic modules". In: *Composite Structures* 95 (2013), pp. 630–638. ISSN: 0263-8223. DOI: `https://doi.org/10.1016/j.compstruct.2012.08.014`. URL: `https://www.sciencedirect.com/science/article/pii/S0263822312003807`.

[178] J. Reinoso, M. Paggi, and P. Areias. "A finite element framework for the interplay between delamination and buckling of rubber-like bi-material systems and stretchable electronics". In: *Journal of the European Ceramic Society* 36.9 (2016). CERMODEL 2015 Modelling and simulation meet innovation in Ceramics Technology, pp. 2371–2382. ISSN: 0955-2219. DOI: `https://doi.org/10.1016/j.jeurceramsoc.2016.01.002`. URL: `https://www.sciencedirect.com/science/article/pii/S0955221916300024`.

[179] O. Sluis, van der et al. "Effect of a hard coat layer on buckle delamination of thin ITO layers on a compliant elasto-plastic substrate: an experimental–numerical approach". English. In: 78 (2011). DOI: `10.1016/j.engfracmech.2011.01.013`.

[180] Timon Rabczuk and Goangseup Zi. "A Meshfree Method based on the Local Partition of Unity for Cohesive Cracks". In: *Computational Mechanics* 39.6 (2007), pp. 743–760. ISSN: 1432-0924. DOI: `10.1007/s00466-006-0067-4`. URL: `https://doi.org/10.1007/s00466-006-0067-4`.

[181] John Dolbow, Nicolas Moës, and Ted Belytschko. "Modeling fracture in Mindlin–Re plates with the extended finite element method". In: *International Journal of Solids and Structures* 37.48 (2000), pp. 7161–7183. ISSN: 0020-7683. DOI: `https://doi.org/10.1016/S0020-7683(00)00194-3`. URL: `https://www.sciencedirect.com/science/article/pii/S0020768300001943`.

[182] S. Natarajan et al. "Natural frequencies of cracked functionally graded material plates by the extended finite element method". In: *Composite Structures* 93.11 (2011), pp. 3082–3092. ISSN: 0263-8223. DOI: `https://doi.org/10.1016/j.compstruct.2011.04.007`. URL: `https://www.sciencedirect.com/science/article/pii/S0263822311001310`.

[183] Pedro M. A. Areias and Ted Belytschko. "Non-linear analysis of shells with arbitrary evolving cracks using XFEM". In: *International Journal for Numerical Methods in Engineering* 62.3 (2005), pp. 384–415. DOI: `https://doi.org/10.1002/nme.1192`. URL: `https://onlinelibrary.wiley.com/doi/abs/10.1002/nme.1192`.

[184] P. Areias, Jeong-Hoon Song, and T. Belytschko. "Analysis of fracture in thin shells by overlapping paired elements". In: *Computer Methods in Applied Mechanics and Engineering* 195 (2006), pp. 5343–5360.

[185] Thanh Chau-Dinh et al. "Phantom-node method for shell models with arbitrary cracks". In: *Computers & Structures* 92-93 (2012), pp. 242–256. ISSN: 0045-7949. DOI: `https://doi.org/10.1016/j.compstruc.2011.10.021`. URL: `https://www.sciencedirect.com/science/article/pii/S0045794911002768`.

[186] F. Caleyron et al. "Dynamic simulation of damage-fracture transition in smoothed particles hydrodynamics shells". In: *International Journal for Numerical Methods in Engineering* 90.6 (2012), pp. 707–738. DOI: `https://doi.org/10.1002/nme.3337`. URL: `https://onlinelibrary.wiley.com/doi/abs/10.1002/nme.3337`.

[187] T. Rabczuk, P. M. A. Areias, and T. Belytschko. "A meshfree thin shell method for non-linear dynamic fracture". In: *International Journal for Numerical Methods in Engineering* 72.5 (2007), pp. 524–548. DOI: `https://doi.org/10.1002/nme.2013`. URL: `https://onlinelibrary.wiley.com/doi/abs/10.1002/nme.2013`.

[188] "An extended isogeometric thin shell analysis based on Kirchhoff–Love theory". In: *Computer Methods in Applied Mechanics and Engineering* 284 (2015). Isogeometric Analysis Special Issue, pp. 265–291. ISSN: 0045-7825. DOI: `https://doi.org/10.1016/j.cma.2014.08.025`.

[189] S. Mostofizadeh, M. Fagerström, and R. Larsson. "Dynamic crack propagation in elastoplastic thin-walled structures: Modelling and validation". In: *International Journal for Numerical Methods in Engineering* 96.2 (2013), pp. 63–86. DOI: `https://doi.org/10.1002/nme.4524`. URL: `https://onlinelibrary.wiley.com/doi/abs/10.1002/nme.4524`.

[190] Pedro M.A. Areias, J.H. Song, and Ted Belytschko. "Analysis of fracture in thin shells by overlapping paired elements". In: *Computer Methods in Applied Mechanics and Engineering* 195.41 (2006). John H. Argyris Memorial Issue. Part II, pp. 5343–5360. ISSN: 0045-7825. DOI: `https://doi.org/10.1016/j.cma.2005.10.024`. URL: `https://www.sciencedirect.com/science/article/pii/S0045782505005475`.

[191] G. Becker, C. Geuzaine, and L. Noels. "A one field full discontinuous Galerkin method for Kirchhoff–Love shells applied to fracture mechanics". In: *Computer Methods in Applied Mechanics and Engineering* 200.45 (2011), pp. 3223–3241. ISSN: 0045-7825. DOI: `https://doi.org/10.1016/j.cma.2011.07.008`. URL: `https://www.sciencedirect.com/science/article/pii/S0045782511002490`.

[192] A. Ahmed, F.P. van der Meer, and L.J. Sluys. "A geometrically nonlinear discontinuous solid-like shell element (DSLS) for thin shell structures". In: *Computer Methods in Applied Mechanics and Engineering* 201-204 (2012), pp. 191–207. ISSN: 0045-7825. DOI: `https://doi.org/10.1016/j.cma.`

2011.10.008. URL: https://www.sciencedirect.com/science/article/pii/S0045782511003203.

[193] Mara Pagani and Umberto Perego. “Explicit dynamics simulation of blade cutting of thin elastoplastic shells using “directional” cohesive elements in solid-shell finite element models”. In: *Computer Methods in Applied Mechanics and Engineering* 285 (2015), pp. 515–541. ISSN: 0045-7825. DOI: https://doi.org/10.1016/j.cma.2014.11.027. URL: https://www.sciencedirect.com/science/article/pii/S0045782514004538.

[194] Fehmi Cirak, Michael Ortiz, and Anna Pandolfi. “A cohesive approach to thin-shell fracture and fragmentation”. In: *Computer Methods in Applied Mechanics and Engineering* 194.21 (2005). Computational Methods for Shells, pp. 2604–2618. ISSN: 0045-7825. DOI: https://doi.org/10.1016/j.cma.2004.07.048.

[195] Pablo D. Zavattieri. “Modeling of Crack Propagation in Thin-Walled Structures Using a Cohesive Model for Shell Elements”. In: *Journal of Applied Mechanics* 73.6 (Dec. 2005), pp. 948–958. ISSN: 0021-8936. DOI: 10.1115/1.2173286.

[196] Weizhou Li and Thomas Siegmund. “An analysis of crack growth in thin-sheet metal via a cohesive zone model”. In: *Engineering Fracture Mechanics* 69.18 (2002), pp. 2073–2093. ISSN: 0013-7944. DOI: https://doi.org/10.1016/S0013-7944(02)00013-9.

[197] Samuel Forest. “Micromorphic Approach for Gradient Elasticity, Viscoplasticity, and Damage”. In: *Journal of Engineering Mechanics* 135.3 (2009), pp. 117–131. DOI: 10.1061/(ASCE)0733-9399(2009)135:3(117).

[198] Tobias Waffenschmidt et al. “A gradient-enhanced large-deformation continuum damage model for fibre-reinforced materials”. In: *Computer Methods in Applied Mechanics and Engineering* 268 (2014), pp. 801–842. ISSN: 0045-7825. DOI: https://doi.org/10.1016/j.cma.2013.10.013.

[199] Aamir Dean et al. “A thermodynamically consistent framework to couple damage and plasticity microplane-based formulations for fracture modeling: development and algorithmic treatment”. In: *International Journal of Fracture* 203 (June 2016), pp. 115–134. DOI: 10.1007/s10704-016-0131-9.

[200] L. Vu-Quoc and X.G. Tan. “Optimal solid shells for non-linear analyses of multilayer composites. I. Statics”. In: *Computer Methods in Applied Mechanics and Engineering* 192.9 (2003), pp. 975–1016. ISSN: 0045-7825. DOI: https://doi.org/10.1016/S0045-7825(02)00435-8.

[201] Y. Başar and Y. Ding. “Shear deformation models for large-strain shell analysis”. In: *International Journal of Solids and Structures* 34.14 (1997), pp. 1687–1708. ISSN: 0020-7683. DOI: https://doi.org/10.1016/S0020-7683(96)00121-7.

[202] P. Betsch, F. Gruttmann, and E. Stein. "A 4-node finite shell element for the implementation of general hyperelastic 3D-elasticity at finite strains". In: *Computer Methods in Applied Mechanics and Engineering* 130.1 (1996), pp. 57–79. ISSN: 0045-7825. DOI: `https://doi.org/10.1016/0045-7825(95)00920-5`.

[203] Boštjan Brank. "Nonlinear shell models with seven kinematic parameters". In: *Computer Methods in Applied Mechanics and Engineering* 194.21 (2005). Computational Methods for Shells, pp. 2336–2362. ISSN: 0045-7825. DOI: `https://doi.org/10.1016/j.cma.2004.07.036`.

[204] Norbert Büchter, Ekkehard Ramm, and Deane Roehl. "Three-dimensional extension of non-linear shell formulation based on the enhanced assumed strain concept". In: *International Journal for Numerical Methods in Engineering* 37.15 (1994), pp. 2551–2568. DOI: `https://doi.org/10.1002/nme.1620371504`.

[205] Christian Miehe. "A theoretical and computational model for isotropic elastoplastic stress analysis in shells at large strains". In: *Computer Methods in Applied Mechanics and Engineering* 155.3 (1998), pp. 193–233. ISSN: 0045-7825. DOI: `https://doi.org/10.1016/S0045-7825(97)00149-7`.

[206] H. Parisch. "A continuum-based shell theory for non-linear applications". In: *International Journal for Numerical Methods in Engineering* 38.11 (1995), pp. 1855–1883. DOI: `https://doi.org/10.1002/nme.1620381105`.

[207] J. Reinoso and A. Blázquez. "Application and finite element implementation of 7-parameter shell element for geometrically nonlinear analysis of layered CFRP composites". In: *Composite Structures* 139 (2016), pp. 263–276. ISSN: 0263-8223. DOI: `https://doi.org/10.1016/j.compstruct.2015.12.009`.

[208] J.C. Simo, M.S. Rifai, and D.D. Fox. "On a stress resultant geometrically exact shell model. Part IV: Variable thickness shells with through-the-thickness stretching". In: *Computer Methods in Applied Mechanics and Engineering* 81.1 (1990), pp. 91–126. ISSN: 0045-7825. DOI: `https://doi.org/10.1016/0045-7825(90)90143-A`.

[209] Matthias Harnau and Karl Schweizerhof. "About linear and quadratic "Solid-Shell" elements at large deformations". In: *Computers & Structures* 80.9 (2002), pp. 805–817. ISSN: 0045-7949. DOI: `https://doi.org/10.1016/S0045-7949(02)00048-2`.

[210] S. Klinkel and W. Wagner. "A geometrical non-linear brick element based on the EAS-method". In: *International Journal for Numerical Methods in Engineering* 40.24 (1997), pp. 4529–4545. DOI: `https://doi.org/10.1002/(SICI)1097-0207(19971230)40:24<4529::AID-NME271>3.0.CO;2-I`.

[211] Marco Schwarze and Stefanie Reese. "A reduced integration solid-shell finite element based on the EAS and the ANS concept—Large deformation problems". In: *International Journal for Numerical Methods in Engineering* 85.3 (2011), pp. 289–329. DOI: `https://doi.org/10.1002/nme.2966`.

[212] M Braun, M Bischoff, and E Ramm. "Nonlinear shell formulations for complete three-dimensional constitutive laws including composites and laminates". In: *Computational Mechanics* 15.1 (1994), pp. 1–18. ISSN: 1432-0924. DOI: `10.1007/BF00350285`.

[213] Klaus-Jürgen Bathe and Eduardo N. Dvorkin. "A four-node plate bending element based on Mindlin/Reissner plate theory and a mixed interpolation". In: *International Journal for Numerical Methods in Engineering* 21.2 (1985), pp. 367–383. DOI: `https://doi.org/10.1002/nme.1620210213`.

[214] M. Bischoff and E. Ramm. "Shear deformable shell elements for large strains and rotations". In: *International Journal for Numerical Methods in Engineering* 40.23 (1997), pp. 4427–4449. DOI: `https://doi.org/10.1002/(SICI)1097-0207(19971215)40:23<4427::AID-NME268>3.0.CO;2-9`.

[215] R. Hauptmann, K. Schweizerhof, and S. Doll. "Extension of the 'solid-shell' concept for application to large elastic and large elastoplastic deformations". In: *International Journal for Numerical Methods in Engineering* 49.9 (2000), pp. 1121–1141. DOI: `https://doi.org/10.1002/1097-0207(20001130)49:9<1121::AID-NME130>3.0.CO;2-F`.

[216] Joze Korelc and Peter Wriggers. "Consistent gradient formulation for a stable enhanced strain method for large deformations". In: *Engineering Computations* 13.1 (Jan. 1996), pp. 103–123. ISSN: 0264-4401. DOI: `10.1108/02644409610111001`.

[217] J.C Simo, F Armero, and R.L Taylor. "Improved versions of assumed enhanced strain tri-linear elements for 3D finite deformation problems". In: *Computer Methods in Applied Mechanics and Engineering* 110.3 (1993), pp. 359–386. ISSN: 0045-7825. DOI: `https://doi.org/10.1016/0045-7825(93)90215-J`.

[218] J. C. Simo and M. S. Rifai. "A class of mixed assumed strain methods and the method of incompatible modes". In: *International Journal for Numerical Methods in Engineering* 29.8 (1990), pp. 1595–1638. DOI: `https://doi.org/10.1002/nme.1620290802`.

[219] R A Fontes Valente et al. "On the use of an enhanced transverse shear strain shell element for problems involving large rotations". In: *Computational Mechanics* 30.4 (2003), pp. 286–296. ISSN: 1432-0924. DOI: `10.1007/s00466-002-0388-x`.

[220] P. Betsch and E. Stein. "An assumed strain approach avoiding artificial thickness straining for a non-linear 4-node shell element". In: *Communications in Numerical Methods in Engineering* 11.11 (1995), pp. 899–909. DOI: `https://doi.org/10.1002/cnm.1640111104`.

[221] Eduardo N Dvorkin and Klaus-Jürgen Bathe. "A continuum mechanics based four-node shell element for general non-linear analysis". In: *Engineering Computations* 1.1 (Jan. 1984), pp. 77–88. ISSN: 0264-4401. DOI: `10.1108/eb023562`.

[222] Rui P. R. Cardoso et al. "Enhanced assumed strain (EAS) and assumed natural strain (ANS) methods for one-point quadrature solid-shell elements". In: *International Journal for Numerical Methods in Engineering* 75.2 (2008), pp. 156–187. DOI: `https://doi.org/10.1002/nme.2250`.

[223] F Gruttmann and W Wagner. "Structural analysis of composite laminates using a mixed hybrid shell element". In: *Computational Mechanics* 37.6 (2006), pp. 479–497. ISSN: 1432-0924. DOI: `10.1007/s00466-005-0730-1`.

[224] Eric P. Kasper and Robert L. Taylor. "A mixed-enhanced strain method: Part II: Geometrically nonlinear problems". In: *Computers & Structures* 75.3 (2000), pp. 251–260. ISSN: 0045-7949. DOI: `https://doi.org/10.1016/S0045-7949(99)00135-2`.

[225] Laurent Adam and Jean-Philippe Ponthot. "Thermomechanical modeling of metals at finite strains: First and mixed order finite elements". In: *International Journal of Solids and Structures* 42.21 (2005). PACAM VIII SPECIAL ISSUE, pp. 5615–5655. ISSN: 0020-7683. DOI: `https://doi.org/10.1016/j.ijsolstr.2005.03.020`.

[226] Raja Gopal Tangella, Pramod Kumbhar, and Ratna Kumar Annabattula. "Hybrid phase-field modeling of thermo-elastic crack propagation". In: *International Journal for Computational Methods in Engineering Science and Mechanics* 0.0 (2021), pp. 1–16. DOI: `10.1080/15502287.2021.1904462`.

[227] Hojjat Badnava et al. "An h-adaptive thermo-mechanical phase field model for fracture". In: *Finite Elements in Analysis and Design* 138 (2018), pp. 31–47. ISSN: 0168-874X. DOI: `https://doi.org/10.1016/j.finel.2017.09.003`.

[228] A. Dean et al. "An invariant-based anisotropic material model for short fiber-reinforced thermoplastics: Coupled thermo-plastic formulation". In: *Composites Part A: Applied Science and Manufacturing* 90 (2016), pp. 186–199. ISSN: 1359-835X. DOI: `https://doi.org/10.1016/j.compositesa.2016.06.015`.

[229] A. Dean et al. "A new invariant-based thermo-plastic model for finite deformation analysis of short fibre reinforced composites: Development and numerical aspects". In: *Composites Part B: Engineering* 125 (2017), pp. 241–258.

[230] Wenya Shu and Ilinca Stanciulescu. "Monolithic and Staggered Strategies Using Solid-Shell Formulations for Nonlinear Coupled Thermoelasticity". In: *Journal of Engineering Mechanics* 145.12 (2019), p. 04019095. DOI: `10.1061/(ASCE)EM.1943-7889.0001669`.

[231] P.K. Asur Vijaya Kumar et al. "Non-linear thermoelastic and fracture analysis of thin-walled structures with cohesive–like interfaces relying on the solid shell concept". In.

[232] Glaucio H.Paulino Kyoungsoo Park. "Cohesive Zone Models: A Critical Review of Traction-Separation Relationships Across Fracture Surfaces". In: *Applied Mechanics Reviews* 64 (2013). ISSN: 0003-6900. DOI: `https://doi.org/10.1115/1.4023110`.

[233] Viggo Tvergaard. "Effect of fibre debonding in a whisker-reinforced metal". In: *Materials Science and Engineering: A* 125.2 (1990), pp. 203–213. ISSN: 0921-5093. DOI: `https://doi.org/10.1016/0921-5093(90)90170-8`.

[234] M. Ortiz and A. Pandolfi. "Finite-deformation irreversible cohesive elements for three-dimensional crack-propagation analysis". In: *International Journal for Numerical Methods in Engineering* 44.9 (1999), pp. 1267–1282. DOI: `https://doi.org/10.1002/(SICI)1097-0207(19990330)44:9<1267::AID-NME486>3.0.CO;2-7`.

[235] Ashwin Hattiangadi and Thomas Siegmund. "A thermomechanical cohesive zone model for bridged delamination cracks". In: *Journal of the Mechanics and Physics of Solids* 52.3 (2004), pp. 533–566. ISSN: 0022-5096. DOI: `https://doi.org/10.1016/S0022-5096(03)00122-4`.

[236] R. Fleischhauer et al. "A thermomechanical interface description and its application to yarn pullout tests". In: *International Journal of Solids and Structures* 69-70 (2015), pp. 531–543. ISSN: 0020-7683. DOI: `https://doi.org/10.1016/j.ijsolstr.2015.04.030`.

[237] R. Fleischhauer and M. Kaliske R. Behnke. "A thermomechanical interface element formulation for finite deformations". In: *Computational Mechanics* 52 (2013), pp. 1039–1058. ISSN: 1432-0924. DOI: `10.1007/s00466-013-0862-7`.

[238] K. Willam, I. Rhee, and B. Shing. "Interface damage model for thermomechanical degradation of heterogeneous materials". In: *Computer Methods in Applied Mechanics and Engineering* 193.30 (2004). Computational Failure Mechanics, pp. 3327–3350. ISSN: 0045-7825. DOI: `https://doi.org/10.1016/j.cma.2003.09.020`.

[239] C. Balzani and W. Wagner. “An interface element for the simulation of delamination in unidirectional fiber-reinforced composite laminates”. In: *Engineering Fracture Mechanics* 75.9 (2008). Fracture of Composite Materials, pp. 2597–2615. ISSN: 0013-7944. DOI: `https://doi.org/10.1016/j.engfracmech.2007.03.013`.

[240] J Reinoso and M Paggi. “A consistent interface element formulation for geometrical and material nonlinearities”. In: *Computational Mechanics* 54.6 (2014), pp. 1569–1581. ISSN: 1432-0924. DOI: `10.1007/s00466-014-1077-2`.

[241] Christian Miehe. “A theoretical and computational model for isotropic elastoplastic stress analysis in shells at large strains”. In: *Computer Methods in Applied Mechanics and Engineering* 155.3 (1998), pp. 193–233. ISSN: 0045-7825. DOI: `https://doi.org/10.1016/S0045-7825(97)00149-7`.

[242] R. Hauptmann and K. Schweizerhof. “A systematic development of ‘solid-shell’ element formulations for linear and non-linear analyses employing only displacement degrees of freedom”. In: *International Journal for Numerical Methods in Engineering* 42.1 (1998), pp. 49–69. DOI: `https://doi.org/10.1002/(SICI)1097-0207(19980515)42:1<49::AID-NME349>3.0.CO;2-2`.

[243] Geralf Hütter. “Coleman–Noll Procedure for Classical and Generalized Continuum Theories”. In: *Encyclopedia of Continuum Mechanics*. Ed. by Holm Altenbach and Andreas Öchsner. Berlin, Heidelberg: Springer Berlin Heidelberg, 2017, pp. 1–8. ISBN: 978-3-662-53605-6. DOI: `$10.1007/978-3-662-53605-6_57-1$`.

[244] A. Turon et al. “A damage model for the simulation of delamination in advanced composites under variable-mode loading”. In: *Mechanics of Materials* 38.11 (2006), pp. 1072–1089. ISSN: 0167-6636. DOI: `https://doi.org/10.1016/j.mechmat.2005.10.003`.

[245] Stigh Ulf Walander Tomas. Biel Anders. “Temperature dependence of cohesive laws for an epoxy adhesive in Mode I and Mode II loading”. In: *International Journal of Fracture* 183.2 (2013), pp. 203–221. ISSN: 1573-2673. DOI: `10.1007/s10704-013-9887-3`.

[246] Wenya Shu and Ilinca Stanciulescu. “Monolithic and Staggered Strategies Using Solid-Shell Formulations for Nonlinear Coupled Thermoelasticity”. In: *Journal of Engineering Mechanics* 145.12 (2019), p. 04019095. DOI: `10.1061/(ASCE)EM.1943-7889.0001669`.

[247] P.Camanho and Carlos G. Davila. “Mixed-mode decohesion finite elements for the simulation of delamination in composite materials”. In: (). ISSN: NASA/TM-2002-211737. URL: `https://ntrs.nasa.gov/citations/20020053651`.

[248] Caroline Danowski et al. “A monolithic computational approach to thermo-structure interaction”. In: *International Journal for Numerical Methods in Engineering* 95.13 (2013), pp. 1053–1078. DOI: `https://doi.org/10.1002/nme.4530`. URL: `https://onlinelibrary.wiley.com/doi/abs/10.1002/nme.4530`.

[249] K.Y. Sze, X.H. Liu, and S.H. Lo. “Popular benchmark problems for geometric nonlinear analysis of shells”. In: *Finite Elements in Analysis and Design* 40.11 (2004), pp. 1551–1569. ISSN: 0168-874X. DOI: `https://doi.org/10.1016/j.finel.2003.11.001`.

[250] J Reinoso, M Paggi, and C Linder. “Phase field modeling of brittle fracture for enhanced assumed strain shells at large deformations: formulation and finite element implementation”. In: *Computational Mechanics* 59.6 (2017), pp. 981–1001. ISSN: 1432-0924. DOI: `10.1007/s00466-017-1386-3`.

[251] Gergely Molnár and Anthony Gravouil. “2D and 3D Abaqus implementation of a robust staggered phase-field solution for modeling brittle fracture”. In: *Finite Elements in Analysis and Design* 130 (2017), pp. 27–38. ISSN: 0168-874X. DOI: `https://doi.org/10.1016/j.finel.2017.03.002`.

[252] Christian Miehe and Lisa-Marie Schänzel. “Phase field modeling of fracture in rubbery polymers. Part I: Finite elasticity coupled with brittle failure”. In: *Journal of the Mechanics and Physics of Solids* 65 (2014), pp. 93–113. ISSN: 0022-5096. DOI: `https://doi.org/10.1016/j.jmps.2013.06.007`.

[253] M.A. Munoz et al. “Early degradation of silicon PV modules and guaranty conditions”. In: *Solar Energy* 85.9 (2011), pp. 2264–2274. ISSN: 0038-092X. DOI: `https://doi.org/10.1016/j.solener.2011.06.011`.

[254] Alberto Sapora and Marco Paggi. “A coupled cohesive zone model for transient analysis of thermoelastic interface debonding”. In: *Computational Mechanics* 53.4 (2014), pp. 845–857. ISSN: 1432-0924. DOI: `10.1007/s00466-013-0934-8`.

[255] Islam M El-Galy, Bassiouny I Saleh, and Mahmoud H Ahmed. “Functionally graded materials classifications and development trends from industrial point of view”. In: *SN Applied Sciences* 1.11 (2019), p. 1378. ISSN: 2523-3971. DOI: `10.1007/s42452-019-1413-4`.

[256] Aditya Kumar et al. “Revisiting nucleation in the phase-field approach to brittle fracture”. In: *Journal of the Mechanics and Physics of Solids* 142 (2020), p. 104027. ISSN: 0022-5096. DOI: `https://doi.org/10.1016/j.jmps.2020.104027`.